

**Dalitz Plot Analysis of  $B^0_d \rightarrow K^+ \pi^- \pi^0$  Decays**

Zhitang Yu

Stanford Linear Accelerator Center  
Stanford University  
Stanford, CA 94309

SLAC-Report-815

Prepared for the Department of Energy  
under contract number DE-AC02-76SF00515

Printed in the United States of America. Available from the National Technical Information Service, U.S. Department of Commerce, 5285 Port Royal Road, Springfield, VA 22161.

This document, and the material and data contained therein, was developed under sponsorship of the United States Government. Neither the United States nor the Department of Energy, nor the Leland Stanford Junior University, nor their employees, nor their respective contractors, subcontractors, or their employees, makes an warranty, express or implied, or assumes any liability of responsibility for accuracy, completeness or usefulness of any information, apparatus, product or process disclosed, or represents that its use will not infringe privately owned rights. Mention of any product, its manufacturer, or suppliers shall not, nor is it intended to, imply approval, disapproval, or fitness of any particular use. A royalty-free, nonexclusive right to use and disseminate same of whatsoever, is expressly reserved to the United States and the University.

DALITZ PLOT ANALYSIS OF  $B_d^0 \rightarrow K^+ \pi^- \pi^0$   
DECAYS

*by*

Zhitang Yu



A dissertation submitted in partial fulfillment of  
the requirements for the degree of

Doctor of Philosophy  
(Physics)

at the

UNIVERSITY OF WISCONSIN-MADISON

2005

## Abstract

This thesis describes a Dalitz plot analysis of  $B^0 \rightarrow K^+\pi^-\pi^0$  decays. The data sample comprises 213 million  $\Upsilon(4S) \rightarrow B\bar{B}$  decays collected with the *BABAR* detector at the PEP-II asymmetric-energy  $B$  Factory at the Stanford Linear Accelerator Center in California (SLAC). Preliminary results are presented for measurements of the inclusive branching fraction, quasi-two-body fractions and  $CP$ -violating charge asymmetries for intermediate states including  $K^*(892)^+\pi^-$  and  $\rho(770)^-K^+$ . Observations of  $B^0$  decays to the  $K\pi$   $S$ -wave intermediate states,  $K_0^*(1430)^+\pi^-$  and  $K_0^*(1430)^0\pi^0$ , are reported. Evidence of the decay  $B^0 \rightarrow K^*(892)^0\pi^0$  is seen. We set upper limits at 90% confidence level on branching fractions of the nonresonant and other less significant intermediate states.

## Declaration

This analysis represents the efforts of many members of the *BABAR* collaboration at the Stanford Linear Accelerator Center in California (SLAC). Although having been presented at the 32nd International Conference on High Energy Physics in 2004, the results reported in this thesis are still preliminary.

Zhitang Yu

## Acknowledgements

I would like to thank my adviser Dr. Sau Lan Wu for her academic guidance and tremendous support in the research and preparation of this thesis. I'm also grateful to Dr. Yibin Pan for his close guidance and fruitful discussions over the past years. Dr. Jose Ocariz has been a close co-author of this analysis. We have discussed every aspect about this analysis, including theoretical and technical details. He has also provided numerous validation tests and technical support to obtain the final results. Dr. Andreas Hoecker has been one of the co-authors and he has provided invaluable expertise to this analysis. He and Dr. Jinwei Wu have developed a technical framework that was then modified and generalized to perform this analysis. I should also thank Dr. Haibo Li and Dr. Mathew Graham for lots of useful discussions.

Finally, I would like to thank Dr. William M. Dunwoodie for very helpful discussions about the  $K\pi$   $S$ -wave parameterizations, and other expertise he has kindly provided. I am also grateful for the very helpful comments and suggestions from my review committee: Dr. Patrick Roudeau (chair), Dr. Giancarlo Piredda, and Dr. Denis Dujmic.

# Contents

<b>Abstract</b>	<b>i</b>
<b>Declaration</b>	<b>ii</b>
<b>Acknowledgements</b>	<b>iii</b>
<b>1 Introduction</b>	<b>1</b>
1.1 Classification of $CP$ Violation . . . . .	2
1.2 $CP$ Violation in the Standard Model . . . . .	4
1.3 Hadronic $B$ -meson Decays . . . . .	10
1.4 Isospin Analysis and $SU(3)$ Flavor Symmetry . . . . .	12
1.5 Analysis of $B_d^0 \rightarrow K^+\pi^-\pi^0$ Decays . . . . .	17
<b>2 The <i>BABAR</i> Experiment</b>	<b>21</b>
2.1 The PEP-II Collider . . . . .	22
2.2 The <i>BABAR</i> Detector . . . . .	24
2.2.1 The Silicon Vertex Tracker (SVT) . . . . .	25
2.2.1.1 Design of the SVT . . . . .	27
2.2.1.2 Performance of the SVT . . . . .	28

2.2.2	The Drift Chamber (DCH) . . . . .	28
2.2.2.1	Design of the DCH . . . . .	29
2.2.2.2	Performance of the DCH . . . . .	32
2.2.3	The Detector of Internally Reflected Cherenkov Light (DIRC) . . . . .	35
2.2.3.1	Design of the DIRC . . . . .	37
2.2.3.2	Performance of the DIRC . . . . .	38
2.2.4	The Electromagnetic Calorimeter (EMC) . . . . .	39
2.2.4.1	Design of the EMC . . . . .	40
2.2.4.2	Performance of the EMC . . . . .	41
2.2.5	The Instrumented Flux Return (IFR) . . . . .	42
2.2.5.1	Design of the IFR . . . . .	42
2.2.5.2	Performance of the IFR . . . . .	43
<b>3</b>	<b>The Decay Dynamics</b>	<b>47</b>
3.1	Dalitz Plot . . . . .	47
3.2	The Square Dalitz Plot . . . . .	53
3.3	Transition Amplitudes . . . . .	56
3.4	Normalization . . . . .	57
3.5	Interference Pattern . . . . .	57
<b>4</b>	<b>The Signal Model for <math>B^0 \rightarrow K^+\pi^-\pi^0</math></b>	<b>58</b>
4.1	Form Factors . . . . .	58
4.2	Higher Resonances . . . . .	62
4.3	Other Concerns . . . . .	64
4.4	The Nominal Signal Model . . . . .	65

<b>5</b>	<b>Data Samples and Event Selection</b>	<b>69</b>
5.1	Data Samples . . . . .	69
5.2	Event Selection . . . . .	71
5.3	Multiple Candidate Selection and Misreconstruction of Signal Events . . . . .	76
5.4	Multivariate Continuum Suppression . . . . .	80
5.5	Correlations . . . . .	83
<b>6</b>	<b><i>B</i>-Related Background</b>	<b>91</b>
6.1	Branching Fractions . . . . .	97
6.2	Background from Charmed <i>B</i> Decays . . . . .	100
6.3	Background from Kaon Resonances . . . . .	100
6.4	The modes $B^+ \rightarrow K^+(\pi\pi)^0$ . . . . .	101
6.5	The mode $B \rightarrow K^*K^{(*)}$ . . . . .	101
6.6	Higher Multiplicities $B \rightarrow K_{(X)}^{(**)}\rho$ . . . . .	102
<b>7</b>	<b>Building the Likelihood</b>	<b>104</b>
7.1	Dalitz Plot PDFs . . . . .	106
7.2	Energy-Substituted Mass and Energy Difference . . . . .	113
<b>8</b>	<b>Studies Using Toy MC Experiments</b>	<b>116</b>
8.1	Nominal Toy Experiments . . . . .	116
8.2	Adding and Omitting a Resonance . . . . .	118
8.3	Local Minima Solutions . . . . .	129
<b>9</b>	<b>Validation Studies</b>	<b>131</b>
9.1	Validation of the Fit Using Offpeak . . . . .	131

9.2	Validation of the Fit Using Full MC . . . . .	131
9.3	Validation of Variable Shapes and Selection Cuts . . . . .	134
9.4	Evaluation of the NN Selection Efficiency . . . . .	134
9.4.1	Validation of event shape PDFs . . . . .	136
9.4.2	Validation of the $m_{ES}$ and $\Delta E$ PDFs . . . . .	137
<b>10</b>	<b>Results</b>	<b>141</b>
10.1	Extraction of Physical Parameters . . . . .	141
10.2	Fit Results and Quasi-Two-Body Results . . . . .	149
<b>11</b>	<b>Systematic Uncertainties</b>	<b>159</b>
<b>12</b>	<b>Conclusions</b>	<b>163</b>
<b>A</b>	<b>Formulae</b>	<b>166</b>
A.1	Kinematic Conversions . . . . .	166
<b>B</b>	<b>Determine the signal <math>\Delta E</math> distribution</b>	<b>167</b>
	<b>Bibliography</b>	<b>172</b>

## List of Figures

1.1	The Unitarity Triangle . . . . .	7
1.2	The Quark process diagrams that contribute to $b$ decays . . . . .	9
1.3	Feynman diagrams for $B^0 \rightarrow K^{*+}\pi^-$ and $B^0 \rightarrow \rho^- K^+$ decays . . . . .	18
2.1	Layout of the PEP-II collider at SLAC . . . . .	23
2.2	PEP-II peak luminosity (left) and the integrated luminosities (right) . .	24
2.3	<i>BABAR</i> detector longitudinal section and end view . . . . .	26
2.4	Schematic views of SVT . . . . .	27
2.5	SVT hit resolution . . . . .	28
2.6	Longitudinal section of the DCH with principal dimensions . . . . .	29
2.7	Schematic layout of drift cells and drift cell isochrones . . . . .	31
2.8	The DCH drift time versus distance relation and DCH position resolution	33
2.9	Measurement of $dE/dx$ in the DCH as a function of track momenta and difference between the measured and the expected . . . . .	34
2.10	The track reconstruction efficiency in the DCH . . . . .	35
2.11	Monte Carlo studies of low momentum tracks in the SVT and recon- struction of low momentum tracks . . . . .	36
2.12	Resolution in track parameters and transverse momentum . . . . .	37

2.13	Schematic of the DIRC system . . . . .	38
2.14	DIRC expected $\pi$ -K separation and Efficiency and misidentification probability for kaon selection . . . . .	39
2.15	A longitudinal cross section of the EMC . . . . .	40
2.16	EMC energy resolution and angular resolution . . . . .	42
2.17	Cross section of a planar RPC . . . . .	44
2.18	Overview of the IFR . . . . .	45
2.19	IFR muon efficiency and pion misidentification probability . . . . .	46
3.1	Convention adopted for the helicity angles . . . . .	50
3.2	Classic and square Dalitz plots from MC . . . . .	54
3.3	Projections of SDP on the $m'$ and $\theta'$ axes . . . . .	55
3.4	The Jacobian determinant . . . . .	56
4.1	$K$ -matrix and RBW parametrizations for $K_0^*(1430)$ . . . . .	62
4.2	Form factor from $e^+e^- \rightarrow \pi^+\pi^-$ annihilation and $\tau^+ \rightarrow \bar{\nu}_\tau \pi^+ \pi^0$ decays	63
5.1	Distributions of $m_{ES}$ and $\Delta E'$ for signal and continuum . . . . .	74
5.2	$\Delta E$ distributions for signal events in different $\pi^0$ energy ranges . . . . .	75
5.3	Number of candidates per event passing the full selection . . . . .	78
5.4	Output distribution for the Neural Network . . . . .	80
5.5	Background efficiency as a function of the signal efficiency . . . . .	81
5.6	Correlation profiles . . . . .	85
5.7	Correlations between $m_{ES}$ and $\Delta E$ before correction . . . . .	86
5.8	Correlations between $m_{ES}$ and $\Delta E$ after correction . . . . .	86

5.9	Profile of $\Delta_{\text{dalitz}}$ along the Dalitz plane . . . . .	87
5.10	Correlation profiles versus Dalitz variables. . . . .	88
5.11	Correlation profiles versus Dalitz variables. . . . .	89
5.12	Correlation profiles versus Dalitz variables. . . . .	90
6.1	Enlarged $\Delta E$ band: signal and backgrounds . . . . .	92
6.2	Enlarged $m_{\text{ES}}$ band: signal and backgrounds . . . . .	93
6.3	Square Dalitz plots for representative $B^0$ -related background modes . . . . .	95
6.4	Square Dalitz plots for representative $B^+$ -related background modes . . . . .	96
7.1	Signal selection efficiency and misreconstruction fraction . . . . .	107
7.2	Resolution of the reconstructed $\rho^-$ mass . . . . .	109
7.3	Mass resolution in SCF events . . . . .	111
7.4	DP Resolution for TM (left) and SCF events . . . . .	112
7.5	Dalitz plot and Square DP distributions for off-resonance events. . . . .	113
7.6	Distribution of $m_{\text{ES}}$ and $\Delta E'$ for $m_{\text{ES}}$ -sideband off-resonance events . . . . .	115
8.1	Distributions of fitted yields and continuum asymmetry . . . . .	120
8.2	Distributions of the fitted $\rho^+ K^-$ amplitude and error . . . . .	123
8.3	Distributions of the fitted amplitudes and phases of $K^*(892)^+ \pi^-$ . . . . .	124
8.4	Distributions of the fitted amplitudes and phases of N.R. . . . .	125
8.5	Distributions of the fitted amplitudes and phases of $K_0^*(1430)^0 \pi^0$ . . . . .	126
8.6	Distributions of the fitted amplitudes and phases of $K_0^*(1430)^+ \pi^-$ . . . . .	127
8.7	Distributions of fitted amplitudes and phases of $K^*(892)^0 \pi^0$ . . . . .	128

8.8	Distribution of negative log-likelihood difference between toy fits with and without $K^*(892)^0\pi^0$ . . . . .	129
8.9	Distributions of negative log-likelihood with randomized initial values for fit parameters . . . . .	130
9.1	Distribution of $m_{\text{ES}}$ for the validation sample, fitted to a Crystal Ball function . . . . .	135
9.2	Distribution of $m_{\text{ES}}$ for the control sample, fitted to a Crystal Ball function for the signal component, and to an ARGUS function for the background . . . . .	136
9.3	Comparison between the control sample and the corresponding MC distributions for several event shape variables . . . . .	138
9.4	Comparison between the control sample data and MC distributions for the Fisher and event shape variables . . . . .	139
9.5	Comparison of the control sample data and MC distributions for the NN discriminant . . . . .	139
9.6	Comparison of the control sample data and MC distributions for $\Delta E$ and $\pi^0$ energy . . . . .	140
10.1	Correlation matrix for the six-resonance Toy MC fit from Table 10.1. . . . .	143
10.2	Likelihood and Confidence Levels as functions of partial $\mathcal{A}_{\text{CP}}$ values for the six-resonance toy experiment . . . . .	146
10.3	Likelihood and Confidence Levels as functions of partial fractions . . . . .	147
10.4	Likelihood and Confidence Levels as functions of partial yields . . . . .	148

10.5 Dalitz plot for the selected $K^+\pi^-\pi^0$ events and goodness of fit - the $-\log \mathcal{L}$ distribution. . . . .	152
10.6 $m_{\text{ES}}$ and $\Delta E'$ projections for the selected $K^+\pi^-\pi^0$ events . . . . .	157
10.7 Projection plots for the mass pairs . . . . .	158
B.1 Single Gaussian parametrization for $\Delta E'$ for events at large $m_{+-}^2$ and double Gaussian parametrization for events at small $m_{+-}^2$ from signal Monte Carlo . . . . .	169
B.2 Dalitz plot dependence of fraction of the core Gaussian of the signal $\Delta E$ distribution . . . . .	170
B.3 Dalitz plot dependence of Gaussian parameters of the signal $\Delta E$ distribution . . . . .	171

## List of Tables

1.1	QCD factorization predictions for some intermediate decays . . . . .	13
1.2	Decomposition of the $B \rightarrow K^*(892)\pi$ and $B \rightarrow \rho(770)^-K^+$ amplitudes	15
1.3	Previous measurements of some intermediate decays . . . . .	19
1.4	Previous measurements of $A_{CP}$ of some intermediate decays . . . . .	20
4.1	Results of the charged and neutral Gounaris-Sakurai model . . . . .	67
4.2	Intermediate states that may contribute to $B^0 \rightarrow K^+\pi^-\pi^0$ Dalitz Plot .	68
5.1	Signal MC that has been generated . . . . .	70
5.2	Relative Cut efficiencies . . . . .	77
5.3	Final signal selection efficiencies . . . . .	79
6.1	Classification of Neutral B backgrounds . . . . .	98
6.2	Classification of Charge B backgrounds . . . . .	99
8.1	Parameters and their input values that are used in toy experiments . .	118
8.2	Parameters and their input values that are used in toy experiments (cont'd) . . . . .	119
8.3	Parameters and their pulls obtained with toy experiments . . . . .	121
8.4	Parameters and their pulls obtained with toy experiments (cont'd) . . .	122

9.1	Pulls of parameters obtained with mock data experiments . . . . .	132
9.2	Pulls of parameters obtained with mock data experiments (cont'd) . . .	133
9.3	Parameters obtained from a fit to validation MC sample using $m_{ES}$ . .	135
10.1	Initial generation values, and fit results for a specific Toy MC experi- ment. . . . .	142
10.2	Q2B Observables calculated from fitted amplitudes and phases . . . . .	145
10.3	Parameters and their fitted values from the nominal fit . . . . .	149
10.4	Parameters and their fitted values from the nominal fit (cont'd) . . . .	150
10.5	Results obtained with the nominal fit to the data . . . . .	153
10.6	Results obtained for the minor intermediate states when they are added to the nominal fit in turn . . . . .	154
10.7	Results obtained with a fit to the data when one intermediate state is added in turn to the nominal fit . . . . .	155
10.8	Results obtained with a fit to the data when one intermediate state is added in turn to the nominal fit (cont'd) . . . . .	156
11.1	Breakdown of systematic errors for the branching fraction measurements.	161
11.2	Breakdown of systematic errors for the $A_{CP}$ measurements. . . . .	162
12.1	Comparison to previous measurements . . . . .	164

# Chapter 1

## Introduction

In the late 1970s, the Standard Model started to serve as a common language for elementary particle physicists. By 1979, particle physicists have already learned that the hadrons were composed of more basic building blocks called quarks, held together by exchanges of gluons. Three interactions, namely the strong, weak, and electromagnetic interactions, had been successfully described by quantum field theories, and the last two were unified into a single “electroweak” interaction. New instruments and techniques have been developed to study interactions between particles. Dedicated experiments were carried out to test predictions by the Standard Model, and to search for phenomena beyond it. Excitingly enough, since the birth of the Standard Model, there have been no well-established results in particle physics that explicitly disagree with this theory. The rise of the Standard Model certainly indicates a great success, as well as a huge step, in further understanding nature.

Before the early 1950s, the three interactions were generally believed to be invariant under the three discrete symmetry operations, namely the charge conjugation ( $C$ ), the spatial inversion (or parity,  $P$ ), and the time inversion ( $T$ ). The discovery in 1957 that parity is not conserved in weak interactions greatly increased interest in

understanding the three discrete symmetry operators and searching for other potential violations. In 1964, violation of the combined  $CP$  invariance was first observed in the decays of neutral kaons [1]. A mechanism for  $CP$  violation was introduced in 1973 by Kobayashi and Maskawa [2] which describes the three-generation quark mixing in weak interactions with a unitary matrix, the so-called Cabibbo-Kobayashi-Maskawa (CKM) matrix.

The motivation of the analysis presented in this thesis is to search for the  $CP$  violating charge asymmetries in  $B_d^0$  decays to the three-body final state  $K^+\pi^-\pi^0$ , by measuring decay rates of intermediate resonant states. The intermediate decays receive contributions mainly from tree level processes and one-loop level penguin processes, where the penguin processes are sensitive to new physics effects beyond the Standard Model. Therefore, this analysis also searches for new physics effects.

The layout of the thesis is as follows: in this chapter, the relevant theoretical framework is briefly reviewed, followed by a summary of previous measurements. Chapter 2 describes the *BABAR* experiment. Chapter 3 and 4 presents the Dalitz plot analysis method and the signal model. Details of the data sample, the event selection, and the maximum likelihood fit approach are discussed in Chapter 5 to 9. The results and the associated systematic uncertainties are given in Chapter 10 and 11. In Chapter 12, the results are compared to those from previously published measurements, and some conclusions are drawn.

## 1.1 Classification of $CP$ Violation

$CP$  violation is usually classified into three categories, in a *model-independent* way [3, 4]:

- *CP* violation in decay, also called direct *CP* violation, when the amplitudes for a decay and its *CP* conjugate process have different magnitudes.

For a meson  $M$  decay to a final state  $f$ , if we define  $A_f \equiv A(M \rightarrow f)$  and  $\bar{A}_{\bar{f}} \equiv A(\bar{M} \rightarrow \bar{f})$ , *CP* violation in decay means

$$\left| \frac{\bar{A}_{\bar{f}}}{A_f} \right| \neq 1 . \quad (1.1)$$

Direct *CP* violation can happen to both charged and neutral meson decays.

- *CP* violation in mixing, which occurs in neutral meson decays when the two neutral mass eigenstates are not the *CP* eigenstates; it is also referred to as indirect *CP* violation.

For a neutral meson with its *CP* eigenstate denoted by  $M^0$ , the mass eigenstates are mixtures of  $M^0$  and  $\bar{M}^0$ :

$$M_1 = pM^0 + q\bar{M}^0 , \quad M_2 = pM^0 - q\bar{M}^0 , \quad (1.2)$$

where  $p$  and  $q$  are complex quantities, and are normalized so that  $|p|^2 + |q|^2 = 1$ .

*CP* violation in mixing occurs when

$$\left| \frac{q}{p} \right| \neq 1 . \quad (1.3)$$

- *CP* violation in the interference between decays with and without mixing, which occurs in neutral decays into final states that are common to the neutral meson and its charge conjugate.

In this scenario, both  $M^0 \rightarrow f$  and  $M^0 \rightarrow \bar{M}^0 \rightarrow f$  occur and

$$\text{Im} \left( \frac{q \bar{A}_f}{p A_f} \right) \neq 0 . \quad (1.4)$$

$CP$  violation has been experimentally observed in neutral  $K$ - and  $B$ - meson decays. Usually, observed  $CP$  violation in a specific decay is the mixed effect of the three types above. All the three types of  $CP$  violation have been established in neutral  $K \rightarrow \pi\pi$  decays, the effects being of the order of  $O(10^{-3})$  or smaller [3]. In 2004, direct  $CP$  violation was also observed for the first time in neutral  $B_d$ -meson decays (to  $K^+\pi^-$ ) at *BABAR* [5] and Belle [6], with much larger effect (of the order of 0.1). Indirect  $CP$  violation was also observed in semileptonic neutral  $K$ -meson decays.  $CP$  violation in the interference between decays with and without mixing has been experimentally established in the neutral  $B_d$ -meson decays at *BABAR* [7] and Belle [8], using a time-dependent analysis of the decay rates.

## 1.2 $CP$ Violation in the Standard Model

In the Standard Model, there are three generations of fundamental spin- $\frac{1}{2}$  particles (fermions) called quarks and leptons. Each generation of quarks is made of an up quark  $U = (u, c, t)$ , of charge  $+\frac{2}{3}e$ , and a down quark  $D = (d, s, b)$ , of charge  $-\frac{1}{3}e$ . Each lepton generation is made of a charged lepton  $l = (e^-, \mu^-, \tau^-)$  and a corresponding neutrino  $\nu = (\nu_e, \nu_\mu, \nu_\tau)$ . The strong and the electroweak interactions between these fermions are mediated by gauge bosons of spin 1 (vector bosons) that are described by the gauge symmetry group:

$$SU(3)_C \times SU(2)_L \times U(1)_Y, \quad (1.5)$$

where  $SU(3)_C$  gives the eight gluon ( $g$ ) fields of the strong interaction between colored quarks described by quantum chromodynamics (QCD),  $SU(2)_L$  generates the three massless gauge bosons  $W_\mu^i$ ,  $i = 1, 2, 3$ , and  $U(1)_Y$  has a  $B_\mu$  generator field to mediate

the electromagnetic interactions. The coupling constants for the three gauge groups are denoted by  $g_s$ ,  $g$ , and  $g'$ , respectively.

Within the Standard Model,  $CP$  symmetry is broken by complex phases in the Yukawa couplings of the Higgs scalar to quarks. After spontaneous symmetry breaking [9], using the Higgs mechanism and defining  $\theta_W \equiv \tan^{-1}(g'/g)$ , fermions and three physical gauge bosons, namely  $W^\pm \equiv (W^1 \mp iW^2)/\sqrt{2}$  and  $Z^0 \equiv -B \sin \theta_W + W^3 \cos \theta_W$ , gain masses, while the photon field ( $\equiv B \cos \theta_W + W^3 \sin \theta_W$ ) remains massless. The massive quarks are not the same as their weak eigenstates, and the matrix relating these quark bases was defined and given an explicit parametrization by Kobayashi and Maskawa [2] via a dramatic generalization of the four-quark case that is described by a single Cabibbo angle [10]. The charged current weak interactions (that is, through exchange of the  $W^\pm$  bosons) for quarks (left-handed only, denoted by the subscript  $L$ ) are now given by

$$\mathcal{L}_{W^\pm} = -\frac{g}{\sqrt{2}} \bar{u}_{Li} V_{ij} d_{Lj} W^\pm + h.c. , \quad (1.6)$$

where  $g$  is the coupling strength of weak interactions, and  $V$  is the Cabibbo-Kobayashi-Maskawa (CKM) quark-mixing matrix.

The CKM matrix  $V$  is often expressed in terms of a  $3 \times 3$  unitary matrix  $V$  to transform the charge  $-e/3$  quark mass eigenstates ( $d$ ,  $s$ , and  $b$ ) to the weak eigenstates ( $d'$ ,  $s'$ , and  $b'$ ):

$$\begin{pmatrix} d' \\ s' \\ b' \end{pmatrix} = \begin{pmatrix} V_{ud} & V_{us} & V_{ub} \\ V_{cd} & V_{cs} & V_{cb} \\ V_{td} & V_{ts} & V_{tb} \end{pmatrix} \begin{pmatrix} d \\ s \\ b \end{pmatrix} \quad (1.7)$$

There are several choices of parameterizations of the CKM matrix. A ‘‘standard’’ one was first introduced by Chau and Keung in 1984 [11] that utilizes three angles

$\theta_{12}$ ,  $\theta_{23}$ ,  $\theta_{13}$ , and a phase,  $\delta_{13}$ :

$$V = \begin{pmatrix} c_{12}c_{13} & s_{12}c_{13} & s_{13}e^{-i\delta_{13}} \\ -s_{12}c_{23} - c_{12}s_{23}s_{13}e^{i\delta_{13}} & c_{12}c_{23} - s_{12}s_{23}s_{13}e^{i\delta_{13}} & s_{23}c_{13} \\ s_{12}s_{23} - c_{12}c_{23}s_{13}e^{i\delta_{13}} & -c_{12}s_{23} - s_{12}c_{23}s_{13}e^{i\delta_{13}} & c_{23}c_{13} \end{pmatrix}, \quad (1.8)$$

with  $c_{ij} = \cos \theta_{ij}$  and  $s_{ij} = \sin \theta_{ij}$ , and  $\delta_{13}$  is the complex phase that accommodates  $CP$  violation. There are a few obvious advantages of this parameterization. First, the unitarity of  $V$  is automatically guaranteed. Second, the rotation angles are defined to describe the mixing of two specific generations, with  $\theta_{12}$  being the Cabibbo angle in the limit  $\theta_{23} = \theta_{13} = 0$ .  $c_{13}$  is known to be almost unity with a deviation of the order of  $10^{-6}$ .

A popular approximation to the CKM matrix was proposed by Wolfenstein in 1983 [12]. This parameterization considers the hierarchy in the size of the angles,  $s_{12} \gg s_{23} \gg s_{13}$ . Setting  $\lambda \equiv s_{12} \simeq 0.22$  and using it as an expansion parameter, the CKM matrix can be written as:

$$V = \begin{pmatrix} 1 - \lambda^2/2 & \lambda & A\lambda^3(\rho - i\eta) \\ -\lambda & 1 - \lambda^2/2 & A\lambda^2 \\ A\lambda^3(1 - \rho - i\eta) & -A\lambda^2 & 1 \end{pmatrix} + \mathcal{O}(\lambda^4), \quad (1.9)$$

where  $A$ ,  $\rho$ , and  $\eta$  are real numbers that were intended to be of order unity. This approximation is widely used for  $B$ -physics [4].

The values of the CKM matrix elements can be determined from weak decays of the relevant quarks. The 90% confidence limits obtained from current experiments for the magnitude of the elements are (Particle Data Group 2004 [3])

$$\begin{pmatrix} |V_{ud}| = 0.9739 \sim 0.9751 & |V_{us}| = 0.221 \sim 0.227 & |V_{ub}| = 0.0029 \sim 0.0045 \\ |V_{cd}| = 0.221 \sim 0.227 & |V_{cs}| = 0.9730 \sim 0.9744 & |V_{cb}| = 0.039 \sim 0.044 \\ |V_{td}| = 0.0048 \sim 0.0014 & |V_{ts}| = 0.037 \sim 0.043 & |V_{tb}| = 0.9990 \sim 0.9992 \end{pmatrix}. \quad (1.10)$$

The unitarity of the CKM matrix leads to various relations between two different rows and columns, each being called a “unitarity triangle” in the complex plane. All the unitarity triangles are equal in area [13]. Unitarity applied to the first and third columns yields the most important “unitarity triangle” in the decays of  $B_d$ -meson (with the quark content  $b\bar{d}$ ):

$$V_{ud}V_{ub}^* + V_{cd}V_{cb}^* + V_{td}V_{tb}^* = 0 , \quad (1.11)$$

which has a geometrical presentation in the complex plan as shown in Fig. 1.1 a. The term “unitarity triangle” (UT) is actually reserved for the relation 1.11, because this triangle is the least squashed one and predicts large  $CP$  asymmetries in  $B$ -meson decays.

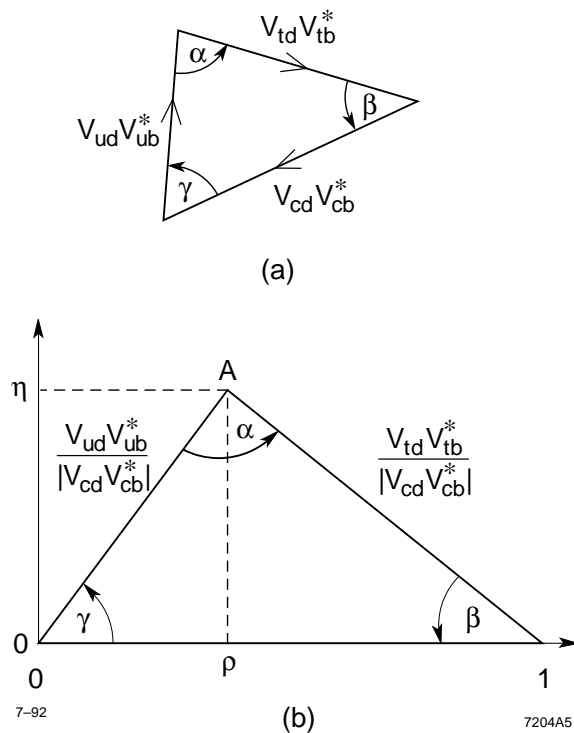


Figure 1.1: *The Unitarity Triangle.*

The three angles in the UT are defined as

$$\alpha \equiv \arg\left(-\frac{V_{td}V_{tb}^*}{V_{ud}V_{ub}^*}\right), \quad \beta \equiv \arg\left(-\frac{V_{cd}V_{cb}^*}{V_{td}V_{tb}^*}\right), \quad \gamma \equiv \arg\left(-\frac{V_{ud}V_{ub}^*}{V_{cd}V_{cb}^*}\right). \quad (1.12)$$

As a common practice, a phase convention is chosen so that  $V_{cd}V_{cb}^*$  is real, and the  $V_{cd}V_{cb}^*$  side is normalized to unity. This scaling presents the Wolfenstein parametrization as shown in Fig. 1.1 b.

The three angles are all physical and can, in principle, be independently measured by measuring the  $CP$  asymmetries in  $B$ -meson decays. The  $CP$  violation in interference of decays with and without mixing has been observed in  $B_d^0 \rightarrow J/\Psi K_S$  that gives  $\sin(2\beta) = 0.731 \pm 0.056$  [3]. The angle  $\gamma$  is simply the complex phase  $\delta_{13}$ .

It is intuitive to study the weak-phase structure of the decay amplitudes for  $B$ -meson decays in the CKM picture. The decay amplitude for the quark process  $b \rightarrow q\bar{q}q'$  can always be written as a sum of three terms with definite CKM element coefficients:

$$A(q\bar{q}q') = V_{tb}V_{tq'}^*P_{q'}^t + V_{cb}V_{cq'}^*(T_{c\bar{c}q'}\delta_{qc} + P_{q'}^c) + V_{ub}V_{uq'}^*(T_{u\bar{u}q'}\delta_{qu} + P_{q'}^u), \quad (1.13)$$

where  $P$  and  $T$  denote contributions from tree and penguin diagrams (the CKM factors being excluded), and the superscripts  $t$ ,  $c$  and  $u$  indicate the internal quark lines. Fig. 1.2 shows the quark diagrams for the tree, gluonic penguin, and electroweak penguin contributions. The weak-phase information is implied in the CKM coefficients, while the strong-phase information is implicitly contained in the  $P$ 's and  $T$ 's.

In the case of  $b \rightarrow u\bar{u}s$  decays, which are of interest in this report, the amplitude reads

$$A(u\bar{u}s) = V_{tb}V_{ts}^*P_s^t + V_{cb}V_{cs}^*P_s^c + V_{ub}V_{us}^*(T_{u\bar{u}s} + P_s^u)$$

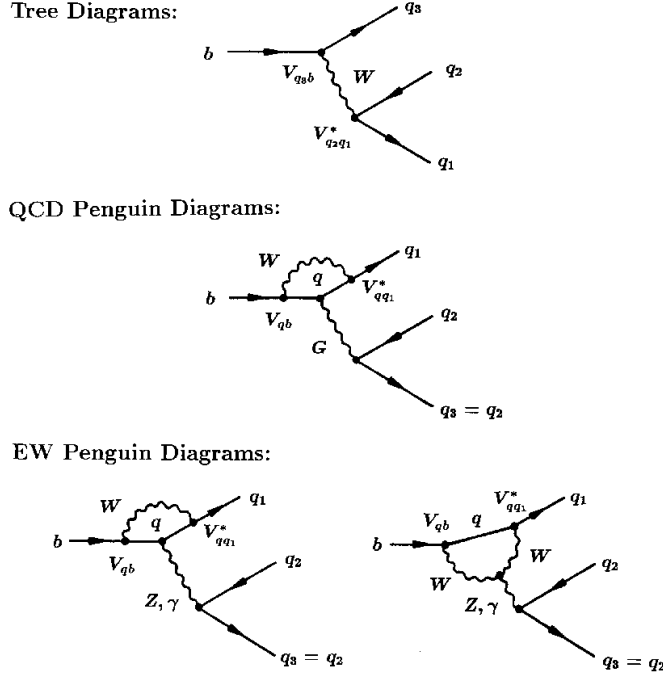


Figure 1.2: *The Quark process diagrams that contribute to  $b$  decays. For the process  $b \rightarrow u\bar{u}s$ ,  $q_1 = s$ ,  $q_2 = \bar{u}$ , and  $q_3 = u$ .*

$$= V_{cb}V_{cs}^*(P_s^c - P_s^t) + V_{ub}V_{us}^*(T_{u\bar{u}s} + P_s^u - P_s^t), \quad (1.14)$$

where in the last step the UT relation (Eq. 1.11) is used to remove the  $V_{tb}V_{ts}^*$  term. Due to hadronic rescattering, the penguin topology is not well defined, but the weak-phase structure is not affected.

For the  $CP$  conjugate process, the (weak) phases contained in the CKM coefficients change signs due to the complex nature of the CKM elements, while the strong phases do not. As one can always use the unitarity relation to remove one term in Eq. 1.13, it is useful to write the effective decay amplitudes as:

$$\begin{aligned} A_f &= |a_1|e^{i(\delta_1+\phi_1)} + |a_2|e^{i(\delta_2+\phi_2)}, \\ \bar{A}_{\bar{f}} &= |a_1|e^{i(\delta_1-\phi_1)} + |a_2|e^{i(\delta_2-\phi_2)}, \end{aligned} \quad (1.15)$$

where  $\delta_1, \delta_2$  are the strong phases,  $\phi_1, \phi_2$  are the weak phases, and  $|a_1|, |a_2|$  contain the magnitudes information. With this formulation, the direct  $CP$  violation is:

$$A_{CP} \equiv \frac{|A_f|^2 - |\overline{A}_f|^2}{|A_f|^2 + |\overline{A}_f|^2} = \frac{\sin(\delta_2 - \delta_1) \sin(\phi_2 - \phi_1)}{R + \cos(\delta_2 - \delta_1) \cos(\phi_2 - \phi_1)}, \quad (1.16)$$

where  $R = (|a_1|^2 + |a_2|^2)/2|a_1 a_2| \geq 1$ . It is obvious that the occurrence of direct  $CP$  violation in the decay requires that there are (at least) two competing diagrams with different strong phases *and* different weak phases. The other two types of  $CP$  violation can also be interpreted with this formulation. For details, see the review of *CP Violation in Meson Decays* in [3].

### 1.3 Hadronic $B$ -meson Decays

In this thesis, the  $B_d^0$  decays to the 3-body final state  $K^+ \pi^- \pi^0$  are investigated. These decays receive contributions from quite a few intermediate resonant decays, *e.g.*,  $B_d^0 \rightarrow K^*(892)^+ \pi^-$ ,  $B_d^0 \rightarrow \rho(770)^- K^+$ ,  $B_d^0 \rightarrow K^*(892)^0 \pi^0$ , and the charmed decay  $B_d^0 \rightarrow \overline{D}^0 \pi^0$  etc..

The study of hadronic  $B$  decays is inevitably complicated by long-distance strong interactions that cannot be tackled with perturbative QCD.  $B$ -mesons, like all other color-neutral hadrons, are bound states of the  $b$  quarks and light quarks such as  $u$  or  $d$ . While understood in principle, the nonperturbative nature of the bound states makes it hard to precisely extract relevant weak-phase information from experiments on  $B$  mesons, even though the perturbative effects can be predicted with high precision for electroweak interactions and are under control for strong interactions. This problem has never been solved in its entirety.

In QCD, the strong interaction gauge coupling  $\alpha_s$  is energy-scale-dependent, as

shown in Eq. 1.17:

$$\alpha_s(Q^2) \simeq \frac{12\pi}{(33 - 2n_f) \log(Q^2/\Lambda^2)} , \quad (1.17)$$

where  $Q$  reflects the energy scale of the interaction,  $\Lambda$  is the energy scale ( $\sim 200$  MeV) for quark confinement, and  $n_f$  is the number of quark flavors. For  $Q^2$  around  $m_W^2$ ,  $\alpha_s$  is of the order of 0.1 and QCD perturbation theory applies. For  $Q^2$  at the quark confinement level, the strong coupling makes QCD perturbation inappropriate.

In weak decays of  $B$ -mesons, three fundamental scales will be involved: the weak interaction scale  $M_W \sim 80$  GeV, the  $b$ -quark mass  $m_b \sim 5$  GeV, and the QCD confinement scale  $\Lambda_{QCD} \sim 200$  MeV. The three energy scales are strongly ordered, *i.e.*,  $m_W \gg m_b \gg \Lambda_{QCD}$ .

Various theoretical approaches and techniques have been developed to deal with the problem, with varying levels of reliability. Some are appropriate to some specific problems, while in some situations the others may work better.

In the Operator Product Expansion (OPE) approach [14], the fact that  $B$  decays involve a wide variety of energy scales enables one to identify the physics at a given scale and to separate it out explicitly. An effective Hamiltonian can be constructed to separate the non-perturbative and perturbative contributions. For a renormalization scale  $\mu$  of the order of  $\mathcal{O}(m_b)$ , low-energy effective Hamiltonians are constructed to yield the transition matrix elements of the structure

$$\langle f | \mathcal{H} | i \rangle \propto \sum_k C_k(\mu) \langle f | O_k(\mu) | i \rangle , \quad (1.18)$$

where  $C_k(\mu)$ 's are the perturbatively calculable Wilson coefficient functions which incorporate strong-interaction effects above the scale  $\mu$ , and the  $\langle f | O_k | i \rangle$ 's are the non-perturbative hadronic matrix elements of the local operators  $O_i$  which contain strong-

interaction effects below the scale  $\mu$ . For  $B$  decays to two mesons, the amplitude is given as

$$\mathcal{A}(B \rightarrow M_1 M_2) = \frac{G_F}{\sqrt{2}} \sum_i \lambda_i C_i(\mu) \langle M_1 M_2 | O_i | B \rangle(\mu), \quad (1.19)$$

where  $\lambda_i$  is a relevant CKM element, and  $O_i$ 's are local four-quark operators. The physical amplitude must not depend on the renormalization scale  $\mu$ , which means the  $\mu$  dependence of the Wilson coefficients has to cancel the  $\mu$  dependence present in the hadronic matrix elements.

Theoretically, the hadronic matrix elements are the most difficult parts to compute. There exist various treatments for this problem. QCD factorization [15] has been widely used in heavy-quark physics to deal with the hadronic matrix elements. Assuming the concept of color transparency [16], the four-quark matrix element is replaced with (factorized into) the product of the matrix elements of two currents. This approach has been used to calculate many hadronic two-body decays, though in some cases, it is not applicable. Table 1.1 shows the QCD factorization predictions for the modes  $B_d^0 \rightarrow K^*(892)^+ \pi^-$ ,  $B_d^0 \rightarrow K^*(892)^0 \pi^0$ , and  $B_d^0 \rightarrow \rho(770)^- K^+$  from Ref. [17].

## 1.4 Isospin Analysis and SU(3) Flavor Symmetry

Strong interactions are nearly invariant under the isospin- $SU(2)$  transformation, with the  $u$  quark and the  $d$  quark forming an isospin doublet. The doublet has isospin  $I = 1/2$ ,  $I_3^u = +1/2$ , and  $I_3^d = -1/2$ . The isospin invariance of strong interactions is very useful to relate amplitudes of decays that involve final states with same isospin constituents, typically with contributions from gluonic penguins.

For the decay  $B_d \rightarrow K^*(892)\pi$ , both the  $B_d$  and  $K^*(892)$  have isospin  $I = 1/2$ , and  $\pi$  has isospin  $I = 1$ . The final state can have a total isospin of  $1/2$  or  $3/2$ . This

Table 1.1: *Branch fractions and CP violating charge asymmetries for some intermediate decays. The predictions are from Ref. [17] (the “combined” scenario) and the experimental results are from [3] (world average). Theoretical errors on the predictions come from uncertainties in input parameters, and in the modeling of power corrections. Details about these errors can be found in [17].*

Mode	Theory BF ( $\times 10^{-6}$ )	Experiment BF ( $\times 10^{-6}$ )
$B_d^0 \rightarrow K^*(892)^+\pi^-$	$8.1_{-1.2}^{+1.4+1.3+0.8+6.2}$	$16_{-5}^{+6}$
$B_d^0 \rightarrow K^*(892)^0\pi^0$	$2.5_{-0.1}^{+0.1+0.5+0.3+2.6}$	$< 3.6$
$B_d^0 \rightarrow \rho(770)^-K^+$	$10.1_{-1.9}^{+1.8+7.1+1.2+10.7}$	$7.3 \pm 1.8$
	Theory $A_{CP}$ ( $\times 10^{-2}$ )	Experiment $A_{CP}$ ( $\times 10^{-2}$ )
$B_d^0 \rightarrow K^*(892)^+\pi^-$	$-12.1_{-0.7}^{+0.6+8.2+5.1+62.5}$	$26 \pm 35$
$B_d^0 \rightarrow K^*(892)^0\pi^0$	$1.0_{-3.2}^{+4.0+4.7+2.7+31.7}$	-
$B_d^0 \rightarrow \rho(770)^-K^+$	$20.0_{-1.4}^{+1.3+4.4+1.9+34.5}$	$28 \pm 19$

decay receives contributions from  $\Delta I = 0$  and  $\Delta I = 1$  processes. One may write the Hamiltonian as  $\mathcal{H} = \mathcal{H}_{\Delta I=0} + \mathcal{H}_{\Delta I=1}$ . As shown in Fig.1.2, the QCD penguin diagram only contributes to  $\Delta I = 0$ , due to the fact the gluon has  $I = 0$ . An isospin analysis (similar to that for  $B \rightarrow \pi K$  [19, 4]) gives

$$\begin{aligned}
A(B^+ \rightarrow K^*(892)^+\pi^0) &= \frac{2}{3}A_{1,3/2} + \frac{1}{3}A_{1,1/2} - \sqrt{\frac{1}{3}}A_{0,1/2} \\
A(B^0 \rightarrow K^*(892)^0\pi^0) &= \frac{2}{3}A_{1,3/2} + \frac{1}{3}A_{1,1/2} + \sqrt{\frac{1}{3}}A_{0,1/2} \\
\sqrt{\frac{1}{2}}A(B^+ \rightarrow K^*(892)^0\pi^+) &= \frac{1}{3}A_{1,3/2} - \frac{1}{3}A_{1,1/2} + \sqrt{\frac{1}{3}}A_{0,1/2} \\
\sqrt{\frac{1}{2}}A(B^0 \rightarrow K^*(892)^+\pi^-) &= \frac{1}{3}A_{1,3/2} - \frac{1}{3}A_{1,1/2} - \sqrt{\frac{1}{3}}A_{0,1/2} , \quad (1.20)
\end{aligned}$$

where the isospin amplitude reads as  $A_{\Delta I, I}$ . Denoting  $A^{+-}$  for  $A(B^0 \rightarrow K^*(892)^+\pi^-)$ , and similarly for the others, we have

$$A^{0+} + \sqrt{2}A^{+0} = \sqrt{2}A^{00} + A^{+-} . \quad (1.21)$$

With some rigorous decomposition of the amplitudes as in Eq. 1.13, one can use Eq. 1.21 to impose constraints on the involved strong and weak phases, as well as on the magnitudes of the  $P$ 's and  $T$ 's. Examples can be found for decays such as  $B \rightarrow \pi\pi$  [18], and  $B \rightarrow \pi K$  [19].

Under the  $SU(3)$  flavor symmetry of strong interactions,  $u$ ,  $d$ , and  $s$  form a triplet, if the mass differences in between are ignored. The  $SU(3)$  flavor symmetry is not an exact one, being broken by the large  $s$  quark mass. The symmetry breaking effects can be usually accounted for by including decay constants of hadrons, with some theoretical hadronic uncertainties.

Under the flavor  $SU(3)$ , decays can be represented in terms of five reduced matrix elements [20]. This decomposition can also be performed in terms of diagrams

of six different topologies. The leading-order decay diagrams are the color-allowed tree ( $T$ ), the color-suppressed tree ( $C$ ), the QCD penguin ( $P$ ), and the color-singlet QCD penguin ( $S$ ). The color-allowed electroweak penguin ( $P_{EW}$ ) and the color-suppressed electroweak penguin ( $P_{EW}^C$ ) can be sizable depending on the quark processes [21, 22]. The remaining diagrams come from the non-spectator weak  $W$ -exchange ( $E$ ) and the weak annihilation ( $A$ ) diagrams. Given that the electroweak penguin contributions can be sizable, four modified amplitudes are defined [23], neglecting the  $E$  and  $A$  contribution:

$$t \equiv T + P_{EW}^C, c \equiv C + P_{EW}, p \equiv P - \frac{1}{3}P_{EW}^C, s \equiv S - \frac{1}{3}P_{EW}. \quad (1.22)$$

In a flavor  $SU(3)$  analysis of experimental data on  $B$  decays to a vector meson and a pseudoscalar meson, as described in [23], a global fit is performed to extract magnitudes and phases for the flavor  $SU(3)$  amplitudes defined in Eq. 1.22, rather than calculating the hadronic elements. The extracted amplitudes are then used to make non-trivial predictions for unknown decay modes, including their  $CP$  content. The analysis even has considerable sensitivity to the CKM angle  $\gamma$ .

Table 1.2: *Decomposition of the  $B \rightarrow K^*(892)\pi$  and  $B \rightarrow \rho(770)^-K^+$  amplitudes.*

Decays	Amplitudes
$B^0 \rightarrow K^*(892)^+\pi^-$	$-(t'_P + p'_P)$
$B^0 \rightarrow K^*(892)^0\pi^0$	$-\sqrt{\frac{1}{2}}(c'_V - p'_P)$
$B^+ \rightarrow K^*(892)^0\pi^+$	$p'_P$
$B^+ \rightarrow K^*(892)^0\pi^+$	$-\sqrt{\frac{1}{2}}(t'_P + c'_V + p'_P)$
$B^0 \rightarrow \rho(770)^-K^+$	$-(t'_V + p'_V)$

As an example, in Table 1.2, we show the decomposition of the decay amplitudes

of  $B \rightarrow K^*(892)\pi$  and  $B^0 \rightarrow \rho(770)^- K^+$ , as is done in Ref.[23]. The primed quantities indicate that the  $s$  quark is involved, in quark processes with strangeness change  $|\Delta S| = 1$ . Since these are  $B$  decays to a vector ( $V$ ) and a pseudoscalar ( $P$ ), the subscript  $P$  or  $V$  indicates the pseudoscalar or the vector picks up the spectator quark. The CKM factors are contained in the flavor  $SU(3)$  amplitudes and can be factorized to make the rest the same as defined in Eq. 1.22. From the point of view of a final analysis, one can always put the CKM factors into the flavor  $SU(3)$  amplitudes to define another set of unknowns. The weak phases and the strong phases are treated as unknowns and will be determined from a fit to experimental data. For example, taking the convention that  $p'_P$  is real and positive, and assuming  $p'_V = -p'_P$  as suggested in Ref. [23], one can rewrite the amplitudes as

$$\begin{aligned}
A(B^+ \rightarrow K^*(892)^0 \pi^+) &= |p'_P| , \\
A(B^0 \rightarrow K^*(892)^+ \pi^-) &= -|p'_P| + |t'_P| e^{i(\delta_P + \gamma)} , \\
\sqrt{2}A(B^0 \rightarrow K^*(892)^0 \pi^0) &= |p'_P| - |c'_V| e^{i(\delta_V + \gamma)} , \\
A(B^0 \rightarrow \rho(770)^- K^+) &= |p'_P| - |t'_V| e^{i(\delta_V + \gamma)} , \tag{1.23}
\end{aligned}$$

where  $\delta_V$  and  $\delta_P$  denote the unknown strong phases, and  $\gamma$  is the weak CKM angle as defined in Eq. 1.12. This makes it feasible to consider relevant experimental inputs and impose constraints on the unknown magnitudes and phases, including the weak phase  $\gamma$ .

It should be pointed out that assumptions in using flavor  $SU(3)$  and the diagrammatic decomposition are not all justified and may be very misleading, as argued by M. Neubert [24], due to potential final-state rescattering effects.

## 1.5 Analysis of $B_d^0 \rightarrow K^+\pi^-\pi^0$ Decays

Charmless three-body  $B$  decays significantly broaden the study of  $B$  meson decay mechanisms and provide additional possibilities for direct  $CP$  violation searches. The  $B_d^0 \rightarrow K^+\pi^-\pi^0$  decay<sup>1</sup> is known to have contributions from the intermediate  $B^0 \rightarrow K^*(892)^+\pi^-$ ,  $K^*(892)^+ \rightarrow K^+\pi^0$  and  $B^0 \rightarrow \rho(770)^-K^+$ ,  $\rho(770)^- \rightarrow \pi^-\pi^0$  decays. Although not yet observed,  $B^0 \rightarrow K^*(892)^0\pi^0$  could also contribute, as well as  $K_0^*(1430)$ ,  $K_2^*(1430)$ ,  $K^*(1680)$ ,  $\rho(1450)$ , and  $\rho(1700)$ . The  $B^0 \rightarrow K^+\pi^-\pi^0$  decay can also occur via long-lived charmed intermediate states, *i.e.*,  $B^0 \rightarrow \bar{D}^0\pi^0$ , and the doubly-Cabibbo-suppressed  $B^0 \rightarrow D^-K^+$ ,  $D^- \rightarrow \pi^-\pi^0$ . Intermediate states with broad resonances are interfering and therefore a full amplitude analysis is required to extract the amplitudes and relative phases. The amplitudes and relative phases are used to obtain the branching ratios and  $CP$ -violating charge asymmetries for the intermediate states. The results can be used to probe the penguin contributions and the weak angle  $\gamma \equiv \arg[-V_{ud}V_{ub}^*/V_{cd}V_{cb}^*]$ .

For the intermediate modes ( $B^0 \rightarrow K^{*+}(K^+\pi^0)\pi^-$  and  $B^0 \rightarrow \rho^-(\pi^-\pi^0)K^+$  etc.), which involve the  $\bar{b} \rightarrow u\bar{u}s$  quark process, the tree diagram contributions are CKM-suppressed, *i.e.*  $\propto V_{ub}^*V_{us} \simeq A\lambda^4$  (Fig. 1.3, left), with  $\lambda \approx 0.22$ . The decays receive comparable or even dominant contributions from the gluonic penguin diagram (Fig. 1.3, right), the amplitude of which is  $\propto V_{tb}^*V_{ts} \simeq A\lambda^2$ . Moreover, the electroweak penguin contribution can be sizable in  $|\Delta S| = 1$  decays [21, 22].

Note that using the  $SU(3)$  flavor symmetry, the above penguin contribution can

---

<sup>1</sup>Unless stated otherwise, charge conjugate is always implied throughout this thesis, and I drop the subscript  $d$  hereafter.

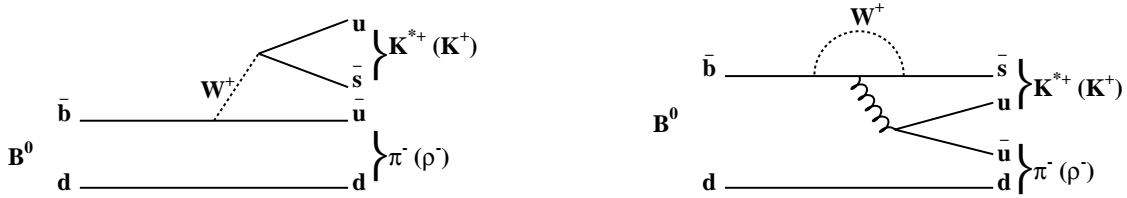


Figure 1.3: *Feynman diagrams for the  $B^0 \rightarrow K^{*+}\pi^-$  and  $B^0 \rightarrow \rho^- K^+$  decays. Left: the tree contribution. Right: the penguin contribution.*

be trivially related to the one in  $B^0 \rightarrow \rho^+\pi^-$ , e.g.,  $p_{B^0 \rightarrow \rho^+\pi^-} = (V_{cd}/V_{cs}) p_{B^0 \rightarrow K^{*+}\pi^-}$  [23]. This provides a sensitive probe on the penguin contribution to charmless  $B \rightarrow VP$  decays, where  $V$  stands for vector meson and  $P$  for pseudoscalar meson.

*A priori* theoretical calculations, based on QCD factorization, have been used to predict charmless  $B \rightarrow VP$  decay rates and  $CP$  asymmetries. Most QCD factorization models do not provide good predictions of branching fractions (BF) of intermediate decays with strangeness change  $|\Delta S| = 1$  [17, 25, 26]. One set of predicted results are shown in Table 1.1.

Measurements of some of the branching fractions and charge asymmetries have been carried out by CLEO [27], *BABAR* [28] and Belle [29], as shown in Table 1.3 and 1.4. These previous measurements all adopted a quasi-two-body (Q2B) approximation, *e.g.* did not investigate the interference patterns among intermediate states. The decay  $B^0 \rightarrow \rho^- K^+$  has been first observed by *BABAR* [28], and the branching fraction

result later from Belle [29] for this mode is not well accommodated into the  $SU(3)$  flavor symmetry. The well established intermediate  $B^0 \rightarrow K^*(892)^+\pi^-$  mode has a significantly larger branching fraction than predicted, suggesting some changes to the QCD factorization models.

Table 1.3: *Previous measurements of branch fractions ( $\times 10^{-6}$ ) for some intermediate decays. For upper limits, central values and errors are quoted in parentheses. Note that in Belle’s measurement,  $K_X^*$  is defined to have  $1.1 \text{ GeV}/c^2 < m(K^+\pi^-,0) < 1.6 \text{ GeV}/c^2$ . The inclusive rate is denoted by “Incl.”, and the nonresonant by “N.R.”.*

Channel	CLEO	Belle	BABAR
$B^0 \rightarrow K^+\pi^-\pi^0$ (Incl.)	$< 40$	$36.6 \pm 4.2 \pm 3.0$	
$B^0 \rightarrow K^*(892)^+\pi^-$	$16 \pm 6 \pm 2$	$14.8 \pm 4.6 \pm 1.5 \pm 2.4$	
$B^0 \rightarrow K^*(892)^0\pi^0$	$< 3.6$ ( $0.0_{-0.0}^{+1.3+0.5}$ )	$< 3.5$ ( $0.4 \pm 1.9 \pm 0.1$ )	
$B^0 \rightarrow \rho(770)^-K^+$	$16 \pm 8 \pm 3$	$15.1 \pm 3.4 \pm 1.5 \pm 2.1$	$7.3 \pm 1.3 \pm 1.3$
$B^0 \rightarrow K_X^{*0}\pi^0$		$6.1 \pm 1.6 \pm 0.6$	
$B^0 \rightarrow K_X^{*0+}\pi^-$		$5.1 \pm 1.5 \pm 0.7$	
$B^0 \rightarrow K^+\pi^-\pi^0$ (N.R.)		$< 9.4$ ( $5.7 \pm 2.7 \pm 0.5$ )	

For the decay  $B^0 \rightarrow K^*(892)^0\pi^0$ , the color-suppressed electroweak penguin  $P_{EW}^c$  and the color-suppressed tree  $C$  may significantly modify the naive gluonic-penguin-dominant picture, predicting a very small branching fraction. Both Belle and CLEO experiments have not observed this mode, which suggests that the gluonic penguin and the electroweak penguin are comparable in magnitude and destructive in phase for this decay.

Charmed intermediate modes, such as  $B^0 \rightarrow \bar{D}^0\pi^0$  with  $\bar{D}^0 \rightarrow K^+\pi^-$  (BF =

Table 1.4: *Previous measurements of charge asymmetry for some intermediate decays*

Channel	CLEO	Belle	BABAR
$B^0 \rightarrow K^+\pi^-\pi^0$ ( <i>Incl.</i> )		$0.07 \pm 0.11 \pm 0.01$	
$B^0 \rightarrow K^*(892)^+\pi^-$	$0.26^{+0.33+0.10}_{-0.34-0.08}$		
$B^0 \rightarrow K^*(892)^0\pi^0$			
$B^0 \rightarrow \rho(770)^-K^+$		$0.22^{+0.22+0.06}_{-0.23-0.02}$	$0.18 \pm 0.12 \pm 0.02$
$B^0 \rightarrow K_X^{*0}\pi^0$			
$B^0 \rightarrow K_X^{*0+}\pi^-$			
$B^0 \rightarrow K^+\pi^-\pi^0$ ( <i>N.R.</i> )			

$11.0 \pm 1.9 \times 10^{-6}$  [3]) and  $B^0 \rightarrow D^-\pi^+$  with  $D^- \rightarrow \pi^-\pi^0$  ( $\text{BF} = 0.5 \pm 0.2 \times 10^{-6}$  [3]), also go to the same  $K^+\pi^-\pi^0$  final state, but the  $D$ 's do weak decays only and thus do not interfere with the above broad-resonance intermediate modes. The branching fraction of  $B^0 \rightarrow \bar{D}^0\pi^0$  is significantly larger than theoretical expectations based on naive QCD factorization, and it is argued that long-distance final state rescattering should be considered [30].

The decay rate of the non-resonant mode is of some theoretical interests too. The measurement can be used to check and tune theoretical models. Belle has presented a large central value of the branching fraction, with a large upper limit as shown in Table 1.3.

## Chapter 2

# The *BABAR* Experiment

The primary goal of the *BABAR* experiment is the systematic study of  $CP$  asymmetries in the decays of neutral  $B$  mesons. In addition, the CKM matrix element,  $V_{ub}$ , can be measured, as can the branching fractions of a number of rare  $B$  meson decays. These measurements will certainly improve the constraints on the CKM matrix, and eventually on the fundamental parameters of the Standard Model.

In order to observe the asymmetries, three things need to be measured: the exclusive final state of one  $B^0$  decay needs to be fully reconstructed; the beauty-quark flavor (beauty or anti-beauty) of the other decaying  $B^0$  meson needs to be tagged with its decay products; and the proper time of the  $B^0$  decay with respect to its production (or the proper-time difference between the vertice of the two  $B$  mesons) needs to be measured. The last issue is very important, because in most cases the  $CP$  asymmetries vanish in time-integrated measurement at  $e^+e^-$  machines.

The *BABAR* experiment consists of two major parts, *i.e.*, the PEP-II collider and the *BABAR* detector.

## 2.1 The PEP-II Collider

The PEP-II project is an  $e^+e^-$  colliding beam storage ring complex, as shown in Fig. 2.1. It is designed to produce a luminosity of at least  $3 \times 10^{33} \text{cm}^{-2} \text{s}^{-1}$  at  $E_{cm} = 10.58 \text{ GeV}$ , the mass of the  $\Upsilon(4S)$  resonance. The machine uses the already-existing SLAC linac as an injector. The high luminosity ensures mass production of  $B$ -mesons, given the  $1 \text{ nb}$  cross-section for the production of  $b\bar{b}$  pairs at the  $\Upsilon(4S)$ . The  $e^+$  beam and  $e^-$  beams are stored in two separate storage rings and are maintained at different energies, 3.1 GeV and 9.0 GeV, respectively. The asymmetric-energy mode results in the  $\Upsilon(4S)$  with significant momentum in the laboratory frame. In the  $\Upsilon(4S)$  reference system, the two  $B$  mesons from the  $\Upsilon(4S) \rightarrow B\bar{B}$  decay are almost at rest because there is not much kinematic energy left for them. It is known that the  $B$  mesons have a lifetime of about 1.5 pico second, or a flight distance of 462 microns at the speed of the light. With this Lorenz boost of  $\beta\gamma = 0.56$ , the decay lengths of the  $B^0$  mesons are around 250 microns in the laboratory frame. They can be measured in the laboratory frame and therefore the proper decay times can be inferred to measure the time-dependence of the decay rates.

The high luminosity of PEP-II is achieved with high beam currents and strong focusing. The high current must be divided into a large number of low-charge bunches to avoid the beam-beam tune-shift limit, and the beams must collide only at the interaction point (IP) to avoid additional tune shift. PEP-II collides the two beams head on but separates the beams horizontally before the next collision at 62cm from IP. Strong focusing requires quadrupoles to be located close to the IP.

The bending near the IP required to separate the beams generates a large syn-

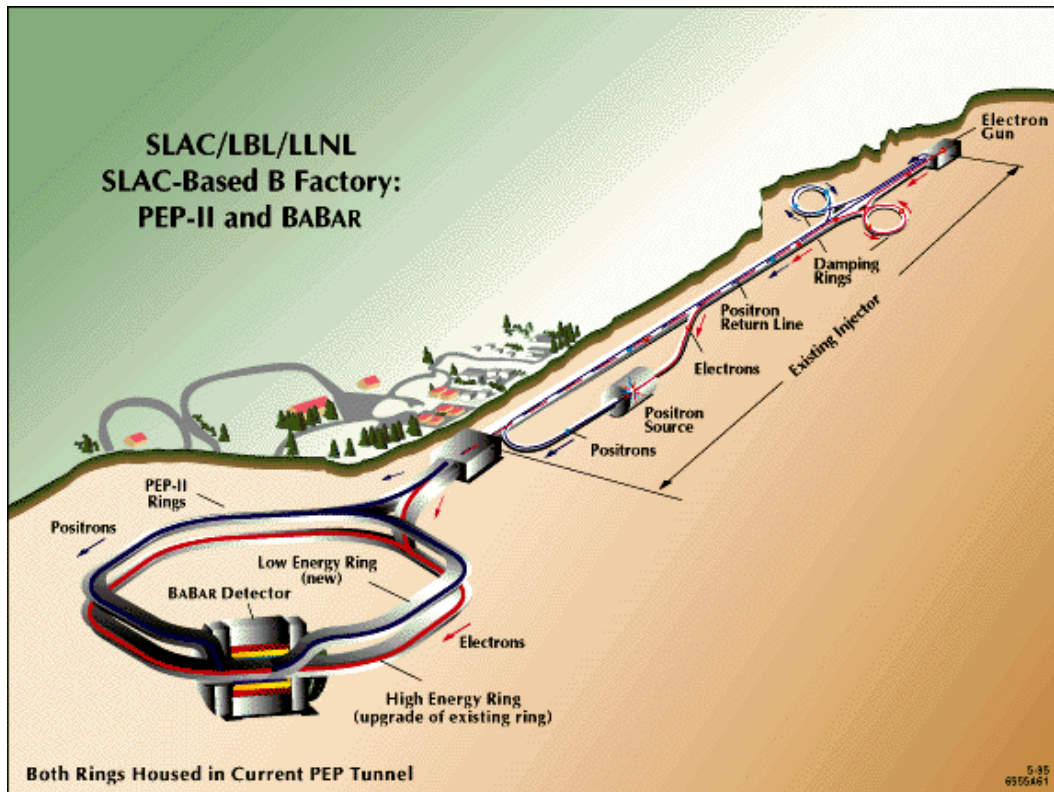


Figure 2.1: *Layout of the PEP-II collider at SLAC*

chrotron radiation flux that is not present in more conventional  $e^+e^-$  colliders. The bending also sweeps off-energy beam particles into the detector. There are also many more bunch crossings within the detector resolving time than in previous colliders. Machine-induced detector backgrounds have been considered and minimized in the PEP-II design.

Machine research and development has been going on all the time. With the conventional injection mode, PEP-II gradually improved the luminosity over time. But this mode requires the detector to be in standby mode for a few minutes about every hour to allow the injection of new bunches of electrons and positions into the storage rings, and the two new beams take some time to get stabilized to the design energies. Trickle injection mode was introduced since November 2003, which allows

the detector to stay in its run mode during injection of additional bunches into the existing beams. The new injection mode further improved the integrated luminosity. PEP-II recorded a peak luminosity of  $9.213 \times 10^{-33} \text{cm}^{-2} \text{s}^{-1}$  on May 21, 2004, a factor of 3 compared to the design goal, see Fig. 2.2. As of January 20, 2005, the integrated PEP-II delivered and *BABAR* recorded luminosities are around  $250 \text{fb}^{-1}$ , as also shown in Fig. 2.2.

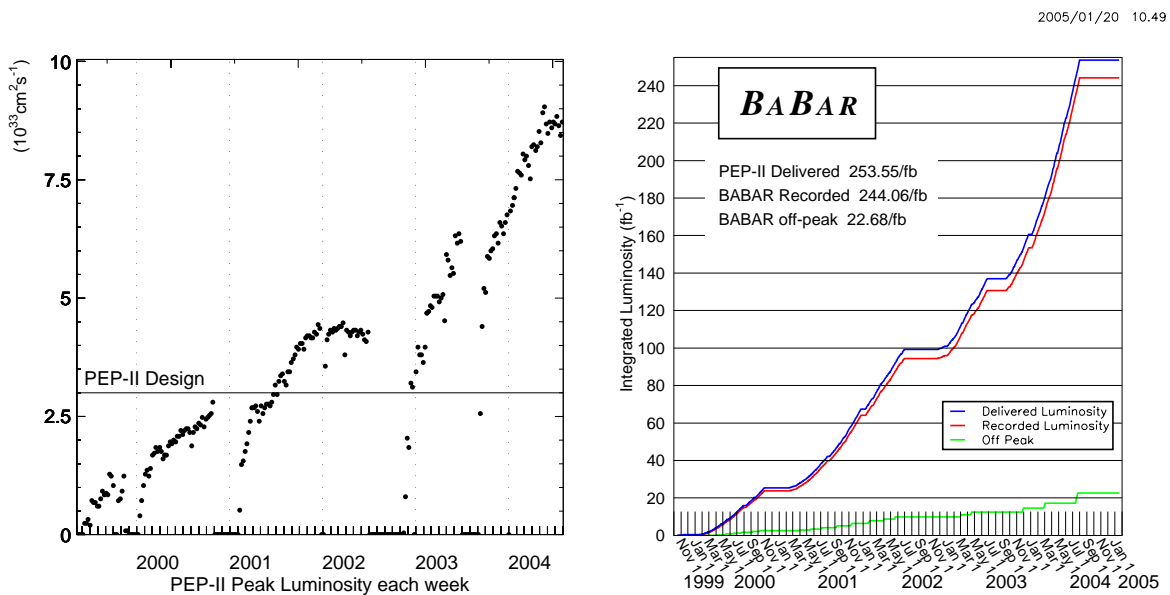


Figure 2.2: *PEP-II* peak luminosity (left) and the integrated luminosities (right)

## 2.2 The *BABAR* Detector

The *BABAR* detector is designed to meet the following stringent requirements:

- A large and uniform acceptance down to small polar angles relative to the boost direction;
- Detector components can tolerate significant radiation doses and operate reliably

under high-background conditions;

- Excellent reconstruction efficiency and momentum resolution for charged particles over the range  $\sim 60 < p_t < 4 \text{ GeV}$ ;
- Excellent detection of photons over a wide energy range of about  $20 \text{ MeV} \sim 5 \text{ GeV}$ ;
- Sufficient identification of  $e, \mu, \pi, K$ , and  $p$  over a wide kinematic range; particularly,  $\pi - K$  discrimination at high momenta ( $2 - 4 \text{ GeV}$ ) is essential.
- Capability to detect neutral hadrons, especially the  $K_L$ 's.

Fig. 2.3 shows a longitudinal section through the detector center, and an end view with the principal dimensions. The coordinate system for the detector is defined as follows: the  $z$ -axis is along the electron beam, while the  $y$ -axis is vertically perpendicular to the beam and  $x$ -axis horizontally perpendicular to the beam to form a right-hand coordinate system. The *BABAR* detector utilizes a superconductor magnet system that provides a 1.5-Tesla field parallel to the  $z$ -direction. A complete description of the *BABAR* detector can be found in Ref. [31].

### 2.2.1 The Silicon Vertex Tracker (SVT)

The SVT is designed to provide precise reconstruction of charged particle trajectories and  $B$ -meson decay vertices near the interaction region, and is the sole tracking device for very low-energy charged particles with transverse momenta less than  $100 \text{ MeV}/c$ .

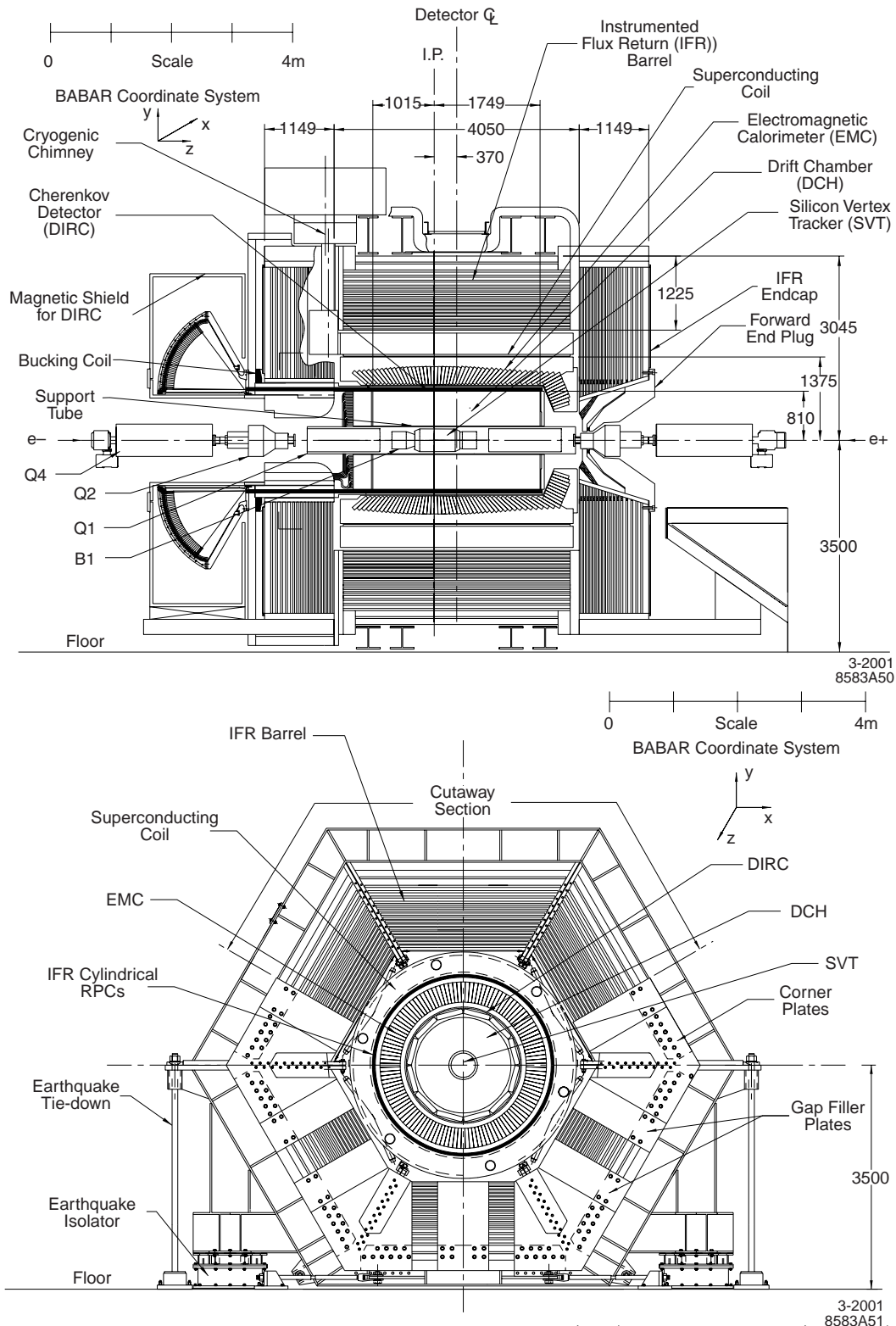


Figure 2.3: BABAR detector longitudinal section (top) and end view (bottom).

### 2.2.1.1 Design of the SVT

Silicon vertex detectors are used to build the SVT. These detectors are double-sided silicon strip detectors. Six types of detectors (I to VI) are needed with different configurations. The layout of SVT is shown in Fig. 2.4. It consists of five concentric cylindrical layers of the silicon detectors. Each layer is divided in azimuth into modules. The inner three layers have six detector modules and are traditional barrel-style structures. The outer two consist respectively of 16 and 18 detector modules, and employ a new arch structure to increase the solid angle coverage. The inner sides of the detectors have strips oriented perpendicular to the beam direction to measure the  $z$  coordinate, whereas the outer sides, with longitudinal strips, allow the  $\phi$  coordinate measurement. In total, the SVT has 340 silicon detectors and around 150,000 readout channels.

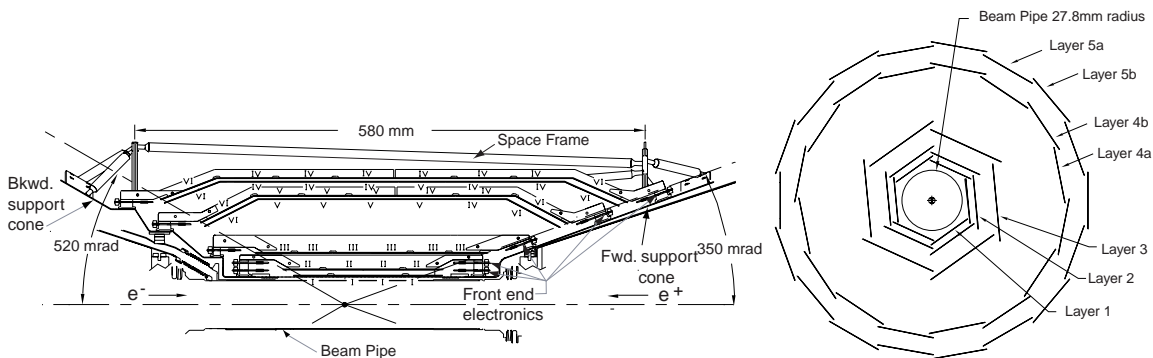


Figure 2.4: *Schematic views of SVT. Left: longitudinal section, the roman numerals label the six different types of sensors. Right: transverse section.*

### 2.2.1.2 Performance of the SVT

The SVT efficiency is measured to be 97%. The spatial resolution of SVT hits is determined by measuring the distance between the track trajectory and the hit, using high-momentum tracks in two prong events. Fig. 2.5 shows the SVT hit resolution for  $z$  and  $\phi$  side hits as a function of track incident angle, for each of the five layers. The measured resolutions are in excellent agreement with expectations from Monte Carlo simulations. The SVT has been operating efficiently since its installation in the *BABAR* experiment in May 1999, with expected and satisfactory performance.

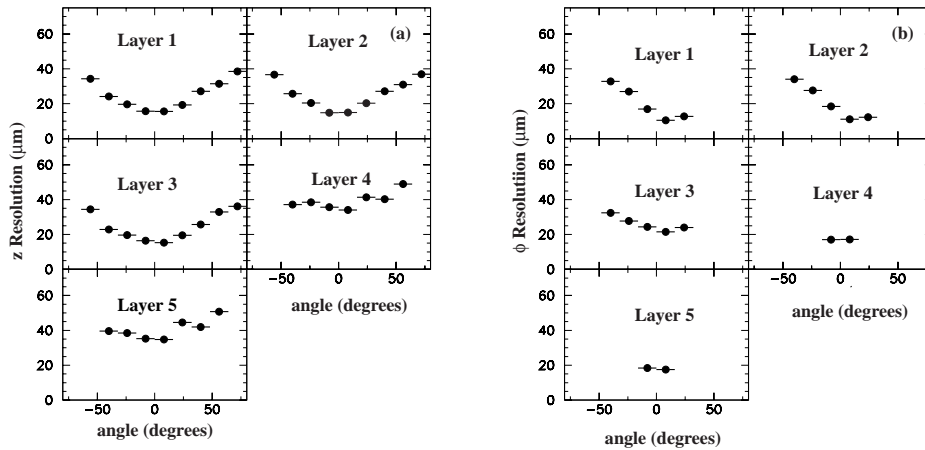


Figure 2.5: *SVT hit resolution in the a)  $z$  and b)  $\phi$  coordinate in microns, plotted as a function of track incident angle in degrees. Each plot shows a different layer of the SVT.*

### 2.2.2 The Drift Chamber (DCH)

The drift chamber is the main tracking device of the *BABAR* detector. Combined with the SVT, the *BABAR* tracking system provides excellent spatial and momentum resolution.

For low momentum particles, the DCH is required to provide particle identification by measurement of ionization loss ( $dE/dx$ ). This capability is complementary to that of the DIRC in the barrel region, while in the extreme backward and forward directions, the DCH is the only device providing discrimination of particles.

### 2.2.2.1 Design of the DCH

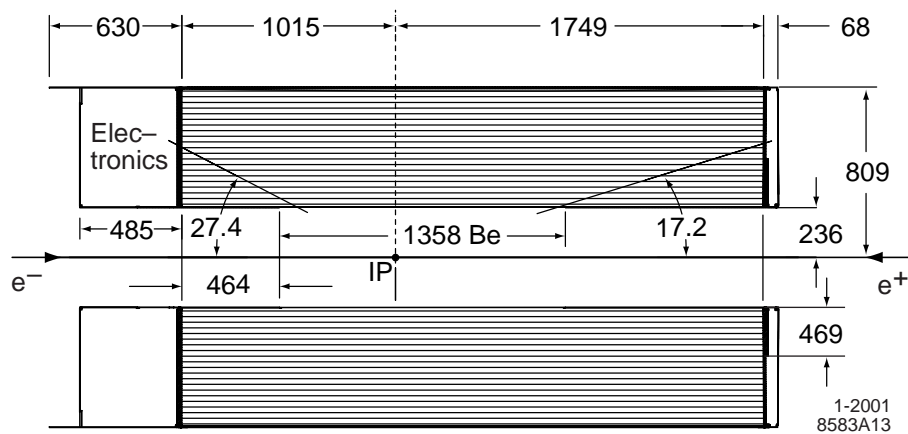


Figure 2.6: *Longitudinal section of the DCH with principal dimensions.*

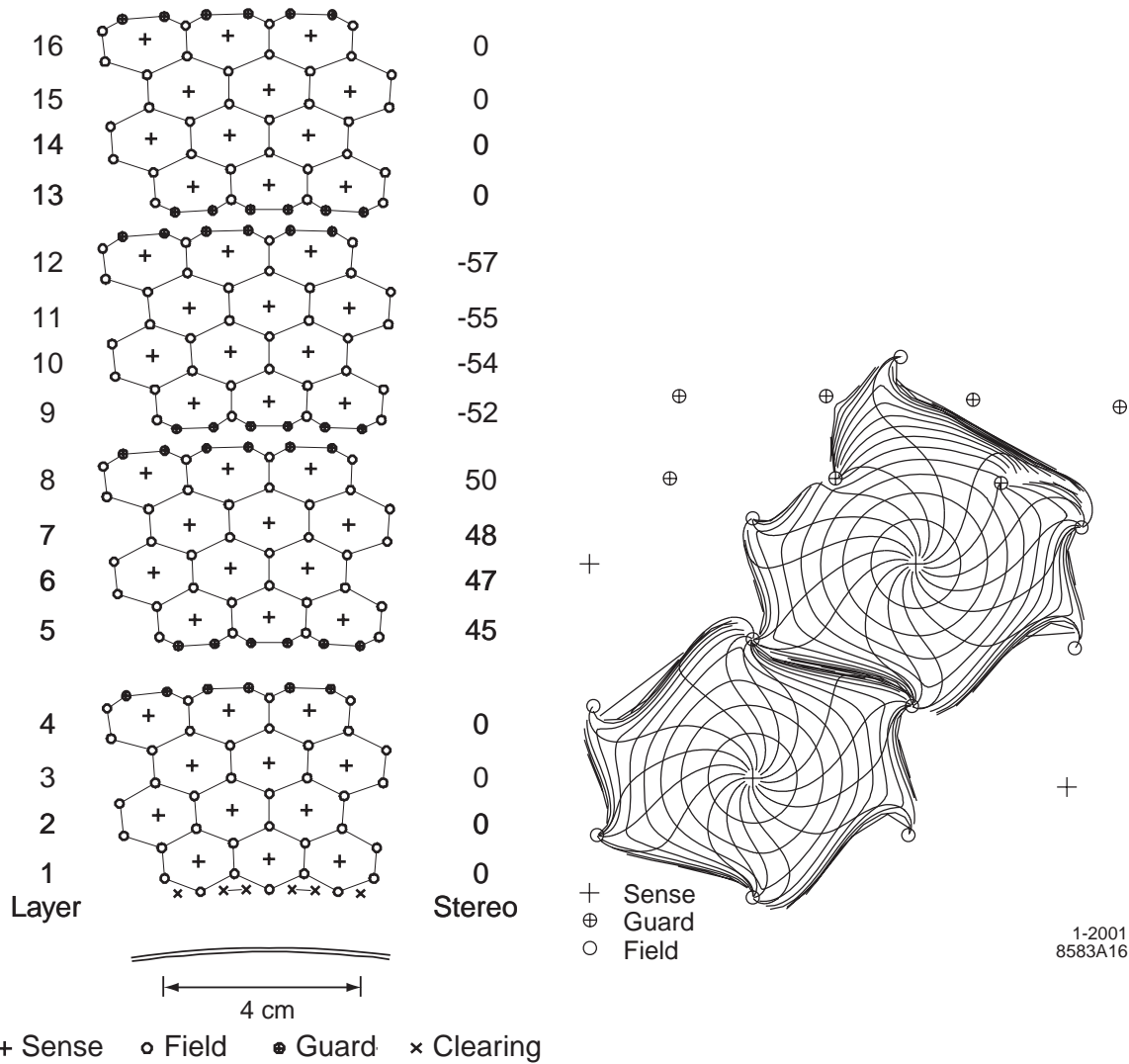
The DCH is relatively small in diameter, but almost 3 meters long. A longitudinal cross section and dimensions of the DCH are shown in Fig. 2.6. The DCH has 40 layers of small hexagonal cells providing up to 40 spatial and ionization loss measurements for charged particles with transverse momentum greater than  $180 \text{ MeV}/c$ . Longitudinal position information is obtained by placing the wires in 24 of the 40 layers at small angles with respect to the  $z$ -axis. By choosing low-mass aluminum field wires and a helium-based gas mixture (80:20 mixture of helium:isobutane), the multiple scattering inside the DCH is minimized to be less than 0.2% radiation lengths ( $X_0$ ) of material. The flat endplates are made of aluminum. Since the *BABAR* events will be boosted in the forward direction, the design of the detector is optimized to

reduce the material in the forward end. The forward endplate is made thinner(12mm) in the acceptance region of the detector compared to the rear endplate (24mm), and all the electronics is mounted on the rear endplate. The inner cylinder is made of 1 mm beryllium, which corresponds to  $0.28\%X_0$ . The outer cylinder consists of two 1.6 mm-thick layers of carbon fiber on a 6 mm-thick honeycomb core.

The drift cells are arranged in 10 superlayers of 4 layers each, for a total of 40 layers. Axial (A) and stereo (U, V) superlayers alternate, following the pattern AUVAUVAUVA as shown in Fig. 2.7. The stereo angle varies from a minimum of 40 mrad in the innermost stereo superlayer, to a maximum of 70 mrad in the outermost stereo superlayer. The 7104 cells are hexagonal with typical dimension of  $1.2 \times 1.8 \text{ cm}^2$ . Fig. 2.7 shows the 50ns isochrones in a typical cell in a 1.5T magnetic field.

The sense wires are  $20 \mu\text{m}$  gold-plated tungsten-rhenium. The field wires are  $120 \mu\text{m}$  and  $80 \mu\text{m}$  gold-plated aluminum. The chosen gas mixture, helium-isobutane (80%:20%), provides good spatial and  $dE/dx$  resolution and reasonably short drift time, with minimal multiple scattering. The gas and the wires total  $0.3\%X_0$  for tracks at  $90^\circ$ . The total thickness of the DCH at normal incidence is  $1.08\%X_0$ .

Nominal voltage of 1960 V for the sense wires and 340 V for the filed shaping wires at the boundaries of the superlayers are supplied by HV assemblies mounted on the feedthroughs of the rear endplate. Other field wires are connected to the ground through metal feedthroughs on the rear endplate. The forward endplate carries no components other than the feedthroughs.



1-2001  
8583A14

Figure 2.7: *Left: Schematic layout of drift cells for the four innermost superlayers. Lines have been added between field wires to aid in visualization of the cell boundaries. The numbers on the right side give the stereo angles (mrad) of sense wires in each layer. The 1 mm-thick beryllium inner wall is shown inside of the first layer. Right: Drift cell isochrones, i.e. contours of equal drift times of ions in cells of layers 3 and 4 of an axial superlayer. The isochrones are spaced by 100 ns.*

### 2.2.2.2 Performance of the DCH

The precision relation between the measured drift time and drift distance is determined from samples of  $e^+e^-$  and  $\mu^+\mu^-$  events, as shown in Fig. 2.8. Fig. 2.8, right, shows the position resolution as a function of the drift distance, separately for the left and the right side of the sense wire. The resolution is taken from Gaussian fits to the distributions of residuals obtained from unbiased track fits.

The specific energy loss,  $dE/dx$ , for charged particles traversing the DCH is derived from measurements of total charge deposited in each drift cell.  $dE/dx$  per track is computed as a truncated mean from the lowest 80% of the individual  $dE/dx$  measurements. Various corrections are applied to remove sources of bias that degrade the accuracy of the primary ionization measurement. Fig. 2.9 shows the distribution of the corrected  $dE/dx$  measurements as a function of track momenta. The superimposed Bethe-Bloch predictions for particles of different masses have been determined from selected control samples. The measured  $dE/dx$  resolution for Bhabha events is shown in Fig. 2.9. The rms resolution achieved to date is typically 7.5%, limited by the number of samples and Landau fluctuations. This resolution will allow  $\pi/K$  separation up to 700 MeV/ $c$ .

As for the charged particle tracking, the reconstruction of charged particle tracks relies on data from both the SVT and the DCH. Charged tracks are defined by five parameters ( $d_0, \phi_0, \omega, z_0, \tan \lambda$ ) and their associated error matrix. These parameters are measured at the point of closest approach to the  $z$ -axis;  $d_0$  and  $z_0$  are the distances of this point from the origin of the coordinate system in the  $x$ - $y$  plane and along the  $z$ -axis, respectively. The angle  $\phi_0$  is the azimuth of the track,  $\lambda$  the dip angle

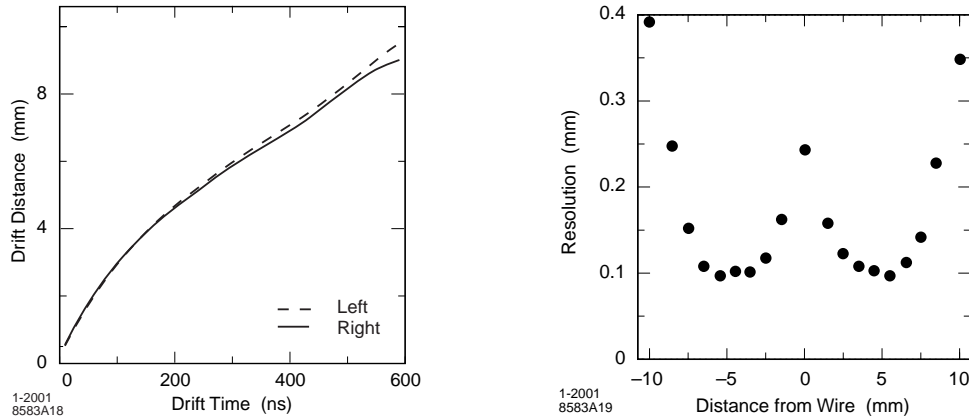


Figure 2.8: *Left: The drift time versus distance relation for the left and right halves of a cell. These functions are obtained from the data averaged over all cells in a single layer of the DCH. Right: DCH position resolution as a function of the drift distance in layer 18, for tracks on the left and right side of the sense wire. The data are averaged over all cells in the layer.*

relative to the transverse plane, and  $\omega = 1/p_t$  is its curvature.  $d_0$  and  $\omega$  are signed variables; their sign depends on the charge of the track. The track finding and the fitting procedures make use of Kalman filter algorithm that takes into account the detailed distribution of material in the detector and the full map of the magnetic field.

The absolute DCH tracking efficiency is determined as the ratio of the number of reconstructed DCH tracks to the number of tracks detected in the SVT, with the requirement that they fall within the acceptance of the DCH. Fig. 2.10 left shows the tracking efficiency study using multi-hadron events. The standalone SVT tracking algorithms have a high efficiency for tracks with low transverse momentum (Fig. 2.11), which is important for the detection of the secondary  $D^*$  decays.

The resolution in the track parameters is monitored using  $e^+e^-$  and  $\mu^+\mu^-$  pair events. It is further investigated offline for tracks in multi-hadron events and cosmic

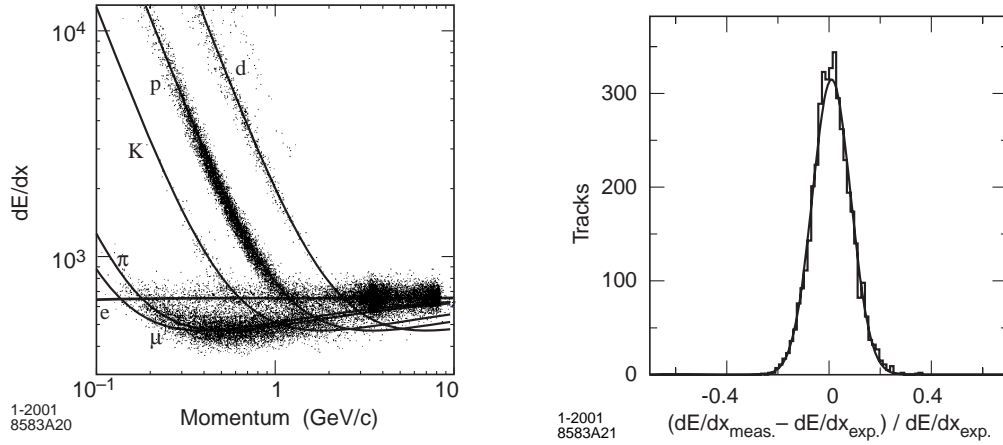


Figure 2.9: *Left: Measurement of  $dE/dx$  in the DCH as a function of track momenta. The curves show the Bethe-Bloch predictions derived from selected control samples of particles of different masses. Right: Difference between the measured and expected energy loss  $dE/dx$  for  $e^\pm$  from Bhabha scattering, measured in the DCH at an operating voltage of 1900V. The curve represents a Gaussian fit to the data with a resolution of 7.5%.*

ray muons. From cosmic ray study, the resolutions for single tracks with transverse momenta above  $3 \text{ GeV}/c$  are found to be

$$\begin{aligned} \sigma_{d_0} &= 23 \mu\text{m} & \sigma_{\phi_0} &= 0.43 \text{ mrad} \\ \sigma_{z_0} &= 29 \mu\text{m} & \sigma_{\tan \lambda} &= 0.53 \cdot 10^{-3}. \end{aligned}$$

The dependence of the resolution in  $d_0$  and  $z_0$  on the transverse momentum  $p_t$  is presented in Figure 2.12 left. The measurement is based on tracks in multi-hadron events.

While the position and angle measurements near the IP are dominated by the SVT measurements, the DCH contributes primarily to the  $p_t$  measurement. Figure 2.12 right shows the resolution in the transverse momentum derived from cosmic

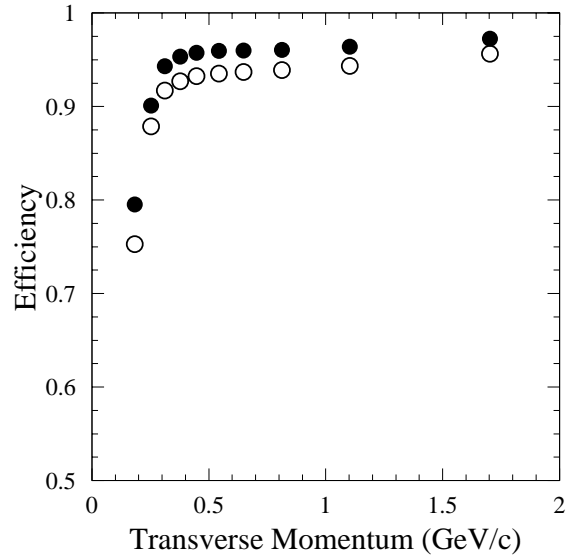


Figure 2.10: *The track reconstruction efficiency in the DCH at operating voltages of 1900 V (open circle) and 1960 V (solid circle), as a function of transverse momentum. The efficiency is measured in multi-hadron events.*

muons. The data are well represented by a linear function,

$$\sigma_{p_t}/p_t = (0.13 \pm 0.01)\% \cdot p_t + (0.45 \pm 0.03)\%,$$

where the transverse momentum  $p_t$  is measured in GeV/c. These values for the resolution parameters are very close to the initial estimates and can be reproduced by Monte Carlo simulations. More sophisticated treatment of the DCH time-to-distance relations and overall resolution function are presently under study.

### 2.2.3 The Detector of Internally Reflected Cherenkov Light (DIRC)

Particle identification (PID) is critical to the study of  $CP$ -violation. The PID system being used in *BABAR* is a new kind of ring-imaging Cherenkov detector called the *Detector of Internally Reflected Cherenkov light* (DIRC). It is expected to be able

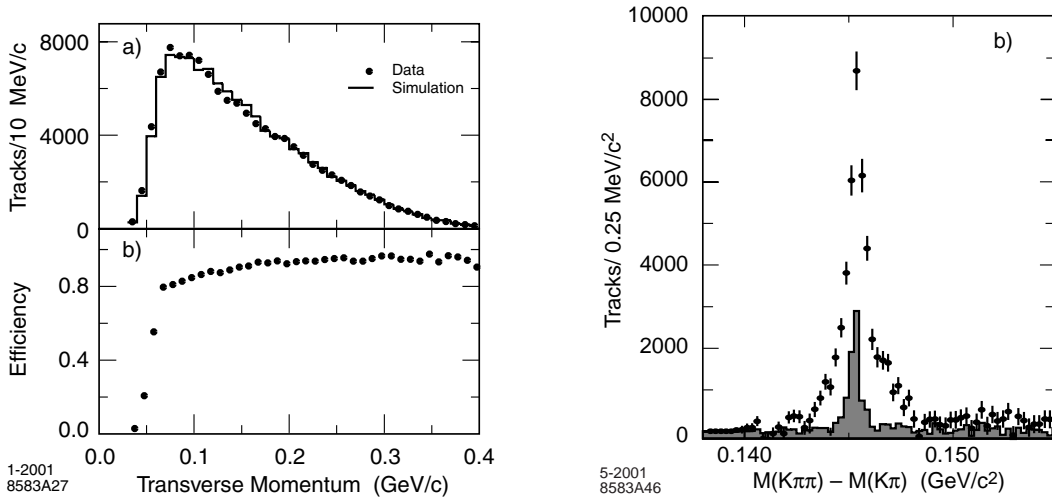


Figure 2.11: *Left: Monte Carlo studies of low momentum tracks in the SVT: a) comparison of data (contributions from combinatoric background and non- $B\bar{B}$  events have been subtracted) with simulation of the transverse momentum spectrum of pions from  $D^{*+} \rightarrow D^0\pi^+$  in  $B\bar{B}$  events, and b) efficiency for slow pion detection derived from simulated events. Right: Reconstruction of low momentum tracks: the mass difference,  $\Delta M = M(K^-\pi^+\pi^+) - M(K^-\pi^+)$ , both for all detected events (data points) and for events in which the low momentum pion is reconstructed both in the SVT and DCH (histogram). Backgrounds from combinatorics and fake tracks, as well as non-resonant data have been subtracted.*

to provide  $\pi/K$  separation of  $\sim 4\sigma$  or greater, for all tracks from  $B$ -meson decays from the pion Cherenkov threshold up to  $4.2 \text{ GeV}/c$ . Cherenkov radiation is emitted whenever charged particles pass through matter with a velocity exceeding the velocity of light in the medium. The charged particles polarize the molecules, which then turn back rapidly to their ground state, emitting prompt radiation. The emitted light forms a coherent wavefront. Cherenkov light is emitted under a constant angle with the particle trajectory, given by  $\cos\theta_c = 1/n\beta$ , where  $n = 1.473$  is the mean index

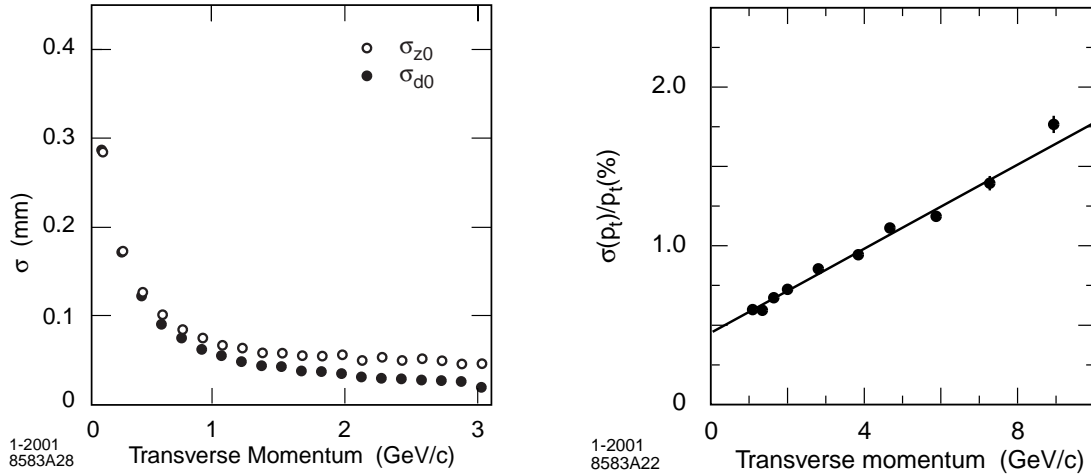


Figure 2.12: *Left: Resolution in the parameters  $d_0$  and  $z_0$  for tracks in multi-hadron events as a function of the transverse momentum. Right: Resolution in the transverse momentum  $p_T$  determined from cosmic ray muons traversing the DCH and SVT.*

of refraction of fused silica,  $\beta = v/c$ ,  $v$  is the velocity of the particle, and  $c$  is the velocity of light. The measurement of  $\theta_c$  is based on the principle that the magnitudes of angles are maintained upon reflection from a flat surface.

### 2.2.3.1 Design of the DIRC

Fig. 2.13 shows a schematic of the DIRC geometry that illustrates the principles of light production, transport, and imaging. The radiator material of the DIRC is synthetic, fused silica in the form of long, thin bars with rectangular cross sections. These bars serve both as radiators and as light pipes. The DIRC is composed of such 144 bars, which are grouped into 12 bar boxes. The bars are 17 mm-thick, 35 mm-wide, and 4.9 m-long. Within a bar box, the 12 bars are optically isolated by an  $\sim 150\mu\text{m}$  air gap between neighboring bars, enforced by custom shims made from aluminum foil. The standoff box, a purified-water-filled expansion region, is made of stainless steel, consisting of a cone, cylinder, and 12 sectors of fast photomultiplier tubes (PMTs).

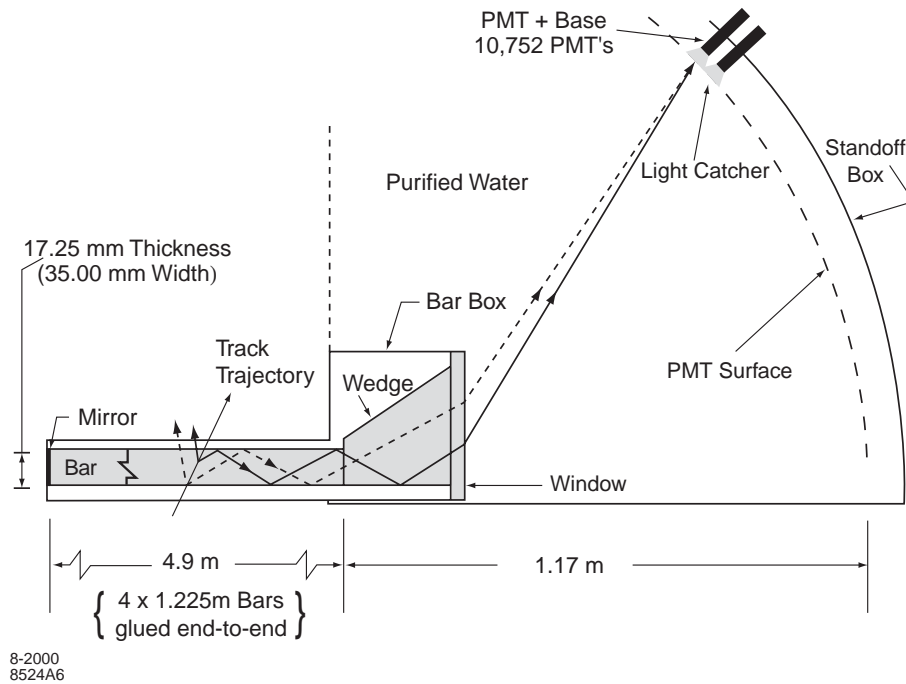


Figure 2.13: *Schematic of the DIRC system.*

In total, there are 10,752 PMTs each with a diameter of 2.9 cm. The DIRC occupies 80 mm of radial space in the central detector volume, with a total thickness of about  $17\%X_0$  at normal incidence. The radiator bars subtend a solid angle corresponding to about 94% of the azimuth and 83% of the center-of-mass (c.m.) polar angle.

### 2.2.3.2 Performance of the DIRC

An unbinned maximum likelihood formalism is used to incorporate the space and time measurements from the DIRC. The emission angle and the arrival time of the Cherenkov photons are reconstructed from the observed space-time coordinates of the PMT signals, transformed into the Cherenkov coordinate system. The expected arrival time is calculated from the track time-of-flight and the photon propagation time. The measured time resolution (from dimuon events) is 1.7 ns, close to the

intrinsic 1.5 ns transit time spread of the PMTs. The routine provides a likelihood value for each of the five stable particle types ( e,  $\mu$ ,  $\pi$ , K, p). The resolution ( $\sigma_{C,track}$ ) on the track Cherenkov angle should scale as

$$\sigma_{C,track} = \frac{\sigma_{C,\gamma}}{\sqrt{N_{pe}}}, \quad (2.1)$$

where  $\sigma_{C,\gamma}$  is the single photon Cherenkov angle resolution which is 10.2 mrad, and  $N_{pe}$  is the number of photons detected, which is between 20 for small polar angles and 65 at large polar angles for dimuon events. As shown in Fig. 2.14 left, the expected separation between kaons and pions at 3 GeV/c is about  $4.2\sigma$ , within 15% of the design goal. The efficiency for correctly identifying a charged kaon is also shown in Fig. 2.14.

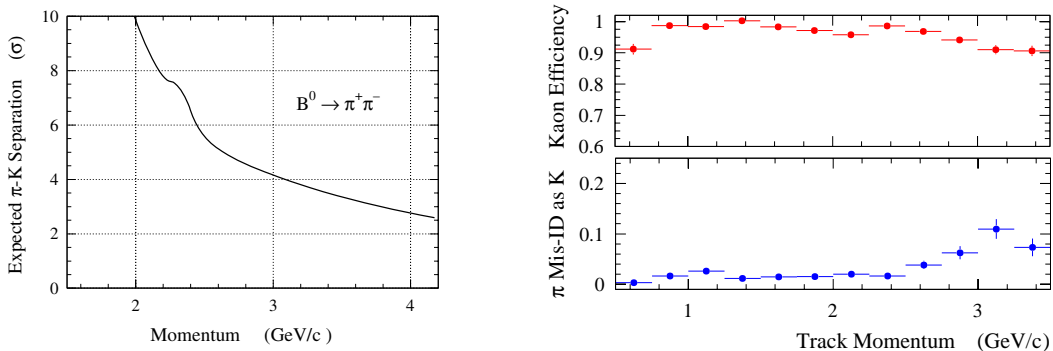


Figure 2.14: *Left: Expected  $\pi$ -K separation in  $B^0 \rightarrow \pi^+\pi^-$  events versus track momentum inferred from the measured Cherenkov angle resolution and number of Cherenkov photons per track in di-muon events. Right: Efficiency and misidentification probability for the selection of charged kaons as a function of track momentum, determined using  $D^0 \rightarrow K^-\pi^+$  decays selected kinematically from inclusive  $D^*$  production.*

#### 2.2.4 The Electromagnetic Calorimeter (EMC)

The electromagnetic calorimeter is designed to measure electromagnetic showers with excellent efficiency, and energy and angular resolution over the energy range

from 20 MeV to 9 GeV. This capability allows the detection of photons from  $\pi^0$  and  $\eta$  decays as well as from electromagnetic and radiative processes. The EMC also helps to identify electrons.

#### 2.2.4.1 Design of the EMC

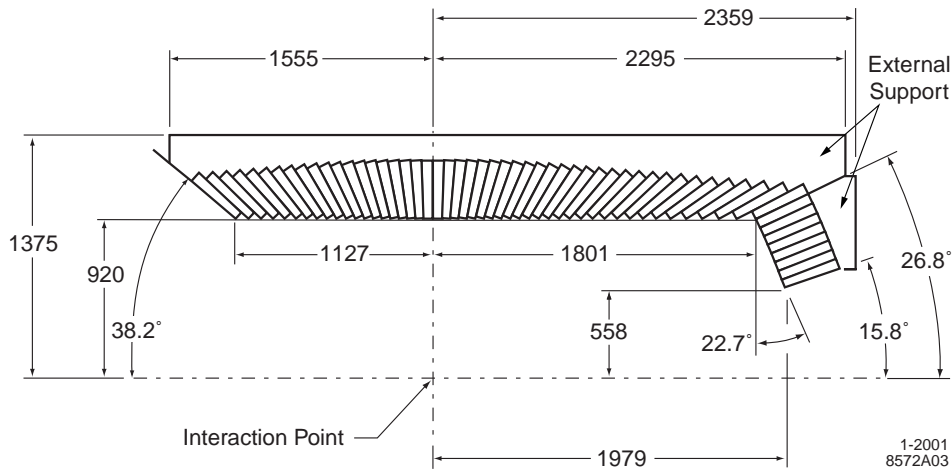


Figure 2.15: A longitudinal cross section of the EMC (only the top half is shown) indicating the arrangement of the 56 crystal rings. The detector is axially symmetric around the  $z$ -axis. All dimensions are given in mm.

The EMC consists of a cylindrical barrel and a conical forward endcap, as shown in Fig. 2.15. The barrel contains 5760 crystals arranged in 48 distinct rings with each ring containing 120 identical crystals, while the endcap holds 820 crystals arranged in eight rings. The calorimeter provides full coverage in azimuth and extends in polar angle from  $15.8^\circ$  to  $141.8^\circ$ . The crystals are 0.1%-Thallium-doped cesium iodide (CsI(Tl)), which has high light yield and small Moliere radius for excellent energy and angular resolution, and a short radiation length (1.85 cm) good for compact design and decent shower containment at *BABAR* energies. The crystals have tapered trapezoidal

cross sections. The transverse dimensions of the crystals for each of the 56 rings vary to achieve the required hermetic coverage. The typical area of the front face is  $4.7 \times 4.7 \text{ cm}^2$ , while the back face area is typically  $6.1 \times 6.0 \text{ cm}^2$ . The length varies from 29.6 cm ( $16 X_0$ ) in the backward to 32.4 cm ( $17.5 X_0$ ) in the forward direction. Each crystal is wrapped in 2 layers of  $165 \mu\text{m}$  tyvek which reflects the scintillation light. In addition, each crystal is further wrapped in  $25 \mu\text{m}$  thick aluminum foil which provides a Faraday shield. The scintillation light is read out by two  $2 \times 1 \text{ cm}^2$  silicon photo-diodes installed on the rear face of the crystals.

#### 2.2.4.2 Performance of the EMC

A typical electromagnetic shower spreads over many adjacent crystals, forming a cluster of energy deposits. Pattern recognition algorithms have been developed to identify such clusters.

The energy resolution at low energy is measured directly with a radioactive source yielding  $\sigma_E/E = 5.0 \pm 0.8\%$  at 6.13 MeV. The energy resolution is further studied with Bhabha scattering and other specific processes, as shown in Fig 2.16. A fit to the energy dependence yields

$$\frac{\sigma_E}{E} = \frac{(2.32 \pm 0.30)\%}{\sqrt[4]{E(\text{GeV})}} \oplus (1.85 \pm 0.12)\%. \quad (2.2)$$

The angular resolution is measured with  $\pi^0$  and  $\eta$  decays to two photons of approximately equal energy. The result is shown in Fig. 2.16. An empirical fit results in

$$\sigma_\theta = \sigma_\phi = \left( \frac{3.87 \pm 0.07}{\sqrt{E(\text{GeV})}} + 0.00 \pm 0.04 \right) \text{ mrad}. \quad (2.3)$$

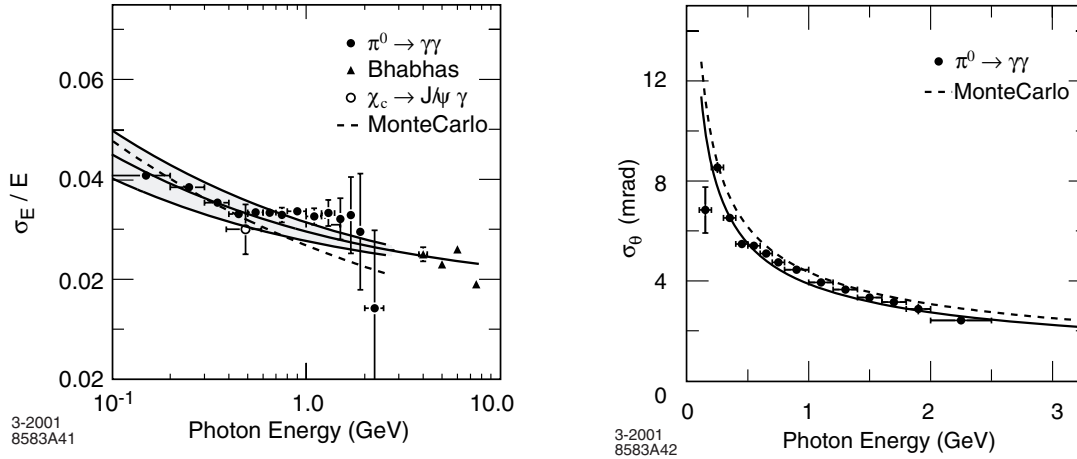


Figure 2.16: *Left: The energy resolution for the EMC measured for photons and electrons from various processes. The solid curve is a fit to Eq. 2.2 and the shaded area denotes the rms error of the fit. Right: The angular resolution of the EMC for photons from  $\pi^0$  decays. The solid curve is a fit to Eq. 2.3.*

## 2.2.5 The Instrumented Flux Return (IFR)

The IFR is designed to detect and identify muons with high efficiency, and to detect neutral hadrons such as  $K_L^0$ 's and neutrons. Muons are important for tagging the flavor of neutral  $B$  mesons via semi-leptonic decays, for the reconstruction of vector mesons such as  $J/\Psi$ , and for the study of semi-leptonic and rare decays involving leptons.

### 2.2.5.1 Design of the IFR

The IFR uses the steel flux return of the magnet as a muon filter and hadron absorber. Single-gap resistive plate chambers (RPCs) with two-coordinate readout are chosen as the active detectors. RPCs detect streamers from ionizing particles via capacitive readout strips, and have the following advantages: simple, low cost con-

struction, and the possibility of covering odd shapes with minimal dead space. Large signals and fast response greatly simplify the front-end electronics and provide good time resolution, typically 1-2 ns. The position resolution depends on the segmentation of the readout; a value of a few mm is achievable. A cross-section of a planar RPC is shown in Fig. 2.17. The RPCs are operated in limited streamer mode, at a high voltage of around 8 kV.

The RPCs are installed in the gaps of the finely segmented steel of the barrel and the end doors of the flux return, as shown in Fig. 2.18. Monte Carlo studies have been used to optimize the steel segmentation. The steel is segmented into 18 plates with their thicknesses increasing from 2 cm for the inner nine plates to 10 cm for the outermost plates. The nominal gap between the steel plates is 3.5 cm in the inner layers of the barrel and 3.2 cm elsewhere. There are 19 RPC layers in the barrel and 18 in the endcaps. In addition, two layers of cylindrical RPCs are installed between the EMC and the magnet cryostat to detect particles exiting the EMC.

In total, there are 806 RPC modules, with 57 in each of the six barrel sectors, 108 in each of the four half end doors, and 32 in the two cylindrical layers. The IFR detectors cover an area of about  $2000 m^2$ . The readout strips have width varying from about 2-4 cm, totalling about 53,000 channels.

### **2.2.5.2 Performance of the IFR**

While muon identification relies primarily on the IFR, other detector systems provide complementary information. A charged track is extrapolated to the IFR to associate it with an IFR cluster. A few variables are introduced to identify a muon candidate:

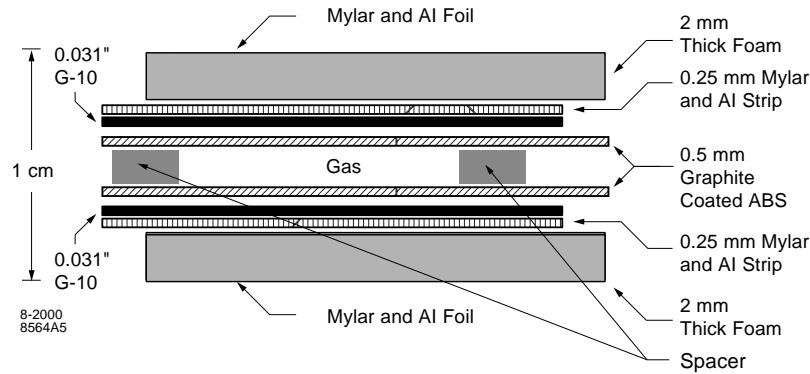


Figure 2.17: *Cross section of a planar RPC.*

- the total number of interaction lengths traversed from the IP to the last RPC layer with an associated cluster;
- the difference between this measured number of interaction lengths and that predicted for a muon;
- the average number and the rms of the distribution of RPC strips per layer;
- the  $\chi^2$  for the geometric match between the projected track and the centroids of clusters in different RPC layers
- the  $\chi^2$  of a polynomial fit to the two-dimensional IFR clusters.

The performance of muon identification has been tested on muon samples from  $\mu\mu e e$  and  $\mu\mu\gamma$  final states and pions from three-prong  $\tau$  decays and  $K_S \rightarrow \pi^+\pi^-$  decays. As shown in Fig. 2.19, the muon identification efficiency is close to 90% with a fake rate for pions of about 6-8%.

$K_L^0$ 's and other neutral hadrons that reach the IFR can be identified IFR clusters that are not associated with any charged tracks. Monte Carlo simulations predict that about 64% of  $K_L^0$ 's with momenta above 1 GeV/c give cluster signatures in the

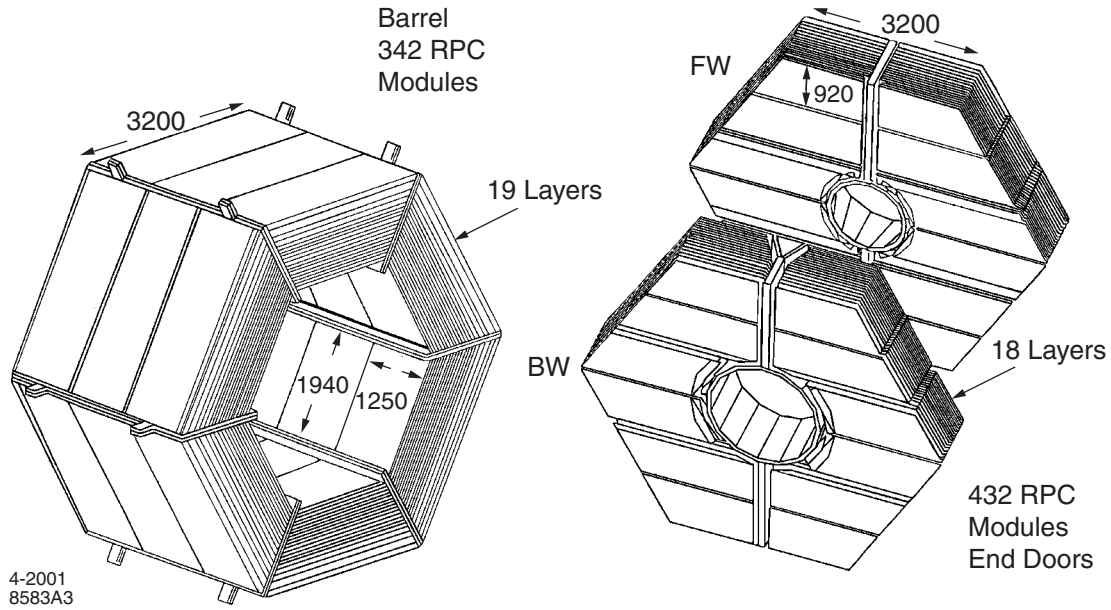


Figure 2.18: Overview of the IFR: Barrel sectors and forward (FW) and backward (BW) end doors; the shape of the RPC modules and their dimensions are indicated.

IFR. With the EMC information being combined, the  $K_L^0$  detection efficiency linearly increases from 20% to 40% when the momentum changes from 1 GeV/c to 4 GeV/c.

During the first year of operation, a large fraction of the RPC modules have suffered significant losses in efficiency. The effect appears to be correlated with high temperatures, but the cause is still under investigation [32]. In some of the affected RPC modules, it was found that the linseed oil (used to reduce dark current or discharge) had failed to cure and had accumulated at various spots under influence of the electric field.

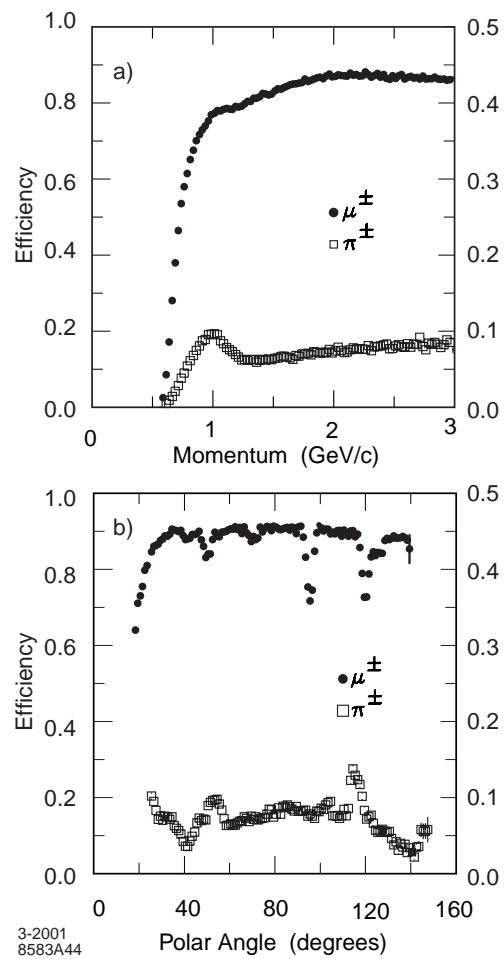


Figure 2.19: Muon efficiency (left scale) and pion misidentification probability (right scale) as a function of a) the laboratory track momentum, and b) the polar angle (for momentum  $1.5 < p < 3.0$  GeV/c).

## Chapter 3

# The Decay Dynamics

The main challenge of the Dalitz plot analysis is the construction of a realistic signal probability density function (PDF), where both the kinematic and dynamical properties are modeled to good accuracy.

### 3.1 Dalitz Plot

We recall here the basic properties of the Dalitz plot as far as it is needed to motivate the various choices we have made. More information may be found in, *e.g.*, Refs. [3, 33, 34].

We consider the decay of a spin-zero  $B^0$  with four-momentum  $p_B$  into the three daughters  $K^+(p_+)$ ,  $\pi^-(p_-)$ ,  $\pi^0(p_0)$ , with corresponding four-momenta. The original number of 12 unknowns in the  $B^0$  rest frame is reduced to 2, taking advantage of the known masses of the four particles involved (4), energy and momentum conservation (4) and the fact that two spatial angles are irrelevant (no direction is preferred) (2). Using as independent (Mandelstam) variables the invariant masses squared

$$s_{+0} = (p_+ + p_0)^2, \quad s_{-0} = (p_- + p_0)^2, \quad (3.1)$$

the invariant mass of the charged kaon and pion pairs,  $s_{+-} = (p_+ + p_-)^2$ , is obtained from energy and momentum conservation:

$$s_{+-} = m_{B^0}^2 + m_{K^+}^2 + m_{\pi^+}^2 + m_{\pi^0}^2 - s_{+0} - s_{-0} . \quad (3.2)$$

Note that in our convention,  $(+, -, 0)$  subscripts in the Mandelstam variables refer to the  $(K^+, \pi^-, \pi^0)$  daughters respectively, and refer to the  $(K^-, \pi^+, \pi^0)$  daughters in the case of  $\bar{B}^0$  decays.

The differential  $B^0$  decay width with respect to the variables defined in Eq. (3.1) (*i.e.*, the *Dalitz plot*) reads

$$d\Gamma(B^0 \rightarrow K^+ \pi^- \pi^0) = \frac{1}{(2\pi)^3} \frac{|\mathcal{A}_{B^0 \rightarrow K^+ \pi^- \pi^0}|^2}{8m_{B^0}^3} ds_{+0} ds_{-0} , \quad (3.3)$$

where  $\mathcal{A}_{B^0 \rightarrow K^+ \pi^- \pi^0}$  is the Lorentz-invariant amplitude of the three-body decay. There is a similar equation for  $\bar{B}^0$  decays. Note that a trivial integration over the spatial angles has been performed prior to Eq. (3.3). We will in the following choose the notation  $\{\text{DP}\}$  for the Dalitz plot coordinates  $\{s_{+0}, s_{-0}\}$ , and, correspondingly,  $\{d\text{DP}\}$  for the Dalitz element  $\{ds_{+0} ds_{-0}\}$ . The boundaries of the Dalitz plot are obtained when, *e.g.*, for a  $K^{*0} \rightarrow K^+ \pi^-$  resonance,  $\mathbf{p}_+$  is parallel (minimum mass-squared) or anti-parallel (maximum mass-squared) to  $\mathbf{p}_0$ . Due to the small mass difference between charged and neutral pions (as compared with  $K^+$  and  $B^0$  masses), the Dalitz plot is almost symmetric with respect to the diagonal. As a function of  $s_{+0}$ , the kinematic boundaries  $s_{-0}[\text{max}]$  and  $s_{-0}[\text{min}]$  are given by

$$s_{-0}[\text{max/min}](s_{+0}) = (E_-^* + E_0^*)^2 - \left( \sqrt{E_-^{*2} - m_+^2} \mp \sqrt{E_0^{*2} - m_0^2} \right)^2 , \quad (3.4)$$

where

$$E_+^* = \frac{s_{+0} - m_0^2 + m_+^2}{2\sqrt{s_{+0}}} , \quad (3.5)$$

$$E_0^* = \frac{s_{+0} - m_+^2 + m_0^2}{2\sqrt{s_{+0}}}, \quad (3.6)$$

$$E_-^* = \frac{m_{B^0}^2 - s_{+0} - m_+^2}{2\sqrt{s_{+0}}}, \quad (3.7)$$

are the energies in the  $K^+\pi^0$  rest frame. Numerically, the minimum and maximum masses squared are  $s_{-0}[\text{max}] = (m_{B^0} - m_+)^2 \simeq 26.465 (\text{GeV}/c^2)^2$  and  $s_{-0}[\text{min}] = (m_+ + m_0)^2 \simeq 0.401 (\text{GeV}/c^2)^2$ . Due to angular momentum conservation, the spin-one  $K^*(892)$  resonance is polarized in a helicity-zero state. We therefore need to compute the cosine of the angle between the negative  $B^0$  momentum in the  $K^{*+}$  rest frame (which is the flight direction of the  $K^{*+}$  resonance in the  $B^0$  rest frame, and the negative flight direction of the  $\pi^-$  in the  $B^0$  rest frame) and the momentum  $\mathbf{p}_0^*$  of the  $\pi^0$  in the  $K^{*+}$  rest frame. It is given by

$$\cos \theta_+ = \frac{2E_+^*E_-^* + m_+^2 + m_-^2 - s_{+-}}{2|\mathbf{p}_+^*||\mathbf{p}_-^*|}, \quad (3.8)$$

and expansion as a function of the Dalitz variables  $s_{+0}$  and  $s_{-0}$  leads to

$$\begin{aligned} \cos \theta_+ &= \left[ s_{+0}(s_{-0} - s_{+-}) - (m_{B^0}^2 - m_+^2)(m_0^2 - m_+^2) \right] \\ &\times \left[ m_+^4 + (s_{+0} - m_0^2)^2 - 2m_+^2(s_{+0} + m_0^2) \right]^{-1/2} \\ &\times \left[ m_{B^0}^4 + (s_{+0} - m_+^2)^2 - 2m_{B^0}^2(s_{+0} + m_+^2) \right]^{-1/2}, \quad (3.9) \end{aligned}$$

where  $s_{+-}$  is obtained from Eq. (3.2). Exchanging  $s_{+0} \leftrightarrow s_{-0}$  in Eq. (3.9) yields the negative cosine of the helicity angle  $-\cos \theta_-$ , and replacing  $s_{+0} \rightarrow s_{+-}$  together with  $m_0 \leftrightarrow m_+$  gives  $-\cos \theta_0$ . Figure 3.1 illustrates the convention we have adopted for the helicity angles:

- $\cos \theta_+$  is defined as the angle between the  $\pi^0$  in the  $K^{*+}$  rest frame and the  $K^{*+}$  flight direction in the  $B^0$  rest frame.

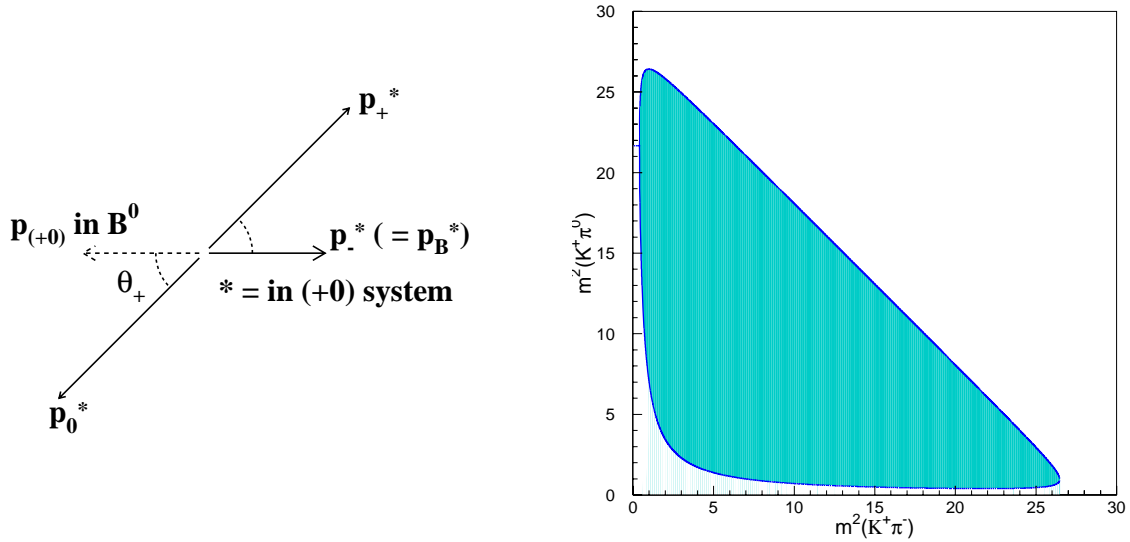


Figure 3.1: *Left: convention adopted for the helicity angles. For vanishing relative strong phases it leads to destructive interference at all points in the Dalitz plot where at least two of the three mass combinations are equal. See text for a geometrical definition. Right: the classic Dalitz Plot.*

- $\cos \theta_-$  is defined as the angle between the  $\pi^-$  in the  $\rho^-$  rest frame and the  $\rho^-$  flight direction in the  $B^0$  rest frame.
- $\cos \theta_0$  is defined as the angle between the  $\pi^+$  in the  $K^{*0}$  rest frame and the  $K^{*0}$  flight direction in the  $B^0$  rest frame.

For vanishing relative strong phases, each resonance overlap comes with a relative minus sign so that maximal destructive interference is observed at all points with equal masses squared.

The amplitude  $\mathcal{A}_{B^0 \rightarrow K^+\pi^-\pi^0}$  contains all the underlying dynamics of the  $B^0 \rightarrow K^+\pi^-\pi^0$  decay. In general, it is the coherent sum of one non-resonant term ( $\mathcal{A}_{\text{NR}}$ ),

which is (assumed to be) constant in the Dalitz plane, and multiple resonant amplitudes  $i$ , with different spins  $J$ , arbitrary real fractions and phase shifts,  $a_i$ ,  $\phi_i$ , and charge combinations  $\{+0, -0, +- \}$ :

$$\mathcal{A}_{B^0 \rightarrow K^+ \pi^- \pi^0}(\text{DP}) = a_{\text{NR}} e^{i\phi_{\text{NR}}} \mathcal{A}_{\text{NR}} + \sum_{\kappa\sigma \in \{+0, -0, +- \}} \sum_i a_i^{\kappa\sigma} e^{i\phi_i^{\kappa\sigma}} \mathcal{A}_i^{\kappa\sigma}(\text{DP}) . \quad (3.10)$$

Each resonant amplitude  $i$  can be written as a product of five terms

$${}^J \mathcal{A}_i^{\kappa\sigma}(\text{DP}) = {}^J F_{B,i} \cdot {}^J F_i(s_{\kappa\sigma}) \cdot {}^J K^{\kappa\sigma}(\text{DP}) \cdot {}^J F_{R,i}(s_{\kappa\sigma}) \cdot A_i^{\kappa\sigma} \quad (3.11)$$

$$\equiv f_{\kappa\sigma}^{(i)}(\text{DP}) \cdot A_i^{\kappa\sigma} , \quad (3.12)$$

where  ${}^J F_{B,i}$  is a an irrelevant constant form factor for the  $B^0$  decay,  ${}^J F_i(s_{\kappa\sigma}) \equiv {}^J F(s_{\kappa\sigma})/{}^J F(m_i^2)$  is the ratio of Blatt-Weisskopf penetration form factors (see below),  ${}^J K(\text{DP})$  is a kinematic function (see below), and  ${}^J F_{R,i}(\text{DP})$  is a relativistic Breit-Wigner function given by

$${}^J F_{R,i}(s_{\kappa\sigma}) = \frac{1}{s_{\kappa\sigma} - m_i^2 + im_i {}^J \Gamma_i(s_{\kappa\sigma})} . \quad (3.13)$$

The  $s$ -dependent (“running”) width is defined by

$${}^J \Gamma_i(s_{\kappa\sigma}) = \Gamma_i^0 \frac{m_i}{\sqrt{s_{\kappa\sigma}}} \left( \frac{k_\pi(s_{\kappa\sigma})}{k_\pi(m_i^2)} \right)^{2J+1} \frac{{}^J F(Rk_\pi(s_{\kappa\sigma}))}{{}^J F(Rk_\pi(m_i^2))} , \quad (3.14)$$

where  $m_i$  is the mass of the resonance  $i$ ,  $\Gamma_i^0 = \Gamma_i(m_i^2)$  its width, and where

$$k_\pi(s_{\kappa\sigma}) = \frac{\sqrt{s_{\kappa\sigma}}}{2} \left( 1 - \frac{(m_a + m_b)^2}{s_{\kappa\sigma}} \right)^{1/2} \left( 1 - \frac{(m_a - m_b)^2}{s_{\kappa\sigma}} \right)^{1/2} , \quad (3.15)$$

is the so-called *breakup* momentum of the resonance decay particles in the resonance frame. The functions  ${}^J F(Rk_\pi(s_{\kappa\sigma}))$  are the nuclear *Blatt-Weisskopf penetration factors* [35]. They are semi-classical and motivated by the potential  $\hbar L(L+1)/(2mr^2)$

occurring in Schrödinger's Equation, expressed in spherical coordinates, for the scattering of a particle with orbital angular momentum  $L > 0$  in a central field. The repulsive potential is equivalent to a rotation energy and can thus be denoted a *centrifugal barrier*. For growing  $L$ , or decreasing radial distance  $r$ , the centrifugal barrier increases, which entails decreasing transition probability. One can empirically determine a radial distance, called *interaction radius*,  $R$ , of the resonance, which separates an outside region (with respect to the centrifugal barrier), with little interaction, from an inside region where the interaction between the particles is strong [36]. The transmission coefficients of the centrifugal barrier are the Blatt-Weisskopf factors. They are derived using spherical Bessel and Hankel functions and for the lowest orbital momenta (spins) are:

$${}^0F = 1, \quad {}^1F(x) = \frac{1}{1+x^2}, \quad {}^2F(x) = \frac{1}{9+3x^2+x^4}. \quad (3.16)$$

We choose  $R = 1.5 \text{ GeV}^{-1} \simeq 0.3 \text{ fm}$  in the following for all resonances.

The kinematic function in Eq. (3.11) depends on the spin of the resonance. For a  $B$  decay into a vector resonance  $\{\kappa\sigma\}$  and a bachelor track  $\{\tau\}$ , it is given by

$$\begin{aligned} {}^1K^{\kappa\sigma}(\text{DP}) &= (p_{B^0} + p_\tau)_\mu \sum_i \varepsilon_i^\mu(p_{\kappa\sigma}) \varepsilon_i^{\nu*}(p_{\kappa\sigma}) (p_\kappa - p_\sigma)_\nu \\ &= s_{\kappa\tau} - s_{\sigma\tau} + \frac{1}{s_{\kappa\sigma}} (m_{B^0}^2 - m_\tau^2) (m_\sigma^2 - m_\kappa^2) \\ &= -4|\mathbf{p}_\kappa||\mathbf{p}_\tau| \cos \theta_{\kappa\tau}, \end{aligned} \quad (3.17)$$

where all four-momenta  $p_i$  are given in the resonance frame and  $\theta_{\kappa\tau}$  is the helicity angle, and where we have used the relation

$$\sum_i \varepsilon_i^\mu(p) \varepsilon_i^{\nu*}(p) = -g^{\mu\nu} + \frac{p^\mu p^\nu}{p^2}, \quad (3.18)$$

for the sum over the polarization four-vectors. The last two lines of Eq. (3.17) reproduce the convention for the cosines of the helicity angles defined in Eq. (3.8) and Fig. 3.1. Note that the occurrence of  $\cos \theta_{\kappa\tau}$  in the propagator substantially enhances the interference between the different vector ( $\rho^-$ ,  $K^{*+}$  etc.) bands in the Dalitz plot. Equivalently, one obtains for scalar and tensor resonances the kinematic functions

$${}^0K^{\kappa\sigma} = 1, \quad (3.19)$$

$${}^2K^{\kappa\sigma}(\text{DP}) = \frac{8}{3} |\mathbf{p}_\kappa|^2 |\mathbf{p}_\tau|^2 (3 \cos^2 \theta_{\kappa\tau} - 1). \quad (3.20)$$

The likelihood fit will determine a global signal yield, which multiplies the coherent amplitude sum (3.10).

To quantify the sub-yields of the different contributors to the model, we define the fraction  $\eta_i$  for the amplitude  $i$  by

$$\eta_i \equiv \frac{\left\langle \left| a_i^{\kappa\sigma} e^{i\phi_i^{\kappa\sigma}} J \mathcal{A}_i^{\kappa\sigma}(\text{DP}) \right|^2 \right\rangle}{\left\langle \left| \mathcal{A}_{B^0 \rightarrow K^+ \pi^- \pi^0}(\text{DP}) \right|^2 \right\rangle}, \quad (3.21)$$

where the expectation values are obtained from high-statistics Monte Carlo integration of the Dalitz plot (3.3). Due to interference, the sum  $\sum_i \eta_i$  of the fractions for all components will in general not be unity.

## 3.2 The Square Dalitz Plot

Due to the generally low final state masses,  $m_{\text{resonance}} \ll m_{B^0}$ , signal events populate the kinematic boundaries of the Dalitz plot. It turns out that due to combinatorics, the dominant  $e^- e^- \rightarrow q\bar{q}$  ( $q = u, d, s, c$ ) continuum background also accumulates at the boundaries so that the representation Eq. (3.3) turns out to be technically inadequate when one wants to use empirical reference shapes in a likelihood fit. We

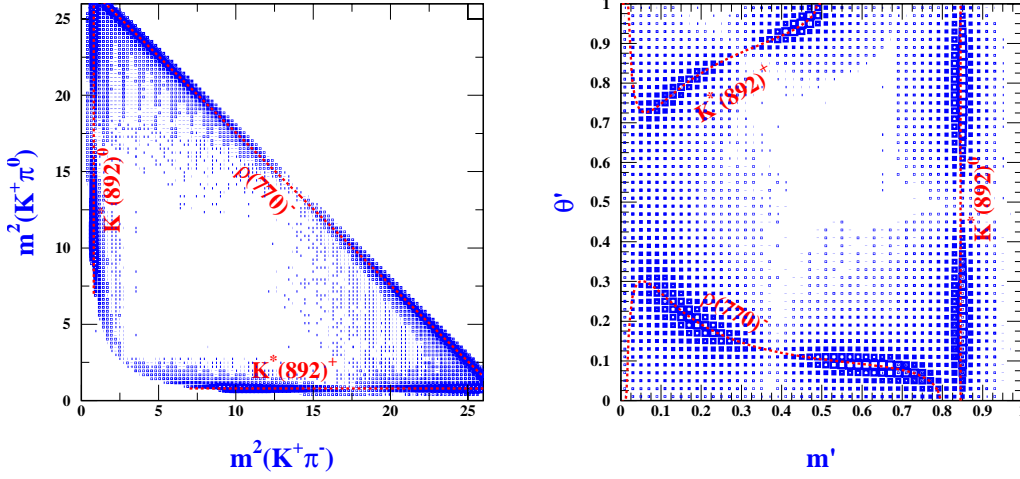


Figure 3.2: *Nominal (left) and square (right)  $B^0 \rightarrow K^+\pi^-\pi^0$  Dalitz plots obtained from Monte Carlo without detector simulation.*

therefore apply the concept of a square Dalitz plot (denoted *Square DP* or *SDP* in the following) [37] and transform

$$ds_{+0} ds_{-0} \longrightarrow |\det J| dm' d\theta', \quad (3.22)$$

where

$$m' \equiv \frac{1}{\pi} \arccos \left( 2 \frac{m_{+-} - m_{+-}[\min]}{m_{+-}[\max] - m_{+-}[\min]} - 1 \right), \quad \text{and} \quad \theta' \equiv \frac{1}{\pi} \theta_{+-}, \quad (3.23)$$

where  $m_{+-}$  is the invariant mass between the charged tracks,  $m_{+-}[\max] = m_{B^0} - m_0$  and  $m_{+-}[\min] = m_+ + m_-$  are the boundaries of  $m_{+-}$ ,  $\theta_{+-}$  is the angle between the positive track and the negative  $B$  momentum in the  $\{+-\}$  rest frame, and  $J$  is the Jacobian of the transformation. The new variables vary between 0 and 1. The determinant of the Jacobian is given by

$$|\det J| = 4 |\mathbf{p}_+^*| |\mathbf{p}_0^*| m_{+-} \cdot \frac{\partial m_{+-}}{\partial m'} \cdot \frac{\partial \cos \theta_{+-}}{\partial \theta'}, \quad (3.24)$$

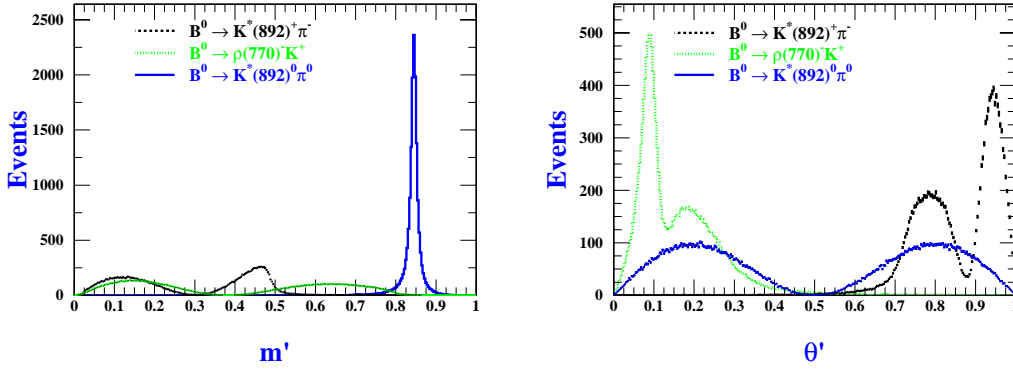


Figure 3.3: Projections on the  $m'$  (left plot) and  $\theta'$  (right plot) axes of  $B^0 \rightarrow K^*(892)^0\pi^0$  (solid blue lines),  $B^0 \rightarrow K^*(892)^+\pi^-$  (dashed black lines) and  $B^0 \rightarrow \rho^-K^+$  (dotted green lines) decays obtained from MC without detector simulation.

where  $|\mathbf{p}_+^*| = \sqrt{E_+^* - m_+^2}$  and  $|\mathbf{p}_0^*| = \sqrt{E_0^* - m_0^2}$ , and where the energies  $E_+^*$  and  $E_0^*$  are in the  $\{+-\}$  rest frame. The partial derivatives in Eq. (3.24) read

$$\frac{\partial m_{+-}}{\partial m'} = -\frac{\pi}{2} \sin(\pi m') (m_{+-}[\text{max}] - m_{+-}[\text{min}]) \quad \text{and} \quad \frac{\partial \cos \theta_{+-}}{\partial \theta'} = -\pi \sin(\theta' \pi) . \quad (3.25)$$

Figure 3.2 shows the original (left hand plot) and the transformed (right hand plot) Dalitz plots for toy Monte Carlo  $B^0 \rightarrow K^+\pi^-\pi^0$  events. The plots illustrate the homogenization of the Dalitz plot obtained after the transformation (3.22). In SDP, the resonance bands are stretched and pulled away a bit from the boundaries. The interference corners are also expanded. This makes the efficiency parameterization technically easier than with the classic DP. Projections on the  $m'$  and  $\theta'$  axes for the various signal modes are plotted in Fig. 3.3. The determinant of the Jacobian (3.24) is shown in Fig. 3.4. It is the distribution one would obtain in the square Dalitz plot for a uniform (non-resonant) prior in the nominal Dalitz plot (DP).

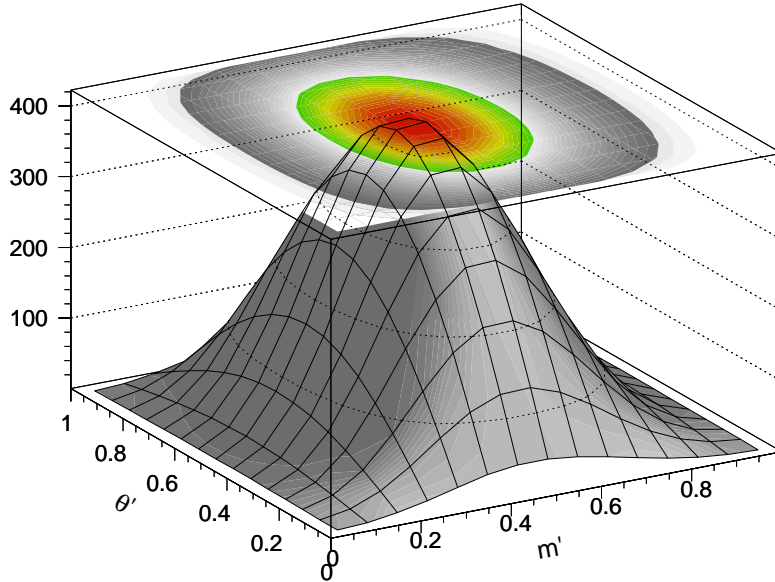


Figure 3.4: *Jacobian determinant (3.24) of the transformation (3.22). The plot shows the distribution one would obtain in the square Dalitz plot for a uniform (non-resonant) prior in the nominal Dalitz plot.*

Note that the transformation (3.22) is not symmetric over the Dalitz plot. The  $K^{*\pm}/\rho^\mp$  overlap region is treated with priority since it corresponds to the most problematic zone where the  $\pi^0$  energy is small and combinatorial background is enhanced.

### 3.3 Transition Amplitudes

For each intermediate decay mode, we use one complex amplitude to describe  $B^0$  decays to this mode and another amplitude for  $\overline{B}^0$  decays to its charge conjugate.

### 3.4 Normalization

When using Eq. (3.3) as probability density function (PDF) in a likelihood fit, one has to normalize it by replacing,

$$|\mathcal{A}_{B^0 \rightarrow K^+ \pi^- \pi^0}|^2 + |\overline{\mathcal{A}}_{B^0 \rightarrow K^- \pi^+ \pi^0}|^2 \longrightarrow \frac{1}{\langle |\mathcal{N}|^2 \rangle} (|\mathcal{A}_{B^0 \rightarrow K^+ \pi^- \pi^0}|^2 + |\overline{\mathcal{A}}_{B^0 \rightarrow K^- \pi^+ \pi^0}|^2) \quad (3.26)$$

where

$$\langle |\mathcal{N}|^2 \rangle = |N|_{B^0}^2 + |\overline{N}|_{B^0}^2, \quad (3.27)$$

and

$$\begin{aligned} |N|_{B^0}^2 &\equiv \langle |\mathcal{A}_{B^0 \rightarrow K^+ \pi^- \pi^0}|^2 \rangle \\ &= \int |\mathcal{A}_{B^0 \rightarrow K^+ \pi^- \pi^0}|^2 dDP, \end{aligned} \quad (3.28)$$

and similarly  $|\overline{N}|_{B^0}^2 \equiv \langle |\overline{\mathcal{A}}_{B^0 \rightarrow K^- \pi^+ \pi^0}|^2 \rangle$ . The complex expectation values  $\langle f_i f_j^* \rangle$  are obtained from high-statistics Monte Carlo integration of the Dalitz plot (Eq.3.3), taking into account acceptance and resolution effects of the detector.

### 3.5 Interference Pattern

It is interesting to study the relative strength of the interfering contribution with respect to the total amplitude. We can check the following quantity

$$\varepsilon \equiv \frac{\sum_{\kappa < \sigma \in \{+, -, 0\}} 2\text{Re}[\mathcal{A}_\kappa \mathcal{A}_\sigma^*]}{|\sum_{\kappa \in \{+, -, 0\}} \mathcal{A}_\kappa|^2} = 1 - \frac{\sum_{\kappa \in \{+, -, 0\}} |\mathcal{A}_\kappa|^2}{|\sum_{\kappa \in \{+, -, 0\}} \mathcal{A}_\kappa|^2}, \quad (3.29)$$

which is confined within  $[-1, 1]$ . A sizable deviation from zero indicates non-negligible interferences among intermediate states.

## Chapter 4

### The Signal Model for $B^0 \rightarrow K^+ \pi^- \pi^0$

We have introduced the kinematic properties together with a simple Breit-Wigner model of the pion form factor in the previous section. We will use this formalism to describe the concrete signal parameterization adopted in the analysis. It is denoted *nominal signal model* in the following.

#### 4.1 Form Factors

There are well-known contributions to the  $B^0 \rightarrow K^+ \pi^- \pi^0$  amplitude from vector resonances, namely the  $B^0 \rightarrow K^*(892)^+ \pi^-$  and  $B^0 \rightarrow \rho(770)^- K^+$ . A large number of parameterizations for  $\rho(770)^-$  can be found in the literature, most of which are capable to describe precise data from  $e^+ e^- \rightarrow \pi^+ \pi^-$  annihilation or  $\tau^+ \rightarrow \bar{\nu}_\tau \pi^+ \pi^0$  decays.  $K^- p$  scattering and  $p \bar{p}$  annihilation experiments have managed to describe  $K\pi$  resonances, with a few particular parametrizations for the  $K\pi$   $S$ -wave spectra. We consider three models in this analysis. They represent analytical functions with a threshold  $(m_+ + m_-)^2$  for a neutral resonance and  $(m_\pm + m_0)^2$  for a charged resonance. Note that we will apply the empirical Blatt-Weisskopf penetration factor correction of the  $s$ -dependent width given in Eq. (3.14) for systematic studies, since we merely

deal with low spin resonances.

- We denote by **RBW** the relativistic Breit-Wigner ansatz for a resonance  $R$  introduced for the vector form factor in Section 3.1,

$${}^1F_R^{\text{RBW}}(s) = \frac{1}{s - m_R^2 + i m_R \Gamma_R(s)}, \quad (4.1)$$

where the  $s$ -dependent width  $\Gamma_R(s)$  is given in Eq. (3.14) for  $J = 1$ , and the ratio of the Blatt-Weisskopf factors is studied only for systematic evaluation. RBW is mainly used for  $K^*(892)$ ,  $K_2^*(1430)$  and  $K^*(1680)$  resonances. It is also widely used in  $D$  meson three-body decay Dalitz analyses for  $\rho$  resonances and we use RBW to cross check the following GS parametrization (see below). Parameters are taken from [3] unless stated otherwise.

- We denote by **GS** another approach used for  $\rho$  parametrization in this analysis. It is the Gounaris-Sakurai (GS) parameterization [38] of the  $p$ -wave scattering amplitude for a broad resonance  $R$ , decaying to the final state pions  $\pi_1\pi_2$ :

$${}^1F_R^{\text{GS}}(s) = \frac{1 + d \cdot \Gamma_R/m_R}{s - m_R^2 - f(s) + i m_R \Gamma_R(s)}, \quad (4.2)$$

where

$$f(s) = \Gamma_R \frac{m_R^2}{k_\pi^3(m_R^2)} \left[ k_\pi^2(s) \left( h(s) - h(m_R^2) \right) + (m_R^2 - s) k_\pi^2(m_R^2) \frac{dh}{ds} \Big|_{s=m_R^2} \right], \quad (4.3)$$

and where  $k_\pi(s)$  is the pion momentum in the  $R$  rest frame (3.15). The  $s$ -dependence is as in the RBW model. The function  $h(s)$  is defined as

$$h(s) = \frac{2}{\pi} \frac{k_\pi(s)}{\sqrt{s}} \ln \left( \frac{\sqrt{s} + 2k_\pi(s)}{2m_\pi} \right), \quad (4.4)$$

with

$$dh/ds|_{m_R^2} = h(m_R^2) \left[ (8k_\pi^2(m_R^2))^{-1} - (2m_R^2)^{-1} \right] + (2\pi m_R^2)^{-1}. \quad (4.5)$$

The normalization condition at  ${}^1F_{R,i}^{\text{GS}}(0)$  fixes the parameter  $d = f(0)/(\Gamma_R m_R)$ .

It is found to be [38]

$$d = \frac{3}{\pi} \frac{m_\pi^2}{k_\pi^2(m_R^2)} \ln \left( \frac{m_R + 2k_\pi(m_R^2)}{2m_\pi} \right) + \frac{m_R}{2\pi k_\pi(m_R^2)} - \frac{m_\pi^2 m_R}{\pi k_\pi^3(m_R^2)}. \quad (4.6)$$

As imposed by unitarity, the GS parameterization satisfies the relation [39]

$$\tan \delta_1^1(s) = \frac{\text{Im} {}^1F_R^{\text{GS}}(s)}{\text{Re} {}^1F_R^{\text{GS}}(s)}, \quad (4.7)$$

where  $\delta_1^1(s)$  is the phase shift of the  $l = 1, I = 1$   $\pi\pi$  scattering form factor.

- It is already known that the  $I = 1/2$   $S$ -wave  $K\pi$  resonance, which is dominated by  $K_0^*(1430)$  below 2 GeV/ $c^2$ , is not a simple Breit-Wigner. Until the  $K\eta'$  threshold the wave has been observed to be rather elastic. An effective-range parameterization was suggested [40] to describe the slowly increasing phase as a function of  $K\pi$  mass. We denote this parameterization by **LASS**. This parameterization was tested for the LASS experiment [41]. First, the parameterization needs to be scaled by  $m/q$  for  $B$  decays [42], where  $m$  is the invariant  $K\pi$  mass and  $q$  is the momentum of the daughters measured in the resonance rest frame.

The form factor now reads:

$$F_R^{\text{LASS}}(s) = \frac{\sqrt{s}}{k(s) \cot \delta_B - i k(s)} + \exp(2i\delta_B) \frac{m_R^2 \Gamma_R / k(m_R^2)}{m_R^2 - s - i m_R \Gamma_R(s)}, \quad (4.8)$$

where

$$\cot \delta_B = \frac{1}{ak(s)} + \frac{1}{2} r k^2(s). \quad (4.9)$$

We use the parameters from a 37-point fit to the LASS data done by [42]:  $m_R = 1415 \pm 3 \text{ MeV}/c^2$ ,  $\Gamma_R = 300 \pm 6 \text{ MeV}/c^2$ ,  $a = 2.07 \pm 0.10$  and  $r = 3.32 \pm 0.34$ . We also try the 34-point fit to make a conservative estimate of the uncertainty from the parameters:  $m_R = 1435 \pm 5 \text{ MeV}/c^2$ ,  $\Gamma_R = 279 \pm 6 \text{ MeV}/c^2$ ,  $a = 1.95 \pm 0.09$  and  $r = 1.76 \pm 0.36$ .

- We also try the ***K*-matrix** parametrization for the  $I = 1/2$  *S*-wave  $K\pi$  resonance.

The *K*-matrix formalism [43] is an elegant and general way of dealing with strongly overlapping resonances and multi-channel dynamics. A  $1 \times 1$  *K*-matrix [41][44] is sufficient:

$$K = \frac{g_0^2}{m_0^2 - m^2} + c_1 + c_2 \cdot m, \quad (4.10)$$

where  $m_0$  is the resonance mass,  $g_0^2 = m_0 \Gamma_0 / \rho(m_0)$ ,  $\rho(m) \equiv 2q/m$  and  $q$  is the breakup momentum. The parameters from the fit to the LASS data [44] are:  $m_0 = 1.342 \pm 0.010 \text{ GeV}/c^2$ ,  $\Gamma_0 = 0.400 \pm 0.020 \text{ GeV}/c^2$ ,  $c_1 = 1.45$  and  $c_2 = -0.55/\text{GeV}$ . The lineshape reads as  $|T|^2$  where

$$T = \rho K (1 - i\rho K)^{-1} \quad (4.11)$$

Fig. 4.1 shows the lineshape and phase shift for  $K_0^*(1430)$  from the *K*-matrix parametrization and the relativistic Breit-Wigner one for comparison. The resonance mass and width extracted from the T-matrix in the complex energy plane are  $m = (1428 \pm 10) \text{ MeV}/c^2$  and  $\Gamma = (280 \pm 15) \text{ MeV}/c^2$  which is in good agreement with LASS [41]. The problem shows up when we have to scale this formfactor by  $m/q$  to suit *B* decay environment: in the low mass region, the magnitude

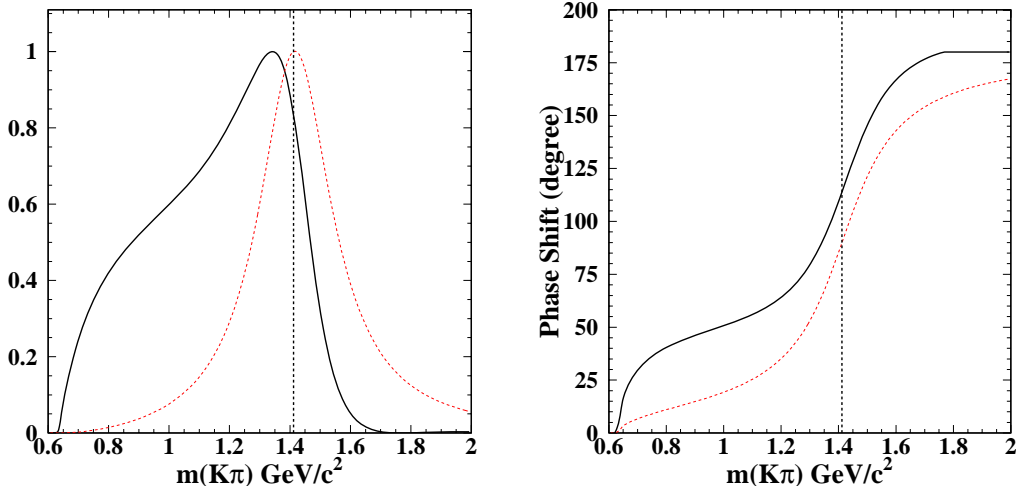


Figure 4.1: *Line shape (Left) and phase shift (Right) for  $K_0^*(1430)$  with  $K$ -matrix parametrization (solid), also shown is the relativistic Breit-Wigner one with running width (dashed).*

goes up much faster than the one in Eq. 4.8. For this reason, we will not use this lineshape.

## 4.2 Higher Resonances

We use the LASS parametrization for  $K_0^*(1430)$ , as discussed above. Higher resonances such as  $K_2^*(1430)$  and  $K^*(1680)$  also decay to  $K\pi$  as well with branching ratios of  $(49.9 \pm 1.2)\%$  and  $(38.7 \pm 2.5)\%$  respectively. We simply use RBW to describe them in our signal model. We also try some other lineshapes in model systematics study.

Higher vector resonances are known to contribute to the  $\pi\pi$  final state in  $e^+e^-$  annihilation and  $\tau$  decays (see, *e.g.*, [45, 46]). They are introduced into the model via the coherent amplitude sum using GS form factors and are studied for model

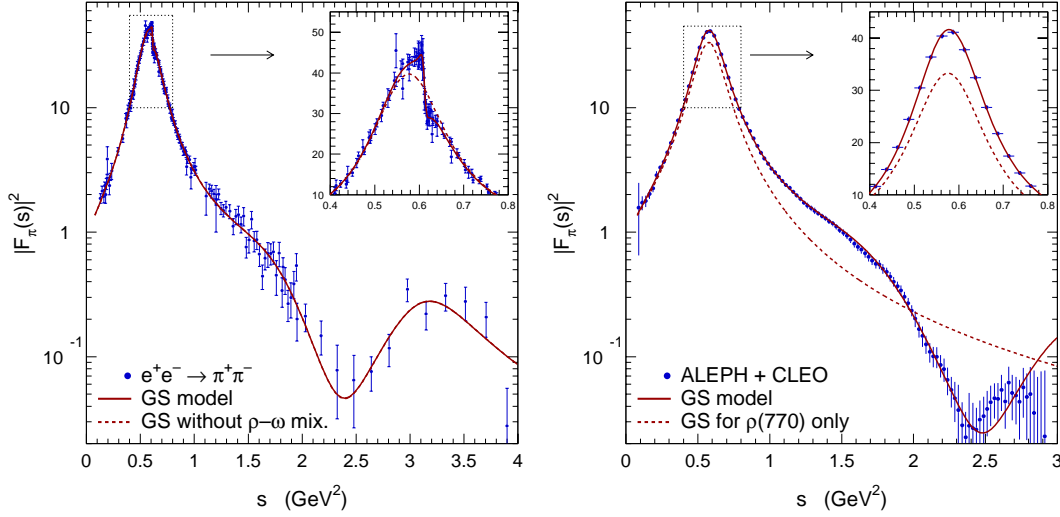


Figure 4.2: Pion form factor from  $e^+e^- \rightarrow \pi^+\pi^-$  annihilation (left) and  $\tau^+ \rightarrow \bar{\nu}_\tau \pi^+ \pi^0$  decays (right).

systematics. As an example, the  $e^+e^- \rightarrow \pi^+\pi^-$  form factor can be written as ([46, 47])

$$F_\pi(s) \propto F_{\rho(770)}(s) \left( \frac{1 + a_{\rho\omega} e^{i\phi_{\rho\omega}} F_{\omega(782)}(s)}{1 + a_{\rho\omega}} \right) + a_{\rho'} e^{i\phi_{\rho'}} F_{\rho(1450)}(s) + a_{\rho''} e^{i\phi_{\rho''}} F_{\rho(1700)}(s), \quad (4.12)$$

where the  $F$  functions can be GS form factors (4.2) that must be normalized to  $F(0) = 1$  due to charge conservation.

Figure 4.2 shows on the left hand side a fit of the model (4.12) to newest  $e^+e^- \rightarrow \pi^+\pi^-$  annihilation data, where the most precise measurements are provided by the CMD2 Collaboration [48]. In these fits, the relative phases between the  $\rho$  resonances have been set to  $\pi$  as expected from simple radial excitation. The complete fit results are given in Table 4.1. Agreement is observed between the model and the data points. The shoulder originates from the significant  $\rho(1450)$  contribution. The additional peak at large masses corresponds to the  $\rho(1700)$ , measured by the DM2 Collaboration [49].

The sharp cut around  $780 \text{ MeV}/c^2$  is due to the interference between the  $\rho(770)$  and the  $\omega(782) \rightarrow \pi^+\pi^-$  amplitude. The right hand plot in Figure 4.2 shows a fit of the same model (but without the isoscalar  $\omega(783)$  amplitude) to the charged  $\rho^+$  measured in  $\tau$  decays [50]. Again, agreement is observed. Also shown is the form factor (4.12) when setting  $a_{\rho'} = a_{\rho''} = 0$ . Correcting for small isospin violating effects, like differences in the charged and neutral pion masses (which affects both the width and the phase space),  $\rho - \omega$  mixing, etc, reasonable agreement is observed between the two data sets [51]. More details can be found in Ref. [52].

### 4.3 Other Concerns

Small contributions are expected from the following phenomena.

- **The  $\kappa$  resonance**

An indication of the presence of the neutral scalar  $\kappa$  as a  $K\pi$  broad resonance was reported by the E791 collaboration  $D^+ \rightarrow K^-\pi^+\pi^+$  decays [53]. The mass and width of the scalar were found to be  $m_\kappa = (797 \pm 19 \pm 43) \text{ MeV}/c^2$  and  $\Gamma_\kappa = (410 \pm 43 \pm 87) \text{ MeV}/c^2$ . Note that we believe this broad resonance is just an alternative parametrization for the  $K\pi$   $S$ -wave in the low mass range and is thus already included in the  $K$ -matrix parametrization for the  $K\pi$   $S$ -wave contribution.

The  $\kappa$  contribution is reported to be small in Belle's study of the  $B^+ \rightarrow K^+\pi^+\pi^-$  decay [54].

## 4.4 The Nominal Signal Model

After the discussion in the previous sections we are set to build the nominal signal model implemented in the DP fits. Variations to this model will be considered as systematic uncertainties.

- The various amplitudes are summed coherently according to Eq. (3.10).
- For the charged Dalitz bands, the  $\rho(770)^-$ ,  $K^*(892)^+$ ,  $K_0^*(1430)^+$  resonance are considered in the nominal signal model.
- For the neutral Dalitz band, we consider the  $K^*(892)^0$  and  $K_0^*(1430)^0$  resonances.
- We consider the non-resonant contribution which we assume is uniform across the classic Dalitz plot.
- We use results from  $\tau$  decays and  $e^+e^-$  annihilation to fix the masses and widths of the  $\rho(X)$  resonances. The fits are performed with the GS parameterization (4.2) and the results are given in Table 4.1 and are plotted in Fig. 4.2. These parameters are strongly correlated among each other so that only the entire set is well defined. Variations of parameters for the purpose of systematic studies must be performed coherently.
- Sub-dominant contributions such as those discussed in Section 4.3 are not part of the nominal signal model. The influence of these modes on the results will be included as systematic error.
- Long-lived modes with the same final states, such as  $B^0 \rightarrow D^-(\rightarrow \pi^-\pi^0)K^+$  and  $B^0 \rightarrow \bar{D}^0(\rightarrow K^+\pi^-)\pi^0$ , are treated as part of the  $B$  background model

(*cf.* Section 6), since they do not interfere with the strongly decaying signal resonances.

A complete list of possible contributors can be found in Table 4.2.

Table 4.1: *Results of the charged and neutral Gounaris-Sakurai model (4.2,4.12) fit to form factor data from  $\tau$  decays (left) and  $e^+e^-$  annihilation. The relative phases  $\phi_{\rho^{(i)}}$  have been fixed in the fit. Leaving them free leads to compatible results. These parameters are used in the nominal form factor parameterization of the signal model. Note that these parameters are strongly correlated among each other so that only the entire set is well defined. Systematic variations of parameters have to be performed coherently.*

Parameter	$\tau^+ \rightarrow \bar{\nu}_\tau(\rho^+ \rightarrow)\pi^+\pi^0$	$e^+e^- \rightarrow (\rho^0 \rightarrow)\pi^+\pi^-$
$m_{\rho(770)}$	$775.5 \pm 0.6$	$773.1 \pm 0.5$
$\Gamma_{\rho(770)}$	$148.2 \pm 0.8$	$148.0 \pm 0.9$
$a_{\rho\omega}$	$\equiv 0$	$0.0020 \pm 0.0001$
$\phi_{\rho\omega}$	$\equiv 0$	$13.0 \pm 2.3$
$m_{\rho(1450)}$		$1409 \pm 12$
$\Gamma_{\rho(1450)}$		$500 \pm 37$
$a_{\rho'}$		$0.166 \pm 0.005$
$\phi_{\rho'}$		$177.8 \pm 5.2$
$m_{\rho(1700)}$		$1749 \pm 20$
$\Gamma_{\rho(1700)}$		$\equiv 235$
$a_{\rho''}$		$0.071 \pm 0.006$
$\phi_{\rho''}$		$\equiv 0$

Table 4.2: *Intermediate states that may contribute to  $B^0 \rightarrow K^+\pi^-\pi^0$  Dalitz Plot. The first six intermediate modes are included in the nominal signal model while the other six are considered for model systematics. Masses and widths are in units of  $\text{GeV}/c^2$ .*

Mode	Resonance Mass	Width	Spin	Form Factor
$K^*(892)^+\pi^-$	0.8917	0.0508	1	RBW
$\rho(770)^-K^+$	0.7821	0.1578	1	GS
$K^*(892)^0\pi^0$	0.8961	0.0507	1	RBW
$K_0^*(1430)^0\pi^0$	1.415	0.300	0	LASS
$K_0^*(1430)^+\pi^-$	1.415	0.300	0	LASS
$K^+\pi^-\pi^0(N.R.)$	NA	NA	NA	Uniform
$\rho(1450)^-K^+$	1.439	0.550	1	GS
$\rho(1700)^-K^+$	1.795	0.278	1	GS
$K_2^*(1430)^0\pi^0$	1.4324	0.109	2	RBW
$K_2^*(1430)^+\pi^-$	1.4256	0.0985	2	RBW
$K^*(1680)^0\pi^0$	1.717	0.322	1	RBW
$K^*(1680)^+\pi^-$	1.717	0.322	1	RBW

## Chapter 5

# Data Samples and Event Selection

### 5.1 Data Samples

The results presented in this thesis are based on *BABAR* data reprocessed in 2004 and Monte Carlo (MC) samples generated in 2004.

The data sample consists of (the corresponding year during which the data were collected is indicated in parentheses):

- Run-1(1999): on-resonance -  $0.47 \text{ fb}^{-1}$ , off-resonance -  $0.0 \text{ fb}^{-1}$ ;
- Run-1(2000): on-resonance -  $20.1 \text{ fb}^{-1}$ , off-resonance -  $2.6 \text{ fb}^{-1}$ ;
- Run-2(2001): on-resonance -  $35.4 \text{ fb}^{-1}$ , off-resonance -  $3.7 \text{ fb}^{-1}$ ;
- Run-2(2002): on-resonance -  $25.4 \text{ fb}^{-1}$ , off-resonance -  $3.2 \text{ fb}^{-1}$ ;
- Run-3(2003): on-resonance -  $30.9 \text{ fb}^{-1}$ , off-resonance -  $2.4 \text{ fb}^{-1}$ .
- Run-4(2004): on-resonance -  $80.9 \text{ fb}^{-1}$ , off-resonance -  $4.2 \text{ fb}^{-1}$ .

The on-resonance data were taken at the  $\Upsilon(4S)$  resonance, while the off-resonance data were taken 40 MeV below the  $\Upsilon(4S)$  resonance. In total, we have  $193.2 \text{ fb}^{-1}$

on-resonance data corresponding to  $213 \times 10^6 B\bar{B}$  events, and  $16 \text{ fb}^{-1}$  off-resonance.

Monte Carlo simulations are required to determine selection efficiencies and to model fit parameters. The full *BABAR* detector simulation is performed using *GEANT* [55]. Simulation of physics events uses the *JETSET* [56] and *EvtGen* [57] programs. The *JETSET* generator simulates the inclusive *B* decays, as well as continuum events, while the *EvtGen* is used for *B* decays to exclusive final states.

The signal MC sample can be found in Table 5.1.

Table 5.1: *Signal MC that have been generated. Note that these events are generated without interference.*

Mode Name	Generated (K)
$B^0 \rightarrow K^*(892)^+\pi^-, K^*(892)^+ \rightarrow K^+\pi^0$	184
$B^0 \rightarrow K^*(892)^0\pi^0, K^*(892)^0 \rightarrow K^+\pi^-$	188
$B^0 \rightarrow \rho(770)^-K^+, \rho(770)^- \rightarrow \pi^+\pi^-$	568
$B^0 \rightarrow (K_0(1430)\pi)^0, K_0(1430) \rightarrow K^+\pi$	300
$B^0 \rightarrow (K_2(1430)\pi)^0, K_2(1430) \rightarrow K^+\pi$	300
$B^0 \rightarrow (K^*(1680)\pi)^0, K^*(1680) \rightarrow K^+\pi$	300
$B^0 \rightarrow K^+\pi^-\pi^0(\text{non-resonant})$	1169
$B^0 \rightarrow D^-K^+, D^- \rightarrow \pi^-\pi^0$	240
$B^0 \rightarrow \bar{D}^0\pi^0, \bar{D}^0 \rightarrow K^+\pi^-$	240

The MC sample for background studies consists of:

- Charmless *B* background modes: more than 100 exclusive charmless two-, three-, and four-body events, equivalent to luminosities of more than  $10,000 \text{ fb}^{-1}$  for those significant modes;

- generic  $B^0\bar{B}^0$  MC (inclusive neutral  $B$  decays):  $207 \times 10^6$  events;
- generic  $B^+B^-$  MC (inclusive charged  $B$  decays):  $191 \times 10^6$  events.

## 5.2 Event Selection

Data collected at the  $\Upsilon(4S)$  resonance are expected to consist of not only  $\Upsilon(4S) \rightarrow \text{Boverline}B$  events, but also  $e^+e^- \rightarrow q\bar{q}$  and  $e^+e^- \rightarrow l^+l^-$  events, where  $q = (u, d, s, c)$  and  $l = (e^-, \mu^-, \tau^-)$ . The  $e^+e^- \rightarrow q\bar{q}$  events are called continuum events hereafter, and are found to be the dominant background in most non-leptonic  $B$  decays with charmless change  $|C| = 0$  (so called charmless decays, to be compared with charmed decays with  $|C| = 1$ ).

The Dalitz plot calculation is very CPU-time-consuming, so the event selection applied here attempts to reduce the total number of events that enter the likelihood fit. This goal is achieved without compromising the signal efficiency by sacrificing the  $m_{\text{ES}}$  and  $\Delta E$  sidebands. The obvious drawback is that due to the lower background level, the fit cannot determine all empirical shape parameters of the continuum background together with the signal parameters. One rather must extrapolate them from sidebands and off-resonance data, which leads to systematic uncertainties. On the other hand, getting rid of the sideband events improves rejection of misreconstructed signal events, where  $B$  candidates are reconstructed from one or more wrong particles. These misreconstructed signal events are referred to as Self-Cross-Feed (SCF) hereafter. The correctly reconstructed signal events are referred to as Truth-Matched

(TM) events<sup>1</sup>.

For practical reasons, the event selection is performed in two stages. The first stage, preselection, applies very loose selection criteria to skim data into ntuples. Then a final selection chooses candidate events from the ntuples and dumps the selected events into ASCII data files.

Two kinematic variables are defined and used for the selection of events:

$$\Delta E \equiv E_B^* - \sqrt{s}/2, \quad m_{ES} \equiv \sqrt{(s/2 + \mathbf{p}_0 \cdot \mathbf{p}_B)^2/E_0^2 - \mathbf{p}_B^2}, \quad (5.1)$$

where  $E_B^*$  is the  $B$  meson candidate energy in the center-of-mass (c.m.) system,  $E_0$  and  $\sqrt{s}$  are the total energies of the  $e^+e^-$  system in the laboratory and c.m. systems, respectively, and  $\mathbf{p}_0$  and  $\mathbf{p}_B$  are the three-momenta of the  $e^+e^-$  system and the  $B$  candidate in the laboratory frame.

The preselection of an event has the following requirements:

- To form a  $B$  candidate that decays to  $K^+\pi^-\pi^0$ , the event must have at least two oppositely-charged tracks and one  $\pi^0$  reconstructed from a pair of photons.
- The tracks are required to originate from the IP (within 1.5 cm in xy-plane

---

<sup>1</sup>Another way to achieve better TM selection efficiency would be to build an estimator

$$\mathcal{E} \equiv \left( \frac{\Delta E - \langle \Delta E \rangle}{\sigma_{\Delta E}} \right)^2 + \left( \frac{m_{ES} - \langle m_{ES} \rangle}{\sigma_{m_{ES}}} \right)^2 + \left( \frac{m_{\pi^0} - \langle m_{\pi^0} \rangle}{\sigma_{m_{\pi^0}}} \right)^2 + \dots,$$

and to select the candidate with the minimum  $\mathcal{E}$ . However, this procedure creates small but not necessarily negligible bumps around the expected values  $\langle \Delta E \rangle$ ,  $\langle m_{ES} \rangle$ , etc. Due to this unwanted behavior we do not apply such a procedure. As another choice, one may use an estimator that combines the reconstructed  $m_{\pi^0}$  and vertexing information of charged tracks. This method has been investigated without any performance improvement.

and 10cm in z direction), to have a minimum of transverse momentum ( $p_t$ ) of 100 MeV/c, and to have at least 12 hits recorded in the DCH.

- The photons to form the  $\pi^0$  candidate must have energy larger than 100 MeV each, and the invariant mass  $0.10 \text{ GeV} < m(\gamma\gamma) < 0.16 \text{ GeV}$ .
- At least one  $B$  candidate is found with  $m_{ES} > 5.21 \text{ GeV}/c^2$  and  $|\Delta E| < 0.45 \text{ GeV}$ , assuming either pion or kaon mass hypothesis for the charged tracks.
- The vertexing of the two tracks must converge using the *GeoKin* vertexing algorithm [58], and the inclusive vertexing of the rest of the event (ROE) must converge as well [58].

The final selection has the further requirements as follows:

- **$\pi^0$  reconstruction:**

- $0.01 < \text{LAT}_\gamma < 0.6$ . The lateral moment is defined as [31]:

$$\text{LAT} \equiv \frac{\sum_1^n E_i r_i^2}{E_1 R_0^2 + E_2 R_0^2 + \sum_3^n E_i r_i^2}, \quad (5.2)$$

where  $n$  is the number of EMC crystals in the cluste,  $E_i$  is the energy of the  $i^{\text{th}}$  crystal (arranged with decreasing energy),  $r_i$  is the radial coordinate of the center of the  $i^{\text{th}}$  crystal, and  $R_0$  is the average distance between two crystals.

- $E_{\gamma,\text{LAB}} > 0.05 \text{ GeV}$ .
- $0.11 < m(\pi^0) < 0.16 \text{ GeV}/c^2$ .

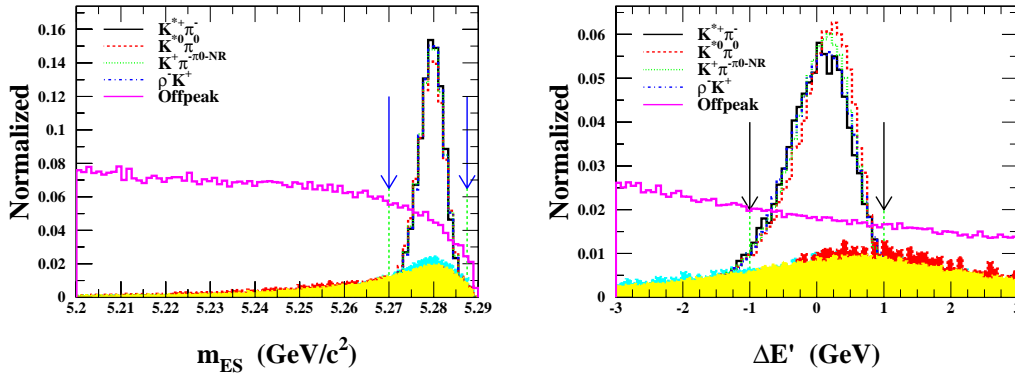


Figure 5.1: *Distributions of  $m_{ES}$  (left plot) and  $\Delta E'$  (right plot) for truth-matched (solid) and misreconstructed  $\rho(\pi\pi)\pi$  events (shaded), and for off-resonance data (dashed). The arrows indicate the cuts applied.*

- Only  $\pi^0$ s constructed from resolved photon pairs are used.

- **Particle Identification (PID):**

- one track should pass the tight kaon selection [59] with valid DIRC acceptance for momentum larger than 0.55  $\text{GeV}/c$ . Another track should fail the loose kaon selection. For signal events, the average efficiency for the tight kaon selection is around 69% (Table 5.2).
- Both tracks must fail the tight electron, muon, proton selection by using the standard PID selectors.

- **Kinematic cuts:**

- $m_{ES}$  is required to have  $5.27 < m_{ES} < 5.2875 \text{ GeV}/c^2$ . See left hand plot in Fig. 10.6 for the signal and continuum distributions of  $m_{ES}$ . Compared to  $\Delta E$ , only a slight dependence of  $m_{ES}$  on the  $\pi^0$  energy is observed. It

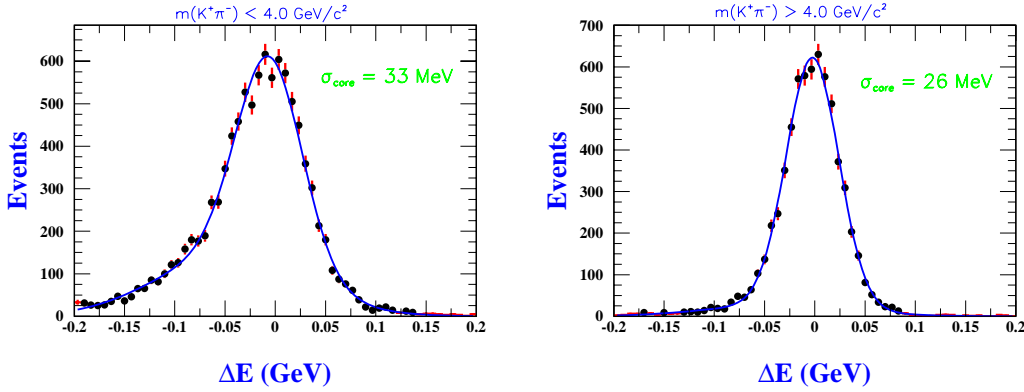


Figure 5.2: Truth-matched  $\Delta E$  distribution for  $B^0 \rightarrow K^*(892)^+\pi^-$  events in different bins of  $m_{+-}$  (estimator of the  $\pi^0$  energy) fit with double Gaussians. The quoted widths are those of the core Gaussians.

is ignored in the selection, but not in the likelihood fit, where, similar to the  $\Delta E$  treatment (see next bullet), a  $m_{+-}$ -dependent parameterization is applied.

- Dependent on the  $\pi^0$  energy, the  $\Delta E$  resolution for TM events varies strongly across the DP. Due to the three-body kinematics, the  $K^+\pi^-$  invariant mass,  $m_{+-}$ , is a good estimator of this dependency. Figure 5.2 shows the  $\Delta E$  distributions for different bins of  $m_{+-}$ . The function corresponds to a fit with a double Gaussian. The width of the core Gaussian varies from 26 MeV (low-energetic  $\pi^0$ 's) to 33 MeV (high-energetic  $\pi^0$ 's). We account for this effect by applying linearly  $m_{+-}$ -dependent cuts on  $\Delta E$ :

$$\Delta E_{\max}(m_{+-}) = c_{\max} - \frac{c_{\max} - \bar{c}}{m_{+-}^{\max}} \cdot m_{+-}, \quad (5.3)$$

$$\Delta E_{\min}(m_{+-}) = c_{\min} - \frac{c_{\min} + \bar{c}}{m_{+-}^{\max}} \cdot m_{+-}, \quad (5.4)$$

where we use  $\bar{c} = 0.045$  GeV,  $c_{\min} = -0.140$  GeV,  $c_{\max} = 0.080$  GeV and

$m_{+-}^{\max} = 25 \text{ GeV}/c^2$ . Since variable cuts complicate the treatment of  $\Delta E$  in the maximum likelihood (ML) fit, we use the redefined quantity

$$\begin{aligned} \Delta E \longrightarrow \Delta E' &= \frac{(\Delta E - \Delta E_{\max}) + (\Delta E - \Delta E_{\min})}{\Delta E_{\max} + \Delta E_{\min}} \\ &= \frac{2 \Delta E m_{+-}^{\max} - (c_{\max} + c_{\min})(m_{+-}^{\max} - m_{+-})}{2 \bar{c} m_{+-} + (c_{\max} - c_{\min})(m_{+-}^{\max} - m_{+-})}, \end{aligned} \quad (5.5)$$

with a validity range after cut of  $\Delta E' \in [-1, 1]$ .

See right hand plot in Fig. 10.6 for the signal and continuum distributions of  $\Delta E'$ . Since it is a linear transformation, the quasi-linear behavior of the continuum background is not altered.

- **MVA:** a description of the dedicated continuum-fighting Multivariate Analyzer (MVA) is given in Section 5.4. We use a four-variable **Neural Network** for which the output is between 0 and 1, and is required to exceed 0.76 in the final selection.

The selection efficiencies relative to the previous cut in the column for signal MC and for onpeak data are given in Table 5.2.

### 5.3 Multiple Candidate Selection and Misreconstruction of Signal Events

Events with multiple  $B$  candidates passing the full selection occur in 16.9% ( $K^*(892)^+\pi^-$ ), 17.0% ( $\rho^- K^+$ ), 7.2% ( $K^*(892)^0\pi^0$ ), 3.2% (non-resonant  $K^+\pi^-\pi^0$ ) and 6.2% (onpeak) of the cases on average (see Fig. 5.3). Most of these multi-candidate events have two  $B$  candidates. Due to the specific kinematics of multi-candidate events, their occurrence strongly depends on the location of the event in the Dalitz plot.

Table 5.2: Selection efficiencies relative to the previous cut for signal MC, and onpeak data. Masses are given in units of  $\text{GeV}/c^2$ .

Cuts	Relative Efficiencies (%)				
	$\varepsilon_{K^{*}(892)^+\pi^-}^{\text{MC}}$	$\varepsilon_{\rho^-K^+}^{\text{MC}}$	$\varepsilon_{K^{*}(892)^0\pi^0}^{\text{MC}}$	$\varepsilon_{K^+\pi^-\pi^0-NR}^{\text{MC}}$	$\varepsilon_{\text{onpeak}}$
Preselection	$63.23 \pm 0.11$	$65.49 \pm 0.06$	$55.82 \pm 0.11$	$55.02 \pm 0.05$	-
$P_t > 100 \text{ MeV}/c$	$100.0 \pm 0.00$	$99.99 \pm 0.00$	$99.96 \pm 0.01$	$99.99 \pm 0.00$	$99.97 \pm 0.00$
DCH #hits $\geq 12$	$99.93 \pm 0.01$	$99.96 \pm 0.00$	$99.53 \pm 0.02$	$99.85 \pm 0.00$	$99.75 \pm 0.00$
Photon Quality	$92.49 \pm 0.08$	$93.50 \pm 0.04$	$96.29 \pm 0.06$	$94.57 \pm 0.03$	$88.23 \pm 0.02$
$0.11 < m_{\pi^0} < 0.16$	$98.17 \pm 0.04$	$98.18 \pm 0.02$	$97.99 \pm 0.04$	$98.23 \pm 0.02$	$96.26 \pm 0.01$
Kaon ID	$66.57 \pm 0.15$	$70.39 \pm 0.08$	$68.99 \pm 0.15$	$69.14 \pm 0.06$	$30.58 \pm 0.03$
Electron Veto	$98.63 \pm 0.04$	$99.03 \pm 0.02$	$98.05 \pm 0.05$	$98.73 \pm 0.02$	$94.85 \pm 0.02$
Muon Veto	$97.56 \pm 0.06$	$98.52 \pm 0.02$	$99.02 \pm 0.04$	$98.18 \pm 0.02$	$98.53 \pm 0.01$
Proton Veto	$99.11 \pm 0.04$	$99.09 \pm 0.02$	$99.09 \pm 0.04$	$99.12 \pm 0.01$	$81.75 \pm 0.04$
$-1 < \Delta E' < 1$	$71.16 \pm 0.17$	$71.83 \pm 0.09$	$80.52 \pm 0.15$	$79.71 \pm 0.06$	$22.92 \pm 0.05$
$m_{es} > 5.27$	$92.30 \pm 0.12$	$90.04 \pm 0.07$	$94.31 \pm 0.01$	$96.56 \pm 0.03$	$11.87 \pm 0.08$
NN > 0.76	$62.07 \pm 0.23$	$62.97 \pm 0.12$	$63.78 \pm 0.02$	$62.45 \pm 0.09$	$5.57 \pm 0.17$
Total Efficiency	$14.85 \pm 0.08$	$16.65 \pm 0.04$	$16.84 \pm 0.08$	$16.29 \pm 0.03$	-

- For the  $K^{*+}\pi^-$  and  $\rho^-K^+$  modes, most multiple candidates arise from mis-assignment of soft photons that form a low-energetic  $\pi^0$ . It thus occurs in the soft  $\pi^0$  region (lower left corner of the DP).
- For  $K^{*0}\pi^0$  events, most multiple candidates arise from mis-assignment of soft tracks. It occurs in the soft- $\pi^-$  and less often in the soft Kaon regions (lower right and upper left corners of the DP).
- Due to the 3-body kinematics of non-resonant  $B^0 \rightarrow K^+\pi^-\pi^0$  decays, soft neu-

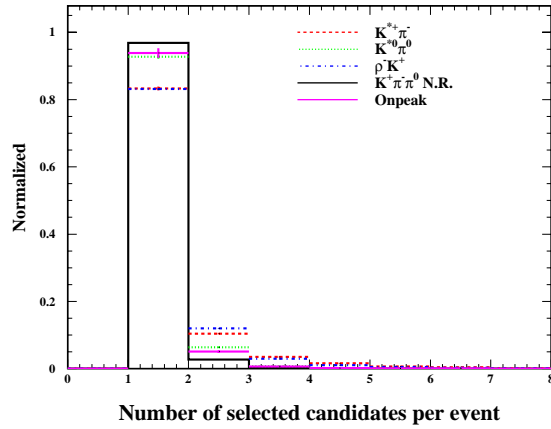


Figure 5.3: *Number of candidates per event passing the full selection.*

tral or charged pions occur less frequently.

- Multiple candidate events for continuum background are less frequent than for signal.

Exploiting the information on the number of multiple candidates in a discriminant variable (*e.g.*, the NN) to suppress background would create correlations between this variable and the DP. It would require an involved multi-dimensional treatment in the fit which is not going to be considered here.

To prevent biasing the PDFs of the discriminant variables that enter the ML fit, we apply the following independent criteria to select a single candidate:

- if the multiple candidates have different  $\pi^0$ 's, we choose the one with a reconstructed  $\gamma\gamma$  mass closest to the nominal  $\pi^0$  mass;
- use random choice for events without multiple  $\pi^0$ 's.

Table 5.3 summarizes the selection efficiencies and fractions of misreconstructed signal events (SCF), obtained for the full  $B^0 \rightarrow K^+\pi^-\pi^0$  candidate selection.

After the full selection, a total of 7220 on-peak events enter the ML fit.

Table 5.3: *Final signal selection efficiencies (overall and truth-matched) and fractions of misreconstructed events (SCF) for the different signal modes after full selection. The errors given are statistical only. Expectations are calculated with world averages for a data luminosity of  $193.2 \text{ fb}^{-1}$ . For the  $K_0^*(1430)\pi$  modes, we assume Belle's branching fractions of  $K_X^*\pi$ .*

Decay mode	$\varepsilon_{\text{TM+SCF}}(\%)$	$\varepsilon_{\text{TM}}(\%)$	$f_{\text{scf}}(\%)$	$N_{\text{exp}}$
$K^*(892)^+\pi^-$	$14.85 \pm 0.08$	$11.34 \pm 0.08$	$23.57 \pm 0.26$	$161.5 \pm 41.1$
$\rho^-K^+$	$16.65 \pm 0.04$	$12.96 \pm 0.04$	$22.19 \pm 0.14$	$319.6 \pm 56.8$
$K^*(892)^0\pi^0$	$16.84 \pm 0.08$	$15.37 \pm 0.08$	$8.74 \pm 0.16$	$14.5 \pm 36.0$
$K^+\pi^-\pi^0$ (N.R.)	$16.29 \pm 0.03$	$15.68 \pm 0.03$	$3.77 \pm 0.04$	$198.0 \pm 97.4$
$K_0^*(1430)^+\pi^-$	$15.51 \pm 0.08$	$14.11 \pm 0.08$	$8.99 \pm 0.16$	$168.8 \pm 54.7$
$K_0^*(1430)^0\pi^0$	$17.37 \pm 0.12$	$16.65 \pm 0.12$	$4.17 \pm 0.15$	$226.1 \pm 63.3$
Total				$1088.5 \pm 150.7$

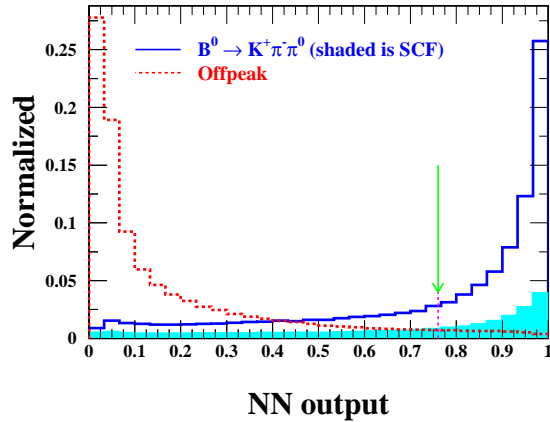


Figure 5.4: *Output distribution for the Neural Network, using the 4 discriminating variables defined in the text. Shown are TM signal (solid line), SCF signal (shaded area), and off-resonance data (dashed line). The arrow indicates the cut applied.*

## 5.4 Multivariate Continuum Suppression

Multivariate Analyzer (MVA) techniques are applied to suppress the dominant continuum background. A dedicated optimization has been performed. Note that since the DP information is explicitly exploited in the ML fit, the reconstructed resonance mass and helicity cannot be used in the MVA anymore. It is found that the combination of the following four leads to close-to optimal results, while maintaining simplicity.

- The **monomials**  $L_n$ , a set of momentum-weighted sums over the tracks in the rest-of-the-event (ROE) with respect to the  $B$  thrust axis  $T_B$  [60]:

$$L_n = \sum_{i=\text{ROE}} p_i \times |\cos(\theta_{T_B,i})|^n . \quad (5.6)$$

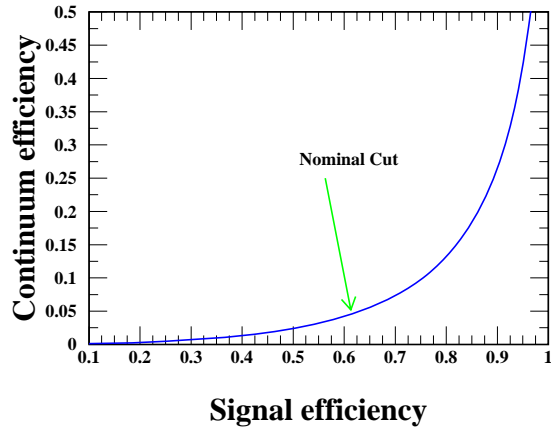


Figure 5.5: *Background efficiency as a function of the signal efficiency (including both TM and SCF) obtained from cuts on the NN output.*

$L_0$  and  $L_2$  are used [61].

- $\cos\theta_{B,z}$ , the cosine of the angle between the c.m.  $B$  direction and the  $z$  axis. With full detector acceptance, it follows a  $\sin^2\theta$  (uniform) distribution for signal (continuum background) events.
- $\cos\theta_{T_B,z}$ , the cosine of the angle between the candidate's thrust axis and the  $z$  axis. With full detector acceptance, it has a uniform for signal and a  $(1 + \cos^2\theta)$  distribution for continuum background.

A non-linear Neural Network (NN) [62] has been studied. This is a *MultiLayerPerceptron* Neural Network with the following architecture:

- number of input variables:  $N_{\text{var}} = 4$ ;
- number of output classes: 2 (signal and background);
- number of layers: 3 (input, output & one hidden layer);

- number of neurons per layer: 4 (input), 10 (hidden), 1 (output);
- number of training cycles: 1000;
- size of the training samples: 10000 signal MC events and 10000 off-resonance data events.

Optimization and training of the NN has been performed using off-resonance data contained in the signal region to reduce residual correlations of the NN with the kinematic variables used in the ML fit (see also the detailed description in Appendix D of Ref. [63]). Moreover, the signal sample is restricted to events that match MC-truth. The exclusion of combinatorial background (SCF) from the training turns out to be beneficial in fighting  $B$ -related backgrounds. In particular, charmless 3-body background mimics the kinematic distributions of SCF events. The reduced overall signal efficiency of the NN due to this training procedure (signal SCF events are treated as ordinary background) is counterbalanced by the improved  $B$ -background suppression.

The NN output distribution for TM signal, SCF signal, and off-resonance data are plotted in Fig. 5.4. As a qualitative measure of the discriminating power, we depict in Fig. 5.5 the background efficiency versus the signal efficiency obtained when cutting on the NN output.

To simplify an empirical fit of the NN output shape for continuum events, one can transform the MVA so that it is confined within  $[-1, 1]$  after selection:

$$\text{NN} \longrightarrow \text{NN}' \equiv 1 - \arccos(2\text{NN} - 1 + \text{offset}) , \quad (5.7)$$

where we use  $\text{offset} = 0.00135$  and  $\text{NN}_{\text{cut}} = 0.76$  (before transformation). The transformed  $\text{NN}'$  is shown in the right hand plot of Fig. 5.5. Because of correlations with the Dalitz variables – see Sec. 5.5 for details –, the NN output is used for the data selection but not in the ML fit.

## 5.5 Correlations

The ML fit applied could use as input all the discriminant variables  $m_{\text{ES}}$ ,  $\Delta E$ , NN and  $\Delta t$ . Yet, the likelihood model is built upon the assumption that these variables do not exhibit correlations among themselves. Violation of this assumption leads to biases in the fit. The effects can be quantified by performing fits to a number of data-size fully simulated Monte Carlo samples.

The correlation profiles of  $m_{\text{ES}}$  vs.  $\Delta E'$ ,  $\text{NN}'$  vs.  $\Delta E'$  and  $m_{\text{ES}}$  vs.  $\text{NN}'$ , for truth-matched and SCF events, and off-resonance events are plotted in Fig. 5.6. Significant correlations are only observed for TM events between  $m_{\text{ES}}$  and  $\Delta E'$ . Their linear correlation coefficient amounts to  $-8.6\%$ , which is a known feature and understood to be dominated by the common uncertainty on the beam energy. It can be approximated by [64, 65]

$$\rho(m_{\text{ES}}, \Delta E) \approx -\frac{\sigma(m_{\text{ES}})}{\sigma(\Delta E)} = -8.4 \cdot 10^{-2} . \quad (5.8)$$

The correlation coefficient is smaller for  $K^{*0}\pi^0$  events ( $-4.3\%$ ) and non-resonant  $K^+\pi^-\pi^0$  decays ( $-7.8\%$ ). Correcting  $\Delta E$  for the error on the beam energy gauged, by  $m_{\text{ES}}$  [66]

$$\Delta E \longrightarrow \Delta E + \delta_{E_{\text{beam}}^*} \approx \Delta E + (m_{\text{ES}} - \langle m_{\text{ES}} \rangle) , \quad (5.9)$$

with  $\langle m_{\text{ES}} \rangle \simeq 5.2795$ , reduces significantly the correlation as indicated in Fig. 5.8. As

a consequence, the  $\Delta E$  resolution for corrected TM events slightly improves from an RMS of 27.0 MeV to 26.8 MeV (*cf.* Fig. 5.7), which corresponds to a quadratic error reduction of about 3 MeV, as expected.

As mentioned above in Sec. 5.4, the NN output is not used in the ML as it is correlated with the Dalitz plot variables  $s_{+0}$  and  $s_{-0}$ . Indeed, events close to the borders of the Dalitz plot are more 'jet-like' than those in the center of the Dalitz plot, where the three mass-squared are of similar magnitude, so that the event exhibits a larger sphericity. Since the latter have kinematics closer to a typical multibody B-decay, they lead to increased (*i.e.*, more signal-like) NN outputs than the former. To show this, the variable  $\Delta_{\text{dalitz}}$  is introduced as a "distance" to the boundaries defined in the Dalitz plane:

$$\Delta_{\text{dalitz}} = \min(s_{+-}, s_{+0}, s_{-0}), \quad (5.10)$$

and as can be seen on Figure 5.9,  $\Delta_{\text{dalitz}}$  has maximal values in the center of the Dalitz plot, and decreases towards its edges. Figures 5.10, 5.11 and 5.12 show the correlation profiles for  $m_{\text{ES}}$ ,  $\Delta E$ ,  $\Delta E'$  and  $NN$  along the Dalitz plane, for truth-matched non-resonance signal, SCF non-resonance and offpeak events, respectively. The correlation profiles are done in terms of  $\Delta_{\text{dalitz}}$ , as well as the square Dalitz plot  $m'$  and  $\theta$  variables.

Note that the last two plots of Fig.5.12 show the correlation profile of  $NN$  versus  $\Delta_{\text{dalitz}}$ . On average,  $NN$  increases with this variable, which establishes its correlation with the Dalitz plot. For this reason,  $NN$  is not used as a discriminating variable in ML fit.

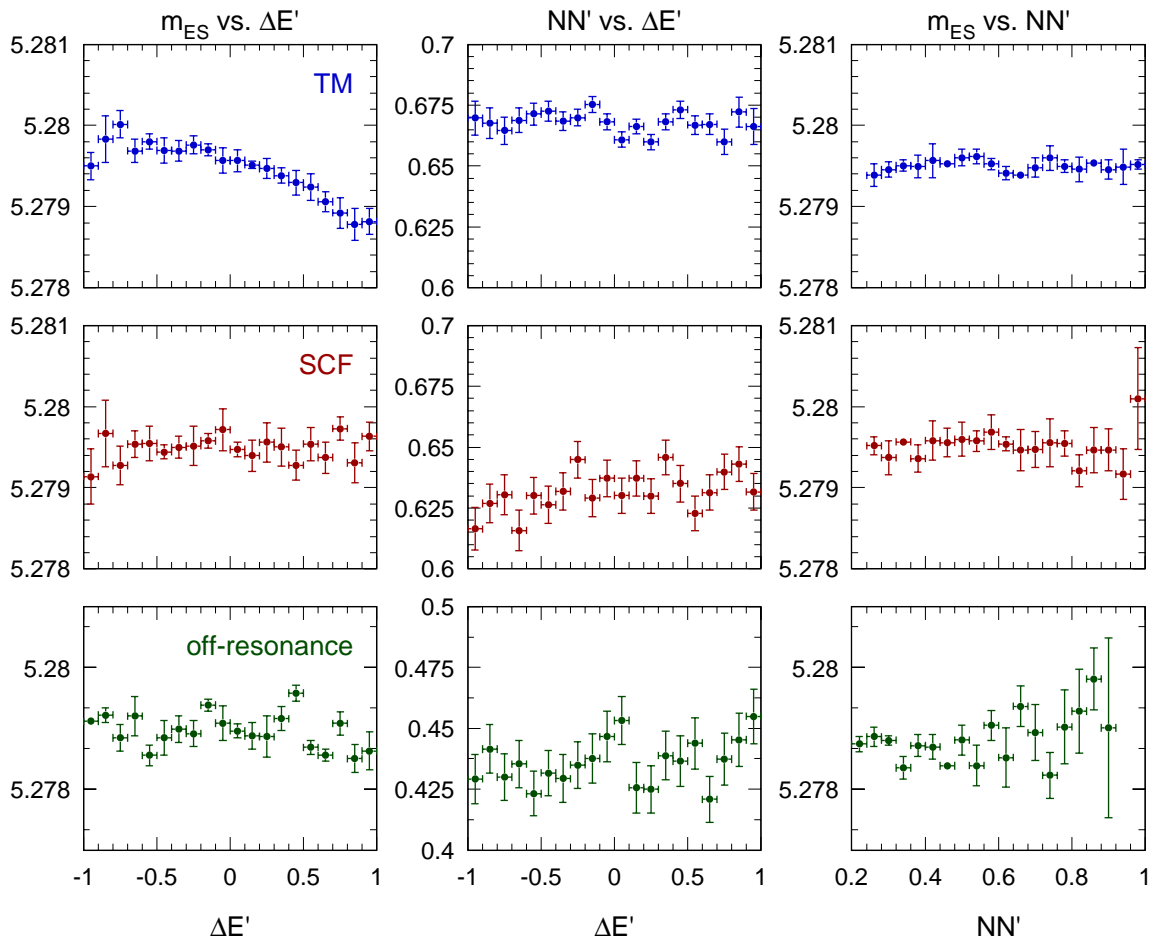


Figure 5.6: Correlation profiles of  $m_{ES}$  versus  $\Delta E'$  (left column),  $NN'$  versus  $\Delta E'$  (center column), and  $m_{ES}$  versus  $NN'$  (right column), for truth-matched events (upper line), SCF (center line) events, and off-resonance events (lower line).

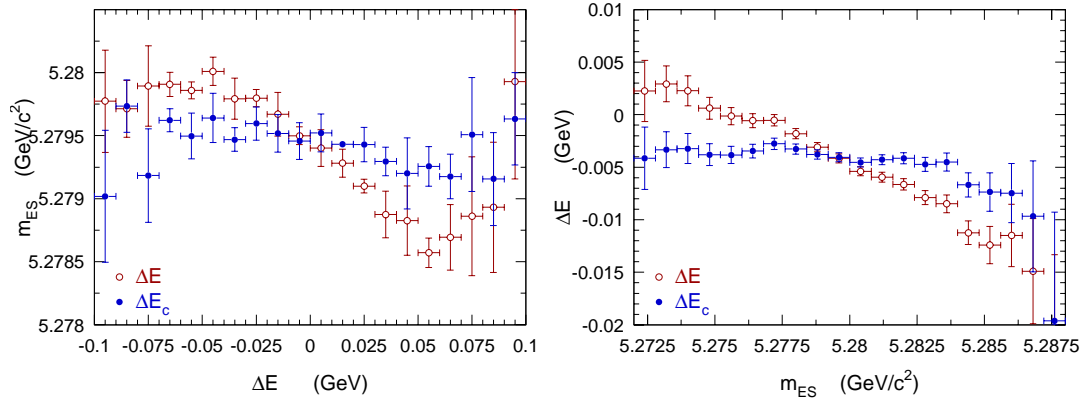


Figure 5.7: Correlations between  $m_{ES}$  and  $\Delta E$  with (full circles) and without (open circles) the  $m_{ES}$ -dependent correction (5.9).

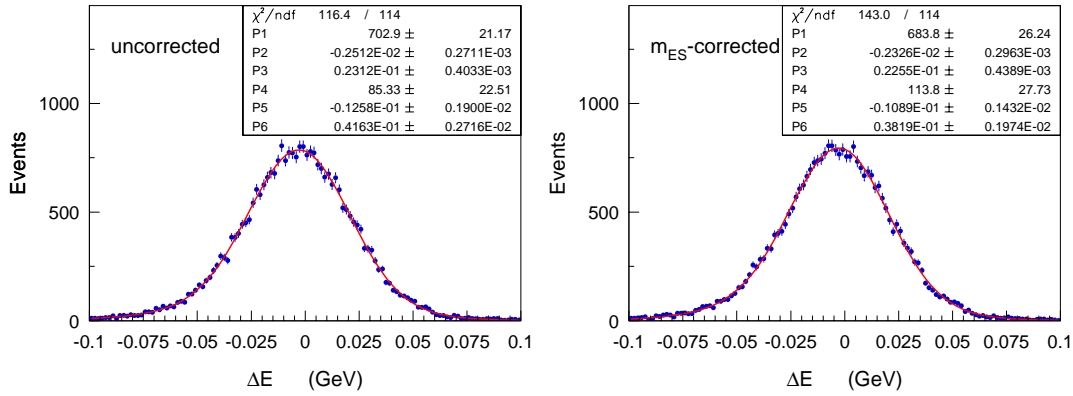


Figure 5.8: Double Gaussian fit to TM events with  $m_{+-} > 4.5 \text{ GeV}/c^2$ , before (left plot) and after (right plot) applying the correction (5.9).

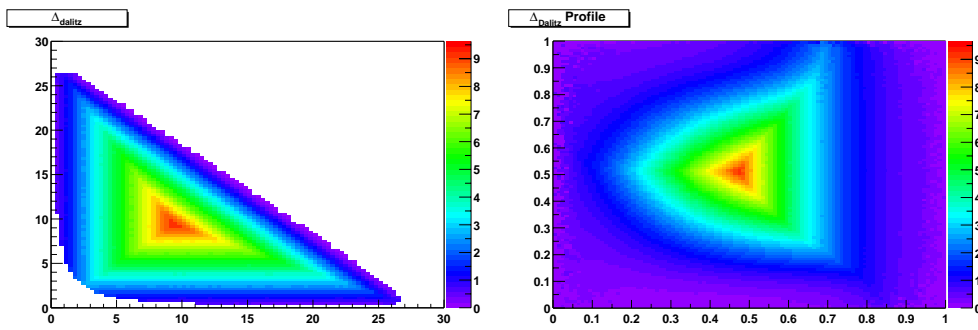


Figure 5.9: Profile of the  $\Delta_{\text{dalitz}}$  variable along the standard (left) and Square (right) Dalitz plane.

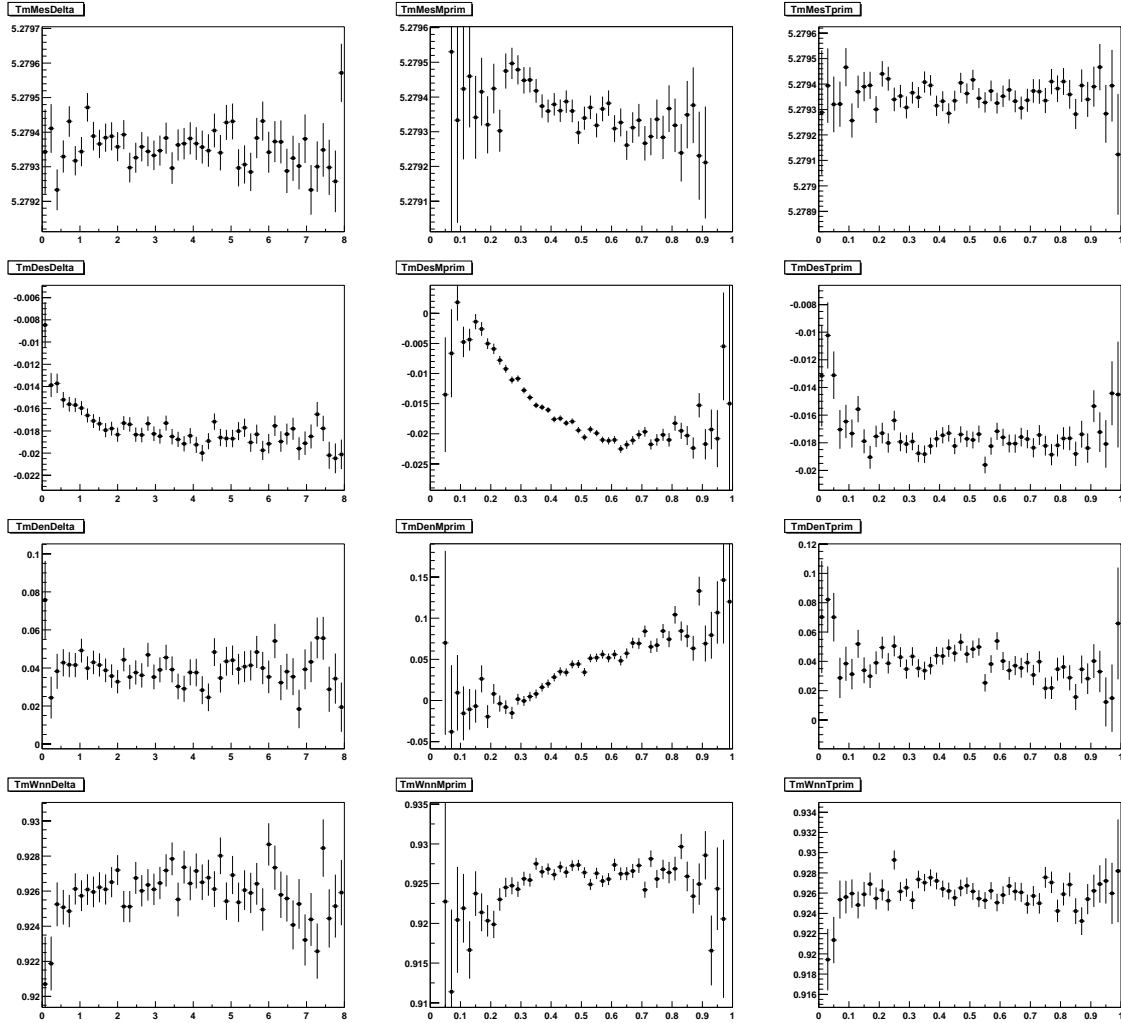


Figure 5.10: Correlation profiles for  $m_{ES}$ ,  $\Delta E$ ,  $\Delta E'$  and  $NN$  versus Dalitz variables for truth-matched signal events. Left (resp. center, right) column profiles corresponds to the  $\Delta_{dalitz}$  (resp.  $m'$ ,  $\theta'$ ) Dalitz variable.

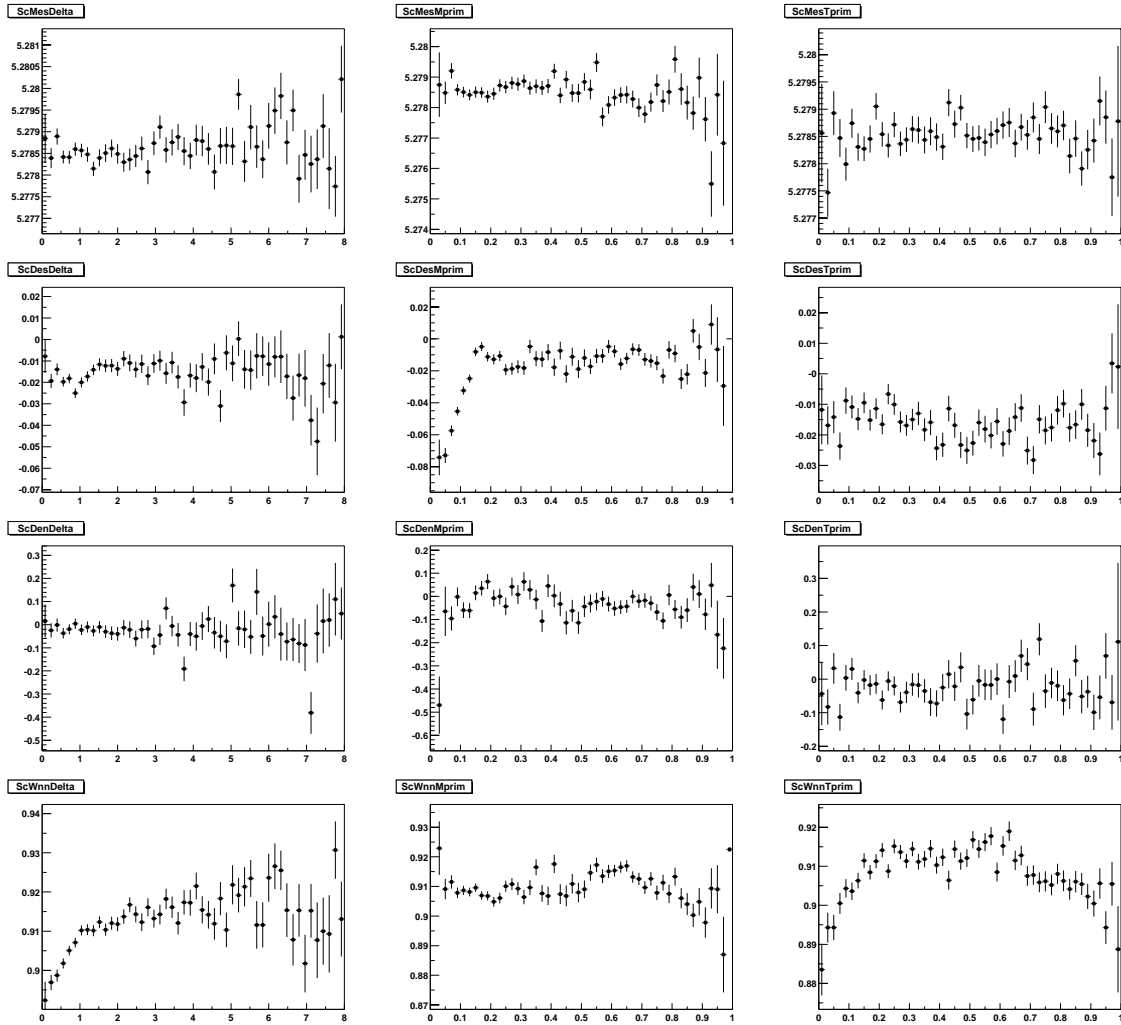


Figure 5.11: Correlation profiles for  $m_{ES}$ ,  $\Delta E$ ,  $\Delta E'$  and  $NN$  versus Dalitz variables for SCF signal events. Left (resp. center, right) column profiles corresponds to the  $\Delta_{dalitz}$  (resp.  $m'$ ,  $\theta'$ ) Dalitz variable.

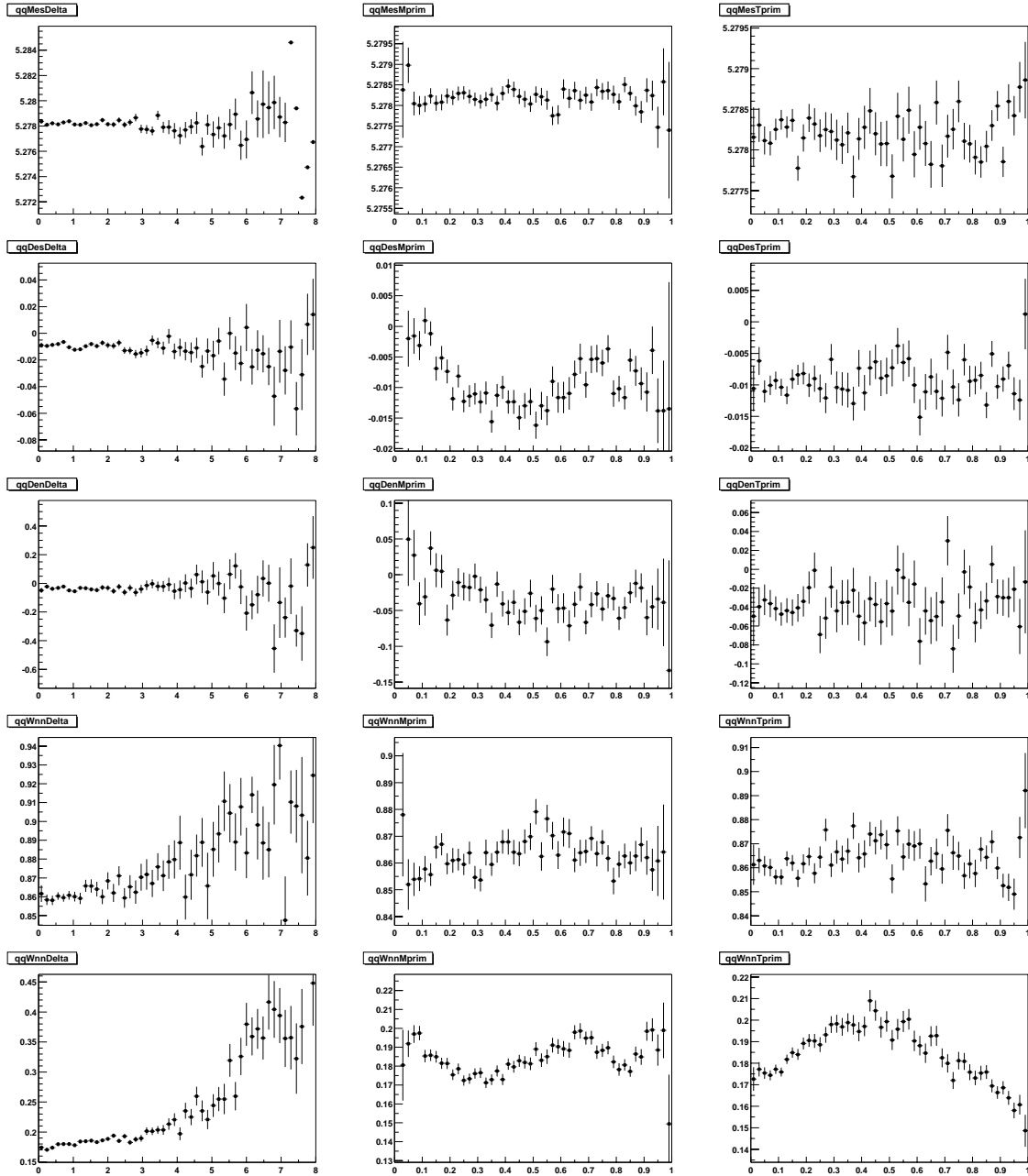


Figure 5.12: Correlation profiles for  $m_{ES}$ ,  $\Delta E$ ,  $\Delta E'$  and  $NN$  versus Dalitz variables for off-resonance events. Left (resp. center, right) column profiles corresponds to the  $\Delta_{dalitz}$  (resp.  $m'$ ,  $\theta'$ ) Dalitz variable. The last row shows the correlation profiles for the  $NN$  variable after relaxing the nominal  $NN > 0.76$  cut.

## Chapter 6

### *B*-Related Background

Since no invariant mass cuts are applied in the DP, and due to the presence of a  $\pi^0$ , the decay  $B^0 \rightarrow K^+\pi^-\pi^0$  suffers from large cross-feed from other charmed and charmless *B*-decays. Some of these *B*-background modes have unknown branching fractions. Moreover, they can exhibit *CP*-violating asymmetries. The cross-feed from other *B* decays are studied using MC simulation. The likelihood-building procedure for signal and backgrounds is discussed in detail in Section 7. The relevant model parameters are given in this section.

A similar strategy is followed as in the  $B^0 \rightarrow \rho^\pm\pi^\mp, \rho^-K^+$  quasi-two-body (Q2B) analysis [28], where a corrective PDF is introduced in the likelihood for classes of major contaminating modes. An extensive list of exclusive charmless  $B\bar{B}$  modes has been studied to evaluate the systematics on the event yields and the *CP* parameters due to cross-feed from these modes. *B* background can be categorized into two-, three- and four-body final states, of which the decay kinematics differ significantly.

- **Two-body modes:** to reconstruct a  $B^0 \rightarrow K^+\pi^-\pi^0$  candidate, one adds an additional object (charged or neutral) taken from the rest of the event: as a

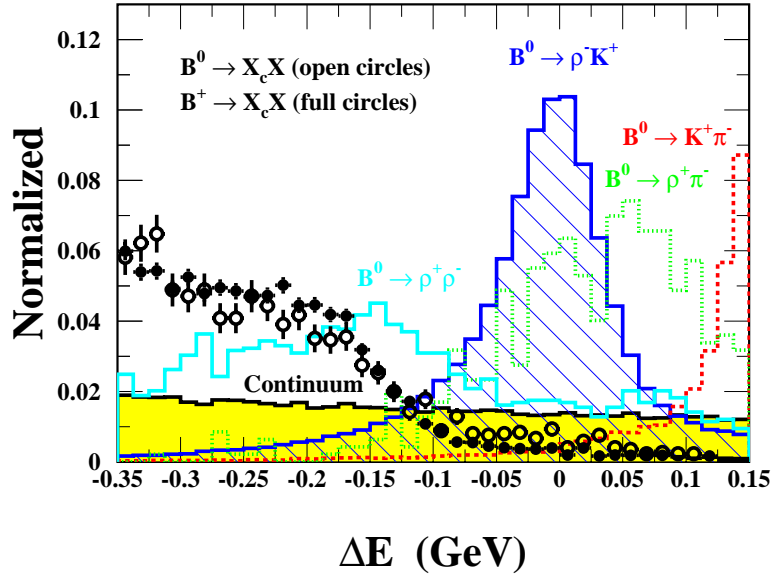


Figure 6.1: *Enlarged  $\Delta E$  band. Shown are signal  $B^0 \rightarrow \rho^- K^+$  events (hatched), neutral and charged  $b \rightarrow c$  events (full and open circles, respectively), and representative four-body (solid), three-body (dotted) and two-body (dashed) background modes, all taken from MC simulation. The shaded band indicates the continuum contribution taken from off-resonance data.*

consequence, these events populate the positive  $\Delta E$  region. A characteristic kinematic property is that they consist of 2 tracks (those from the original two-body decay) oriented back-to-back in the  $\Upsilon(4S)$  center-of-mass and the invariant mass of these 2 tracks is equal to the mass of the  $B$ . The rates of the two-body decays are well-known experimentally.

- **Three-body modes:** by exchanging (mostly) soft photons or tracks between the signal  $B$  and the rest of the event (ROE), or by picking up fake  $\pi^0$ s, one

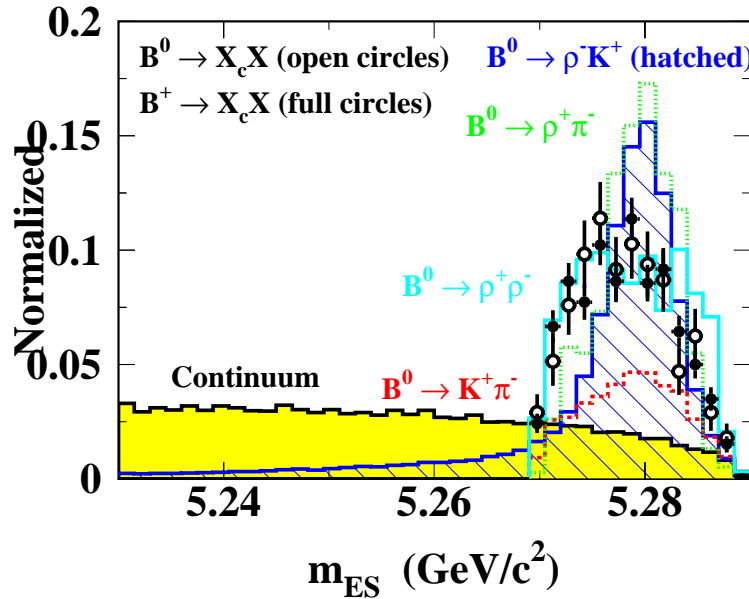


Figure 6.2: *Enlarged  $m_{ES}$  band. Shown are signal  $B^0 \rightarrow \rho^- K^+$  events (hatched), neutral and charged  $b \rightarrow c$  events (full and open circles, respectively), and representative four-body (solid), three-body (dotted) and two-body (dashed) background modes, all taken from MC simulation. The shaded band indicates the continuum contribution taken from off-resonance data.*

can reconstruct a  $B^0 \rightarrow K^+ \pi^- \pi^0$  candidate from another three-body mode. This approximately leaves  $\Delta E$  unaltered, *i.e.*,  $\Delta E(\text{three-body}) \sim 0$  – albeit with worse resolution. The kinematics of these processes resembles that of the  $B^0 \rightarrow K^+ \pi^- \pi^0$  signal, so that the three-body cross-feed is difficult to suppress without compromising the signal efficiency. In particular, three-body background exhibits similar kinematic properties as  $B^0 \rightarrow K^+ \pi^- \pi^0$  signal self-cross-feed. The branching fractions of most of the three-body modes have been measured, although with mediocre accuracy in some cases.

- **Four-body modes:** by using only 3 particles of a four-body decay, one can reconstruct a  $B^0 \rightarrow K^+\pi^-\pi^0$  candidate, which accumulates in the negative  $\Delta E$  region. Most of the four-body decays have not been measured yet.
- **Higher multiplicity modes:** the rates of modes with five or more particles in the final state are unknown in general and thus cannot be accounted for in a systematic way in the analysis. Kinematically, these modes resemble the charmed background due to the large negative  $\Delta E$  values. The associated uncertainties have been estimated in Ref. [63] by means of a fit of the inclusive  $b \rightarrow c(X)$ -background contribution, using an enlarged  $\Delta E$  region with increased sensitivity to high multiplicity background. It was found that the MC predicts the  $b \rightarrow c$  contribution within approximately 22%, which is sufficient for the purpose of this analysis.

The  $\Delta E$  distributions for signal, for the different multi-body backgrounds, and for the neutral and charged  $b \rightarrow c$  components, are shown in an enlarged acceptance window in Fig. 6.1. We also show the  $m_{ES}$  distributions for comparison in Fig. 6.2.

The square Dalitz plot distributions for representative modes are given in Figs. 6.3 and 6.4 (to be compared with signal in Fig. 3.2). Indicated on the plots are the  $\rho^-, K^*(892)^{+,0}$  bands. The last plot in Fig. 6.3 shows the DP for simulated neutral  $b \rightarrow c$ -background events that pass the event selection. Clustering is observed at the masses  $m_{+-} = m(D^0)$  which is due to the color-suppressed  $B^0 \rightarrow \bar{D}^0(\rightarrow K^+\pi^-)\pi^0$  decay. The last plot in Fig. 6.4 shows the DP for simulated charged  $b \rightarrow c$ -background events that pass the event selection. Clustering is again observed at the masses  $m_{+-} = m(D^0)$  which is due to the  $B^+ \rightarrow \bar{D}^0\rho^+$  decay, with a soft  $\pi^0$  from  $\rho^+$  decay

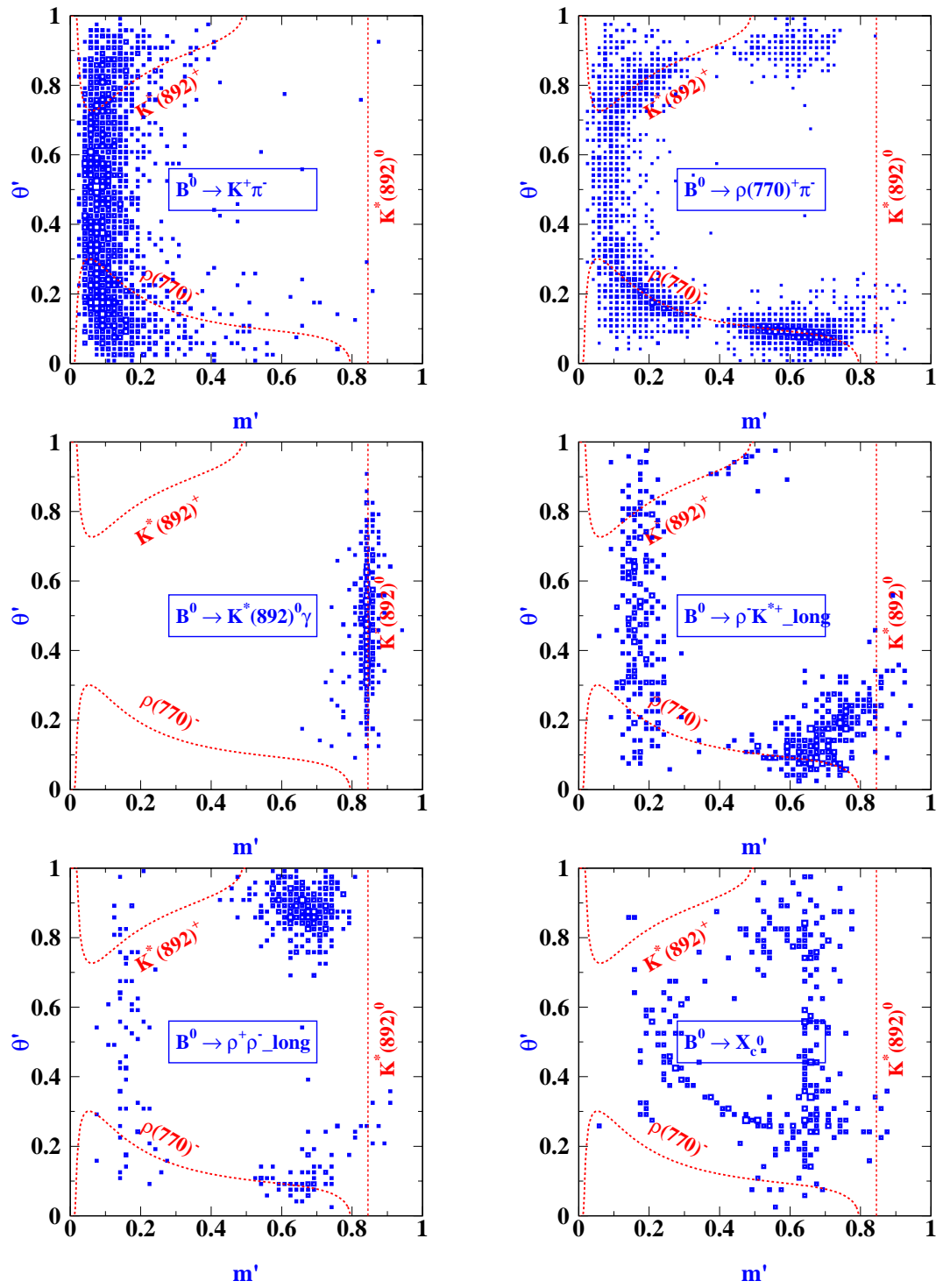


Figure 6.3: Square Dalitz plots for representative  $B^0$ -related background modes.

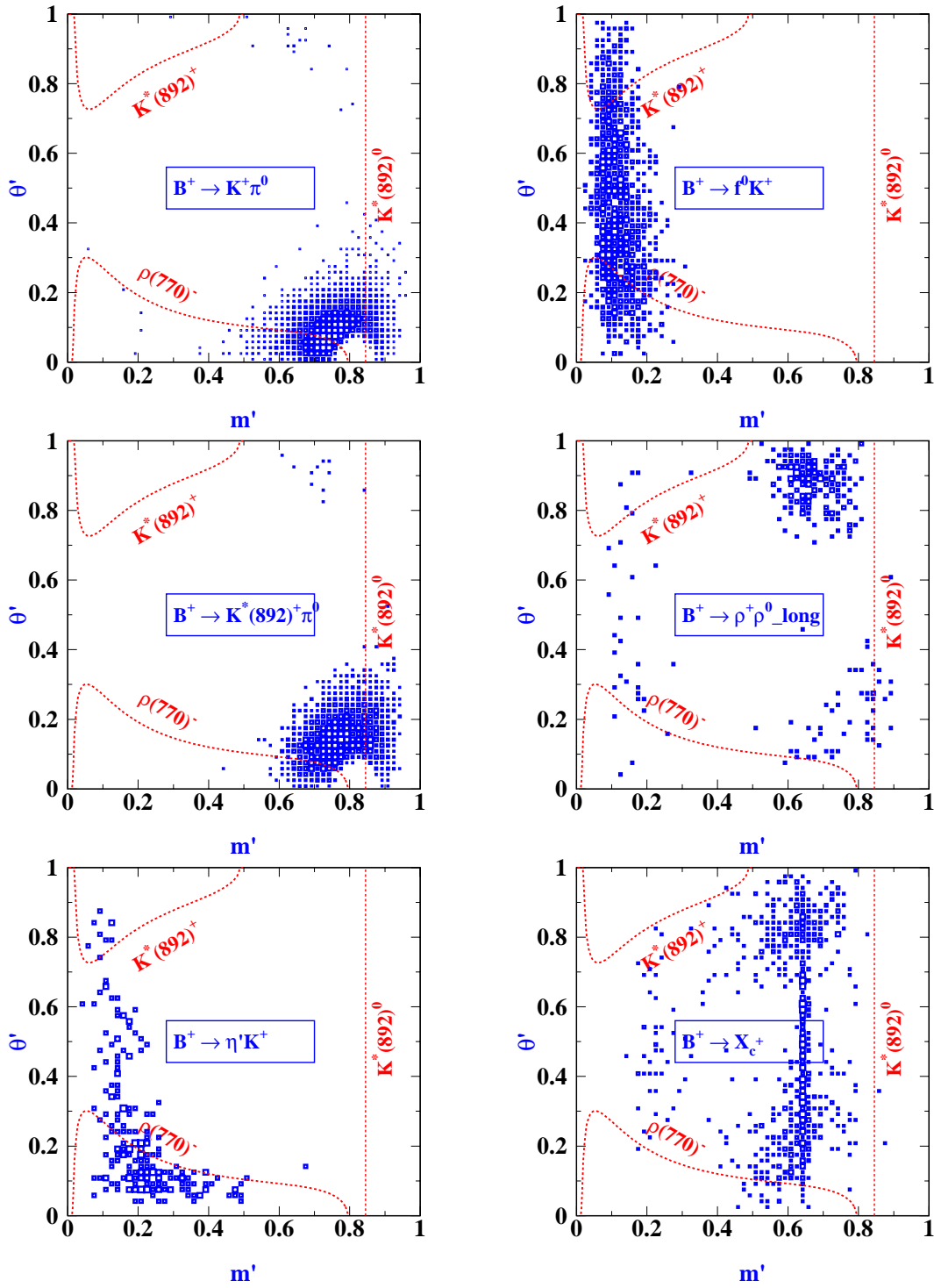


Figure 6.4: Square Dalitz plots for representative  $B^+$ -related background modes.

being excluded from the signal  $B$  reconstruction.

## 6.1 Branching Fractions

We use the world average branching fractions for the experimentally known decay modes. In cases where only upper limits are given, we translate the limits into branching fractions using the available information from the related publications. Educated guesses are used to deduce the branching fractions for the unknown modes. This is done using wherever possible similar modes that are known, together with rules based on isospin symmetry and/or form factor arguments, where naive factorization of the matrix elements is assumed in the latter cases. If not available, we rely on ad hoc assumptions that consequently entail large systematic uncertainties.

In  $B$  decays into two vector mesons the vector-vector state can have  $L = 0, 1, 2$  orbital angular momenta corresponding to longitudinal and transverse polarizations. Only longitudinally polarized particles create sufficiently fast decay pions and kaons to produce significant background after selection. We assume in the following in cases when the polarization is unknown that the corresponding modes be longitudinally saturated, which is in accordance with recent experimental results [67].

We refer to the extensive mode-by-mode discussion of the branching fractions given in Ref. [63]. Only those modes where significant changes with respect to Ref. [63] occur are revisited here.

Individual modes with expected contaminations of one or more events after selection are classified within four classes for charged  $B$  decays and six classes for neutral  $B$  decays. The classes regroup modes with similar PDFs and each class represents a

Table 6.1: *Classification of background from neutral B decays. The efficiencies are obtained from MC simulation. The expected number of events in the selected data sample correspond to an integrated on-resonance luminosity of  $193.2\text{fb}^{-1}$ . Each block represents a class including modes that contributes at least one event.*

Mode	BF ( $\times 10^{-6}$ )	Eff. (%)	$N_{expected}$	$N_{gen}(K)$
$B^0 \rightarrow K^+\pi^-$	$18.16 \pm 0.79$	$0.23 \pm 0.00$	$8.9 \pm 0.3$	834
$B^0 \rightarrow \pi^+\pi^-$	$4.55 \pm 0.44$	$0.02 \pm 0.00$	$0.2 \pm 0.0$	340
$B^0 \rightarrow \pi^+\pi^-\pi^0(NR)$	$0.0 \pm 5.0$	$0.57 \pm 0.00$	$0.0 \pm 6.0$	996
$B^0 \rightarrow \rho^0\pi^0$	$1.4 \pm 1.0$	$0.47 \pm 0.00$	$1.4 \pm 1.0$	453.5
$B^0 \rightarrow K_S(\pi^+\pi^-)\pi^0$	$3.8 \pm 0.5$	$0.31 \pm 0.01$	$2.6 \pm 0.3$	149
$B^0 \rightarrow K^+K^-\pi^0(incl.)$	$< 19$	$1.89 \pm 0.05$	$< 76.6$	66
$B^0 \rightarrow K^{*-}(K^+\pi^0)K^+$	$< 19$	$2.2 \pm 0.06$	$< 90.3$	57
$B^0 \rightarrow K^{*0}(K^+\pi^-)\gamma$	$27.8 \pm 1.5$	$0.82 \pm 0.04$	$48.5 \pm 2.6$	42
$B^0 \rightarrow K^{*0}(1410)\gamma$	$< 130$	0.06	$< 16.3$	138
$B^0 \rightarrow K^{*0}(1430)\gamma$	$12.4 \pm 2.4$	$0.23 \pm 0.1$	$6.2 \pm 1.2$	67
$B^0 \rightarrow K^{*0}(1680)(K^+\pi^-)\gamma$	$5.0 \pm 5.0$	$0.16 \pm 0.02$	$1.7 \pm 1.7$	132
$B^0 \rightarrow \rho^\pm\pi^\mp$	$24.0 \pm 2.5$	$0.60 \pm 0.01$	$30.8 \pm 4.0$	470
$B^0 \rightarrow \rho(1450)^\pm\pi^\mp$	$2.0 \pm 2.0$	0.87	$3.6 \pm 3.6$	126
$B^0 \rightarrow K^{*+}(K^+\pi^0)\rho_{long}^-$	$2.0 \pm 2.0$	$0.62 \pm 0.02$	$2.6 \pm 2.6$	86.5
$B^0 \rightarrow K^{*+}(K^+\pi^0)\rho_{tran}^-$	$2.0 \pm 2.0$	0.0	$0.0 \pm 0.0$	67
$B^0 \rightarrow K^{*0}(K^+\pi^-)\rho_{long}^0$	$1.0 \pm 1.0$	$0.40 \pm 0.02$	$0.9 \pm 0.9$	81.5
$B^0 \rightarrow K^*(1680)^+(K^+\pi^-)\rho^-$	$2.0 \pm 2.0$	$0.16 \pm 0.02$	$0.7 \pm 0.7$	37
$B^0 \rightarrow \rho^+\rho_{long}^-$	$26.6 \pm 8.2$	$0.12 \pm 0.00$	$6.9 \pm 2.1$	368
$B^0 \rightarrow \rho^0\rho_{long}^0$	$0.0 \pm 2.1$	0.03	$0.0 \pm 0.2$	25
$B^0 \rightarrow a_1^+(\rho^0\pi^+)\pi^-$	$35.0 \pm 25.0$	0.02	$0.9 \pm 0.7$	41
$B^0 \rightarrow \overline{D}^0\pi^0, \overline{D}^0 \rightarrow K^+\pi^-$	$11.0 \pm 1.9$	$16.74 \pm 0.09$	$392.9 \pm 68.0$	144
$B^0 \rightarrow D^-K^+, D^- \rightarrow \pi^-\pi^0$	$0.5 \pm 0.2$	$16.93 \pm 0.07$	$18.1 \pm 7.2$	240
$B^0 \rightarrow othercharm$	inclusive	$1.46 \pm 0.09 \times 10^{-6}$	$147.1 \pm 44.0$	190,936
Subtotal			$670.6 \pm 81.4$	

Table 6.2: *Classification of background from charged B decays. The efficiencies are obtained from MC simulation. The expected number of events in the selected data sample correspond to an integrated on-resonance luminosity of  $193.2\text{fb}^{-1}$ .*

Mode	BF ( $\times 10^{-6}$ )	Eff. (%)	$N_{expected}$	$N_{gen}(K)$
$B^+ \rightarrow K^+\pi^0$	$12.8 \pm 1.1$	$0.56 \pm 0.00$	$15.3 \pm 1.2$	1124
$B^+ \rightarrow \pi^+\pi^0$	$5.27 \pm 0.79$	0.04	$0.5 \pm 0.0$	63
$B^+ \rightarrow K^{*0}(K^+\pi^-)\pi^+$	$8.1 \pm 1.7$	0.0	$0.0 \pm 0.0$	123
$B^+ \rightarrow K^{*+}(K^+\pi^0)\pi^0$	$4.0 \pm 2.0$	$1.91 \pm 0.04$	$16.3 \pm 8.1$	101
$B^+ \rightarrow K^+\pi^+\pi^-(NR)$	$13.5 \pm 6.4$	$0.17 \pm 0.00$	$5.0 \pm 2.4$	1262
$B^+ \rightarrow K^+f^0(\pi^+\pi^-)$	$9.3 \pm 2.1$	$0.85 \pm 0.02$	$16.9 \pm 3.8$	148
$B^+ \rightarrow \pi^+\rho^0$	$9.1 \pm 1.1$	$0.10 \pm 0.00$	$1.9 \pm 0.2$	150
$B^+ \rightarrow \pi^0\rho^+$	$11.0 \pm 2.7$	$0.12 \pm 0.00$	$2.8 \pm 0.7$	711
$B^+ \rightarrow K_0^*(1430)\pi$	$60.7 \pm 7.0$	$0.135 \pm 0.01$	$17.5 \pm 2.1$	40
$B^+ \rightarrow K_2^*(1430)\pi$	$< 15.3$	$0.23 \pm 0.02$	$< 7.6$	37
$B^+ \rightarrow K^{*+}\gamma$	$41.8 \pm 3.3$	$0.01 \pm 0.00$	$1.0 \pm 0.2$	176
$B^+ \rightarrow K(1410)^{*+}\gamma$	$< 50$	0.04	$< 4.3$	140
$B^+ \rightarrow K(1430)^{*+}\gamma$	$14.4 \pm 4.2$	0.04	$1.2 \pm 0.3$	68
$B^+ \rightarrow K(1680)^{*+}\gamma$	$14.4 \pm 14.4$	0.02	0.0	140
$B^+ \rightarrow K^{*+}\bar{K}^{*0}(K^+\pi^-)_{long}$	$5.0 \pm 5.0$	0.09	$1.0 \pm 1.0$	66
$B^+ \rightarrow K^{*+}\bar{K}^{*0}(K^+\pi^-)_{tran}$	$5.0 \pm 5.0$	0.01	0.0	66
$B^+ \rightarrow K^{*0}(K^+\pi^-)\rho_{long}^+$	$8.0 \pm 4.0$	$0.41 \pm 0.00$	$7.1 \pm 3.4$	673.5
$B^+ \rightarrow K^{*+}(K^+\pi^0)\rho_{long}^0$	$3.5 \pm 1.3$	$0.26 \pm 0.01$	$1.9 \pm 0.7$	85.5
$B^+ \rightarrow K^{*+}(K^+\pi^0)\rho_{tran}^0$	$3.0 \pm 3.0^*$	0.0	$0.0 \pm 0.0$	67
$B^+ \rightarrow \eta'(\rho^0\gamma)K^+$	$21.4 \pm 1.7$	$0.25 \pm 0.01$	$11.2 \pm 0.9$	84.5
$B^+ \rightarrow \eta'(\rho^0\gamma)\pi^+$	$3.0 \pm 3.0^*$	0.03	$0.2 \pm 0.2$	85.5
$B^+ \rightarrow K^*(1680)\rho$	$15 \pm 15^*$	0.50	$16.2 \pm 16.2$	36
$B^+ \rightarrow \rho^+\rho_{long}^0$	$26.4 \pm 6.1$	$0.13 \pm 0.00$	$7.2 \pm 1.7$	232
$B^+ \rightarrow charm$	inclusive	$3.5 \pm 0.1 \times 10^{-6}$	$356.3 \pm 106.8$	207,326
Subtotal			$473.6 \pm 108.4$	
T otal neutral and charged B backgrounds			$1144.2 \pm 135.6$	

corrective term in the likelihood. A summary of their branching fractions, selection efficiencies and expected number of events, computed for an integrated on-resonance luminosity of  $193.2 \text{ fb}^{-1}$ , are given in Table 6.1 and 6.2.

## 6.2 Background from Charmed $B$ Decays

Charmed neutral  $B$  mesons can decay into the  $K^+\pi^-\pi^0$  final state via the Q2B states  $\bar{D}^0\pi^0$  and  $D^-K^+$  for which the branching fractions have been measured. These two are treated in two dedicated classes in the  $B$  background model. The most important of them is the decay  $B^0 \rightarrow \bar{D}^0(\rightarrow K^+\pi^-)\pi^0$  from which we expect about 393 events in our selected sample (*cf.* Table 6.1). Since it is fully reconstructed and due to its large final state mass, this mode is only marginally affected by continuum background. We will measure the branching fraction of this mode. In the fit, we float its yield and use it to better determine the signal shape parameters of the discriminant variables used. In terms of parametrization, the modeling for the charmless signal  $m_{\text{ES}}$  and  $\Delta E$  is used with common shape parameters; a signal Gaussian with floating mean and width is used for reconstructed  $D^0$  mass and a 5th order polynomial is used for the helicity distribution to take into account the reconstruction and selection effects. Contributions from other charmed  $B$  Decays are inclusively obtained with MC of generic  $B$  decays and are fixed in the fit. (See Table 6.1 and 6.2.)

## 6.3 Background from Kaon Resonances

The derivation of the background from charmless  $B$  decays to  $K\pi\pi(X)$  final states is rather involved, so that we shall discuss it to some detail in this section. Since for about 15% of the events PID information is much reduced due to absence

of either or both of the kaons in the DIRC, background from  $KK\pi(X)$  events is significant in the  $B^0 \rightarrow K^+\pi^-\pi^0$  signal.

## 6.4 The modes $B^+ \rightarrow K^+(\pi\pi)^0$

Belle has performed a Dalitz Plot analysis on  $B^+ \rightarrow K^+\pi^+\pi^-$  [54]. From this paper we see:

$$\mathcal{B}(B^+ \rightarrow K_0^*(1430)^0\pi^+, K_0^*(1430)^0 \rightarrow K^+\pi^-) = 25.0 \pm 1.6_{-2.1}^{+2.4+0.0} \times 10^{-6},$$

$$\mathcal{B}(B^+ \rightarrow K_2^*(1430)^0\pi^+, K_2^*(1430)^0 \rightarrow K^+\pi^-) < 3.4 \times 10^{-6},$$

$$\mathcal{B}(B^+ \rightarrow K^*(1680)^0\pi^+, K^*(1680)^0 \rightarrow K^+\pi^-) < 5.3 \times 10^{-6},$$

$$\mathcal{B}(B^+ \rightarrow K^+\pi^+\pi^-(N.R.)) = 13.5 \pm 1.7_{-1.1}^{+1.3+6.3} \times 10^{-6}.$$

A not-yet published *BABAR* measurement on  $B^+ \rightarrow K^{*+}\pi^0$  [68] reports  $\mathcal{B}(B^+ \rightarrow K^{*+}\pi^0, K^{*+} \rightarrow K^+\pi^0) = 4.0 \pm 1.3 \pm 0.6 \times 10^{-6}$  and  $\mathcal{A}_{CP}(B^+ \rightarrow K^{*+}\pi^0) = 0.24 \pm 0.33 \pm 0.13$ .

We use these measured branching fractions in this analysis. Particularly, we derive  $\mathcal{B}(B^+ \rightarrow (K_0^*(1430)\pi)^+) = 60.7 \pm 7.0 \times 10^{-6}$  and  $\mathcal{B}(B^+ \rightarrow K_2^*(1430)\pi)^+ < 15.3 \times 10^{-6}$ .

## 6.5 The mode $B \rightarrow K^*K^{(*)}$

The modes  $B^0 \rightarrow K^{*+}(\rightarrow K^+\pi^0)K^-$  leads to the same topology as the  $B^0 \rightarrow K^+\pi^-\pi^0$  signal if one kaon is misidentified as a pion. This background is signal-like in  $m_{ES}$  and shifted to low end in  $\Delta E$ . So far, there is an upper limit on the inclusive branching fraction of  $B^0 \rightarrow K^+K^-\pi^0$ , which is  $19 \times 10^{-6}$  by CLEO.

An upper limit of  $5.3 \times 10^{-6}$  on the branching fraction of  $B^+ \rightarrow \overline{K}^{*0}K^+$  was set

by CLEO. A not-yet published measurement on  $B^+ \rightarrow \overline{K}^{*0} K^+$  [69] at *BABAR* brings the limit down to  $1.5 \times 10^{-6}$ . This suggests that the contribution from  $B \rightarrow K^* K$  should be rather small.

The modes  $B^0 \rightarrow K^{*+}(\rightarrow K^+ \pi^0) K^{*-}(\rightarrow K^- \pi^0)$  may also contribute if one kaon is misidentified as a pion and a soft  $\pi^0$  is dropped. An upper limit of  $141 \times 10^{-6}$  was set by CLEO. Based on the known limit on  $B^+ \rightarrow \overline{K}^{*0} K^+$ , we use  $5.0 \pm 5.0 \times 10^{-6}$  instead and do not expect any contribution.

None of the  $B \rightarrow K^* K^{(*)}$  modes have been observed so far. Thus we expect very small contamination from these modes. We assume no contributions from these modes in the nominal model and later assume conservative uncertainties on the branching fractions to study the systematics.

## 6.6 Higher Multiplicities $B \rightarrow K_{(X)}^{(**)} \rho$

$\mathcal{B}(B^+ \rightarrow K^{*+} \rho^0)$  has been measured by *BABAR* [70], giving a branching fraction of  $(10.6_{-2.6}^{+3.0} \pm 2.4) 10^{-6}$  (with a fraction of longitudinal polarization of  $0.96_{-0.15}^{+0.04} \pm 0.04$ ). There are also unpublished measurements performed at *BABAR* on  $B^0 \rightarrow K^{*+} \rho^-$  [71] and  $B^+ \rightarrow K^{*0} \rho^+$  [72]. The former gives  $\mathcal{B}(B^0 \rightarrow K^{*+} \rho^-) = 11.5 \pm 3.4 \pm 3.2 \times 10^{-6}$  with a fraction of longitudinal polarization of  $0.27 \pm 0.31 \pm 0.06$ . The latter gives  $\mathcal{B}(B^+ \rightarrow K^{*0} \rho^+) = 15.4 \pm 2.6 \pm 0.7 \times 10^{-6}$  with a fraction of longitudinal polarization of  $0.77 \pm 0.08$ . We expect negligible contribution from the color suppressed  $B^0 \rightarrow K^{*0} \rho^0$ .

We use this as a basis for an estimate with an inflated error:  $\mathcal{B}(B^0 \rightarrow K^{*+} (K^{*+} \rightarrow K^+ \pi^0) \rho^-)_{long} \simeq (2.0 \pm 2.0) \times 10^{-6}$ ;  $\mathcal{B}(B^+ \rightarrow K^{*+} (K^{*+} \rightarrow K^+ \pi^0) \rho^0)_{long} \simeq (3.5 \pm 1.3) \times$

$10^{-6}$ ;  $\mathcal{B}(B^+ \rightarrow K^{*0}(K^{*0} \rightarrow K^+\pi^-)\rho^+)_{long} \simeq (8.0 \pm 4.0) \times 10^{-6}$ .

To estimate the background from  $B \rightarrow K_X^{(**)}\rho$  we assume  $\mathcal{B}(B^0 \rightarrow K_X^{(**)}\rho) = \mathcal{B}(B^0 \rightarrow K_X^{(**)}\pi)$  and  $\mathcal{B}(B^+ \rightarrow K_X^{(**)}\rho) = \mathcal{B}(B^+ \rightarrow K_X^{(**)}\pi)$ , and assign an uncertainty of 100 % to these branching fractions. Only  $K_X^{(**)}$  decays to  $K\pi$  final states are taken into account. All other charge combinations are inferred from this estimate using isospin symmetry with assumed penguin dominance. The expected backgrounds from these modes are small.

## Chapter 7

### Building the Likelihood

The selected on-resonance data sample consists of signal, continuum-background and  $B$ -background components. The variables  $m_{ES}$ ,  $\Delta E'$ , and the DP discriminate signal from background. The signal likelihood consists of the sum of a correctly reconstructed (TM) component and a misreconstructed (SCF) component .

The likelihood  $\mathcal{L}$  for  $N$  events is

$$\begin{aligned}
 \mathcal{L} = & e^{-N'} \prod_{i=1}^N \left\{ N_{sig} \left[ (1 - \bar{f}_{SCF}) \mathcal{P}_{sig-TM,i} + \bar{f}_{SCF} \mathcal{P}_{sig-SCF,i} \right] \right. \\
 & + N_{q\bar{q}} \frac{1}{2} (1 + q_{K,i} A_{q\bar{q}}) \mathcal{P}_{q\bar{q},i} \\
 & + \sum_{j=1}^{N_{classes}^{B^+}} N_{B^+}^j f_{B^+}^j \frac{1}{2} (1 + q_{K,i} A_{B^+}^j) \mathcal{P}_{B^+,i}^j \\
 & \left. + \sum_{j=1}^{N_{classes}^{B^0}} N_{B^0}^j f_{B^0}^j \frac{1}{2} (1 + q_{K,i} A_{B^0}^j) \mathcal{P}_{B^0,i}^j \right\}, \tag{7.1}
 \end{aligned}$$

where,

- $N'$  is the sum of all the yields that are involved, *ie.*,  $N_{sig} + N_{q\bar{q}} + \sum_{j=1}^{N_{classes}^{B^+}} N_{B^+}^j + \sum_{j=1}^{N_{classes}^{B^0}} N_{B^0}^j$ ;

- $N_{sig}$  is the total number of signal ( $B^0 \rightarrow K^+\pi^-\pi^0$  and  $\bar{B}^0 \rightarrow K^-\pi^+\pi^0$ ) events in the data sample;
- $\bar{f}_{SCF}$  is the fraction of misreconstructed signal events (SCF) averaged over the Dalitz plot (DP); note that SCF events will be described by convolution in the DP (*cf.* Section 7.1);
- $\mathcal{P}_{3\pi-TM,i}$  and  $\mathcal{P}_{3\pi-SCF,i}$  are the products of PDFs of the discriminating variables, for truth-matched (TM) and SCF events respectively;
- $N^{q\bar{q}}$  is the number of continuum events;
- $q_{K,i}$  is the Kaon charge of the event; we use  $q_{K,i} = 1$  for  $B^0$  and  $q_{K,i} = -1$  for  $\bar{B}^0$ ;
- $A_{q\bar{q}}$  parameterizes possible charge asymmetry in continuum events due to detection, reconstruction or selection;
- $\mathcal{P}_{q\bar{q},i}$  is the continuum PDF;
- $N_{classes}^{B^+}$  ( $N_{classes}^{B^0}$ ) is the number of charged (neutral)  $B$ -related background classes considered (*cf.* Section 6);
- $N_{B^+}^j$  ( $N_{B^0}^j$ ) is the number of expected events in the charged (neutral)  $B$ -related background class  $j$ ;
- $f_{B^+j}$  ( $f_{B^0j}$ ) is the fraction of charged (neutral)  $B$ -related background events of class  $j$ ;

- $A_{B^+}^j$  ( $A_{B^0}^j$ ) describes the charge asymmetry in charged (neutral)  $B$  background of class  $j$ ; this charge asymmetry could come from physics, or detector effect;
- $\mathcal{P}_{B^+,i}^j$  is the PDF for  $B^+$ -background class  $j$ ;
- $\mathcal{P}_{B^0,i}^j$  is the PDF for  $B^0$ -background class  $j$ ;

The PDFs  $\mathcal{P}_X$  are the product of the PDFs of the four discriminating variables  $x_k$ ,  $k = 1, \dots, 4$ :

$$\mathcal{P}_{X,i}^{(j)} \equiv \prod_k P_{X,i}^{(j)}. \quad (7.2)$$

The individual PDFs in Eq. (7.1) are discussed in the following sections.

## 7.1 Dalitz Plot PDFs

- **DP-dependent selection efficiency and SCF fraction.**

Dalitz plot PDFs and DP-averaged quantities, like normalization or SCF fractions, require knowledge of the DP-dependent relative selection efficiency  $\varepsilon = \varepsilon(m', \theta')$ . It is a decay-dynamics-invariant quantity and is obtained from high statistics MC simulation. It is shown in the left hand plots of Fig. 7.1 for the DP (upper) and the square DP (lower), where the symmetric property of the DP has been used in the latter to effectively double the available statistics. One observes a rather flat efficiency over the main DP, with an increase along rising  $m'$  ( $m_{+-}$ ) values, due to the larger  $\pi^0$  energies. The efficiency drops close to the extreme corners of the DP, which is where two particles are back-to-back, while the third is (almost) in rest, and acceptance is necessarily low due to the minimum  $p_T$  (tracks) or  $E_\gamma$  (neutrals) requirements.

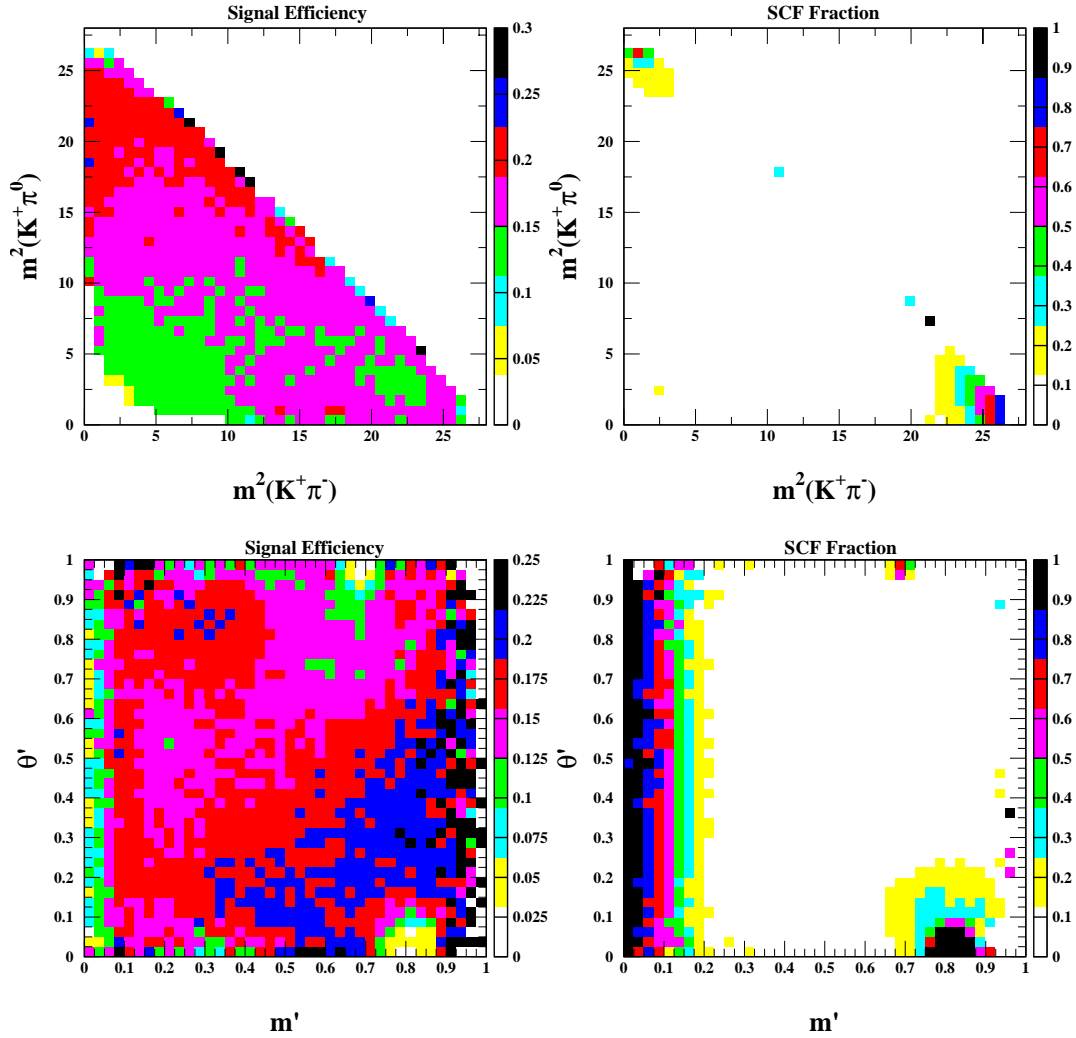


Figure 7.1: Selection efficiency of  $B^0 \rightarrow K^+\pi^-\pi^0$  events (left plots) and fraction of misreconstructed events (right plots), in the nominal Dalitz plot (upper plots) and the square Dalitz plot (lower plots). The plots are made with a sample of 2.7 million signal MC events.

Moreover, the DP part in the likelihood component for TM and SCF signal (*cf.* Eq. (7.1)) must be expanded to account for a DP-dependent SCF fraction  $f_{\text{SCF}} = f_{\text{SCF}}(m', \theta')$ . Again, the DP-dependent SCF fraction does not depend on the decay dynamics. For an event  $i$ , we have the PDF (*cf.* Eq. (7.2)).

$$P_{3\pi\text{-TM},i} = \varepsilon_i (1 - f_{\text{SCF},i}) |\det J_i| \frac{|\mathcal{A}_{B^0 \rightarrow K^+\pi^-\pi^0}|^2 + |\overline{\mathcal{A}}_{\overline{B}^0 \rightarrow K^-\pi^+\pi^0}|^2}{\langle |\mathcal{N}_{\text{TM}}|^2 \rangle}, \quad (7.3)$$

$$P_{3\pi\text{-SCF},i} = \varepsilon_i f_{\text{SCF},i} |\det J_i| \frac{|\mathcal{A}_{B^0 \rightarrow K^+\pi^-\pi^0}|^2 + |\overline{\mathcal{A}}_{\overline{B}^0 \rightarrow K^-\pi^+\pi^0}|^2}{\langle |\mathcal{N}_{\text{SCF}}|^2 \rangle}, \quad (7.4)$$

The normalization constants  $\langle |\mathcal{N}_{\text{TM}}|^2 \rangle$  and  $\langle |\mathcal{N}_{\text{SCF}}|^2 \rangle$  are those from Eq. (3.28), with the difference that now the phase space integration has to take into account the DP-dependent efficiencies and SCF fractions

$$|\mathcal{N}_{\text{TM}}|^2 = \text{Re} \sum_{\kappa, \sigma} (A^\kappa A^{\sigma*} + \overline{A}^\kappa \overline{A}^{\sigma*}) \langle \varepsilon (1 - f_{\text{SCF}}) |\det J| f^\kappa f^{\sigma*} \rangle, \quad (7.5)$$

$$|\mathcal{N}_{\text{SCF}}|^2 = \text{Re} \sum_{\kappa, \sigma} (A^\kappa A^{\sigma*} + \overline{A}^\kappa \overline{A}^{\sigma*}) \langle \varepsilon f_{\text{SCF}} |\det J| f^\kappa f^{\sigma*} \rangle, \quad (7.6)$$

The indices  $\kappa, \sigma$  run over all resonances of the signal model (*cf.* Section. 4).

The expectation values occurring in Eqs. (7.5, 7.6) are model-dependent and are computed with high statistics MC integration over the square DP:

$$\langle \varepsilon (1 - f_{\text{SCF}}) |\det J| f^\kappa f^{\sigma*} \rangle = \frac{\int_0^1 \int_0^1 \varepsilon (1 - f_{\text{SCF}}) |\det J| f^\kappa f^{\sigma*} dm' d\theta'}{\int_0^1 \int_0^1 \varepsilon |\det J| f^\kappa f^{\sigma*} dm' d\theta'} , \quad (7.7)$$

and similarly for  $\langle \varepsilon |\det J| f^\kappa f^{\sigma*} \rangle$ , where all quantities in the integrands are DP-dependent. Note that the integral (7.7) depends on the dynamics (form factors) assumed for the signal model. If parameters of this model are determined from a fit to data, the determination of Eq. (7.7) has to be iterative.

The DP-dependent SCF fractions obtained from MC simulation are plotted in

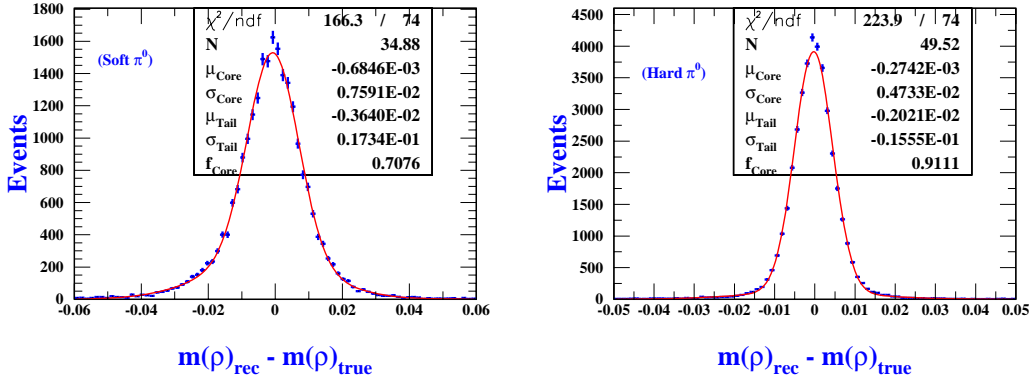


Figure 7.2: Resolution of the reconstructed  $\rho^-$  mass in the  $B^0 \rightarrow \rho^- K^+$  MC for soft  $\pi^0$  (left plot) and hard  $\pi^0$  (right plot) in TM events. The parameters correspond to a double Gaussian fit.

Fig. 7.1 (right), for the DP (upper) and the square DP (lower plot). The distribution pattern of the SCF fractions over the DP is a consequence of the same kinematic property that is responsible for the efficiency drop in the Dalitz corners. Combinatorial background is high (close to one) in the presence of soft neutrals or tracks. Misreconstructed signal events are almost absent in the center of the DP.

- **DP-averaged SCF fraction.**

Equation (7.1) invokes the quasi-two-body-like phase space-averaged SCF fraction  $\bar{f}_{\text{SCF}}$ . As for the PDF normalization, it is decay-dynamics dependent, since it is obtained from an integral of the decay amplitude-squared over the Dalitz plot

$$\bar{f}_{\text{SCF}} = \frac{\int_0^1 \int_0^1 \varepsilon f_{\text{SCF}} |\det J_i| (|\mathcal{A}_{B^0 \rightarrow K^+ \pi^- \pi^0}|^2 + |\bar{\mathcal{A}}_{B^0 \rightarrow K^- \pi^+ \pi^0}|^2) dm' d\theta'}{\int_0^1 \int_0^1 \varepsilon |\det J_i| (|\mathcal{A}_{B^0 \rightarrow K^+ \pi^- \pi^0}|^2 + |\bar{\mathcal{A}}_{B^0 \rightarrow K^- \pi^+ \pi^0}|^2) dm' d\theta'} . \quad (7.8)$$

It has to be computed iteratively, though the associated systematic uncertainty

is expected to be small.

- **TM resolution.**

The intrinsic width of the dominant  $\rho(770)$  resonance expressed in standard deviations of a double Gaussian fit function gives approximately (the form factor  $F_{\rho(770)}$  is expressed as a function of the linear mass here)

$$\sigma_{\text{core}}(F_{\rho(770)}) \approx 0.5 \Gamma_{\rho(770)} \approx 75 \text{ MeV}/c^2, \quad (7.9)$$

$$\sigma_{\text{tail}}(F_{\rho(770)}) \approx 2.0 \Gamma_{\rho(770)} \approx 300 \text{ MeV}/c^2. \quad (7.10)$$

It can be compared with the mass resolution for TM events plotted in Fig. 7.2 for soft  $\pi^0$ 's (left plot) and hard  $\pi^0$ 's (right plot). Recall that the soft  $\pi^0$  region is where the TM efficiency is low and the SCF fraction rises. Even the worst tail-Gaussian resolution of  $20.6 \text{ MeV}/c^2$  is more than a factor of three narrower than the core width of the double Gaussian fit to the  $\rho(770)$  form factor. We therefore do not account for resolution effects in the TM model and do fits to data-size full MC samples to study the effect on the final results.

- **SCF resolution.**

Misreconstructed events are concentrated in the corners of the Dalitz plot and have a mass resolution that dramatically varies across the DP. Figure 7.3 shows the  $K^*(892)^+$  and  $K^*(892)^0$  mass resolution for simulated  $B^0 \rightarrow K^*(892)^+\pi^-$  and  $B^0 \rightarrow K^*(892)^0\pi^0$  events. Unlike for TM events, the resolution effects cannot be ignored anymore for SCF events. We therefore introduce a  $2 \times 2$ -dimensional convolution function

$$R_{\text{SCF}}(m'_r, \theta'_r, m'_t, \theta'_t), \quad (7.11)$$

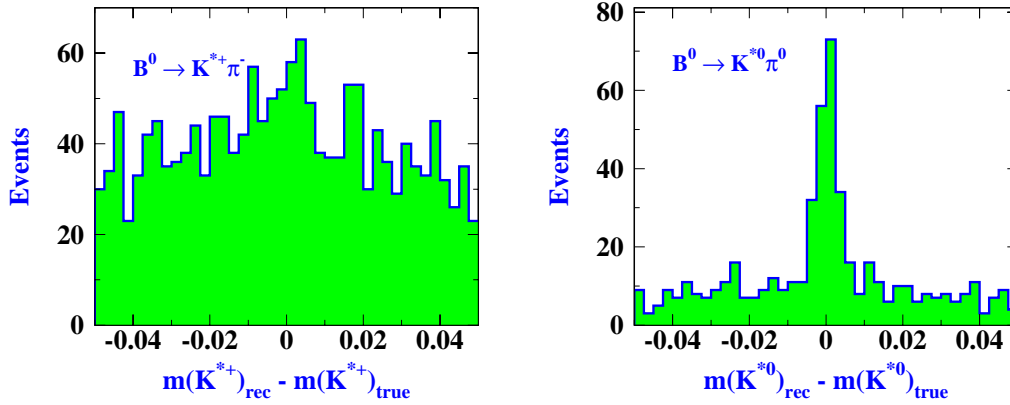


Figure 7.3: *Difference between reconstructed and true  $K^*(892)^+$  (left) and  $K^*(892)^0$  mass (right) in the MC for misreconstructed  $B^0 \rightarrow K^*(892)^+\pi^-$  (left) and  $B^0 \rightarrow K^*(892)^0\pi^0$  events (right).*

which represents the probability to reconstruct at the coordinate  $(m'_r, \theta'_r)$  an event that has the true coordinate  $(m'_t, \theta'_t)$ . It obeys the unitarity condition

$$\int_0^1 \int_0^1 R_{\text{SCF}}(m'_r, \theta'_r, m'_t, \theta'_t) dm'_r d\theta'_r = 1, \quad \forall (m'_t, \theta'_t) \in \text{SDP}. \quad (7.12)$$

The  $R_{\text{SCF}}$  function is obtained from MC simulation and implemented as four-dimensional smoothed histogram, and is computed only once. Figure 7.4 shows the resolution function of TM (left) and SCF events (right) for two arbitrary generated values  $(m'_t = 0.10, \theta'_t = 0.25)$  and  $(m'_t = 0.72, \theta'_t = 0.04)$

- **Parameterization of Signal Dalitz plot:**

The reference distribution for the physical Dalitz plot (efficiency and resolution corrections have been discussed in the previous bullets) is obtained from the signal model described in Section 4. It depends on the underlying resonance structure.

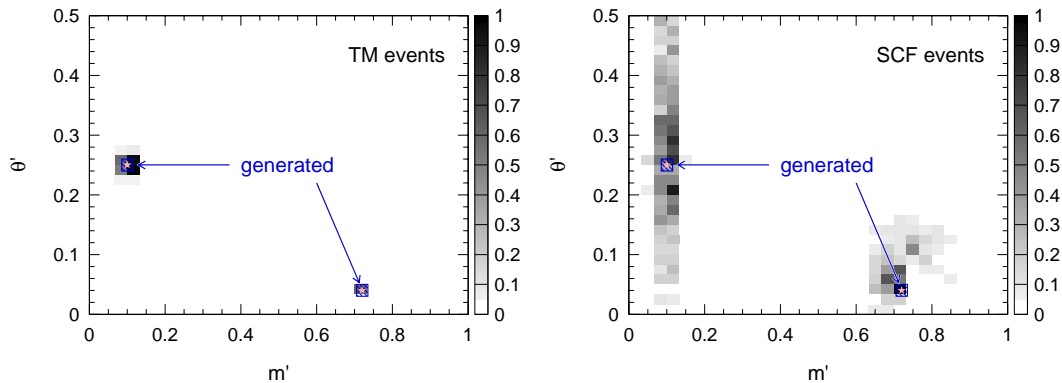


Figure 7.4: Resolution for TM (left) and SCF events (right) for two chosen generated values in the square DP, indicated by the open stars (see text for the numerical values).

- **B-background parameterization.**

We use smoothed histograms as parameterization for neutral  $B$  backgrounds or charged  $B$ -backgrounds.

- **Continuum parameterization.**

- The **Dalitz plot** treatment of continuum events is similar to the one used for  $B$  background. The continuum contribution to the likelihood (7.1) invokes the parameter  $A_{q\bar{q}}$ , multiplied by the kaon charge  $Q_K$ . It parameterizes possible direct CPV in these events and is determined by the fit.

It is the particularity of the approach adopted in this analysis that the square DP PDF for continuum events is obtained from off-resonance data using the signal region (SR), and  $m_{\text{ES}}$  sideband(SB) region where  $m_{\text{ES}} > 5.20 \text{ GeV}/c^2$ .

Since the fit does not determine the empirical shape parameters of the

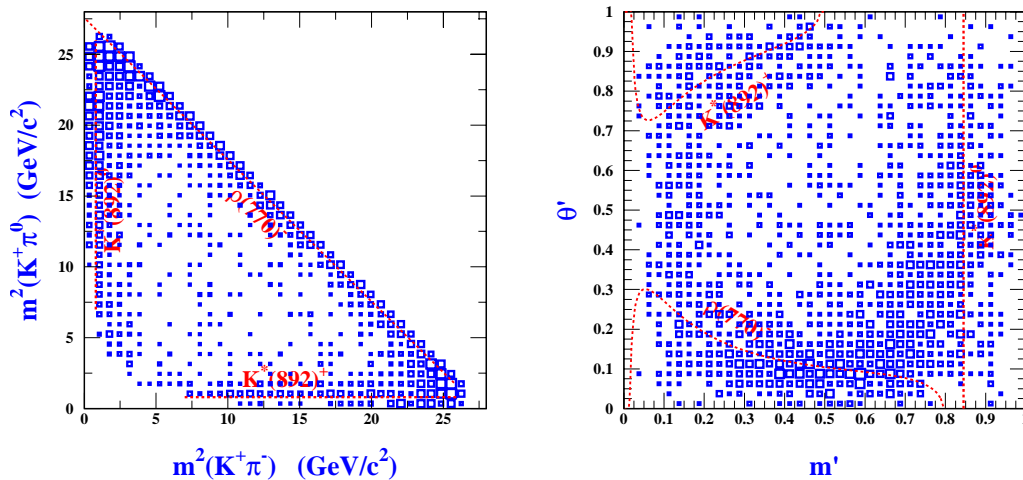


Figure 7.5: *Dalitz plot (left) and square DP (right) distributions for off-resonance events.*

PDFs simultaneously with the signal parameters, we have to worry about the validity of the SB-to-SR extrapolation. We will come back to this point in Section 11. Since continuum events are the dominant background, we also must ensure a high fidelity of the empirical shape parameterization. This has been the main motivation that led to the development of the square DP (3.22), since continuum events cluster at low invariant masses (compared to  $m_B$ ), and thus populate the kinematic borders of the DP (see Fig. 7.5).

## 7.2 Energy-Substituted Mass and Energy Difference

Due to the tight cuts on both  $m_{\text{ES}}$  and  $\Delta E'$ , correlations between these variables are small in signal and  $B$  background, with the exception being TM events (see discussion in Section 5.5 and below).

- **Signal parameterization.**

- $m_{\text{ES}}$ . The distribution of TM events is parameterized by the Crystal Ball function [73],  $\text{CB}(m_0, \sigma, \alpha, n)$ , where  $\alpha = 1.25$ ,  $n = 84.3$ ,  $\sigma = 0.0026 \text{ GeV}/c^2$ , as determined with signal MC, and the parameter  $m_0$  is determined by the fit. A slight dependence of the mass resolution on the  $\pi^0$  momentum is observed but is neglected.

SCF events are parameterized with nonparametric PDFs [74], where the  $m_{+-}^2$  dependence of the  $m_{\text{ES}}$  shape is also neglected (see left hand plot in Fig. 10.6).

- $\Delta E'$ . The distribution of TM events is parameterized by a double Gaussian function, where all five parameters depend linearly on  $m_{+-}^2$  as described in Appendix B.

Self-cross-feed events are parameterized by a broad single Gaussian, where the small  $m_{+-}^2$  dependence of the  $\Delta E'$  shape is neglected (see right hand plot in Fig. 10.6). They do not exhibit correlations between  $m_{\text{ES}}$  and  $\Delta E'$ .

- **$B$ -background parameterization.**

Both  $m_{\text{ES}}$  and  $\Delta E'$  are parameterized by two-dimensional Keys PDFs for all  $B$ -background classes.

- **Continuum-background parameterization.**

As for the  $B$  background, the  $m_{\text{ES}}$  and  $\Delta E'$  PDFs factorize for continuum background.

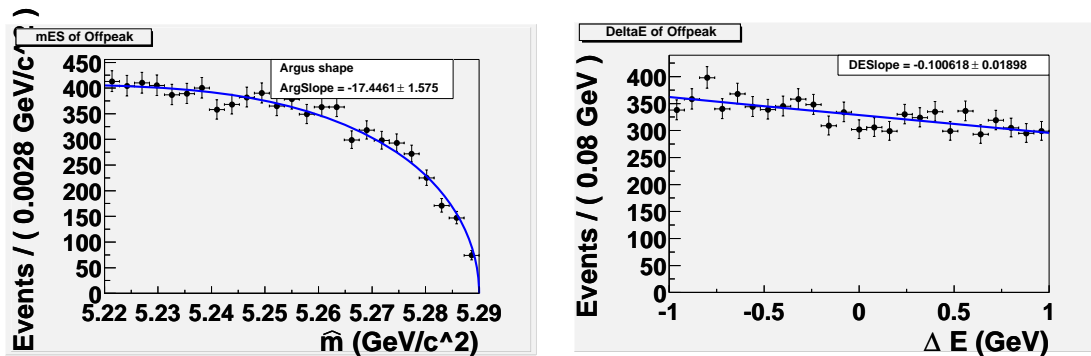


Figure 7.6: *Distribution of  $m_{\text{ES}}$  (left) and  $\Delta E'$  (right) for  $m_{\text{ES}}$ -sideband off-resonance events. The solid lines show the fit projections of the PDF models. The fit parameters are given in the text.*

- The  $m_{\text{ES}}$  PDF is parameterized with an Argus shape function [75]. The shape parameter  $\xi$  is determined simultaneously with the signal parameters by the fit. The kinematic endpoint is fixed to  $5.2897 \text{ GeV}/c^2$ , and a fit using  $m_{\text{ES}}$  sideband off-resonance events determines  $\xi = -17.4 \pm 1.6$  (see left hand plot in Fig. 7.6).
- The linear  $\Delta E \rightarrow \Delta E'$  transformation (B.1) does not alter the quasi-linear behavior of the continuum shape around the signal region. A first order polynomial is used to parameterize  $\Delta E'$  with a slope determined simultaneously by the fit. (See the right hand plot in Fig. 7.6.) The slope is found to be  $-0.10 \pm 0.02$  using  $m_{\text{ES}}$  and  $NN$  sideband off-resonance events.

## Chapter 8

# Studies Using Toy MC Experiments

Toy Monte-Carlo experiments have been carried out to check the fitter, in which events are generated in terms of discriminating variables, using Monte-Carlo sampling of the PDFs. The variables used to discriminate signal and background are  $m_{ES}$ ,  $\Delta E'$ ,  $m'$  and  $\theta'$ . The probability for a single event is the sum of the probabilities over all components. For details of the parametrization, see Sec. 7.

### 8.1 Nominal Toy Experiments

For each toy experiment, a data luminosity of  $192.3\text{fb}^{-1}$  being assumed, the toy data sample consists of 1230 signal events, 4806 continuum background, 671 neutral  $B$ -background split into 6 classes, and 473 charged  $B$ -background split into 4 classes. The numbers of events of the species are Poissonized and events are generated with the corresponding component PDFs. The yields for  $B$ -background species and the charge asymmetries for  $B$ -background due to reconstruction are fixed at MC expectations and are varied for systematics studies.

A complete list of fit parameters used in the nominal fit configuration can be found in Table 8.1 and 8.2. For signal, the fit determines a global signal yield, 11

amplitudes and 10 phases of six possibly-significant intermediate states (Table ??). Because there exists an arbitrary normalization in a Dalitz plot analysis, the amplitude for  $B^0 \rightarrow \rho^- K^+$  are fixed to 1.4, and the two phases for both  $B^0 \rightarrow \rho^- K^+$  and  $\bar{B}^0 \rightarrow \rho^+ K^-$  to 0.0. Input values of the amplitudes and the phases are obtained from a fit to data. The average SCF to signal fraction is iteratively determined with fitted amplitudes and phases from the fits to data and then fixed in the fits; it is fixed to this obtained value in toy experiments. The continuum background yield is determined simultaneously with the signal yield and is compared with the expectation estimated from off-peak and on-peak sideband data. For continuum background, the Argus slope of the  $m_{ES}$  PDF and the slope of the  $\Delta E'$  PDF are fixed to the results from a fit to data which has a relaxed selection  $m_{ES} > 5.23 GeV/c^2$ . Charmless and charmed B-background yields are fixed to the MC expectations.

A total of 500 toy experiments are performed. The distributions of the fitted parameters are shown in Fig. 8.1 to 8.7. A summary of the results from toy experiments can be found in Table 8.3 and 8.4. We observe some biases in the signal yield (an 18 events shift) and in the non-resonant amplitudes. Some pull distributions are not Gaussian-like. When the non-resonant component is removed from the toy experiments, the bias in the signal yield shrinks to only 7.7 events. It is possible that the biases come from weak constraint on the interference terms due to limited statistics.

It is also tried to choose the intermediate decay  $B^0 \rightarrow K^*(892)^+ \pi^-$  as the reference mode instead of  $B^0 \rightarrow \rho^- K^+$ . In this case, one of the amplitudes and both the phases of  $B^0 \rightarrow K^*(892)^+ \pi^-$  are fixed rather than those of  $B^0 \rightarrow \rho^- K^+$ . One key observation is that the failure rate, which is the ratio of the number of toy experiments

Table 8.1: *Parameters and their input values that are used in the toy experiments. They are allowed to vary in the fit unless stated fixed. In total, there are 28 floating parameters in the fit (see also Table 8.2).*

Parameter	Description	Value
$N_{K^+\pi^-\pi^0}$	Number of $B^0 \rightarrow K^+\pi^-\pi^0$ events	1230
$m_{B^0}$	$B^0$ mass	5.2794 GeV/c <sup>2</sup>
$\sigma_{B^0}$	$B^0$ mass resolution	0.00263 GeV/c <sup>2</sup>
$\bar{f}_{SCF}$	the average SCF fraction	12.9% ( <i>fixed</i> )
$N_{Continuum}$	Number of continuum events	4806
$A_{Continuum}$	Charge asymmetry in continuum	$-0.04 \pm 0.01$
$\xi$	Cont. Argus function slope	$-17.783$ ( <i>fixed</i> )
$\Delta E'_{p1}$	Cont. $\Delta E'$ linear term	$-0.0586$ ( <i>fixed</i> )
$N_{B^0 \rightarrow \bar{D}^0 \pi^0}$	Number of $B^0 \rightarrow \bar{D}^0 \pi^0 \rightarrow K^+\pi^-\pi^0$ events	447.3
$m_{D^0}$	the $D^0$ mass in $B^0 \rightarrow \bar{D}^0 \pi^0 \rightarrow K^+\pi^-\pi^0$	1.8645 GeV/c <sup>2</sup>
$\sigma_{D^0}$	the $D^0$ mass resolution in $B^0 \rightarrow \bar{D}^0 \pi^0$	0.007 GeV/c <sup>2</sup>

that fail to converge to the total number of toy experiments performed, goes from 7% to about 16%. This must be because of statistical effects, *e.g.*, the expected yield of  $B^0 \rightarrow K^*(892)^+\pi^-$  is less than a half of that of  $B^0 \rightarrow \rho^-K^+$ . Other intermediate states have not been experimentally established and are not used as the reference mode. In the nominal fit, the decay  $B^0 \rightarrow \rho^-K^+$  is chosen as the reference mode.

## 8.2 Adding and Omitting a Resonance

Because the total decay amplitude is not known *a priori*, there are uncertainties in assuming contributing amplitudes in the total amplitude. In principle, one can include and float all possibly contributing amplitudes. However, this is difficult for

Table 8.2: *Parameters and their input values that are used in the toy experiments. Parameters are allowed to float in the fit unless stated fixed. Continued from Table 8.1.*

Parameter	Description	Value
$A_{B^0 \rightarrow \rho^- K^+}$	Magnitude of $B^0 \rightarrow \rho^- K^+$	1.4 (fixed)
$\phi_{B^0 \rightarrow \rho^- K^+}$	phase of $B^0 \rightarrow \rho^- K^+$	0.0 (fixed)
$A_{\overline{B}^0 \rightarrow \rho^+ K^-}$	Magnitude of $\overline{B}^0 \rightarrow \rho^+ K^-$	1.4
$\phi_{\overline{B}^0 \rightarrow \rho^+ K^-}$	phase of $\overline{B}^0 \rightarrow \rho^+ K^-$	0.0 (fixed)
$A_{B^0 \rightarrow K^*(892)^+ \pi^-}$	Magnitude of $B^0 \rightarrow K^*(892)^+ \pi^-$	1.0
$\phi_{B^0 \rightarrow K^*(892)^+ \pi^-}$	phase of $B^0 \rightarrow K^*(892)^+ \pi^-$	0.0
$A_{\overline{B}^0 \rightarrow K^*(892)^- \pi^+}$	Magnitude of $\overline{B}^0 \rightarrow K^*(892)^- \pi^+$	1.0
$\phi_{\overline{B}^0 \rightarrow K^*(892)^- \pi^+}$	phase of $\overline{B}^0 \rightarrow K^*(892)^- \pi^+$	0.0
$A_{B^0 \rightarrow K^+ \pi^- \pi^0 - N.R.}$	Magnitude of $B^0 \rightarrow K^+ \pi^- \pi^0 - N.R.$	15.0
$\phi_{B^0 \rightarrow K^+ \pi^- \pi^0 - N.R.}$	phase of $B^0 \rightarrow K^+ \pi^- \pi^0 - N.R.$	0.0
$A_{\overline{B}^0 \rightarrow K^- \pi^+ \pi^0 - N.R.}$	Magnitude of $\overline{B}^0 \rightarrow K^- \pi^+ \pi^0 - N.R.$	15.0
$\phi_{\overline{B}^0 \rightarrow K^- \pi^+ \pi^0 - N.R.}$	phase of $\overline{B}^0 \rightarrow K^- \pi^+ \pi^0 - N.R.$	0.0
$A_{B^0 \rightarrow K_0^*(1430)^0 \pi^0}$	Magnitude of $B^0 \rightarrow K_0^*(1430)^0 \pi^0$	95.0
$\phi_{B^0 \rightarrow K_0^*(1430)^0 \pi^0}$	phase of $B^0 \rightarrow K_0^*(1430)^0 \pi^0$	0.0
$A_{\overline{B}^0 \rightarrow \overline{K}_0^*(1430)^0 \pi^0}$	Magnitude of $\overline{B}^0 \rightarrow \overline{K}_0^*(1430)^0 \pi^0$	95.0
$\phi_{\overline{B}^0 \rightarrow \overline{K}_0^*(1430)^0 \pi^0}$	phase of $\overline{B}^0 \rightarrow \overline{K}_0^*(1430)^0 \pi^0$	0.0
$A_{B^0 \rightarrow K_0^*(1430)^+ \pi^-}$	Magnitude of $B^0 \rightarrow K_0^*(1430)^+ \pi^-$	90.0
$\phi_{B^0 \rightarrow K_0^*(1430)^+ \pi^-}$	phase of $B^0 \rightarrow K_0^*(1430)^+ \pi^-$	0.0
$A_{\overline{B}^0 \rightarrow K_0^*(1430)^- \pi^+}$	Magnitude of $\overline{B}^0 \rightarrow K_0^*(1430)^- \pi^+$	90.0
$\phi_{\overline{B}^0 \rightarrow K_0^*(1430)^- \pi^+}$	phase of $\overline{B}^0 \rightarrow K_0^*(1430)^- \pi^+$	0.0
$A_{B^0 \rightarrow K^*(892)^0 \pi^0}$	Magnitude of $B^0 \rightarrow K^*(892)^0 \pi^0$	0.85
$\phi_{B^0 \rightarrow K^*(892)^0 \pi^0}$	phase of $B^0 \rightarrow K^*(892)^0 \pi^0$	0.0
$A_{\overline{B}^0 \rightarrow \overline{K}^*(892)^0 \pi^0}$	Magnitude of $\overline{B}^0 \rightarrow \overline{K}^*(892)^0 \pi^0$	0.85
$\phi_{\overline{B}^0 \rightarrow \overline{K}^*(892)^0 \pi^0}$	phase of $\overline{B}^0 \rightarrow \overline{K}^*(892)^0 \pi^0$	0.0

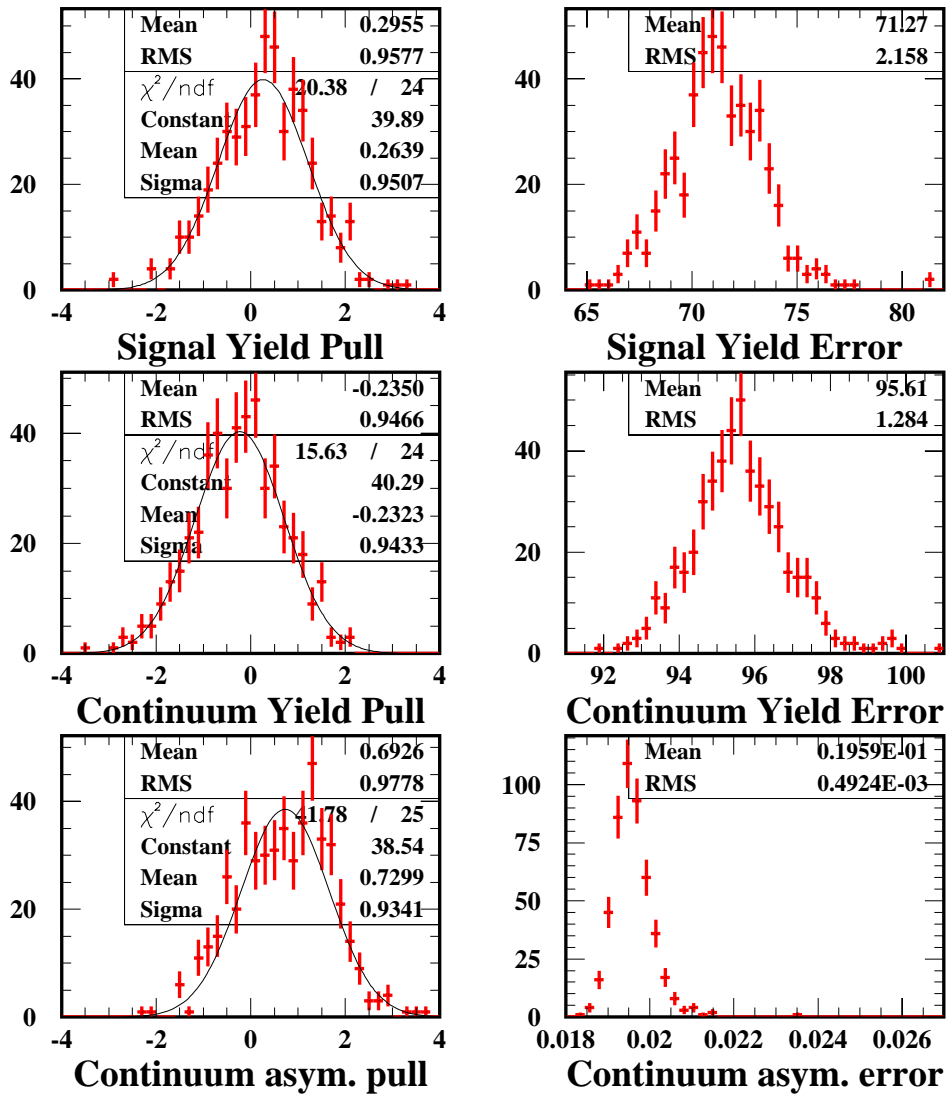


Figure 8.1: Distributions of the fitted signal yield, the continuum yield, and the continuum charge asymmetry. When applicable, the solid line indicates a Gaussian fit.

Table 8.3: *Parameters and their pulls obtained from toy experiments. Around 1% of the toy experiments fail to converge. Parameters are allowed to vary in the fit unless stated fixed. Note that the distributions are usually not Gaussian-like.  $m_{B^0}$  and  $\sigma_{B^0}$  are in units of  $\text{GeV}/c^2$ . See also Table 8.4.*

Parameter	Input Value	Avg. of Fitted	Avg. of Error	$\mu_{Pull}$	$RMS_{Pull}$
$N_{K^+\pi^-\pi^0}$	1230	1252.7	71.3	0.26	0.929
$m_{B^0}$	5.2794	5.279	0.00014	0.991	
$\sigma_{B^0}$	0.00263	0.00263	-0.05	1.020	
$\bar{f}_{SCF}$	12.5%(fixed)				
$N_{Continuum}$	4806	4787	95.6	-0.23	0.960
$A_{Continuum}$	0.0	0.0	0.025	-0.011	0.987
$\xi$	$-17.783 \pm 2.1$	(fixed)			
$\Delta E'_{p1}$	$-0.0586 \pm 0.017$	(fixed)			
$N_{B^0 \rightarrow \bar{D}^0 \pi^0}$	447.3	446.8	22.7	0.022	0.996
$m_{D^0}$	1.8645 $\text{GeV}/c^2$	1.865	0.0005	0.046	1.06
$\sigma_{D^0}$	0.007 $\text{GeV}/c^2$	0.007	0.0004	-0.105	1.04

two reasons. First, doing toy experiments with very minor modes biases the fits. Second, it takes much more CPU time to search the parameter space to constrain the parameters for the minor modes, and the fit is more likely to pick some local minima due to fluctuations. This in turn may bias the parameters for the major modes. As is common practice, for the nominal fit, several modes that are most likely to be significant are included, while crosschecks are performed by adding or omitting insignificant modes.

In the nominal fit, six modes are included: the nonresonant  $K^+\pi^-\pi^0$ ,  $\rho^-K^+$ ,  $K^*(892)^+\pi^-$ ,  $K_0^*(1430)^{+0}\pi^{-,0}$  and  $K^*(892)^0\pi^0$ . It is known that the  $K^*(892)^0\pi^0$  is

Table 8.4: Parameters and their pull obtained with 800 toy experiments. Parameters are allowed to vary in the fit unless stated fixed. Continued from Table 8.3.

Parameter	Input Value	Avg. of Fitted	Avg. of Error	$\mu_{Pull}$	$RMS_{Pull}$
$A_{B^0 \rightarrow \rho^- K^+}$	1.4 (fixed)				
$\phi_{B^0 \rightarrow \rho^- K^+}$	0.0 (fixed)				
$A_{\overline{B}^0 \rightarrow \rho^+ K^-}$	1.4	1.421	0.197	-0.02	0.952
$\phi_{\overline{B}^0 \rightarrow \rho^+ K^-}$	0.0 (fixed)				
$A_{B^0 \rightarrow K^{*(892)+} \pi^-}$	1.0	1.017	0.173	0.008	0.939
$\phi_{B^0 \rightarrow K^{*(892)+} \pi^-}$	0.0	6.66	49.9	0.157	1.142
$A_{\overline{B}^0 \rightarrow K^{*(892)-} \pi^+}$	1.0	1.007	0.173	-0.046	0.930
$\phi_{\overline{B}^0 \rightarrow K^{*(892)-} \pi^+}$	0.0	7.88	49.3	0.160	1.151
$A_{B^0 \rightarrow K^+ \pi^- \pi^0 - N.R.}$	15.0	15.9	4.39	0.231	0.894
$\phi_{B^0 \rightarrow K^+ \pi^- \pi^0 - N.R.}$	0.0	1.09	42.2	0.015	1.237
$A_{\overline{B}^0 \rightarrow K^- \pi^+ \pi^0 - N.R.}$	15.0	15.9	4.40	0.252	0.895
$\phi_{\overline{B}^0 \rightarrow K^- \pi^+ \pi^0 - N.R.}$	0.0	2.75	41.4	0.111	1.28
$A_{B^0 \rightarrow K_0^{*(1430)0} \pi^0}$	95.0	96.9	16.9	0.009	0.99
$\phi_{B^0 \rightarrow K_0^{*(1430)0} \pi^0}$	0.0	-2.43	45.3	-0.01	1.18
$A_{\overline{B}^0 \rightarrow \overline{K}_0^{*(1430)0} \pi^0}$	95.0	96.4	16.75	-0.033	0.992
$\phi_{\overline{B}^0 \rightarrow \overline{K}_0^{*(1430)0} \pi^0}$	0.0	0.59	44.2	0.066	1.22
$A_{B^0 \rightarrow K_0^{*(1430)+} \pi^-}$	90.0	93.0	16.2	0.082	0.935
$\phi_{B^0 \rightarrow K_0^{*(1430)+} \pi^-}$	0.0	3.71	51.9	0.12	1.18
$A_{\overline{B}^0 \rightarrow K_0^{*(1430)-} \pi^+}$	90.0	92.0	16.2	0.01	0.947
$\phi_{\overline{B}^0 \rightarrow K_0^{*(1430)-} \pi^+}$	0.0	4.44	51.4	0.09	1.26
$A_{B^0 \rightarrow K^{*(892)0} \pi^0}$	0.85	0.835	0.163	-0.150	0.963
$\phi_{B^0 \rightarrow K^{*(892)0} \pi^0}$	0.0	1.03	45.3	-0.02	1.11
$A_{\overline{B}^0 \rightarrow \overline{K}^{*(892)0} \pi^0}$	0.85	0.821	0.16	-0.22	0.957
$\phi_{\overline{B}^0 \rightarrow \overline{K}^{*(892)0} \pi^0}$	0.0	4.2	44.7	-0.05	1.22

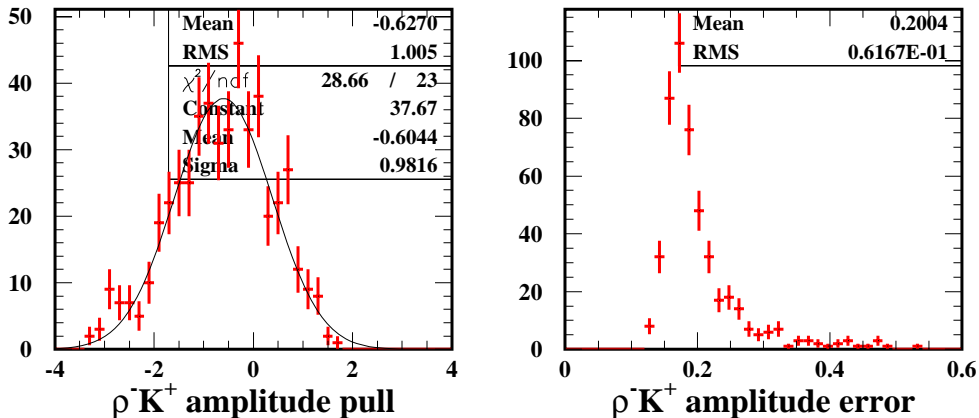


Figure 8.2: *Distributions of fitted  $\rho^+K^-$  amplitude pull (left) and the error in the amplitude from the fit (right).*

likely a minor mode. Toy experiments are performed with respect to this mode to study the effect of adding or omitting it in the fit.

The toy experiments are set up as follows: first 500 toy data sets are generated without the  $K^*(892)^0\pi^0$  mode, then two fits are performed to each toy data set, with and without  $K^*(892)^0\pi^0$ , respectively.

The first observation is that the fit with  $K^*(892)^0\pi^0$  is indeed more likely to fail, as expected. About 20% of the fits either fail to converge or hit the non-negative magnitude boundary.

The effects on the five major modes are very small, though. An interesting observation is that the log-likelihood increases by about 2 units on average when  $K^*(892)^0\pi^0$  is included in the fit, as shown in Fig. 8.8. This suggests the usual estimate of significance defined as  $\sqrt{2\log\Delta\mathcal{L}}$  may be biased. This is considered for the significance

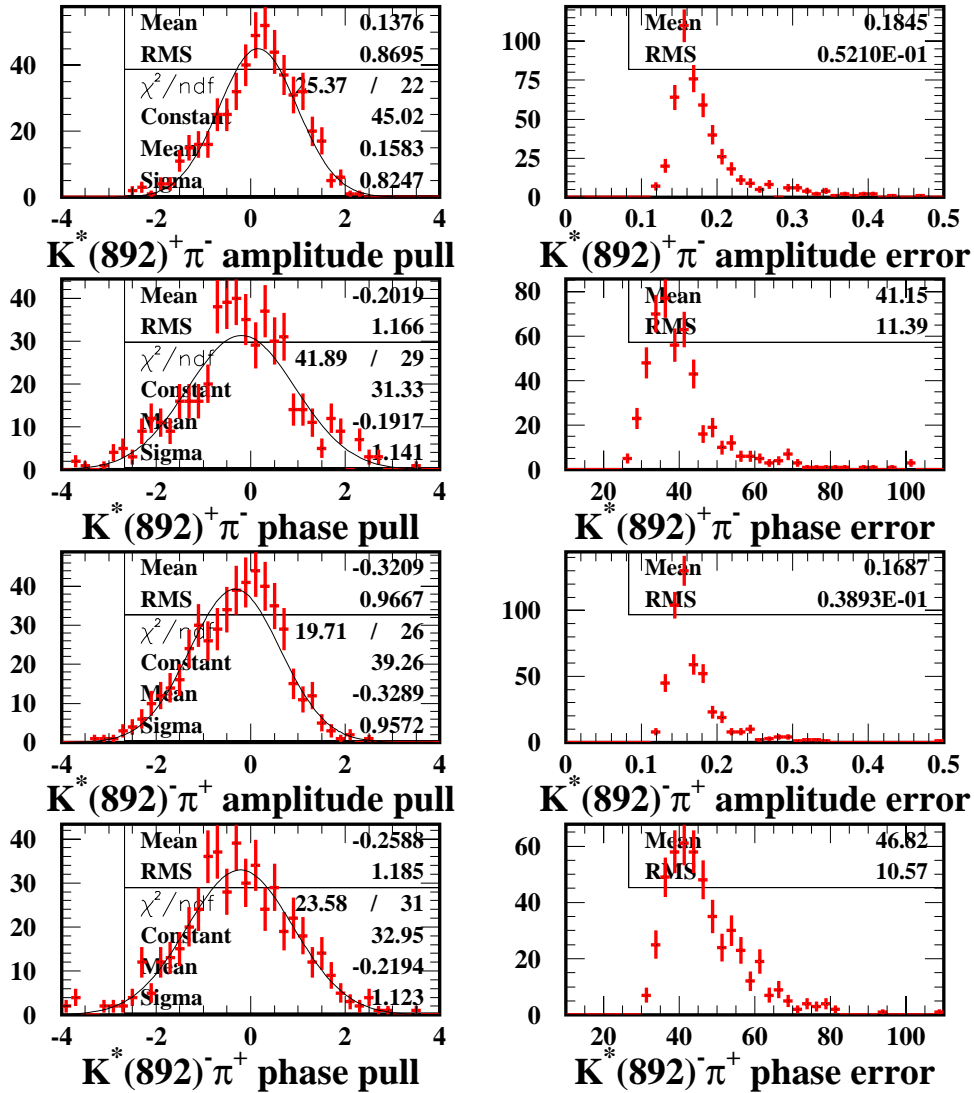
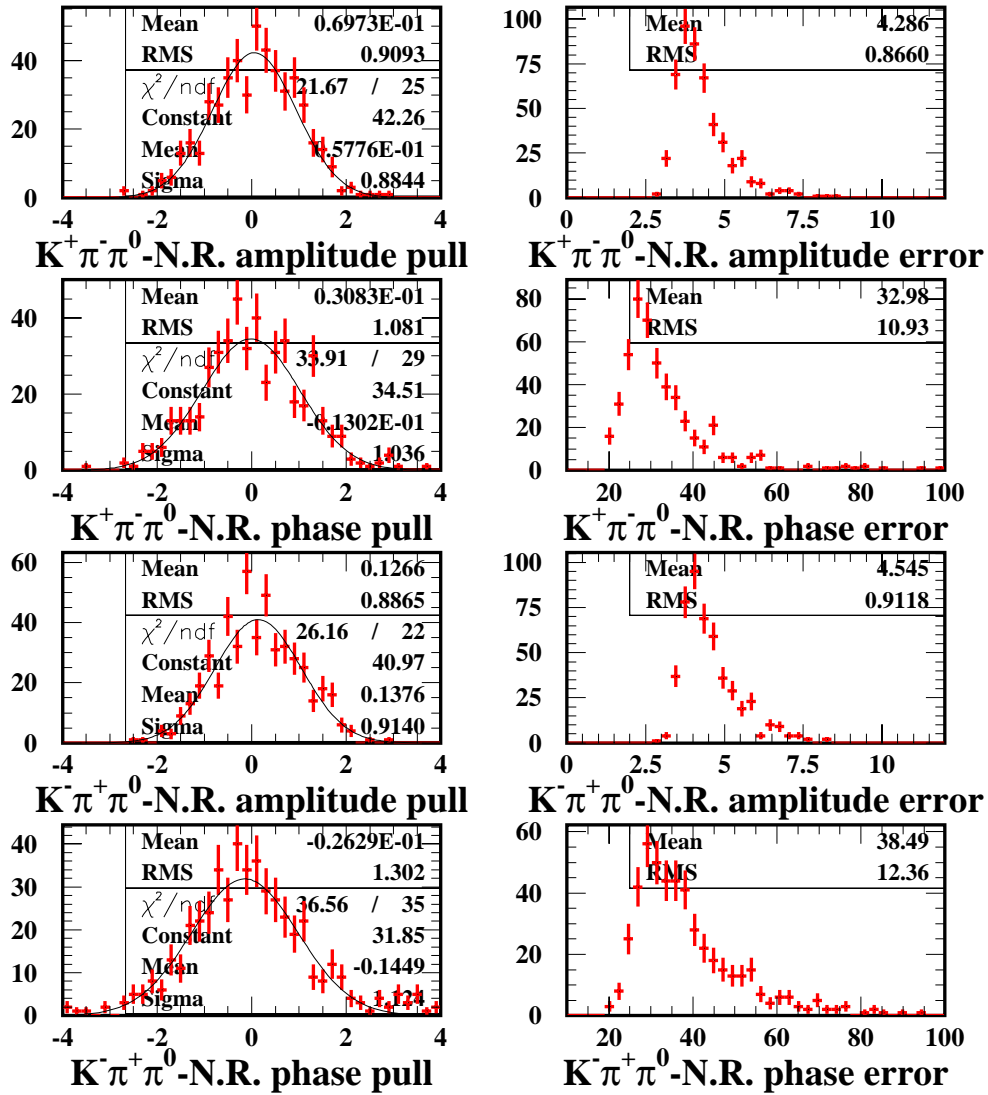


Figure 8.3: Distributions of fitted amplitudes and phases of  $K^*(892)\pi^-$

Figure 8.4: *Distributions of fitted amplitudes and phases of N.R.*

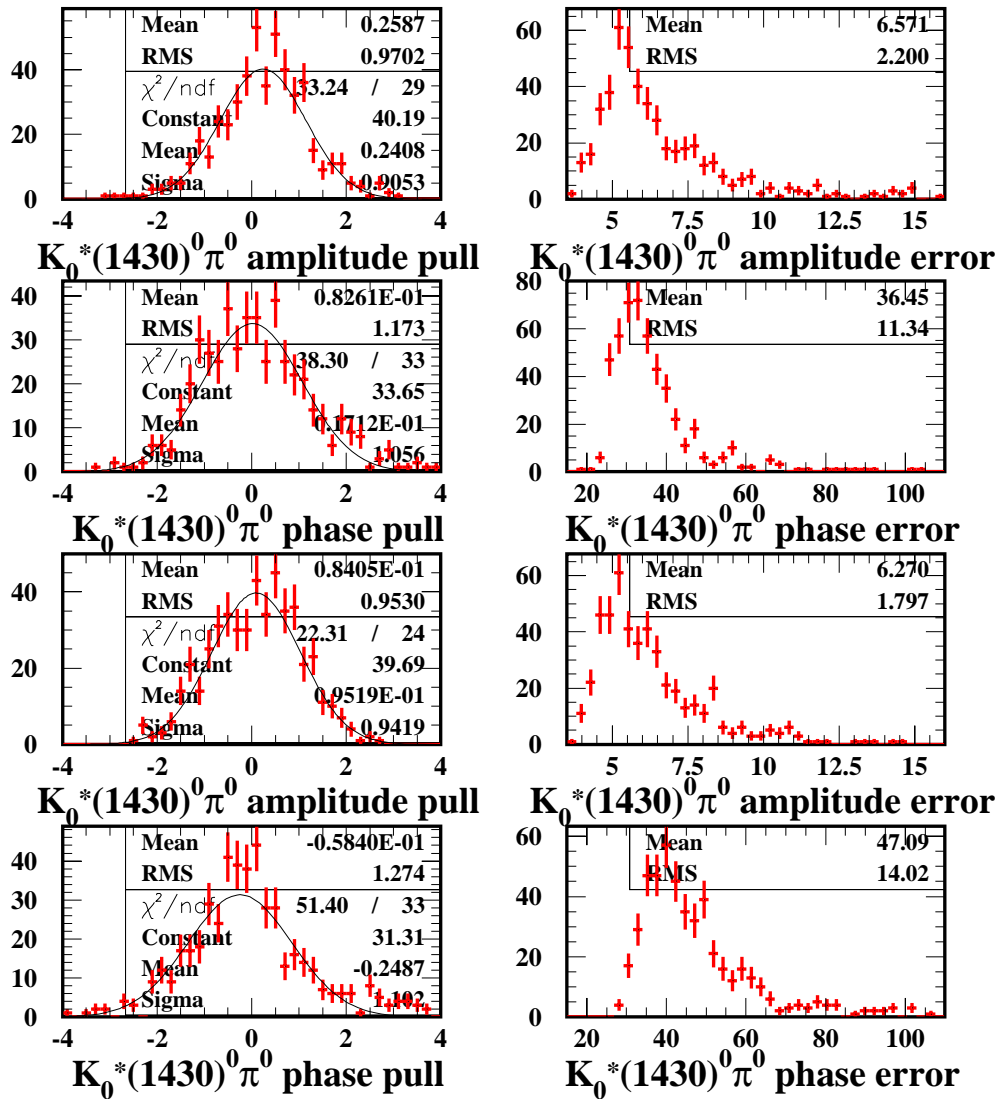


Figure 8.5: Distributions of fitted amplitudes and phases of  $K_0^*(1430)^0 \pi^0$

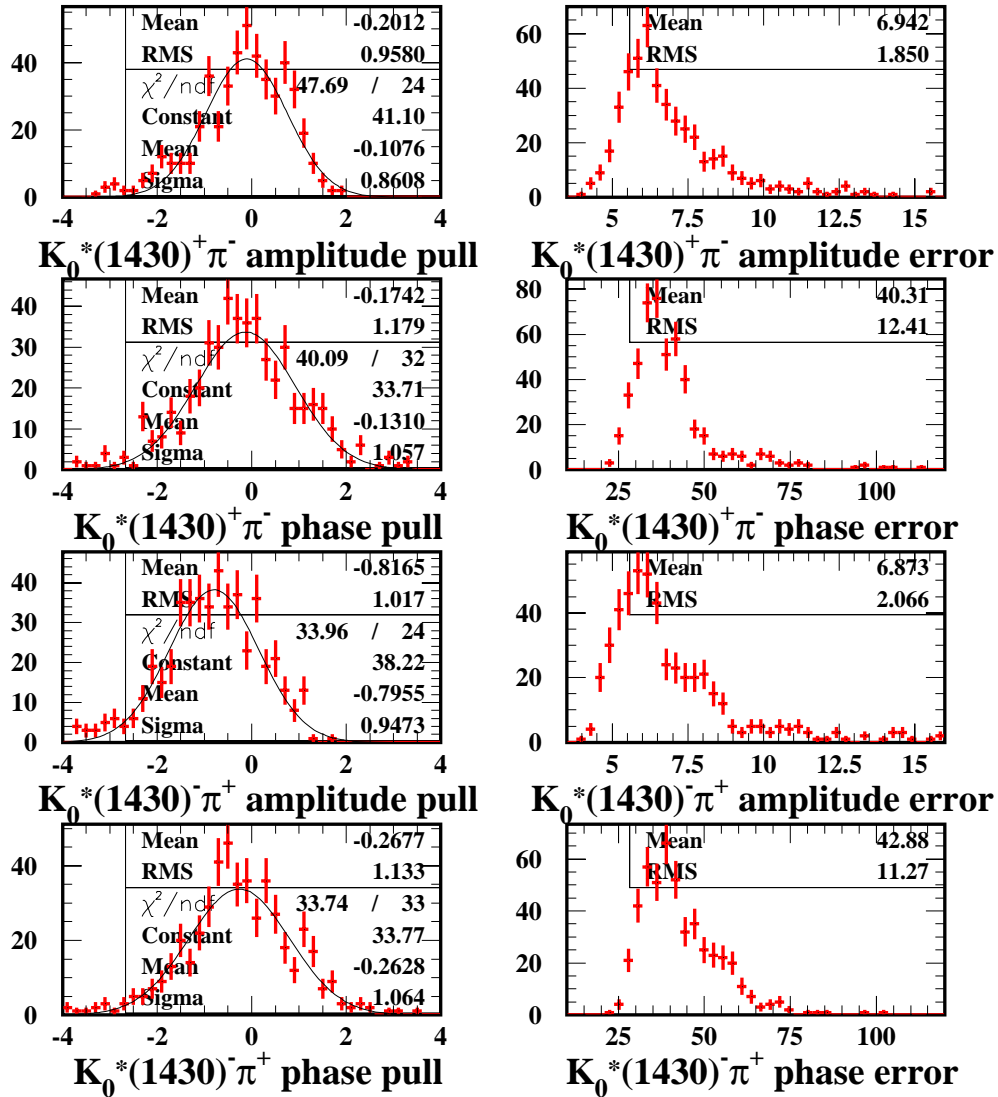


Figure 8.6: Distributions of fitted amplitudes and phases of  $K_0^*(1430)\pi^-$

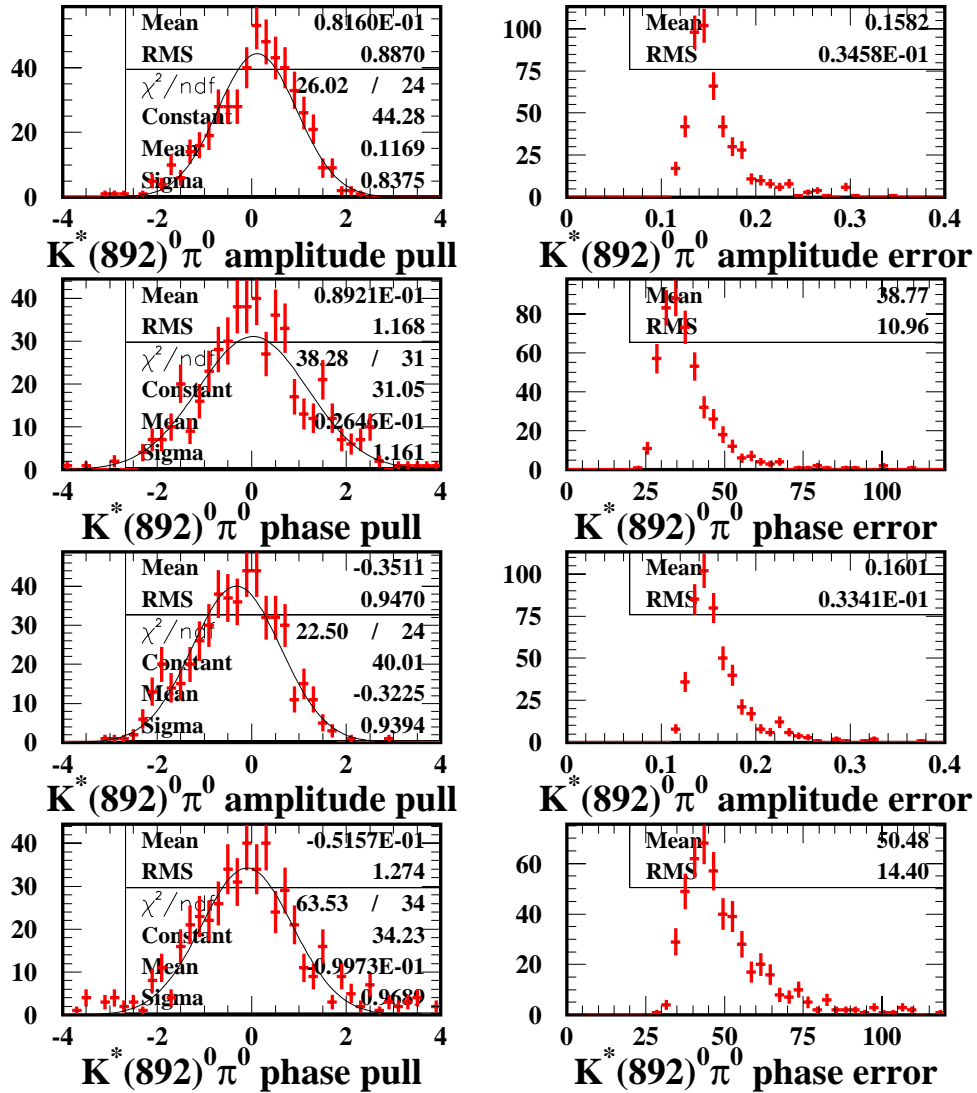


Figure 8.7: Distributions of fitted amplitudes and phases of  $K^*(892)^0\pi^0$

estimate later.

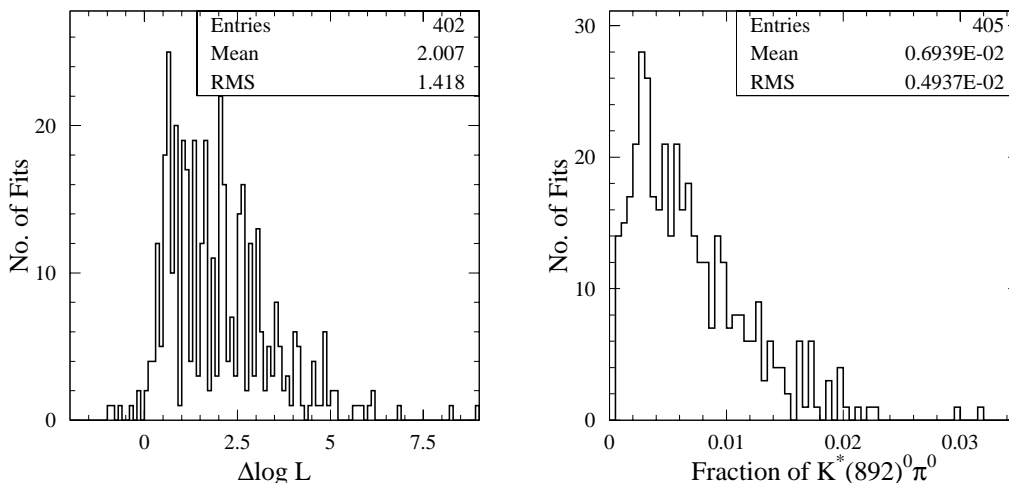


Figure 8.8: *Toy experiments that assume null  $K^*(892)^0\pi^0$  signal in generating but are fitted with and without  $K^*(892)^0\pi^0$ . Left plot: distribution of negative log-likelihood difference between toy fits with and without  $K^*(892)^0\pi^0$ . Right plot: distribution of the fitted fraction of  $K^*(892)^0\pi^0$  when it's included in the fit.*

### 8.3 Local Minima Solutions

It is noticed that local minima solutions occur for Dalitz analyses. To study this phenomenon, we randomize the initial values of the free amplitudes and phases before starting a MINUIT fit and then repeat the fit. As a result, about one third to one half of the fits end up with other solutions (local minima solutions) as shown in the likelihood distributions. Usually the secondary peak is very close to the first peak, *i.e.* within less than half a unit, as shown in Fig. 8.9. The behavior can be studied/predicted with toy experiments, as shown in the right plot in Fig. 8.9.

The fits that are under each narrow likelihood peak give almost identical results

with negligible spread. Parameters from the two peaks usually give very close values except for the phases of  $K^*(892)^0$  and  $K_0^*(1430)^0$ . This is confirmed with toy experiments. Our strategy is to choose the fits that give the largest likelihood to obtain our nominal results and consider other solutions in the systematic uncertainty unless stated otherwise.

Genetic Algorithms (GA) have been considered without much of success, the major reason being too CPU-time consuming. So we will stick to the trivial way, *i.e.*, repeat fits with randomized initial values and choose the fits under the first peak to quote the results.

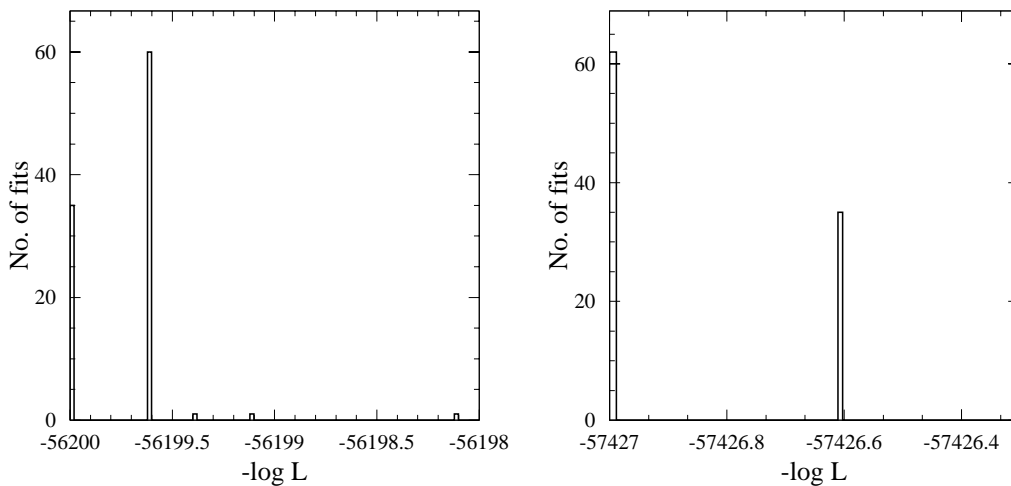


Figure 8.9: *Distributions of  $-\log\mathcal{L}$  (negative log-likelihood) with randomized initial values for fit parameters. Left: fits to the data. Right: toys experiments. Vertical axis shows number of fits. Note that the likelihood values obtained with fits to one toy data set has sizable difference from the data ones, because of Poissonization effect.*

## Chapter 9

### Validation Studies

#### 9.1 Validation of the Fit Using Offpeak

The offpeak  $m_{ES}$  sideband (2108 events with  $m_{ES} > 5.20 \text{ GeV}/c^2$ ) is used to check if we can correctly model the major continuum background. To do this, all amplitudes and phases are fixed, and  $B$ -backgrounds components are removed from the model. We also turn off the other discriminating variables ( $m_{ES}, \Delta E$ ) and use only the two DP variables. The fit to the offpeak gives  $N_{signal} = 38.0 \pm 37.2$ ,  $N_{continuum} = 2069.9 \pm 58.4$  and  $A_{continuum} = 0.029 \pm 0.022$ . No significant shifts are found. Including  $\Delta E$  in the fit helps to reduce the shifts.

#### 9.2 Validation of the Fit Using Full MC

Data-size fully simulated MC samples are used to check if the model is sufficient to describe the data. There are two issues of interest to check: first the model must correctly describe the data given its assumptions; second, the assumptions must be reasonably good, *e.g.*, residual correlations among discriminating variables must be small as assumed. Using fully simulated MC samples, one can address these two

issues in a straightforward way.

To prepare signal events (with any possible interference) for the validation study, we reweight non-resonant full MC signal events as well as non-interfering resonant full MC signal events, using coherent sum of the amplitudes of possibly contributing intermediate states. Because there is not enough fully simulated continuum background, toy continuum events are generated instead. We do the same thing for generic charmed B-backgrounds, but double check with full generic MC. Events of all components, including full MC  $B$ -backgrounds, are split into around 7 data-size samples. Nominal fits are then performed to these samples (mock data) to get distributions of fitted values of parameters floating in the fit. See Table 9.1 and 9.2 for the validation check results. We see some fitted values are off by about one sigma of statistical error.

Table 9.1: *Pulls of parameters obtained with 7 mock data experiments. Parameters are let to vary in the fit unless stated fixed otherwise. See also Table 9.2.*

Parameter	Input Value	Avg. of Fitted	R.M.S. of fitted	Avg. of Error
$N_{K^+\pi^-\pi^0}$	726	757.0	44.1	45.0
$m_{B^0}$ (GeV/ $c^2$ )	5.2794	5.280	0.00007	0.00014
$\overline{f}_{SCF}$	5.8% ( <i>fixed</i> )			
$N_{Continuum}$	2800	2774	32.5	64.3
$A_{Continuum}$	0.0	0.004	0.02	0.02
$\xi$	$-17.783 \pm 2.1$	(fixed)		
$\Delta E'_{p1}$	$-0.0586 \pm 0.017$	(fixed)		
$N_{B^0 \rightarrow \overline{D}^0 \pi^0}$	228.4	214.2	13.1	15.8
$m_{D^0}$ (GeV/ $c^2$ )	1.8645	1.865	0.0006	0.0005
$\sigma_{D^0}$	0.007 GeV/ $c^2$	0.0068	0.0006	0.0005

Table 9.2: *Pulls of parameters obtained with 7 mock data experiments. Continued from Table 9.1.*

Parameter	Input Value	Avg. of Fitted	R.M.S. of fitted	Avg. of Error
$A_{B^0 \rightarrow \rho^- K^+}$	1.4 (fixed)			
$\phi_{B^0 \rightarrow \rho^- K^+}$	0.0 (fixed)			
$A_{\overline{B}^0 \rightarrow \rho^+ K^-}$	1.4	1.37	0.14	0.23
$\phi_{\overline{B}^0 \rightarrow \rho^+ K^-}$	0.0 (fixed)			
$A_{B^0 \rightarrow K^*(892)^+ \pi^-}$	1.0	0.79	0.20	0.21
$\phi_{B^0 \rightarrow K^*(892)^+ \pi^-}$	0.0	78.9	112.3	70.3
$A_{\overline{B}^0 \rightarrow K^*(892)^- \pi^+}$	1.0	0.84	0.15	0.20
$\phi_{\overline{B}^0 \rightarrow K^*(892)^- \pi^+}$	0.0	-34.6	75.5	49.0
$A_{B^0 \rightarrow K^+ \pi^- \pi^0 - N.R.}$	29.0	31.1	3.3	6.4
$\phi_{B^0 \rightarrow K^+ \pi^- \pi^0 - N.R.}$	0.0	-10.1	49.4	29.2
$A_{\overline{B}^0 \rightarrow K^- \pi^+ \pi^0 - N.R.}$	29.0	32.4	4.1	5.8
$\phi_{\overline{B}^0 \rightarrow K^- \pi^+ \pi^0 - N.R.}$	0.0	-8.8	23.5	24.9
$A_{B^0 \rightarrow K_0^*(1430)^0 \pi^0}$	41.0	43.2	5.8	9.9
$\phi_{B^0 \rightarrow K_0^*(1430)^0 \pi^0}$	0.0	-6.4	33.6	37.2
$A_{\overline{B}^0 \rightarrow \overline{K}_0^*(1430)^0 \pi^0}$	41.0	45.4	6.7	10.0
$\phi_{\overline{B}^0 \rightarrow \overline{K}_0^*(1430)^0 \pi^0}$	0.0	-28.6	29.8	30.9
$A_{B^0 \rightarrow K_0^*(1430)^+ \pi^-}$	44.0	34.9	4.4	7.5
$\phi_{B^0 \rightarrow K_0^*(1430)^+ \pi^-}$	0.0	27.3	45.5	38.6
$A_{\overline{B}^0 \rightarrow K_0^*(1430)^- \pi^+}$	44.0	41.3	15.2	8.7
$\phi_{\overline{B}^0 \rightarrow K_0^*(1430)^- \pi^+}$	0.0	-15.9	31.6	32.4
$A_{B^0 \rightarrow K^*(892)^0 \pi^0}$	0.85	0.92	0.11	0.19
$\phi_{B^0 \rightarrow K^*(892)^0 \pi^0}$	0.0	1.07	120.8	77.5
$A_{\overline{B}^0 \rightarrow \overline{K}^*(892)^0 \pi^0}$	0.85	0.94	0.13	0.19
$\phi_{\overline{B}^0 \rightarrow \overline{K}^*(892)^0 \pi^0}$	0.0	6.1	158.4	61.4

### 9.3 Validation of Variable Shapes and Selection Cuts

In the nominal fit, signal PDF parameters are obtained from large-statistics  $B^0 \rightarrow K^+\pi^-\pi^0$  MC. This section describes validation studies performed on a sample of fully reconstructed charged  $B$  to  $K^+\pi^-\pi^+\pi^0$  decays via  $D^0$  or  $D^{*0}$  mesons. This sample is obtained from on-resonance data, using a selection similar to that discussed in Chapter 5, and is called *control sample* hereafter. Corresponding fully simulated  $B \rightarrow K^+\pi^-\pi^+\pi^0$  Monte-Carlo sample is also generated and is called *validation MC sample* hereafter.

As in the nominal selection, a cut on  $NN < 0.76$  is performed, and the efficiency of this cut is evaluated on both the control sample and the validation MC.

The control sample events with a daughter  $\pi^0$  have a non-negligible background contamination. To subtract the background, the *sPlots* technique described in Ref. [77] is used, where each event is given a statistical weight that depends on the PDFs and covariance matrix from a fit excluding the variable being plotted. A two-species (signal and background) ML fit is performed using only the  $m_{ES}$  variable, and the fit results are used to evaluate the distribution of other event shape variables.

A Crystal Ball function is used to model the PDF for signal  $m_{ES}$ , with parameters estimated from the corresponding MC sample (see Fig. 9.1 and Tab. 9.3).

### 9.4 Evaluation of the NN Selection Efficiency

Figure 9.2 show the distribution of  $m_{ES}$  on the control sample, before and after the NN cut is applied. An ARGUS function is used to model the background  $m_{ES}$

Table 9.3: *Parameters obtained from a fit to validation MC sample using  $m_{\text{ES}}$  (see also Fig. 9.1).*

SigMesAlpha	$1.404 \pm 0.009$
SigMesMean	5.2794 GeV (error negligible)
SigMesSigma	$2.628 \pm 0.007$ MeV
SigMesN	$3.7 \pm 0.1$

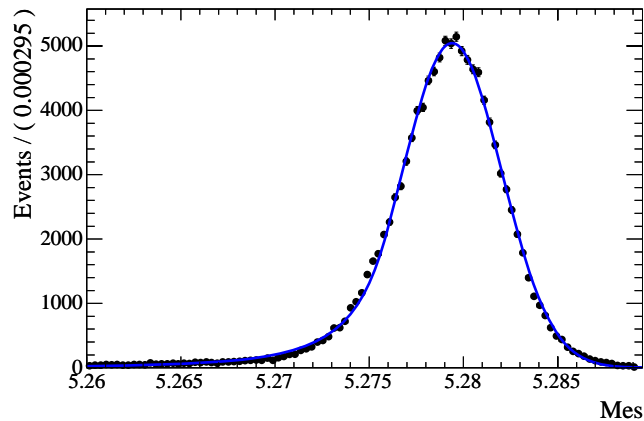


Figure 9.1: *MC distribution of  $m_{\text{ES}}$  for the validation sample, fitted to a Crystal Ball function (see also Tab. 9.3).*

distribution. A  $m_{\text{ES}} > 5.22$  cut is performed, as a deficit of background events at low values tends to push the ARGUS shape parameter towards exceedingly large values. To compensate for a well-known mean shift in the simulation, the mean value of the signal PDF is allowed to float in the fit to data, and the result is  $5.27991 \pm 0.00006$  and  $5.27997 \pm 0.00006$  GeV on the fits without and with the NN cut, respectively. Similarly, the ARGUS shape parameter is fitted to  $-19.7 \pm 4.6$  and  $-10 \pm 11$ , respectively.

The fit for no NN cut give  $3759.2 \pm 74.7$  signal events and  $2432.2 \pm 65.2$  back-

ground events. After the NN cut is applied, the fit give  $1997.0 \pm 48.6$  signal events and  $314.7 \pm 26.0$  background events. The cut efficiency is extracted from these fit results to be  $\varepsilon = (53.1 \pm 0.8)\%$ . Efficiency on the validation MC sample is estimated to be  $\varepsilon = 59.129 \pm 0.079\%$ .

On the other hand, the efficiency on signal  $B^0 \rightarrow \rho^- K^+$  MC is  $\varepsilon = (57.7 \pm 0.1)\%$ . With the large MC samples available, statistical errors on the MC efficiencies become negligible. A possible estimator of systematics on the NN cut could be the data/MC difference evaluated on the control sample. This would give a  $\sim 6\%$  systematic to the BR estimations. In order to understand this large systematic effect, further studies are described in the next 9.4.1 section.

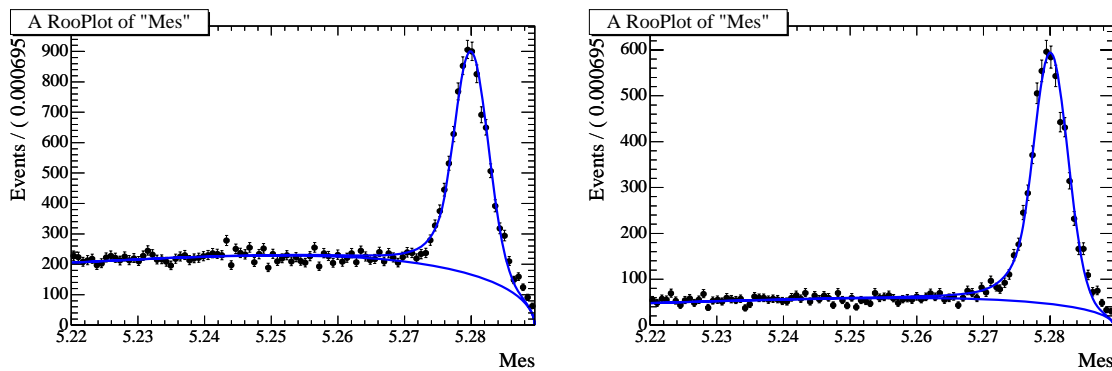


Figure 9.2: *Distribution of  $m_{ES}$  for the control sample, fitted to a Crystal Ball function for the signal component, and to an ARGUS function for the background. Figure on the left (right) shows the data sample before (after) the cut on  $NN > 0.76$ .*

#### 9.4.1 Validation of event shape PDFs

Fig. 9.3 shows the distributions of the  $L_0$ ,  $L_2$ ,  $\cos\theta_{B,z}$  and  $\cos\theta_{T_{B,z}}$  event shape variables obtained on the control sample, both for the data (background-subtracted

using the *sPlots* technique) and the MC samples. The *sPlot* fit was performed only using the  $m_{\text{ES}}$  variable, and has no *a priori* knowledge about these variables. Also shown in Fig. 9.4 are the distributions for the Fisher and  $|\cos(\theta_S)|$  variables. These variables are used neither in the selection nor in the fit, and are shown only as further validation of the NN inputs.

For the  $\cos\theta_{B,z}$  and  $\cos\theta_{T_{B,z}}$  event shape variables, good agreement is observed between data and MC. On the other hand, the variables  $L_0$  and  $L_2$  are noticeably shifted in data and MC. This effect has also been observed elsewhere[61, 76] and reflects the fact that  $L_0$  and  $L_2$  are functions of the total “detected” energy. Note that these shifts are substantively cancelled out when they are combined in a Fisher variable, which is defined as  $\mathcal{F} = 0.5 - 0.6 \times L_0 + 1.3 \times L_2$ .

Also, this suggests that the NN discriminant spoils the quasi-cancellation of data/MC mismatch in the linear Fisher, as the NN will exploit the (existing) non-linear correlations to optimise separation. Neural network MVAs can be then over-sensitive to the simulation of “detected” energy and are therefore subject to larger systematics.

#### 9.4.2 Validation of the $m_{\text{ES}}$ and $\Delta E$ PDFs

The fit to the control sample gives a mean  $m_{\text{ES}}$  value of about 1 MeV larger than the MC value. Also, the width of the gaussian term in the  $m_{\text{ES}}$  shape is slightly larger in data than in simulation, *i.e.* 2.6 MeV for MC and 2.75 MeV for data, respectively. These shifts are used as estimators of the systematic uncertainty on the  $m_{\text{ES}}$  distribution for the signal modes.

The signal  $\Delta E$  shape can also be studied with the *sPlots* technique. Figure 9.6

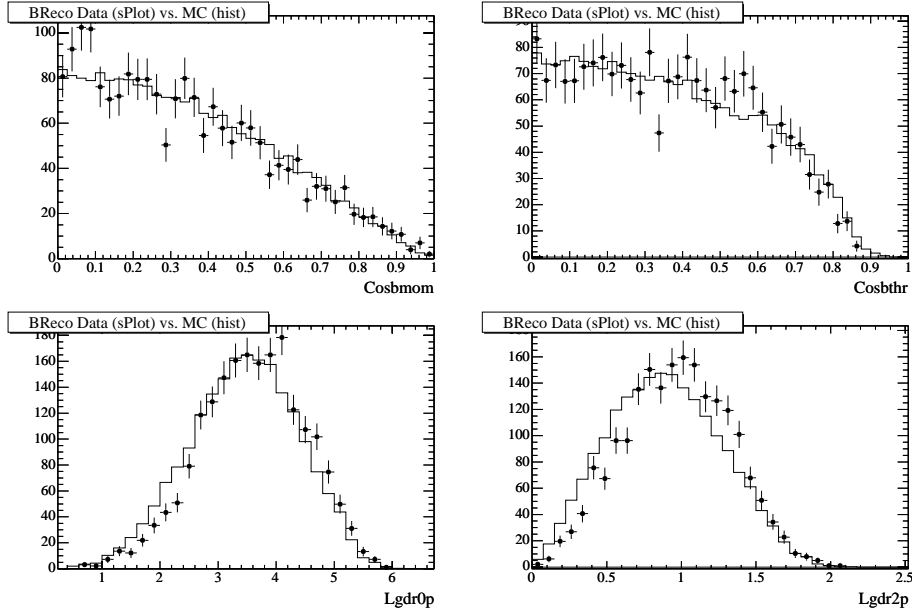


Figure 9.3: *Comparison between the control sample and the corresponding MC distributions for event shape variables. Background is subtracted to the control sample. Upper plots: Distributions for  $\cos\theta_{B,z}$  (left) and  $\cos\theta_{T_{B,z}}$  (right). Overall, good agreement is also observed. Lower plots: distributions for the monomials  $L_0$  (left) and  $L_2$  (right). As discussed in the text, background-subtracted signal and simulated MC signal do not match well.*

shows the distributions of MC signal and background-subtracted data for  $\Delta E$  and the  $\pi^0$  energy. Depending on the mode considered, our signal can have daughter  $\pi^0$ 's with harder momentum; nevertheless, since the main concern for neutral simulation relates to the low-energy EMC measurement, the control sample used will not underestimate the sensitivity to  $\pi^0$  momentum. The  $\Delta E$  distribution is both shifted towards more negative values, and broader, especially on the low-energy side. The differences will be used to estimate the analysis sensitivity to the  $\Delta E$  shape.

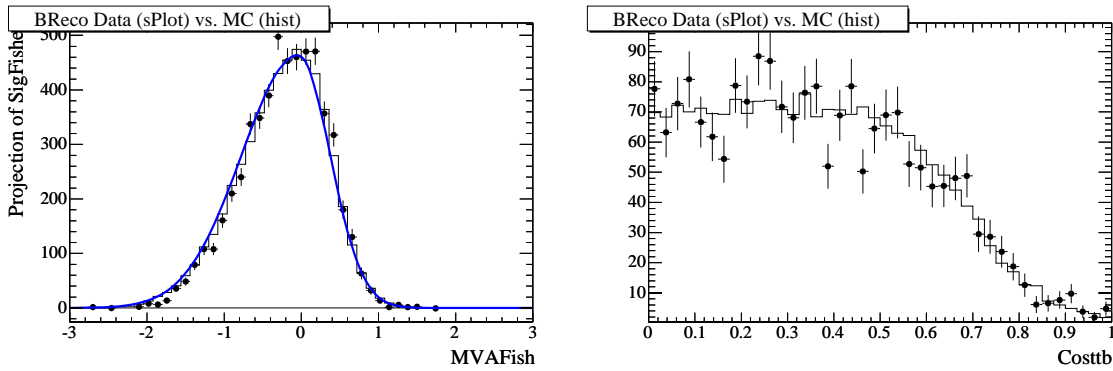


Figure 9.4: Comparison between the control sample data and MC distributions for the Fisher (left) and *costtb* (right) event shape variables. Good agreement is observed. Overlaid to the Fisher distributions is also the PDF obtained from signal MC  $B \rightarrow \pi\pi$  events.

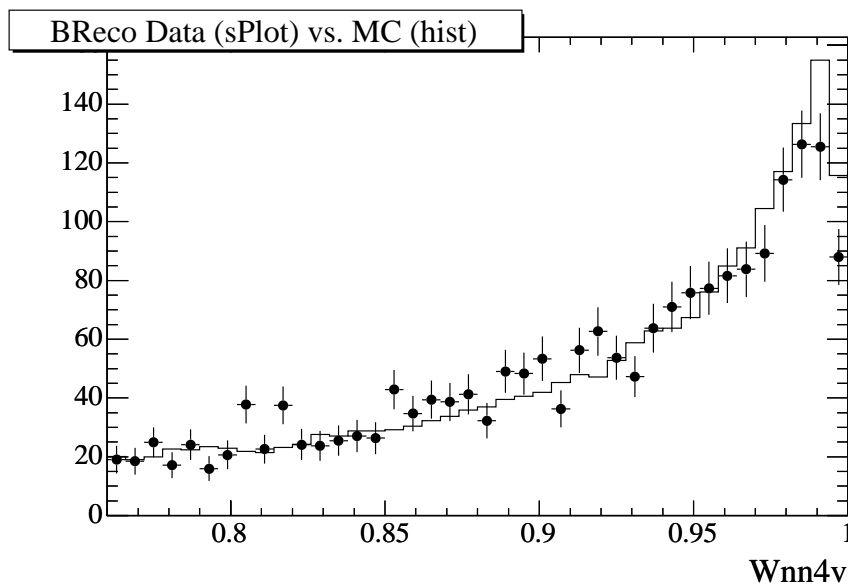


Figure 9.5: Comparison of the control sample data and MC distributions for the NN discriminant. As discussed in the text, mismatch arises from the  $L_0$  and  $L_2$  discrepancy shown in Fig. 9.3.

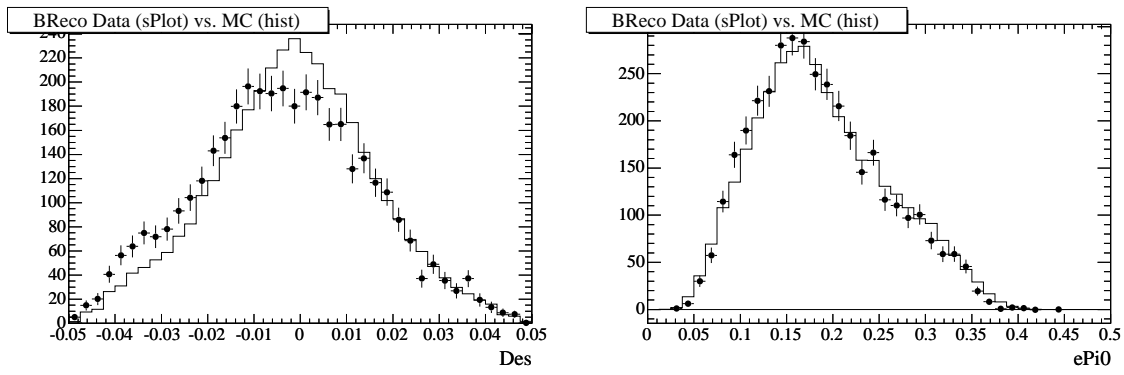


Figure 9.6: Comparison of the control sample data and MC distributions for  $\Delta E$  (left) and  $\pi^0$  energy (right).

# Chapter 10

## Results

### 10.1 Extraction of Physical Parameters

The signal model is built in terms of amplitudes and phases. The physical parameters of interest are partial yields and CP asymmetries. These parameters are non-trivial functions of the fit parameters, as can be seen on Figure 10.1, which shows the correlation matrix obtained from a fit result to a toy MC experiment, generated and fitted with the nominal six-resonance model. Initial generation values, and fitted results on this particular toy experiment are shown on Table 10.1.

In order to estimate their mean values and errors out of the fit result, we use a Lagrange Multiplier approach: call  $X_i$  ( $i = 1, N$ ) the  $N$  parameters estimated in the fit, and  $f(X_i)$  the physical parameter one is interested in (i.e. a CP asymmetry). Then one defines a  $\chi^2$  function as

$$\chi^2(f) = \sum_{i,j} (X_i - X_i^{\text{fit}}) \mathcal{C}_{ij}^{-1} (X_j - X_j^{\text{fit}}) + \left( \frac{f - F(X_i)}{\sigma_f} \right)^2, \quad (10.1)$$

where  $X_i^{\text{fit}}$  are the fitted values, and  $\mathcal{C}$  is the fit covariance matrix. The first term in the R.H.S. is such that  $\chi^2$  will be minimum (in fact, zero) when the fit parameters  $X_i$  are equal to those obtained from the fit. The second term is a penalty, defined to

Table 10.1: *Initial generation values, and fit results for a specific Toy MC experiment.*

Parameter Name	Generation Value	Fit Result
AcpCont	0	$(0.037 \pm 0.026)$
BBkgNb3	228.4	$(248.6 \pm 17.1)$
Bmass0	5.2796	$(5.27957 \pm 0.00013)$
T-k0st-1430-m	90	$(100.2 \pm 19.0)$
T-k0st-1430-p	90	$(93.3 \pm 19.7)$
T-k0st-1430z-m	95	$(77.78 \pm 12.49)$
T-k0st-1430z-p	95	$(95.39 \pm 23.35)$
T-kst-892-m	1	$(0.938 \pm 0.165)$
T-kst-892-p	1	$(0.710 \pm 0.182)$
T-kst-892z-m	0.85	$(0.916 \pm 0.153)$
T-kst-892z-p	0.85	$(1.003 \pm 0.153)$
T-non-res-m	15	$(25.11 \pm 3.82)$
T-non-res-p	15	$(12.57 \pm 4.85)$
T-rho-770-m	1.4	$(1.586 \pm 0.189)$
contNb	2800	$(2690.97 \pm 68.75)$
mD0	1.8646	$(1.8650 \pm 0.0006)$
mD0-width	0.007	$(0.00747 \pm 0.00045)$
phT-k0st-1430-m	0	$(47.3 \pm 33.7)$
phT-k0st-1430-p	0	$(109.69 \pm 50.296)$
phT-k0st-1430z-m	0	$(-34.5 \pm 29.76)$
phT-k0st-1430z-p	0	$(-80.85 \pm 57.03)$
phT-kst-892-m	0	$(38.33 \pm 32.09)$
phT-kst-892-p	0	$(121.91 \pm 54.21)$
phT-kst-892z-m	0	$(-20.05 \pm 25.52)$
phT-kst-892z-p	0	$(-38.55 \pm 63.23)$
phT-non-res-m	0	$(26.9 \pm 19.8)$
phT-non-res-p	0	$(124.07 \pm 64.36)$
sigNb	726	$(808.51 \pm 50.40)$

### Fit Result Correlation Matrix

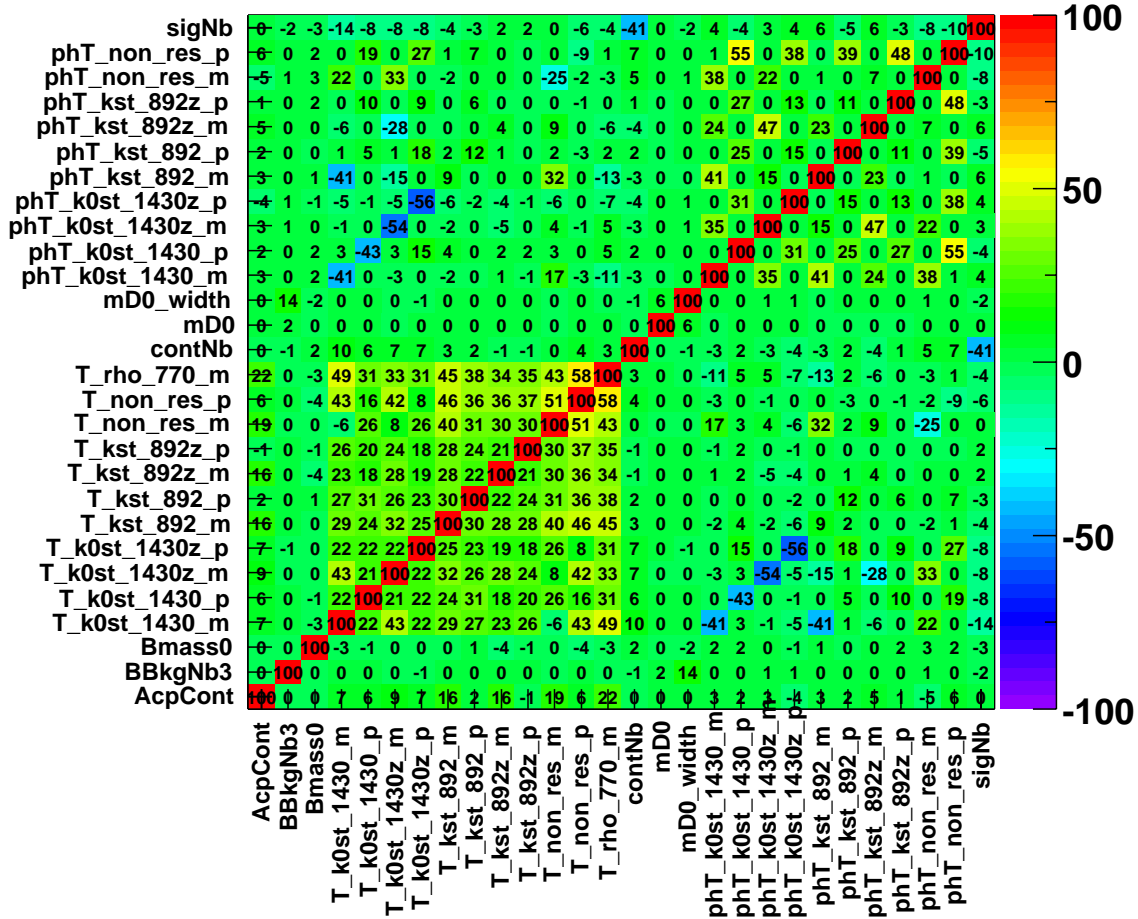


Figure 10.1: Correlation matrix for the six-resonance Toy MC fit from Table 10.1.

ensure that, for a given value of the test parameter  $f$ , the  $\chi^2$  function will be minimal for the best possible agreement between the  $f$  value and the function  $F(X_i)$ . One can then scan different values of the parameter  $f$  and fit the  $X_i$  parameters to evaluate the variation of  $\chi^2(f)$ . The “error”  $\sigma_f$  is an (arbitrary) small parameter, typically adapted to the scan step size.

The (unnormalized) likelihood distribution for the parameter  $f$  will be given by  $\mathcal{L}(f) = \exp(-\frac{1}{2}\chi^2)$ , and the confidence level by  $CL(f) = \text{PROB}(\chi^2, 1)$ . One can then

infer the  $1 - \sigma$  ( $2 - \sigma$ ) intervals by looking for the  $f$  values for which  $CL = 32\%$  ( $5\%$ ), and they take correctly into account the (potentially) non-trivial correlations between the fit parameters and the physical quantity one is interested in.

The  $\mathcal{A}_{\text{CP}}(R_i)$  parameter for a given resonance  $R_i$  is given by:

$$A_{\text{CP}}(R_i) = \frac{|\overline{T}_i|^2 - |T_i|^2}{|\overline{T}_i|^2 + |T_i|^2}, \quad (10.2)$$

where  $|T_i|$  is the fitted module of  $B^0$  decay amplitude for this resonance, and  $|\overline{T}_i|$  its counterpart for the CP-conjugated mode, with resonance  $\overline{R}_i$ . The partial fractions  $f(R_i)$  are defined as

$$f(R_i) = \frac{|T_i e^{i\theta_i} f_i|^2 + |\overline{T}_i e^{i\overline{\theta}_i} f_i|^2}{|\sum_j T_j e^{i\theta_j} f_j|^2 + |\sum_j \overline{T}_j e^{i\overline{\theta}_j} f_j|^2}, \quad (10.3)$$

where  $T_i$ ,  $\theta_i$  are the fitted amplitudes and phases for the resonance  $R_i$ , and similarly  $\overline{T}_i$  and  $\overline{\theta}_i$  correspond to the CP-conjugated mode with resonance  $\overline{R}_i$ . The  $f_i f_j^*$  terms correspond to the Dalitz phase space normalizations for the interference of resonances  $R_i$  and  $R_j$ . The inclusive branching fraction  $\mathcal{B}_{\text{Incl.}}$  and the quasi-two-body (Q2B) branching ratios  $\mathcal{B}(R_i)$  are given by

$$\mathcal{B}_{\text{Incl.}} = \frac{N_{\text{sig}}}{\overline{\varepsilon} N_{B\overline{B}}}, \quad \mathcal{B}(R_i) = \mathcal{B}_{\text{Incl.}} \times f(R_i), \quad (10.4)$$

where  $N_{\text{sig}}$  is the total signal observed in the data,  $\overline{\varepsilon}$  is the signal efficiency averaged over the Dalitz plot, and  $N_{B\overline{B}}$  is the total number of  $B\overline{B}$  pairs produced, respectively.

As an example, we use the the nominal six-resonance signal model on toy data, with input values as defined in ??, to extract the partial  $\mathcal{A}_{\text{CP}}$  asymmetries, and relative yields. Figures 10.2, 10.3 and 10.4 shows the confidence levels as functions of the  $\mathcal{A}_{\text{CP}}$  values, partial quasi-two-body (Q2B) fractions, and partial yields respectively, for the six contributions to the signal model, and Table 10.2 summarizes the obtained results.

Table 10.2:  $Q2B$  Observables calculated from fitted amplitudes and phases

$\rho^- K^+$	$\mathcal{A}_{\text{CP}}$	$(-0.123^{+0.126}_{-0.114})$
$K^*(892)^+ \pi^-$	$\mathcal{A}_{\text{CP}}$	$(-0.273^{+0.260}_{-0.249})$
$K^*(892)^0 \pi^0$	$\mathcal{A}_{\text{CP}}$	$(0.092^{+0.184}_{-0.188})$
$K_0^*(1430)^+ \pi^-$	$\mathcal{A}_{\text{CP}}$	$(-0.072^{+0.259}_{-0.254})$
$K_0^*(1430)^0 \pi^0$	$\mathcal{A}_{\text{CP}}$	$(0.203^{+0.221}_{-0.280})$
(n.r.)	$\mathcal{A}_{\text{CP}}$	$(-0.598^{+0.264}_{-0.229})$
$\rho^- K^+$	Fraction	$(0.281^{+0.032}_{0.029})$
$K^*(892)^+ \pi^-$	Fraction	$(0.074^{+0.022}_{-0.022})$
$K^*(892)^0 \pi^0$	Fraction	$(0.096^{+0.023}_{-0.021})$
$K_0^*(1430)^+ \pi^-$	Fraction	$(0.216^{+0.062}_{-0.053})$
$K_0^*(1430)^0 \pi^0$	Fraction	$(0.174^{+0.049}_{-0.045})$
(n.r.)	Fraction	$(0.121^{+0.030}_{-0.029})$
$\rho^- K^+$	Yield	$(227.0^{+30.3}_{-26.6})$
$K^*(892)^+ \pi^-$	Yield	$(59.0^{+18.6}_{-17.3})$
$K^*(892)^0 \pi^0$	Yield	$(78.9^{+17.7}_{-17.7})$
$K_0^*(1430)^+ \pi^-$	Yield	$(175.0^{+50.03}_{-42.9})$
$K_0^*(1430)^0 \pi^0$	Yield	$(141.0^{+41.7}_{-38.4})$
(n.r.)	Yield	$(97.0^{+27.5}_{-24.0})$

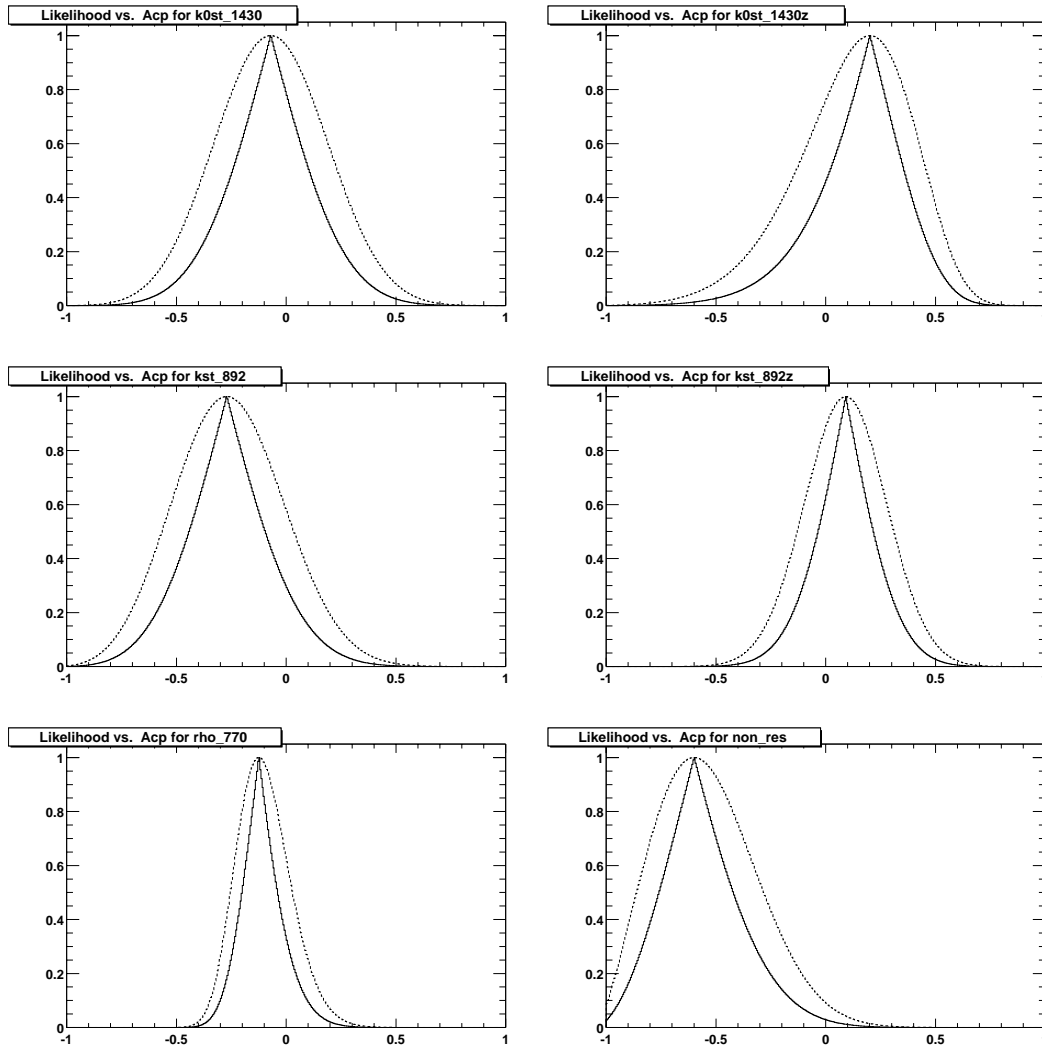


Figure 10.2: Likelihood (dashed) and Confidence Levels (solid) as functions of partial  $A_{CP}$  values for the six-resonance toy experiment described in Table. 10.1.

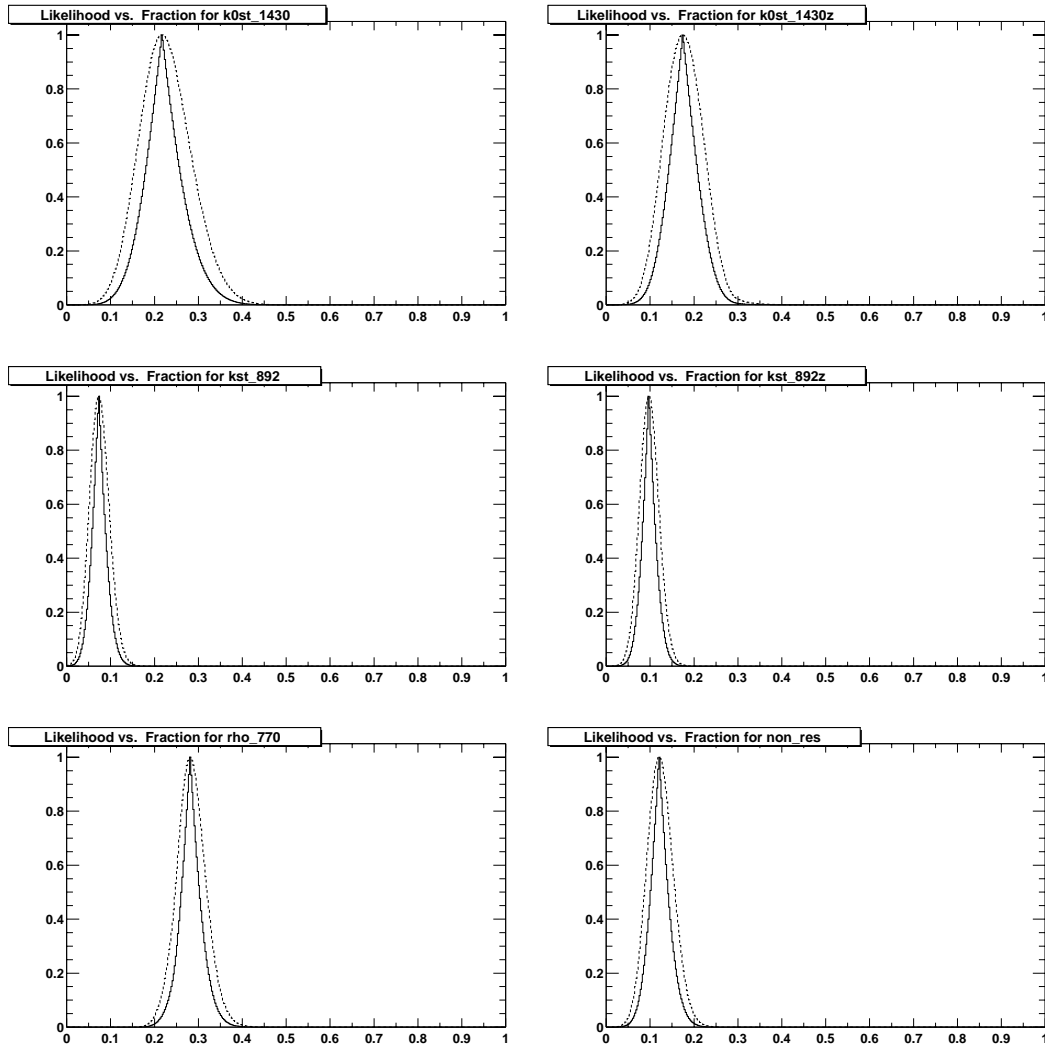


Figure 10.3: *Likelihood (dashed) and Confidence Levels (solid) as functions of partial fractions, as defined in Eq. 10.3, for the six-resonance toy experiment described in Table. 10.1.*

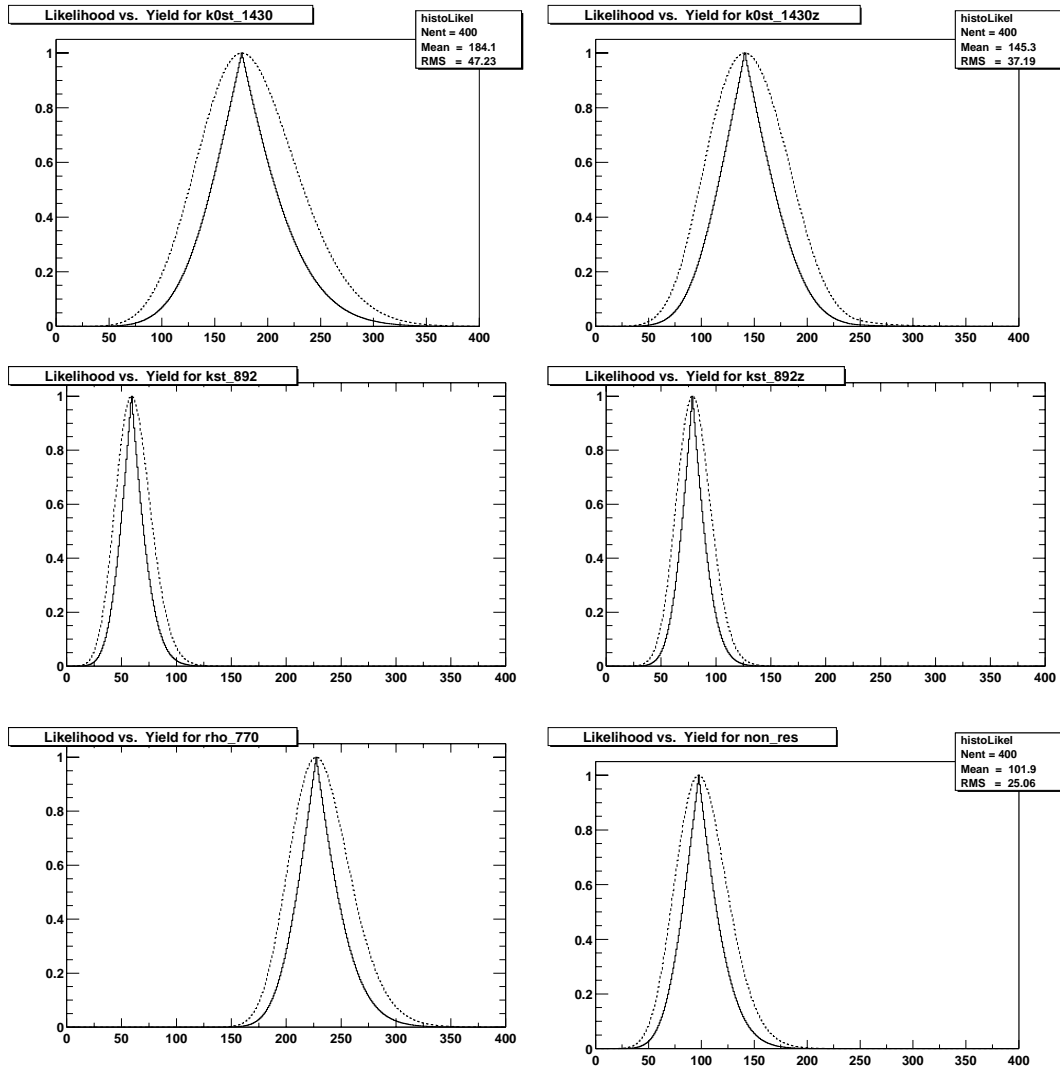


Figure 10.4: *Likelihood (dashed) and Confidence Levels (solid) as functions of partial yields, as defined in Eq. ??, for the six-resonance toy experiment described in Table. 10.1.*

## 10.2 Fit Results and Quasi-Two-Body Results

Table 10.3: *Parameters and their fitted values obtained from the nominal fit. Parameters are let to float in the fit unless stated fixed. In total, there are 29 floating parameters in the fit. See also Table 10.3 for more results.*

Parameter	Description	Value
$N_{K^+\pi^-\pi^0}$	Number of $B^0 \rightarrow K^+\pi^-\pi^0$ events	$1230.0 \pm 75.4$
$m_{B^0}$ (GeV/ $c^2$ )	$B^0$ mass	$5.27997 \pm 0.00013$
$\sigma_{B^0}$ (GeV/ $c^2$ )	$B^0$ mass resolution	$0.0030 \pm 0.0001$
$\bar{f}_{SCF}$	the average SCF fraction	12.9% ( <i>fixed</i> )
$N_{Continuum}$	Number of continuum events	$4806.0 \pm 98.8$
$A_{Continuum}$	Charge asymmetry in continuum	$-0.028 \pm 0.021$
$\xi$	Cont. Argus function slope	$-17.783 \pm 2.1$ ( <i>fixed</i> )
$\Delta E'_{p1}$	Cont. $\Delta E'$ linear term	$-0.0586 \pm 0.017$ ( <i>fixed</i> )
$N_{B^0 \rightarrow \bar{D}^0 \pi^0}$	Number of $B^0 \rightarrow \bar{D}^0 \pi^0$ events	$454.0 \pm 23.7$
$m_{D^0}$ (GeV/ $c^2$ )	the $D^0$ mass in $B^0 \rightarrow \bar{D}^0 \pi^0 \rightarrow K^+\pi^-\pi^0$	$1.8653 \pm 0.0004$
$\sigma_{D^0}$ (GeV/ $c^2$ )	the $D^0$ mass resolution in $B^0 \rightarrow \bar{D}^0 \pi^0$	$0.0075 \pm 0.0037$

The preliminary results are obtained with a nominal fit to the data sample. The fitted parameters are shown in Table 10.3 and 10.4. The quasi-two-body results calculated from Table 10.3 and 10.4 are shown in Table 10.5. The Dalitz plot for the selected  $K^+\pi^-\pi^0$  events is shown in Fig. 10.5, the left hand plot, and the  $m_{ES}$  and  $\Delta E'$  projections are shown in Fig. 10.6.

The log  $\mathcal{L}$  from the nominal fit is 56200.0, which agrees with toy MC expectation as shown in Fig. 10.5, the right hand plot. We obtain  $1230.0 \pm 74.3(stat.)$  charmless signal events and  $454.2 \pm 23.7$   $B^0 \rightarrow \bar{D}^0 \pi^0, \bar{D}^0 \rightarrow K^+\pi^-$  events from the data sample.

Table 10.4: *Parameters and their fitted values obtained from the nominal fit. Continued from Table 10.3.*

Parameter	Description	Value
$A_{B^0 \rightarrow \rho^- K^+}$	Magnitude of the amplitude of $B^0 \rightarrow \rho^- K^+$	1.4 (fixed)
$\phi_{B^0 \rightarrow \rho^- K^+}$	phase of the amplitude of $B^0 \rightarrow \rho^- K^+$	0.0 (fixed)
$A_{\bar{B}^0 \rightarrow \rho^+ K^-}$	Magnitude of the amplitude of $\bar{B}^0 \rightarrow \rho^+ K^-$	$1.60 \pm 0.24$
$\phi_{\bar{B}^0 \rightarrow \rho^+ K^-}$	phase of the amplitude of $\bar{B}^0 \rightarrow \rho^+ K^-$	0.0 (fixed)
$A_{B^0 \rightarrow K^*(892)^+ \pi^-}$	Magnitude of the amplitude of $B^0 \rightarrow K^*(892)^+ \pi^-$	$1.23 \pm 0.21$
$\phi_{B^0 \rightarrow K^*(892)^+ \pi^-}$	phase of the amplitude of $B^0 \rightarrow K^*(892)^+ \pi^-$	$138.4 \pm 35.0$
$A_{\bar{B}^0 \rightarrow K^*(892)^- \pi^+}$	Magnitude of the amplitude of $\bar{B}^0 \rightarrow K^*(892)^- \pi^+$	$0.95 \pm 0.19$
$\phi_{\bar{B}^0 \rightarrow K^*(892)^- \pi^+}$	phase of the amplitude of $\bar{B}^0 \rightarrow K^*(892)^- \pi^+$	$174.1 \pm 42.4$
$A_{B^0 \rightarrow K^+ \pi^- \pi^0 - N.R.}$	Magnitude of $B^0 \rightarrow K^+ \pi^- \pi^0 - N.R.$	$17.8 \pm 4.7$
$\phi_{B^0 \rightarrow K^+ \pi^- \pi^0 - N.R.}$	phase of the amplitude of $B^0 \rightarrow K^+ \pi^- \pi^0 - N.R.$	$54.7 \pm 28.0$
$A_{\bar{B}^0 \rightarrow K^- \pi^+ \pi^0 - N.R.}$	Magnitude of $\bar{B}^0 \rightarrow K^- \pi^+ \pi^0 - N.R.$	$15.7 \pm 4.9$
$\phi_{\bar{B}^0 \rightarrow K^- \pi^+ \pi^0 - N.R.}$	phase of the amplitude of $\bar{B}^0 \rightarrow K^- \pi^+ \pi^0 - N.R.$	$78.8 \pm 27.8$
$A_{B^0 \rightarrow K_0^*(1430)^0 \pi^0}$	Magnitude of the amplitude of $B^0 \rightarrow K_0^*(1430)^0 \pi^0$	$46.0 \pm 6.9$
$\phi_{B^0 \rightarrow K_0^*(1430)^0 \pi^0}$	phase of the amplitude of $B^0 \rightarrow K_0^*(1430)^0 \pi^0$	$46.9 \pm 40.1$
$A_{\bar{B}^0 \rightarrow \bar{K}_0^*(1430)^0 \pi^0}$	Magnitude of the amplitude of $\bar{B}^0 \rightarrow \bar{K}_0^*(1430)^0 \pi^0$	$32.1 \pm 6.0$
$\phi_{\bar{B}^0 \rightarrow \bar{K}_0^*(1430)^0 \pi^0}$	phase of the amplitude of $\bar{B}^0 \rightarrow \bar{K}_0^*(1430)^0 \pi^0$	$7.6 \pm 42.3$
$A_{B^0 \rightarrow K_0^*(1430)^+ \pi^-}$	Magnitude of the amplitude of $B^0 \rightarrow K_0^*(1430)^+ \pi^-$	$54.5 \pm 7.9$
$\phi_{B^0 \rightarrow K_0^*(1430)^+ \pi^-}$	phase of the amplitude of $B^0 \rightarrow K_0^*(1430)^+ \pi^-$	$115.1 \pm 33.5$
$A_{\bar{B}^0 \rightarrow K_0^*(1430)^- \pi^+}$	Magnitude of the amplitude of $\bar{B}^0 \rightarrow K_0^*(1430)^- \pi^+$	$50.5 \pm 7.9$
$\phi_{\bar{B}^0 \rightarrow K_0^*(1430)^- \pi^+}$	phase of the amplitude of $\bar{B}^0 \rightarrow K_0^*(1430)^- \pi^+$	$148.5 \pm 34.9$
$A_{B^0 \rightarrow K^*(892)^0 \pi^0}$	Magnitude of the amplitude of $B^0 \rightarrow K^*(892)^0 \pi^0$	$0.82 \pm 0.17$
$\phi_{B^0 \rightarrow K^*(892)^0 \pi^0}$	phase of the amplitude of $B^0 \rightarrow K^*(892)^0 \pi^0$	$-101.6 \pm 48.3$
$A_{\bar{B}^0 \rightarrow \bar{K}^*(892)^0 \pi^0}$	Magnitude of the amplitude of $\bar{B}^0 \rightarrow \bar{K}^*(892)^0 \pi^0$	$0.82 \pm 0.17$
$\phi_{\bar{B}^0 \rightarrow \bar{K}^*(892)^0 \pi^0}$	phase of the amplitude of $\bar{B}^0 \rightarrow \bar{K}^*(892)^0 \pi^0$	$-143.5 \pm 41.3$

The results obtained with the nominal model are shown in Table 10.5. The total sum of the fractions obtained with the nominal fit is 98.3%. Table 10.6 shows the results for less significant modes, which are obtained by adding in turn one mode to the nominal fit. These results are compatible with those from the nominal fit.

The inclusive charmless signal efficiency is estimated to be 16.6% with the observed Dalitz plot structure. We measure the inclusive charmless branching fraction to be:

$$\mathcal{B}(B^0 \rightarrow K^+\pi^-\pi^0) = (34.9 \pm 2.1(stat.) \pm 3.9(syst.)) \times 10^{-6}. \quad (10.5)$$

We find

$$\mathcal{B}(B^0 \rightarrow \overline{D}^0\pi^0) = (3.3 \pm 0.2(stat.) \pm 0.4(syst.)) \times 10^{-4}. \quad (10.6)$$

The signal significance for  $\mathcal{B}(B^0 \rightarrow K^*(892)^0\pi^0)$ , including statistical and systematic errors, is  $4.2\sigma$ , so this decay is evident in our data sample.

An upper limit is set on the branching fraction of the non-resonant decay,  $\mathcal{B}(B^0 \rightarrow K^+\pi^-\pi^0 \text{ non-resonant}) < 4.7 \times 10^{-6}$ , at 90% confidence level, with systematic error taken into account.

There exists another solution with  $\log \mathcal{L} = 56199.6$ . This solution gives results that are very compatible with  $\log \mathcal{L} = 56200.0$  ones, except for a two-sigma effect on the relative phases of  $B^0$  decays to  $K_0^*(1430)^0$  and  $K^*(892)^0$ . For these phases, the values corresponding to the largest likelihood value are quoted and half of the differences are included in the systematic errors.

Projection plots of the invariant mass pairs are shown in Fig. 10.7.

The changes in likelihood and the quasi-two-body observables, when a less significant intermediate state is added, are shown in Table 10.7 and 10.8. These results

show some fluctuations in the  $CP$  parameters, and more fluctuations in the fractions of the major modes. We quote the observed difference in the  $CP$  parameters as systematic error. We hesitate to quote the observed difference in the fractions as systematic error because they are not from a simultaneous fit to data and correlations between modes are thus not correctly considered. To estimate the systematic errors in the fractions due to minor modes, fits with all 12 modes included are performed. Each fit typically takes dozens of CPU hours.

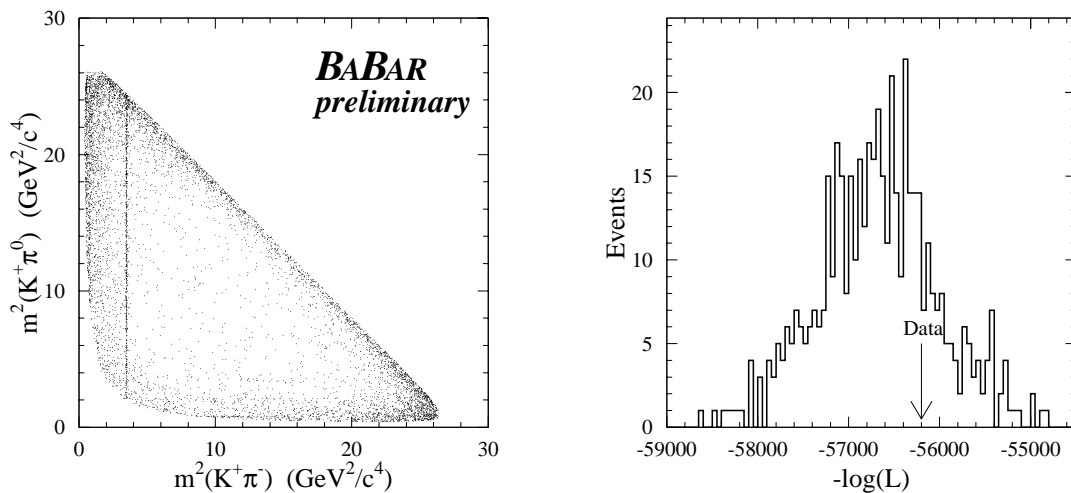


Figure 10.5: *Left: Dalitz plot for the selected  $K^+\pi^-\pi^0$  events. The visible narrow band comes mainly from the  $B^0 \rightarrow \bar{D}^0\pi^0$  decays. Right: Distribution of  $-\log \mathcal{L}$  from nominal toy experiments, in which the parameters are set to the values obtained from the nominal fit to the data. The arrow indicates the  $-\log \mathcal{L}$  from the nominal fit to the data.*

Table 10.5: Results obtained with the nominal fit to the data. The first error is statistical while the second and the third (when present) are systematic and model systematic errors as discussed in Chapter 11. The last column, the log-likelihood change, is defined as  $\Delta \log \mathcal{L} \equiv \log \mathcal{L}_{NEW} - \log \mathcal{L}_{BASE}$ , where the subscript BASE refers to the nominal fit and NEW refers to the fit with the mode being omitted from the fit. The BF's in this table are not corrected for branching fractions of the resonance decays (e.g.,  $K^*(892)^+ \rightarrow K^+ \pi^-$ ).

Mode	$f$ (%)	$\phi / \bar{\phi}$ (degree)	BF ( $\times 10^{-6}$ )	ACP	$\Delta \log \mathcal{L}$
$K^*(892)^+ \pi^-$	$10.4^{+2.1}_{-2.0}$	$138.4 \pm 35.0$ $174.1 \pm 42.4$	$4.0 \pm 0.8 \pm 0.5$	$-0.25^{+0.17}_{-0.17} \pm 0.02 \pm 0.06$	-42.5
$\rho(770)^- K^+$	$24.6^{+3.6}_{-2.9}$	0.0 (fixed) 0.0 (fixed)	$8.5 \pm 1.2 \pm 1.0$	$0.13^{+0.17}_{+0.14} \pm 0.04 \pm 0.24$	-48.3
$K_0^*(1430)^+ \pi^-$	$32.2 \pm 3.8$	$115.1 \pm 33.5$ $148.5 \pm 34.9$	$12.0 \pm 1.4 \pm 1.3$	$-0.07^{+0.12}_{-0.12} \pm 0.06 \pm 0.32$	-92.9
$K_0^*(1430)^0 \pi^0$	$22.5 \pm 4.0$	$46.9 \pm 40.4 \pm 59.1$ $7.6 \pm 42.3$	$7.5 \pm 1.3 \pm 1.7$	$-0.34^{+0.15}_{-0.15} \pm 0.07 \pm 0.37$	-71.4
$K^*(892)^0 \pi^0$	$5.8^{+1.7}_{-1.5}$	$-101.6 \pm 48.3 \pm 57.8$ $-143.5 \pm 41.3$	$2.0^{+0.6}_{-0.5} \pm 0.2$	$-0.01^{+0.22}_{+0.24} \pm 0.07 \pm 0.08$	-23.8
N.R.	$7.1^{+3.6}_{-2.9}$	$54.7 \pm 28.0$ $78.8 \pm 27.8$	$2.6 \pm 1.3 \pm 0.3$	$-0.12^{+0.37}_{+0.36} \pm 0.20 \pm 0.15$	-7.3

Table 10.6: *Results obtained for the minor intermediate states when they are added to the nominal fit in turn. Upper limits (U.L.) are set at 90% confidence level on the branching fractions, the systematic errors being considered. The last column indicates the likelihood change.*

Mode	Fraction (%)	$\mathcal{BF} (\times 10^{-6})$	U.L. ( $10^{-6}$ )	$\Delta \log \mathcal{L}$
$K_2^*(1430)^+\pi^-$	$3.5^{+2.0}_{-1.5}$	$1.3^{+0.7}_{-0.6} \pm 0.1$	2.4	7.3
$K_2^*(1430)^0\pi^0$	$1.6^{+1.7}_{-1.4}$	$0.5^{+0.5}_{-0.4} \pm 0.1$	1.2	3.4
$K^*(1680)^+\pi^-$	$3.9^{+2.3}_{-1.7}$	$1.6^{+1.0}_{-0.7} \pm 0.2$	3.0	5.8
$K^*(1680)^0\pi^0$	$0.8^{+1.4}_{-0.8}$	$0.3^{+0.5}_{-0.5} \pm 0.0$	1.4	1.6
$\rho(1450)^-K^+$	$5.0^{+2.8}_{-2.7}$	$1.7^{+1.0}_{-0.9} \pm 0.2$	3.1	3.6
$\rho(1700)^-K^+$	$2.5^{+1.8}_{-1.5}$	$0.8^{+0.6}_{-0.5} \pm 0.1$	1.6	2.1

Table 10.7: Results obtained with a fit to the data when one intermediate state is added in turn to the nominal fit.  $\delta A_{CP}$  is calculated with respect to the results obtained with the nominal fit. See also Table 10.8 for more results.

Mode	Fraction (%)	Phases ( $\phi / \bar{\phi}$ )	$\delta A_{CP}$
<b>Adding <math>K_2^*(1430)^+\pi^-</math></b>			
$K^*(892)^+\pi^-$	$10.2 \pm 2.1$	$124.2 \pm 41.5 / 154.5 \pm 42.2$	0.04
$\rho(770)^-K^+$	$22.6 \pm 3.2$	0 (fixed) / 0 (fixed)	0.05
$K_0^*(1430)^+\pi^-$	$25.0 \pm 3.8$	$97.3 \pm 40.9 / 128.6 \pm 35.8$	-0.15
$K_0^*(1430)^0\pi^0$	$24.9 \pm 4.0$	$153.7 \pm 64.1 / 75.5 \pm 42.3$	-0.20
$K_0^*(892)^0\pi^0$	$5.9 \pm 1.7$	$-141.9 \pm 65.4 / -143.7 \pm 41.1$	-0.03
$K^+\pi^-\pi^0$ N.R.	$7.3 \pm 3.6$	$96.3 \pm 46.4 / 78.9 \pm 27.3$	0.05
<b>Adding <math>K_2^*(1430)^0\pi^0</math></b>			
$K^*(892)^+\pi^-$	$10.5 \pm 2.1$	$128.6 \pm 35.9 / 164.3 \pm 43.3$	0.0
$\rho(770)^-K^+$	$23.4 \pm 3.6$	0 (fixed) / 0 (fixed)	0.01
$K_0^*(1430)^+\pi^-$	$31.6 \pm 3.8$	$104.6 \pm 34.8 / 139.7 \pm 37.3$	-0.02
$K_0^*(1430)^0\pi^0$	$18.1 \pm 4.0$	$-10.4 \pm 41.4 / 21.4 \pm 38.0$	0.07
$K_0^*(892)^0\pi^0$	$5.8 \pm 1.7$	$-156.8 \pm 42.7 / -127.0 \pm 38.3$	-0.01
$K^+\pi^-\pi^0$ N.R.	$7.1 \pm 3.6$	$42.9 \pm 31.9 / 75.0 \pm 28.7$	-0.01
<b>Adding <math>K^*(1680)^+\pi^-</math></b>			
$K^*(892)^+\pi^-$	$10.1 \pm 2.0$	$130.9 \pm 33.0 / 50.7 \pm 48.5$	0.04
$\rho(770)^-K^+$	$22.4 \pm 3.2$	0 (fixed) / 0 (fixed)	-0.10
$K_0^*(1430)^+\pi^-$	$25.4 \pm 3.6$	$114.3 \pm 31.2 / 13.1 \pm 48.9$	-0.16
$K_0^*(1430)^0\pi^0$	$22.2 \pm 4.0$	$-2.5 \pm 39.2 / 75.3 \pm 41.9$	0.30
$K_0^*(892)^0\pi^0$	$5.7 \pm 1.7$	$-146.7 \pm 40.7 / -82.1 \pm 49.2$	0.0
$K^+\pi^-\pi^0$ N.R.	$6.8 \pm 3.6$	$61.3 \pm 27.9 / 24.3 \pm 29.7$	-0.05

Table 10.8: Results obtained with a fit to the data when one intermediate state is added in turn to the nominal fit.  $\delta A_{CP}$  is calculated with respect to the results obtained with the nominal fit. Continued from Table 10.7.

Mode	Fraction (%)	Phases ( $\phi / \bar{\phi}$ )	$\delta A_{CP}$
<b>Adding <math>K^*(1680)^0\pi^0</math></b>			
$K^*(892)^+\pi^-$	$10.4 \pm 2.1$	$139.6 \pm 36.0 / 179.3 \pm 42.5$	0.01
$\rho(770)^-K^+$	$24.7 \pm 3.6$	0 (fixed) / 0 (fixed)	0.02
$K_0^*(1430)^+\pi^-$	$31.2 \pm 3.8$	$116.0 \pm 34.6 / 151.8 \pm 34.6$	-0.02
$K_0^*(1430)^0\pi^0$	$18.1 \pm 4.0$	$-10.2 \pm 43.4 / 5.0 \pm 36.1$	-0.01
$K_0^*(892)^0\pi^0$	$5.7 \pm 1.7$	$-155.2 \pm 45.5 / -138.1 \pm 38.2$	-0.02
$K^+\pi^-\pi^0$ N.R.	$6.6 \pm 3.5$	$57.5 \pm 29.5 / 87.2 \pm 29.3$	-0.05
<b>Adding <math>\rho(1450)^-K^+</math></b>			
$K^*(892)^+\pi^-$	$10.4 \pm 2.1$	$150.3 \pm 41.4 / 19.0 \pm 50.0$	0.02
$\rho(770)^-K^+$	$23.0 \pm 3.6$	0 (fixed) / 0 (fixed)	0.12
$K_0^*(1430)^+\pi^-$	$26.4 \pm 3.8$	$128.9 \pm 39.5 / -17.3 \pm 52.7$	-0.21
$K_0^*(1430)^0\pi^0$	$30.1 \pm 3.6$	$130.3 \pm 47.5 / 82.9 \pm 34.6$	-0.01
$K_0^*(892)^0\pi^0$	$5.7 \pm 1.7$	$-16.6 \pm 53.1 / -79.8 \pm 36.4$	-0.04
$K^+\pi^-\pi^0$ N.R.	$6.8 \pm 3.5$	$67.4 \pm 40.6 / 20.6 \pm 33.8$	-0.02
<b>Adding <math>\rho(1700)^-K^+</math></b>			
$K^*(892)^+\pi^-$	$10.5 \pm 2.1$	$131.4 \pm 37.4 / 78.0 \pm 67.9$	0.01
$\rho(770)^-K^+$	$23.1 \pm 3.6$	0 (fixed) / 0 (fixed)	0.17
$K_0^*(1430)^+\pi^-$	$29.0 \pm 3.6$	$111.2 \pm 35.7 / 55.0 \pm 73.3$	-0.10
$K_0^*(1430)^0\pi^0$	$29.9 \pm 4.2$	$119.5 \pm 46.4 / 73.8 \pm 42.2$	-0.06
$K_0^*(892)^0\pi^0$	$5.9 \pm 1.7$	$-26.9 \pm 51.3 / -94.2 \pm 44.9$	-0.06
$K^+\pi^-\pi^0$ N.R.	$6.8 \pm 3.6$	$53.4 \pm 37.1 / 39.2 \pm 32.7$	-0.11

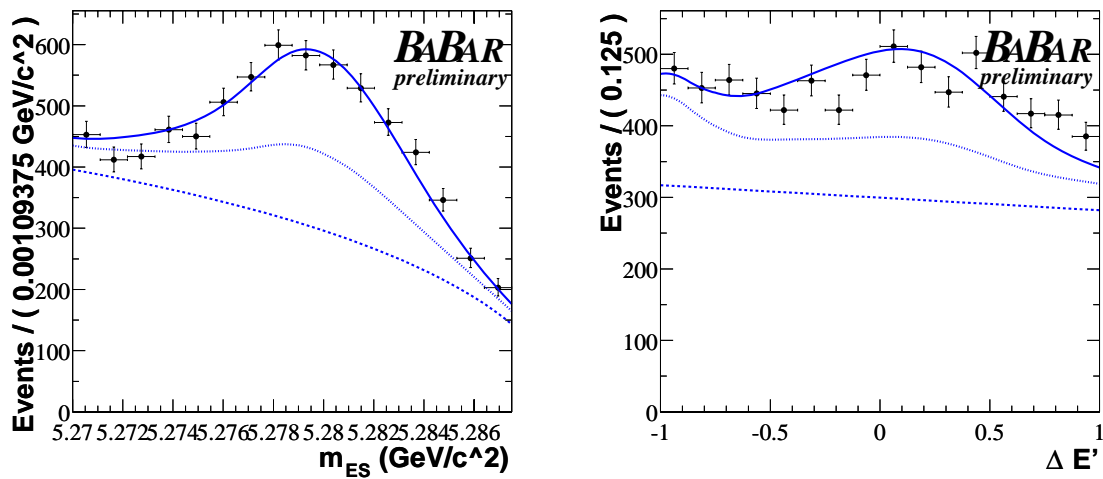


Figure 10.6:  $m_{ES}$  (left) and  $\Delta E'$  (right) projections for the selected  $K^+\pi^-\pi^0$  events. The data are the points with error bars. The fit result is the (top) solid line. The (bottom) dashed line represents the continuum background and the (middle) dotted line is the  $B$  background added on top of the continuum background. Note that the  $B$  background includes the  $B^0 \rightarrow \bar{D}^0\pi^0$ ,  $\bar{D}^0 \rightarrow K^+\pi^-$  decays.

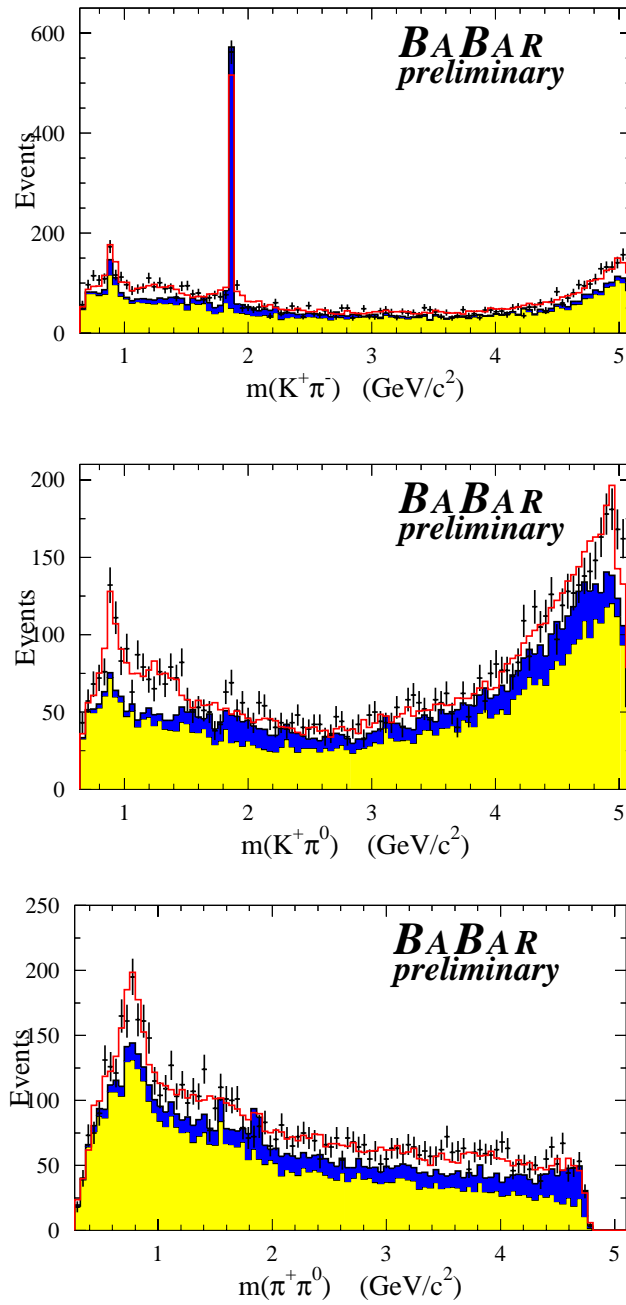


Figure 10.7: Projection plots for the mass pairs. The data are the black points with error bars (statistical only). The total fit result is the solid (red) line. The continuum background is the light shaded (yellow) and the B-background is the dark shaded (blue) added on top of the continuum background.

## Chapter 11

# Systematic Uncertainties

The systematic errors in the branching fractions and  $CP$ -violating charge asymmetries due to assumptions about the total decay dynamics are referred to as “model systematic uncertainties”. They are obtained by varying the resonance parameters within their uncertainties. Results that are obtained with the other less significant (but possibly contributing) resonances added to the nominal model contribute to the model systematic errors in the  $CP$ -violating charge asymmetries. They are dominant in the model systematic errors.

The other systematic errors in the branching fractions are obtained by adding in quadrature the systematic uncertainties in the signal yield, the systematic uncertainties in efficiencies of tracking, particle identification, and  $\pi^0$  reconstruction and finally the systematic uncertainties on the other selection cuts. The other systematic errors in the  $A_{CP}$  measurements are introduced by the uncertainties in the treatment of the  $B$ -background and by possible charge biases of the detector.

The systematic uncertainties in the signal yield are due primarily to the modeling of the signal, the  $B$ -backgrounds and the continuum in the ML fit. They are estimated by either varying the fixed parameters according to their uncertainties in the fit, or by

fitting them in the fit. The differences in the signal yield are added in quadrature and contribute to the systematic uncertainty in the signal yield. Parameters for the signal  $m_{\text{ES}}$  PDF are left to vary in the nominal fit to data. Parameters for the signal  $\Delta E'$  PDF are allowed to vary in the fit to the data to estimate the corresponding systematic uncertainty. The expected yields from the background modes are varied according to the uncertainties in the measured or estimated branching fractions. Biases observed in toy MC fits are added in quadrature and assigned as a systematic uncertainty of the fit procedure, which is referred to as the “fitting procedure” error in Table 11.1.

The basis for evaluating the systematic uncertainties on the cuts that are applied in the selection process is to study the differences in the  $m_{\text{ES}}$ ,  $\Delta E'$  and NN distributions between on-resonance data and Monte Carlo simulation. The corrections and uncertainties in the signal efficiencies are summarized in Table 11.1. Parameters for the signal  $m_{\text{ES}}$  and  $\Delta E'$  PDFs are obtained from the fit to data and are used to estimate the systematic errors due to the  $m_{\text{ES}}$  cut and the  $\Delta E'$  cut, respectively. The difference between data and Monte Carlo distributions of the NN is extracted from fully-reconstructed  $B^+ \rightarrow K^+\pi^-\pi^0\pi^+$  decays via intermediate  $D^0$  or  $D^*$  mesons, and is used to estimate the systematic error due to the NN cut.

Since  $B$  background modes may exhibit direct  $CP$  violation, the corresponding parameters ( $A_{CP}$ 's) are varied by  $\pm 0.5$  (absolute) to estimate the uncertainties.

Table 11.1 summarizes the various sources contributing to the systematic errors in the branching fractions. The dominant systematic errors are due to the neutral correction, the  $\Delta E'$  cut, and the NN cut. Table 11.2 summarizes the possible sources contributing to the systematic errors in the charge asymmetries.

Table 11.1: *Breakdown of systematic errors for the branching fraction measurements. The error from each source varies slightly for each intermediate state and the most conservative estimate is quoted.*

	Charmless yield (events)	$\overline{D}^0\pi^0$ yield (events)
Continuum $m_{ES}$ PDF	4.3	0.0
Continuum $\Delta E$ PDF	2.0	0.0
Signal $\Delta E$ PDF	50.0	12.4
$B$ backgrounds	2.7	11.2
Fitting procedure	22.7	0.0
Sub-total (relative)	55.2 ( 4.5% )	16.7 ( 3.7% )
	Efficiency and scaling systematics (relative)	
Tracking efficiency correction	1.6%	
PID for tracks	2.0%	
Neutral correction	6.4%	
$\Delta E$ cut efficiency	4.6%	
$m_{ES}$ cut efficiency	0.4%	
NN cut efficiency	6.0%	
$N(B\overline{B})$	1.1%	
Sub-total	10.3%	
Total	11.2%	10.9%

Table 11.2: *Breakdown of systematic errors for the  $A_{CP}$  measurements.*

	$K^*(892)^+$	$\rho(770)^-$	$K_0^*(1430)^+$	$K_0^*(1430)^0$	$K^*(892)^0$	N.R.
Detector bias			0.01			
$B$ backgrounds	0.02	0.04	0.06	0.07	0.07	0.20
Total	0.02	0.04	0.06	0.07	0.07	0.20

## Chapter 12

### Conclusions

Due to lack of knowledge of final state interactions in  $B \rightarrow K^+\pi^-\pi^0$  decays, this Dalitz analysis assumes uniform phase space for the non-resonant decay amplitude and utilizes parameterizations obtained from non- $B$ -meson experiments to model intermediate resonant states. Non-unique parameterizations of the decay amplitude are covered in systematic uncertainties.

A comparison with other measurements is summarized in Table 12.1.

The measured branching fraction of  $B^0 \rightarrow \bar{D}^0\pi^0$  is  $(3.3 \pm 0.2(stat.) \pm 0.4(syst.)) \times 10^{-4}$ , in good agreement with the current world average  $(2.7 \pm 0.8) \times 10^{-4}$  [3], but significantly larger than theoretical expectations based on naive factorization.

The measured branching fractions and charge asymmetries of the decay  $B^0 \rightarrow \rho(770)^-K^+$  and  $B^0 \rightarrow K^*(892)^+\pi^-$  are in agreement with the previously reported measurements [27, 28, 29].

The intermediate  $S$ -wave decays  $B^0 \rightarrow K_0^*(1430)^+\pi^-$  and  $B^0 \rightarrow K_0^*(1430)^0\pi^0$  are observed, with the LASS parameterization [41]. No significant direct  $CP$  violation are seen in these two decay modes.

Table 12.1: Comparison between measurements of branch fractions ( $\times 10^{-6}$ ) and CP-violating charge asymmetries. Results in this table are corrected for the secondary decay branching fractions except for the  $K_0^*(1430)$ 's. The BABAR previously published results on  $\rho^- K^+$  were obtained with a subset of  $81 \text{ fb}^{-1}$  of the data, and are listed in the parentheses.

	CLEO	Belle	BaBar
$\mathcal{B}(B^0 \rightarrow K^+ \pi^- \pi^0 \text{ Incl.})$	$< 40$	$36.6 \pm 4.2 \pm 3.0$	$34.9 \pm 2.1 \pm 3.9$
$A_{\text{CP}}(B^0 \rightarrow K^+ \pi^- \pi^0 \text{ Incl.})$	-	$0.07 \pm 0.11 \pm 0.01$	-
$\mathcal{B}(B^0 \rightarrow K^*(892)^+ \pi^-)$	$16 \pm 6 \pm 2$	$14.8 \pm 4.6 \pm 1.5 \pm 2.4$	$12.0 \pm 2.4 \pm 1.5$
$A_{\text{CP}}(B^0 \rightarrow K^*(892)^+ \pi^-)$	$0.26^{+0.33+0.19}_{-0.34-0.08}$	-	$-0.25 \pm 0.17 \pm 0.02 \pm 0.06$
$\mathcal{B}(B^0 \rightarrow K^*(892)^0 \pi^0)$	$< 3.6$	$< 3.5$	$3.0 \pm 0.9 \pm 0.8$
$A_{\text{CP}}(B^0 \rightarrow K^*(892)^0 \pi^0)$	-	-	$-0.01^{+0.24}_{-0.22} \pm 0.07 \pm 0.08$
$\mathcal{B}(B^0 \rightarrow \rho(770)^- K^+)$	$16 \pm 8 \pm 3$	$15.1 \pm 3.4 \pm 1.5 \pm 2.1$	$8.5 \pm 1.2 \pm 1.0$ ( $7.3 \pm 1.3 \pm 1.3$ )
$A_{\text{CP}}(B^0 \rightarrow \rho(770)^- K^+)$	-	$0.22^{+0.22+0.06}_{-0.23-0.02}$	$0.13^{+0.14}_{-0.17} \pm 0.04 \pm 0.24$ ( $0.18 \pm 0.12 \pm 0.02$ )
$\mathcal{B}(B^0 \rightarrow K_0^*(1430)^0 \pi^0)$	-	$6.1^{+1.6+0.5}_{-1.5-0.6}$	$7.5 \pm 1.3 \pm 1.7$
$A_{\text{CP}}(B^0 \rightarrow K_0^*(1430)^0 \pi^0)$	-	-	$-0.34 \pm 0.15 \pm 0.07 \pm 0.37$
$\mathcal{B}(B^0 \rightarrow K_0^*(1430)^+ \pi^-)$	-	$5.1 \pm 1.5^{+0.6}_{-0.7}$	$12.0 \pm 1.4 \pm 1.3$
$A_{\text{CP}}(B^0 \rightarrow K_0^*(1430)^+ \pi^-)$	-	-	$-0.07 \pm 0.12 \pm 0.06 \pm 0.32$
$\mathcal{B}(B^0 \rightarrow K^+ \pi^- \pi^0 \text{ N.R.})$	-	$< 9.4$	$< 4.7$

Evidence of  $B^0 \rightarrow K^*(892)^0 \pi^0$  decay is observed for the first time with a branching fraction in agreement with the reported upper limit [29].

The non-resonant decay is measured to be sizable, but because its significance is marginal, an upper limit is set on the branching fraction at 90% confidence level. Upper limits are also set on the branching fractions of the other six less significant intermediate states.

For the intermediate decays that have been theoretically calculated with QCD factorization approaches, the results are consistent with the predictions (Table 1.1), given the large uncertainties in the predictions.

# Appendix A

## Formulae

We provide a compendium of useful formulae for the Dalitz analysis.

### A.1 Kinematic Conversions

Given is  $m'$ ,  $\theta'$ . We obtain from Eqs. (3.23)

$$m_{+-} = \frac{1}{2} (1 + \cos(\pi m')) (m_{+-}[\text{max}] - m_{+-}[\text{min}]) + m_{+-}[\text{min}] , \quad (\text{A.1})$$

$$\cos \theta_{+-} = \cos(\pi \theta') , \quad (\text{A.2})$$

so that the nominal DP variables  $s_{+0}$  and  $s_{-0}$  are obtained as follows

$$s_{-0} = \frac{1}{2} \left( m_{B^0}^2 + m_{K^+}^2 + m_{\pi^-}^2 + m_{\pi^0}^2 - m_{+-}^2 \right) - 2 \cos \theta_{+-} \left[ -m_{\pi^+}^2 + \frac{m_{+-}^2}{4} \right]^{1/2} \left[ -m_{\pi^0}^2 + \left( \frac{-m_{B^0}^2 + m_{\pi^0}^2 + m_{+-}^2}{2m_{+-}} \right)^2 \right]^{1/2} \quad (\text{A.3})$$

$$s_{+0} = m_{B^0}^2 + m_{K^+}^2 + m_{\pi^-}^2 + m_{\pi^0}^2 - m_{+-}^2 - s_{-0} . \quad (\text{A.4})$$

## Appendix B

### Determine the signal $\Delta E$ distribution

The treatment of signal  $\Delta E$  has been described in the main text. In this appendix, the technical procedure is discussed.

Signal  $\Delta E$  is described by the a double Gaussian shape that depends on the  $m_{+-}^2$  linearly on the Dalitz plot, as shown in Eq. B.1 and B.2.

$$\mathcal{P}(\Delta E') = f_{core} \frac{1}{\sqrt{2\pi}\sigma_{core}} e^{-\frac{(\Delta E' - \mu_{core})^2}{2\sigma_{core}^2}} + (1 - f_{core}) \frac{1}{\sqrt{2\pi}\sigma_{tail}} e^{-\frac{(\Delta E' - \mu_{tail})^2}{2\sigma_{tail}^2}}, \quad (\text{B.1})$$

where,

$$\begin{aligned} f_{core} &= f_{c,0} + b_{f,c} m_{+-}^2 \\ \mu_{core} &= \mu_{c,0} + b_{\mu,c} m_{+-}^2 \\ \sigma_{core} &= \sigma_{c,0} + b_{\sigma,c} m_{+-}^2 \\ \mu_{tail} &= \mu_{t,0} + b_{\mu,t} m_{+-}^2 \\ \sigma_{tail} &= \sigma_{t,0} + b_{\sigma,t} m_{+-}^2 . \end{aligned} \quad (\text{B.2})$$

The following parameters need to be determined:

- $\sigma_{c,0}$  The width of the core Gaussian extrapolated to  $m_{+-}^2 = 0$

- $\mu_{c,0}$  The mean of the core Gaussian extrapolated to  $m_{+-}^2 = 0$
- $\sigma_{t,0}$  The width of the tail Gaussian extrapolated to  $m_{+-}^2 = 0$
- $\mu_{t,0}$  The mean of the tail Gaussian extrapolated to  $m_{+-}^2 = 0$
- $f_{c,0}$  The fraction of the core Gaussian extrapolated to  $m_{+-}^2 = 0$
- $b_{\sigma,c}$  The slope of the core width
- $b_{\mu,c}$  The slope of the core mean
- $b_{\sigma,t}$  The slope of the tail width
- $b_{\mu,t}$  The slope of the tail mean
- $b_{f,c}$  The slope of the core fraction

It is worthwhile to point out that the linear dependency on the  $m_{+-}^2$  is a crude approximation. In reality, the  $\Delta E$  shape is a complicated function of the both Dalitz plot variables. It is clearly seen with high statistics non-resonance Monte Carlo. Therefore, the  $\Delta E$  parameters determined from Monte Carlo slightly depend on which decay mode of signal Monte Carlo to use. We use all available signal Monte Carlo to determine the  $\Delta E$  shape. The determination of the above parameters is not unique. We use the following approach where the linear dependency is more clear.

- Monte Carlo sample is split into  $m_{+-}^2$  bin. A double Gaussian fit is performed in each bin. Two examples are given in Fig. B.1. The left plot shows that it is almost sufficient to use a single Gaussian to represent  $\Delta E$  at the high  $m_{+-}^2$  region of the Dalitz plot, so we get high correlation between the fitted parameters when

a double gaussian fit is performed. The right plot shows the events in the small  $m_{+-}^2$  region and, obviously, we must use more than one Gaussian in representing the shape due to the presense of hard  $\pi^0$ 's.

- For the five parameters that describe the double Gaussian, we perform linear fit as a function of  $m_{+-}^2$ . They are shown in Fig. B.3 and Fig. B.2.

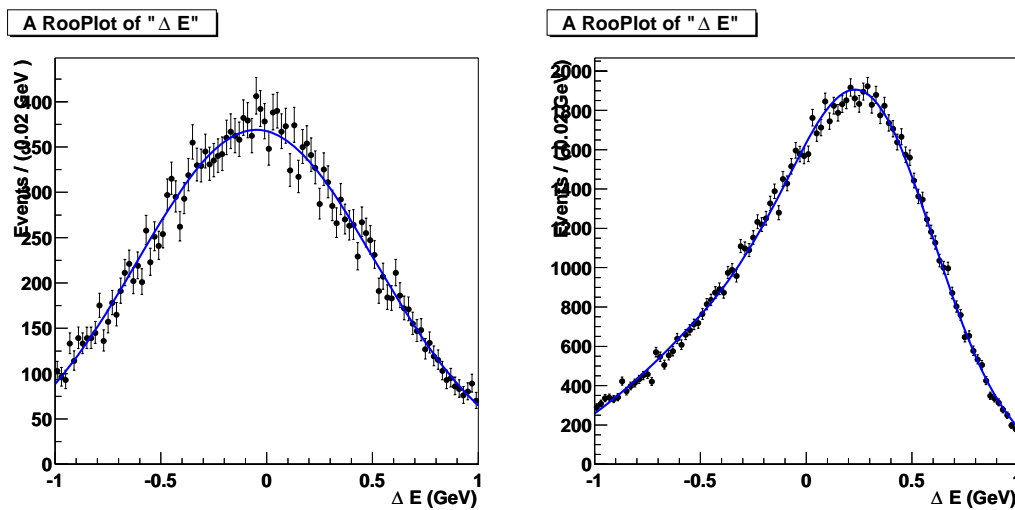


Figure B.1: *Single Gaussian parametrization for  $\Delta E'$  for events at large  $m_{+-}^2$  (left plot) and double Gaussian parametrization for events at small  $m_{+-}^2$  (right plot) from signal Monte Carlo.*

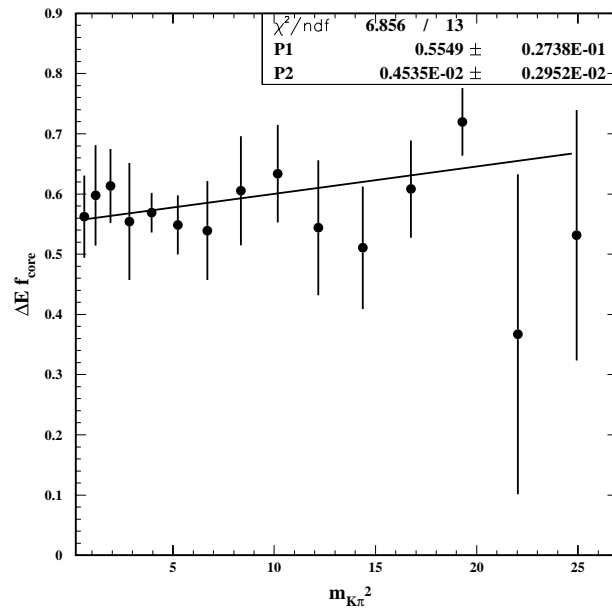


Figure B.2: *Dalitz plot dependence of fraction of the core Gaussian of the signal  $\Delta E$  distribution.*

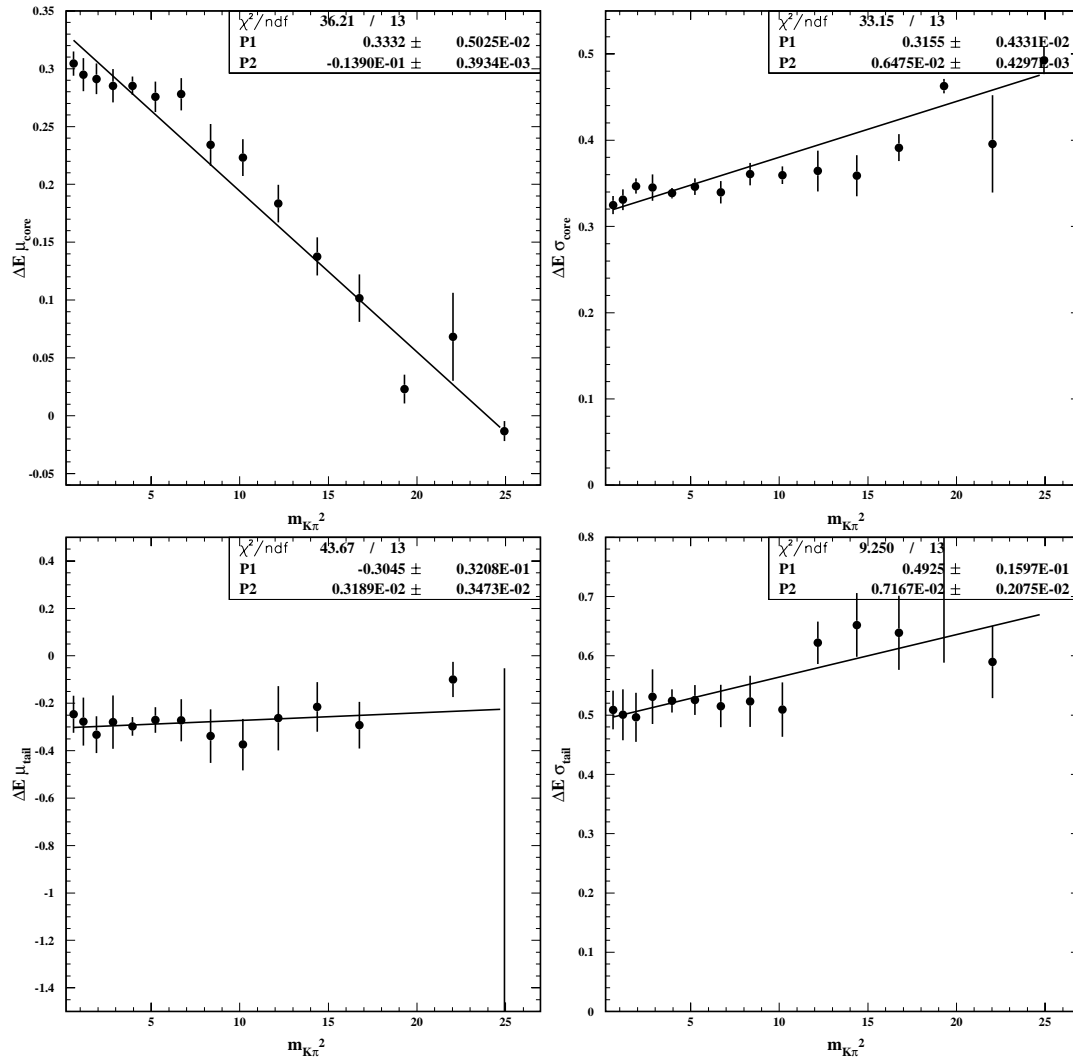


Figure B.3: *Dalitz plot dependence of Gaussian parameters of the signal  $\Delta E$  distribution.*

## Bibliography

- [1] J.H. Christenson *et al.*, *Phys. Rev. Lett.* **13**, 138 (1964).
- [2] M. Kobayashi and T. Maskawa, *Prog. Theor. Phys.* **49**, 652 (1973).
- [3] Particle Data Group, S. Eidelman *et al.*, *Phys. Lett.* **B 592**, (2004).
- [4] *BABAR* Collaboration, “*The BABAR Physics Book*”, (P. Harrison and H. Quinn eds.) (2002)
- [5] *BABAR* Collaboration, B. Aubert *et al.*, *Phys. Rev. Lett.* **93**, 131801 (2004).
- [6] Belle Collaboration, K. Abe *et al.*, *Phys. Rev. Lett.* **93**, 191802 (2004).
- [7] *BABAR* Collaboration, B. Aubert *et al.*, *Phys. Rev. Lett.* **87**, 091801 (2001).
- [8] Belle Collaboration, K. Abe *et al.*, *Phys. Rev. Lett.* **87**, 091802 (2001).
- [9] S. Weinberg, *Phys. Rev. Lett.* **19**, 1264 (1967);  
A. Salam, p.367 of *Elementary Particle Theory*, ed. N. Svartholm (Almquist and Wiksells, Stockholm, 1969);  
S.L. Glashow, J. Iliopoulos, and L. Maiani, *Phys. Rev.* **D 2**, 1285 (1970).
- [10] N. Cabibbo, *Phys. Rev. Lett.* **10**, 531 (1963).

- [11] L.L. Chau and W.-Y. Keung, Phys. Rev. Lett. **53**, 1802 (1984).
- [12] L. Wolfenstein, Phys. Rev. Lett. **51**, 1945 (1983).
- [13] C. Jarlskog and R. Stora, Phys. Lett. **B 208**, 268 (1988).
- [14] G. Buchalla, A. J. Buras, and M. .E. Lautenbacher, Rev. Mod. Phys. **68**, 1125 (1996).
- [15] M. Beneke, G. Buchalla, M. Neubert, and C. .T. Sachrajda, Nucl. Phys. **B 591**, 313 (2000).
- [16] J. D. Bjorken, Nucl. Phys. **B Proc. Suppl. 11**, 325 (1989).
- [17] M. Beneke, M. Neubert, Nucl.Phys. **B 675**, 333 (2003).
- [18] M. Gronau and D. London, Phys. Rev. Lett. **65**, 3381 (1990).
- [19] Y. Nir and H. R. Quinn, Phys. Rev. Lett. **67**, 541 (1991).
- [20] D. Zeppenfeld, Z. Phys. **C 8**, 77 (1981).
- [21] R. Fleischer, Z. Phys. **C 62**, 81 (1994);
- [22] N. G. Deshpande and X.-G. He, Phys. Rev. Lett. **74**, 26 (1995).
- [23] C.W. Chiang, M. Gronau, Z.L. Luo, J.L. Rosner, D.A Suprun, Phys. Rev. **D69**, 034001 (2004).
- [24] M. Neubert, Phys. Lett. **B 424**, 152 (1998).
- [25] R. Aleksan, P.-F. Giraud, V. Morenas, O. Pene and A.S. Safir, Phys. Rev. **D67** 094019 (2003).

- [26] D. Du, J. Sun, D. Yang and G. Zhu, Phys. Rev. **D67**, 014023 (2003).
- [27] CLEO Collaboration (E. Eckhart *et al.*), Phys. Rev. Lett. **89**, 251801 (2002).
- [28] BABAR Collaboration, B. Aubert *et al.*, Phys. Rev. Lett. **91**, 201802 (2003).
- [29] Belle Collaboration (K. Abe *et al.*), BELLE-CONF-0317 EPS-ID: 535 (2003);  
LP03-ID: 284 (2003).
- [30] H. Y. Cheng, C. K. Chua and A. Soni, Phys. Rev. **D 71**, 014030 (2005).
- [31] BABAR Collaboration, B. Aubert *et al.*, Nucl. Instrum. Methods **A479**, 1-116  
(2002).
- [32] BABAR Collaboration, F. Anulli *et al.*, Nucl. Instrum. Methods **A494**, 455-463  
(2002).
- [33] CLEO Collaboration (S. Kopp *et al.*) Phys. Rev. **D63**, 092001 (2001).
- [34] S.M. Spanier, BABAR Analysis Document #303 (2001).
- [35] J. Blatt and V. Weisskopf, “*Theoretical Nuclear Physics*”, John Wiley & Sons,  
New York, (1956).
- [36] F. von Hippel and C. Quigg, Phys. Rev. **D5**, 624 (1972).
- [37] W.M. Dunwoodie, “*Suggestion for the Parameterization of Dalitz Plot Efficiency*”,  
[http://www.slac.stanford.edu/~wmd/bbkinematics/dalitz\\_efficiency.note](http://www.slac.stanford.edu/~wmd/bbkinematics/dalitz_efficiency.note)  
(2002).

- [38] G.J. Gounaris and J.J. Sakurai, Phys. Rev. Lett. **21** 244, (1968).
- [39] S. Gardner and H.B. O'Connell, Phys. Rev. **D59**, 076002 (1999).
- [40] P. Estabrooks, Phys. Rev. **D 19**, 2678 (1979).
- [41] D. Aston *et al.*, Nucl. Phys. **B 296**, 493 (1988).
- [42] W.M. Dunwoodie,  
[http://www.slac.stanford.edu/~wmd/kpi\\_swave\\_fit.note](http://www.slac.stanford.edu/~wmd/kpi_swave_fit.note), (2002).
- [43] E.P. Wigner, Phys. Rev. **70** 15 (1946);  
E.P. Wigner and L. Eisenbud, Phys. Rev. **72** 29 (1947).
- [44] A. Abele *et al.*, Phys. Rev. **D 57**, 3860 (1998).
- [45] L.M. Barkov *et al.* (OLYA, CMD Collaboration), Nucl. Phys. **B256**, 365 (1985).
- [46] ALEPH Collaboration, (R. Barate *et al.*), Z. Phys. **C76**, 15 (1997).
- [47] J.H. Kühn and A. Santamaria, Z. Phys. **C48**, 445 (1990).
- [48] CMD-2 Collaboration, (R.R. Akhmetshin *et al.*), Phys. Lett. **B527**, 161 (2002).
- [49] DM2 Collaboration, (D. Bisello *et al.*), Phys. Lett. **B220**, 321 (1989).
- [50] ALEPH Collaboration, ALEPH 2002-030 CONF 2002-019, (July 2002).
- [51] M. Davier, S. Eidelman, A. Höcker and Z. Zhang, LAL-02-81, Eur. Phys. J. **C27**, 497-521 (2003).
- [52] N. Arnaud, M.T. Graham, W. Gradl, A. Höcker, S. Laplace, A. Mihalyi, Y. Pan, J. Wu, and S.L. Wu, *BABAR* Analysis Document #637 (2003).

- [53] E791 Collaboration (E.M. Aitala *et al.*). Phys. Rev. Lett. **89**, 121801 (2002).
- [54] BELLE Collaboration (K. Abe *et al.*). BELLE-CONF-0338; EPS-ID 577 (2003).
- [55] S. Agostinelli, *et al.*, Nucl. Instrum. Methods **A506**, 250-303 (2002).
- [56] T. Sjostrand, PYTHIA 5.7 and JETSET 7.4, CERN-TH-7112-93 (1995).
- [57] D.J. Lange, Nucl. Instrum. Methods **A462**, 152-155 (2001).
- [58] F. Martínez-Vidal *et al.*, *BABAR* Analysis Document #102 (2001).
- [59] G. Mancinelli, S. M. Spanier, *BABAR* Analysis Document #116 (2001).
- [60] A. Höcker, S. Laplace F. Le Diberder, V. Shelkov *et al.*, *BABAR* Analysis Document #141 (2001).
- [61] N. Danielson, A. Höcker, H.M. Lacker, F. Le Diberder, R. Liu, J. Ocariz, M. Pivk, L. Roos, J. Wu, *BABAR* Analysis Document #346 (2001).
- [62] P. Gay, B. Michel, J. Proriol, and O. Deschamps, “*Tagging Higgs Bosons in Hadronic LEP-2 Events with Neural Networks.*”, In Pisa 1995, New computing techniques in physics research, 725 (1995).
- [63] R. Aleksan, P.F. Giraud, A. Höcker, S. Laplace, F. Le Diberder, R. Liu, H. Li, Y. Pan, V. Shelkov, J. Stark, J. von Wimmersperg-Toeller, J. Wu, S.L. Wu and C. Yèche, *BABAR* Analysis Document #350 (2003).
- [64] J. Smith, A. Soffer and R. Waldi, *BABAR*Note 497 (1999).
- [65] M. Pivk, Thesis, LPNHE and Université de Paris VI (2003).

- [66] J. Albert,  
<http://babar-hn.slac.stanford.edu:5090/HyperNews/get/EHBDOC/272/1.html>  
(2001).
- [67] A. Gritsan and L.M. Mir, *BABAR* Analysis Document #483 (2003);  
A. Gritsan, Y. Groysman and L.M. Mir, *BABAR* Analysis Document #604  
(2003);  
A.J. Bevan, G.A Schott, C. Touramanis, C. Yeche, *BABAR* Analysis Document  
#634 (2003).
- [68] D. Bowerman, J. Gaillard, I.G. Eschrich, G. Morton, *BABAR* Analysis Document  
#814 (2004).
- [69] J. P. Burke, *BABAR* Analysis Document #635 (2004).
- [70] *BABAR* Collaboration, *Phys. Rev. Lett.* **91**, 171802, (2003).
- [71] B. Cheng, H. Li, A. Mihalyi, S.L. Wu, *BABAR* Analysis Document #892 (2004).
- [72] G. Schott, S. Emmerly, *BABAR* Analysis Document #692 (2004).
- [73] J.E. Gaiser *et al.*, *Phys. Rev.* **D34**, 711 (1986).
- [74] K.S. Cranmer, *Comput. Phys. Commun.* **136**, 198 (2001), hep-ex/0011057,  
ALEPH 99-144 (1999).
- [75] ARGUS Collaboration, H. Albrecht *et al.*, *Z. Phys.* **C48**, 543 (1990).
- [76] J. Malclès, J. Ocariz, *BABAR* Analysis Document #952 (2004).
- [77] M. Pivk and F.R. Le Diberder, physics/0402083 (2004).